



HAL
open science

A method based on poloidal-toroidal potentials applied to the von Kármán flow in a finite cylinder geometry

Piotr Boronski

► **To cite this version:**

Piotr Boronski. A method based on poloidal-toroidal potentials applied to the von Kármán flow in a finite cylinder geometry. Fluid Dynamics [physics.flu-dyn]. Ecole Polytechnique X, 2005. English. NNT: . tel-00162594

HAL Id: tel-00162594

<https://pastel.hal.science/tel-00162594>

Submitted on 14 Jul 2007

HAL is a multi-disciplinary open access archive for the deposit and dissemination of scientific research documents, whether they are published or not. The documents may come from teaching and research institutions in France or abroad, or from public or private research centers.

L'archive ouverte pluridisciplinaire **HAL**, est destinée au dépôt et à la diffusion de documents scientifiques de niveau recherche, publiés ou non, émanant des établissements d'enseignement et de recherche français ou étrangers, des laboratoires publics ou privés.



École Polytechnique

THÈSE

présentée pour l'obtention du grade de

Docteur de l'École Polytechnique
Specialité: Mécanique des fluides

par

Piotr BORONSKI

sujet:

MÉTHODE DES POTENTIELS POLOÏDAL-TOROÏDAL APPLIQUÉE À L'ÉCOULEMENT DE VON KÁRMÁN EN CYLINDRE FINI

Présentée le 23 septembre 2005 devant le jury composé de :

M. Marc BRACHET	Rapporteur
M. Olivier DAUBE	Invité
M. François DAVIAUD	Examineur
M. Emmanuel DORMY	Examineur
M. Pierre HALDENWANG	Examineur
M. Jacques LÉORAT	Invité
M. Francisco MARQUES	Rapporteur
Mme. Laurette S. TUCKERMAN	Directeur de thèse



**A METHOD BASED ON POLOIDAL-TOROIDAL
POTENTIALS APPLIED TO THE VON KÁRMÁN FLOW IN A
FINITE CYLINDER GEOMETRY**

by

Piotr BOROŃSKI

A dissertation submitted for the degree of

Doctor of Philosophy
(Fluid Mechanics)

at the

École Polytechnique
Orsay, France

(Defended on September 23, 2005)

Contents

1	Introduction	1
1.1	Motivation	1
1.2	Outline of this thesis	4
1.3	Magnetohydrodynamic equations	6
1.3.1	Maxwell equations	6
1.3.2	Navier-Stokes equations	8
1.3.3	Magnetohydrodynamics equations	9
1.4	Dynamo effect	10
1.4.1	Concluding remarks	15
I	System description	17
2	The von Kármán flow	19
2.1	Brief overview of studies	19
2.1.1	History	19
2.1.2	Stability analysis	20
2.1.3	Turbulence	21
2.2	Mathematical model	21
2.2.1	System description	21
2.2.2	Dimensionless equations	23
2.2.3	Equations of magnetohydrodynamics	24
3	Poloidal-toroidal decomposition	25
3.1	Motivation	25
3.2	Poloidal-toroidal decomposition and the gauge freedom	26
3.3	Potential form of the MHD equations	27
3.4	Compatibility condition	28
3.4.1	Equivalence of potential and primitive variable formulation	28
3.4.2	Hydrodynamic compatibility condition	30
3.4.3	Magnetic compatibility condition	31
3.5	Hydrodynamic boundary conditions	31
3.6	Magnetic boundary conditions	33
3.6.1	General case	33

3.6.2	Conductor/vacuum configuration	36
3.7	Discussion	37
3.7.1	Advantages/disadvantages	37
3.7.2	Concluding remarks	38
II	Numerical method – Spectral solver	41
4	Spectral discretization	43
4.1	Introduction	43
4.1.1	Local methods	43
4.1.2	Spectral precision	43
4.1.3	Advantages and limitations of spectral methods	44
4.2	Azimuthal direction	45
4.3	Axial direction	46
4.4	Radial direction	48
4.4.1	Regularity condition	48
4.4.2	Regularization of an arbitrary spectral basis	51
4.4.3	Regular basis of radial polynomials	52
4.4.4	Differential operators	53
4.5	Discretization in 3D	54
4.6	Boundary condition regularization	55
4.6.1	Overview of singularity treatment techniques	55
4.6.2	Boundary velocity regularization	57
5	Spectral solver	61
5.1	Introduction	61
5.2	Poisson solver	61
5.2.1	τ method – one dimension	62
5.2.2	Partial diagonalization method – two/three dimensions	65
5.2.3	Solving the Helmholtz equation – τ -method in radial direction	67
5.3	High order PDE solver	70
5.3.1	2D Navier-Stokes in streamfunction formulation	71
5.3.2	Multi-Poisson solver	72
5.4	Influence matrix	76
5.4.1	Green function method	76
5.4.2	Discrete Green functions method – influence matrix	79
5.4.3	Towards an invertible influence matrix	95
5.5	Tests - Stokes problem in 2D	101
5.5.1	Polynomial solutions	102
5.5.2	Non-polynomial case	104
5.6	Towards an MHD solver	108
5.6.1	External solution in vacuum	109
5.6.2	Continuity conditions	111

5.6.3	Multi-Poisson solver for induction equation	113
5.6.4	Influence matrix for the magnetic problem	114
5.6.5	Elimination of external solution	118
5.7	Concluding remarks	119
6	Stability/Validation	121
6.1	Nonlinear term	121
6.1.1	Evaluation of $-\mathbf{u} \times \boldsymbol{\omega}$	122
6.1.2	Regularity of the nonlinear term	123
6.2	Time integration	127
6.3	Tests	131
6.3.1	Axisymmetric rotor-stator configuration	131
6.3.2	First instability in 3D	132
6.4	Spectral convergence	134
6.5	Parallelization	135
6.6	Concluding remarks	136
7	Applications & perspectives	137
7.1	Turbulent bifurcation	137
7.1.1	The effect of blades	138
7.1.2	Preliminary results	139
7.2	Axisymmetric turbulence	150
7.2.1	Theoretical framework	150
7.2.2	Experimental confirmations	151
7.2.3	Numerical results	152
7.2.4	Imposed axisymmetry	154
8	Concluding remarks	159
A	Recursive formulas for radial polynomials	163
B	Remarks concerning MPI parallelization	165

Résumé

Motivation.

Au début du 20^{ème} siècle, Larmor [42] a proposé que les champs magnétiques de la terre et d'autres objets célestes proviennent d'un effet dynamo auto-entretenu : un écoulement d'un fluide conducteur générerait un champ magnétique qui maintiendrait à son tour l'écoulement. La plupart des travaux qui ont suivi cette prédiction ont été théoriques. Ces travaux et, plus tard, des travaux numériques, ont été menés en géométrie sphérique, pour des raisons de commodité théorique et aussi de pertinence géophysique.

Il existe actuellement un effort international important pour vérifier expérimentalement l'existence d'une dynamo fluide auto-entretenu. Une collaboration d'équipes françaises dirigées par F. Daviaud (CEA-Saclay), S. Fauve (ENS-Paris) et J.-F. Pinton (ENS-Lyon) a participé à la construction et l'exploitation d'une expérience "lourde" en sodium liquide au CEA-Cadarache, et une expérience "légère" en eau au CEA-Saclay. Dans les deux expériences, le fluide est contenu dans un cylindre, et mis en mouvement par des disques en contra-rotation (écoulement dit de von Kármán), renforcés par des pales. Ce projet est nommé VKS.

La simulation numérique de la configuration de l'expérience VKS permettrait d'apporter une meilleure compréhension au comportement très compliqué d'un champ magnétique couplé à un champ de vitesse en régime turbulent et aussi de calculer des nombreuses quantités qui, pour des raisons techniques, ne peuvent pas être mesurées expérimentalement. Notre motivation est de développer et implémenter un code numérique adéquat au problème ici présenté.

Plan de la thèse

Chapitre 1. Dans ce chapitre introductif, après avoir expliqué notre motivation pour cette recherche, nous présentons les équations de Maxwell et de Navier-Stokes qui nous servent à dériver les équations de la magnétohydrodynamique. Après avoir résumé les principaux faits théoriques concernant les théorèmes anti-dynamos nous présentons, d'une manière qualitative, un mécanisme d'induction (dit alpha-omega) par lequel l'effet dynamo peut se produire dans une configuration de l'expérience VKS.

Chapitre 2. Après une discussion de l'état de l'art concernant des études menées dans un contexte de l'écoulement de von Kármán nous présentons le modèle mathématique de la configuration étudiée. Nous écrivons les équations et les conditions aux limites adimensionnées décrivant le problème.

Chapitre 3. Nous expliquons notre motivation pour l'utilisation de la formulation potentielle. Nous introduisons une décomposition poloïdale-toroïdale des champs de vitesse et magnétique et nous écrivons les équations et les conditions aux limites dans une formulation potentielle.

Chapitre 4. Nous présentons des détails concernant la discrétisation spectrale dans chacune des directions spatiales. Nous considérons notamment le problème de la singularité à l'axe du cylindre présent dans le système des coordonnées polaires ainsi que les méthodes pour traiter des conditions aux limites discontinues.

Chapitre 5. Dans ce chapitre nous décrivons l'algorithme spectral pour résoudre les équations de magnétohydrodynamique en formulation potentielle. Nous mettons en évidence une relation entre la méthode classique de fonction de Green et la méthode de *matrice d'influence* que nous utilisons pour imposer les conditions aux limites couplées. Après avoir validé le code dans le régime hydrodynamique (sans champ magnétique) nous proposons une nouvelle méthode pour assurer les conditions de continuité du champ magnétique à la frontière entre le cylindre et le vide.

Chapitre 6. Dans ce chapitre nous discutons les différents problèmes concernant la stabilité de notre code. Nous proposons une méthode évitant des contributions singulières qui peuvent apparaître en géométrie cylindrique pendant l'évaluation du terme non-linéaire utilisant une approche pseudo-spectrale. Nous argumentons aussi notre choix du schéma d'intégration temporelle. Finalement, nous validons notre solveur Navier-Stokes sur les cas-tests bien documentés dans la littérature.

Chapitre 7. Dans ce chapitre nous présentons deux projets : dans le premier, nous nous intéressons au phénomène d'une bifurcation turbulente qui a été observée récemment dans l'expérience VKE (von Kármán Eau). Dans le second projet, nous simulons la turbulence axisymétrique et nous comparons les résultats avec les prédictions théoriques et des observations expérimentales. Les résultats que nous présentons dans ce chapitre sont préliminaires et peuvent être considérés comme des perspectives pour la future exploitation de notre code.

Chapitre 8. Conclusions concernant les chapitres 3 à 7.

Équations MHD

Équations de Maxwell

Les équations de Maxwell décrivent la dynamique des champs magnétique et électrique.

$$\nabla \times \mathbf{E} = -\frac{\partial \mathbf{B}}{\partial t} \quad (1a)$$

$$\nabla \times \mathbf{H} = \mathbf{j} \quad (1b)$$

$$\nabla \cdot \mathbf{D} = \chi \quad (1c)$$

$$\nabla \cdot \mathbf{B} = 0 \quad (1d)$$

où $\mathbf{E}, \mathbf{H} \equiv \mathbf{B}/\mu$ sont les champs électrique et magnétique, $\mathbf{D} = \epsilon \mathbf{E}$, \mathbf{B} sont les champs d'induction électrique et magnétique et χ et \mathbf{j} sont les densités des charges électriques libres et des courants respectivement. Les quantités μ et ϵ sont la perméabilité magnétique et la constante diélectrique. Dans l'équation (1b) nous avons négligé le courant de déplacement $\frac{\partial \mathbf{D}}{\partial t}$ (approximation quasi-stationnaire : pas d'ondes électro-magnétiques).

L'expression pour \mathbf{j} est donnée par la loi d'Ohm généralisée :

$$\mathbf{j} = \sigma (\mathbf{E} + \mathbf{u} \times \mathbf{B}), \quad (2)$$

où \mathbf{u} est la vitesse du milieu conducteur (ici du fluide) et σ est sa conductivité électrique. Les conditions à la frontière entre les deux milieux non-ferromagnétiques peuvent être écrites sous la forme suivante :

$$[\hat{\mathbf{n}} \times \mathbf{E}] = 0 \quad (3a)$$

$$[\hat{\mathbf{n}} \times \mathbf{B}] = 0 \quad (3b)$$

où la notation $[\cdot]$ indique un saut d'une quantité à la frontière entre deux domaines et $\hat{\mathbf{n}}$ est un vecteur unité normal à la surface de cette frontière.

Équations de Navier-Stokes

Les équations de Navier-Stokes régissant l'évolution d'un fluide incompressible sont :

$$\frac{\partial \mathbf{u}}{\partial t} + (\mathbf{u} \cdot \nabla) \mathbf{u} = -\frac{1}{\rho} \nabla p + \frac{1}{\rho} \mathbf{f} + \nu \Delta \mathbf{u}$$

$$\nabla \cdot \mathbf{u} = 0$$

où \mathbf{u} est la vitesse du fluide, p est la pression et où \mathbf{f} représente les forces externes. Les quantités ρ et ν sont la densité du fluide et sa viscosité cinématique. Pour un fluide conducteur en présence d'un champ magnétique cette force correspond à la *force de Laplace* :

$$\mathbf{f} = \mathbf{j} \times \mathbf{B}. \quad (5)$$

But de la thèse

La solution numérique d'un problème dynamo constitue une tâche particulièrement difficile. Des nombreuses contraintes théoriques concernant la symétrie d'un écoulement capable de produire l'effet dynamo ont été démontrées et sont connues sous le nom de *théorèmes anti-dynamos*, le plus connu étant le théorème de Cowling [16]. Ces théorèmes ont exclu les champs magnétiques axisymétriques ou indépendants d'une des coordonnées Cartésiennes. Ils interdisent aussi les écoulements plans et toroïdaux. En conséquence, les simulations de l'effet dynamo doivent être effectuées dans un régime tri-dimensionnel. À la difficulté d'une simulation tridimensionnelle s'ajoutent les complications d'une géométrie confinée (ici un cylindre), de la singularité sur l'axe du cylindre, de la condition de divergence nulle traduisant l'incompressibilité du champ de vitesse du fluide et de l'absence de monopôles magnétiques dans le cas du champ magnétique, ainsi que du couplage entre les deux champs. Dans cette thèse nous décrivons un algorithme de résolution des équations de Navier-Stokes pour un fluide incompressible et nous proposons une méthode qui rend possible l'extension du code au problème magnétique.

Modèle mathématique

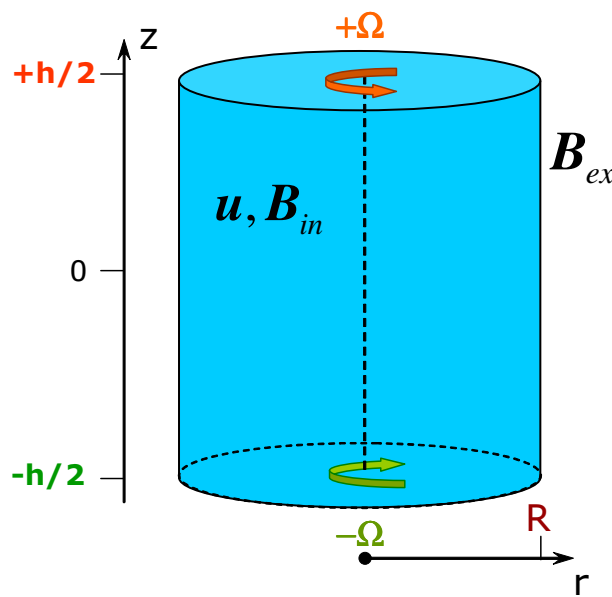


Figure 1: Modèle schématique de la géométrie de la configuration von Kármán cylindrique.

Nous considérons un fluide conducteur enfermé dans un récipient cylindrique de rayon $R = 1$ et de hauteur h . Le fluide est mis en mouvement par les deux bases du cylindre tournant avec les vitesses données par Ω_+ et Ω_- . Les indices $+$ et $-$ correspondent respectivement aux disques situés à $+h/2$ et $-h/2$. La paroi latérale est immobile. Après avoir combiné les équations (1) et (4) on peut écrire les équations de la magnétohydrodynamique régissant l'évolution

temporelle des champs magnétique et de vitesse dans une forme adimensionnée:

$$\left\{ \begin{array}{l} \frac{\partial \mathbf{u}}{\partial t} + (\mathbf{u} \cdot \nabla) \mathbf{u} = -\nabla \left(p + \frac{B^2}{2} \right) + (\mathbf{B} \cdot \nabla) \mathbf{B} + \frac{1}{Re} \Delta \mathbf{u}, \\ \frac{\partial \mathbf{B}}{\partial t} = \nabla \times (\mathbf{u} \times \mathbf{B}) + \frac{1}{Rm} \Delta \mathbf{B}, \\ \nabla \cdot \mathbf{u} = 0, \\ \nabla \cdot \mathbf{B} = 0. \end{array} \right. \quad \begin{array}{l} (6a) \\ (6b) \\ (6c) \\ (6d) \end{array}$$

où $Re \equiv \frac{R^2 \Omega}{\nu}$ est le nombre de Reynolds et $Rm \equiv \mu \sigma R^2 \Omega$ est le nombre de Reynolds magnétique. Les conditions aux limites sont l'adhérence (7) pour la vitesse et la continuité (8a) pour le champ magnétique :

$$\left\{ \begin{array}{l} \mathbf{u}|_{r=1} = 0 \\ \mathbf{u}|_{z=\pm \frac{h}{2}} = r \Omega_{\pm} \hat{\mathbf{e}}_{\theta} \end{array} \right. \quad \begin{array}{l} (7a) \\ (7b) \end{array}$$

$$\left\{ \begin{array}{l} [\mathbf{B}] \equiv (\mathbf{B}_{in} - \mathbf{B}_{ex})|_{\partial} = 0 \\ \lim_{(r,z) \rightarrow \infty} \mathbf{B}_{ex} = 0 \end{array} \right. \quad \begin{array}{l} (8a) \\ (8b) \end{array}$$

où $|_{\partial}$ indique une quantité évaluée à la surface du cylindre. L'équivalence de (3) et (8a) est démontrée dans la section 3.6.

Décomposition poloïdale-toroïdale

Un champ vectoriel solénoïdal peut être représenté par deux potentiels scalaires. Pour les champs de vitesse et magnétique nous avons :

$$\mathbf{u} = \nabla \times (\psi_u \hat{\mathbf{e}}_z) + \nabla \times \nabla \times (\phi_u \hat{\mathbf{e}}_z), \quad (9a)$$

$$\mathbf{B} = \nabla \times (\psi_B \hat{\mathbf{e}}_z) + \nabla \times \nabla \times (\phi_B \hat{\mathbf{e}}_z), \quad (9b)$$

où ψ_u, ψ_B sont les potentiels toroïdaux du champs de vitesse et du champ magnétique respectivement et ϕ_u, ϕ_b sont les potentiels poloïdaux correspondants. Les écoulements toroïdal et poloïdal sont représentés sur la figure 2. Le but de la décomposition toroïdale-poloïdale est d'assurer le solénoïdité de \mathbf{u} et de \mathbf{B} .

Après avoir substitué (9a) dans (6a) et (9b) dans (6b) les potentiels $\psi_u, \phi_u, \psi_B, \phi_B$ peuvent être découplés dans les termes provenant de la diffusion : pour la vitesse \mathbf{u} nous écrivons les équations pour la composante $\hat{\mathbf{e}}_z$ du rotationnel et du double rotationnel de (6a) et pour le champ magnétique nous considérons la composante $\hat{\mathbf{e}}_z$ de l'équation (6b) et de son rotationnel (6b).

Problème hydrodynamique :

$$\hat{\mathbf{e}}_z \cdot \nabla \times (6a) \Rightarrow (\partial_t - Re^{-1} \Delta) \Delta_h \psi_u = \hat{\mathbf{e}}_z \cdot \nabla \times \mathbf{s}_u \quad (10a)$$

$$\hat{\mathbf{e}}_z \cdot \nabla \times \nabla \times (6a) \Rightarrow (\partial_t - Re^{-1} \Delta) \Delta \Delta_h \phi_u = -\hat{\mathbf{e}}_z \cdot \nabla \times \nabla \times \mathbf{s}_u \quad (10b)$$

$$\mathbf{s}_u \equiv (\mathbf{u} \cdot \nabla) \mathbf{u} - (\mathbf{B} \cdot \nabla) \mathbf{B} \quad (10c)$$

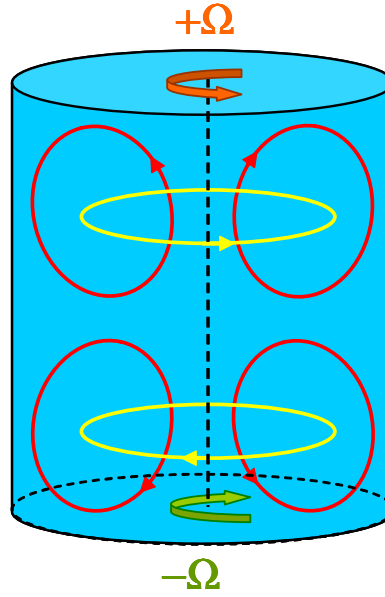


Figure 2: Structure qualitative des écoulements toroïdal (jaune/claire) et poloïdal (rouge/sombre) dans la configuration axisymétrique en contra-rotation.

Les conditions d'adhérence pour le champ de vitesse peuvent s'écrire sous la forme suivante :

$$\left. \begin{aligned} r^{-1}\partial_{\theta}\psi_u + \partial_z\partial_r\phi_u &= 0 & (11a) \\ \partial_r\psi_u &= 0 & (11b) \\ -\Delta_h\phi_u &= 0 & (11c) \\ \phi_u &= 0 & (11d) \\ \partial_{rz}^2\Delta_h\psi_u - \frac{1}{r}\partial_{\theta}\Delta\Delta_h\phi_u &= 0 & (11e) \end{aligned} \right\} r = 1$$

$$\left. \begin{aligned} \psi_u &= -\frac{\Omega_{\pm}\pi r^2}{2} & (12a) \\ \partial_z\phi_u &= 0 & (12b) \\ -\Delta_h\phi_u &= 0 & (12c) \end{aligned} \right\} z = \pm\frac{h}{2}$$

où l'équation (11e) est la *condition de compatibilité*¹ par laquelle les équations en forme potentielle doivent être complétées pour assurer que la solution correspond à celle des équations de Navier-Stokes (6a).

Problème magnétique (conducteur/vide) :

$$\hat{\mathbf{e}}_z \cdot (6b) \Rightarrow (\partial_t - Rm^{-1}\Delta)\Delta_h\phi_B = \hat{\mathbf{e}}_z \cdot \mathbf{s}_B \quad (13a)$$

$$\hat{\mathbf{e}}_z \cdot \nabla \times (6b) \Rightarrow (\partial_t - Rm^{-1}\Delta)\Delta_h\psi_B = \hat{\mathbf{e}}_z \cdot \nabla \times \mathbf{s}_B \quad (13b)$$

$$\mathbf{s}_B \equiv -\nabla \times (\mathbf{u} \times \mathbf{B}) \quad (13c)$$

$$\Delta\phi^{vac} = 0 \quad (13d)$$

¹Cette forme est valide pour le cas hydrodynamique ($\mathbf{B} = 0$).

Les conditions aux limites sont :

$$\left. \begin{aligned} \frac{1}{r} \partial_\theta \psi_B + \partial_r (\partial_z \phi_B - \phi^{vac}) &= 0 & (14a) \\ \partial_r \psi_B &= 0 & (14b) \\ \Delta \phi_B &= 0 & (14c) \\ \partial_z \phi_B - \phi^{vac} &= 0 & (14d) \\ \left(\partial_t - Rm^{-1} (\Delta - r^{-2}) \right) \left(r^{-1} \partial_\theta \psi_B + \partial_r \partial_z \phi_B \right) + Rm^{-1} \frac{2}{r^3} \partial_z \partial_\theta \phi_B &= 0 & (14e) \end{aligned} \right\} r = 1$$

$$\left. \begin{aligned} \frac{1}{r} \partial_\theta \psi_B + \partial_r (\partial_z \phi_B - \phi^{vac}) &= 0 & (15a) \\ -\partial_r \psi_B + \frac{1}{r} \partial_\theta (\partial_z \phi_B - \phi^{vac}) &= 0 & (15b) \\ \Delta_h \phi_B + \partial_z \phi^{vac} &= 0 & (15c) \end{aligned} \right\} z = \pm \frac{h}{2}$$

où (14e) correspond à la condition de compatibilité magnétique. La dérivation de conditions aux bords (11), (12), (14), (15) est présentée dans le chapitre 3.

La résolution numérique du problème donné par (10)-(15) est le sujet principal de cette thèse. L'avantage de la formulation potentielle est surtout l'imposition de la condition de solénoïdité des champs ($\nabla \cdot \mathbf{u} = \nabla \cdot \mathbf{B} = 0$) par construction – une tâche qui est difficile à accomplir dans les méthodes basées sur les variables primitives. La difficulté majeure est l'ordre polynomial élevé des équations et des conditions aux limites ainsi que le couplage entre certaines conditions.

Discrétisation spatiale

Nous utilisons la décomposition spectrale dans les trois directions spatiales. Dans la direction azimutale, ce sont les fonctions trigonométriques qui sont le mieux adaptées. Dans la direction axiale, nous utilisons les polynômes de Chebyshev $\mathcal{T}_k(z)$. Pour la dépendance radiale, la régularité de la solution à l'origine du système des coordonnées nécessite l'utilisation des fonctions adaptées à la géométrie polaire. Suivant Matsushima & Marcus [58] nous utilisons les polynômes radiaux $Q_n^m(r)$ satisfaisant aux conditions de régularité entre leur ordre polynomial n et la parité du mode de Fourier m correspondant :

$$\begin{aligned} \text{parité} & \quad n + m \text{ doit être pair} \\ \text{ordre} & \quad n \geq |m| \end{aligned} \tag{16}$$

Finalement une fonction scalaire f en géométrie de cylindre fini peut être écrite sous la forme suivante:

$$f(r, \theta, z) \approx \sum_{m=-\lfloor \frac{M}{2} \rfloor}^{\lfloor \frac{M}{2} \rfloor} \sum_{k=0}^{K-1} \sum_{\eta=0}^{N-\lfloor \frac{m}{2} \rfloor-1} [\hat{f}^m]_{k\eta} e^{im\theta} Q_{m+2\eta}^m(r) \mathcal{T}_k\left(\frac{2z}{h}\right) \tag{17}$$

où M, K, N sont les résolutions spatiales dans les directions azimutale, axiale et radiale respectivement. La forme des polynômes radiaux $Q_n^m(r)$ est donnée dans la section 4.4.

Régularisation des conditions aux bords

La situation où le bord latéral est immobile et les bases du cylindre sont en rotation représente une singularité (discontinuité) de vitesse dans les points de jonction des disques placés à $z = \pm \frac{h}{2}$ avec le bord situé à $r = 1$. Afin d'éviter l'effet de Gibbs, il est indispensable d'entreprendre une des approches que nous discutons dans la section 4.6. Dans notre méthode nous utilisons la régularisation des conditions aux limites singulières en variant la vitesse azimutale $r\Omega \equiv r\Omega(r)$ de sorte que les vitesses des disques s'accordent avec le bord latéral. Pour cela, deux méthodes d'appliquer la régularisation s'imposent : varier le profil de la vitesse azimutale sur les bases du cylindre $u_\theta(r, z = \pm \frac{h}{2})$ ou sur le bord latéral $u_\theta(z, r = 1)$ (voir fig. 3)

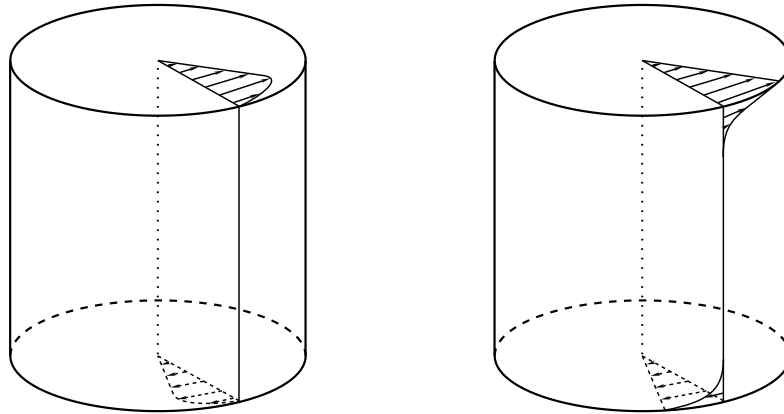


Figure 3: Les profils régularisés utilisés pour éliminer la discontinuité de vitesse dans les coins à $r = 1, z = \pm \frac{h}{2}$. Gauche – régularisation sur les disques : $u_\theta|_{z=\pm \frac{h}{2}}(r) = r \left(1 - e^{\frac{r-1}{\delta}}\right)$. Droite – régularisation sur le bord latéral: $u_\theta|_{r=1}(z) = \Omega_+ e^{-(1-\frac{2z}{h})/\delta} + \Omega_- e^{-(1+\frac{2z}{h})/\delta}$, $u_\theta|_{z=\pm \frac{h}{2}}(r) = r\Omega_\pm$

Solveur spectral

La partie la plus importante de cette thèse est la présentation de la méthode de solution du problème en formulation potentielle (10)-(15). Dans le chapitre 5 nous présentons de façon détaillée l'algorithme spectral appliqué au cas hydrodynamique ($\mathbf{B} = 0$). Pour simplifier la notation nous posons $\psi_u \equiv \psi$, $\phi_u \equiv \phi$, $\mathbf{s}_u \equiv \mathbf{s}$. L'idée générale est de résoudre l'équation (10) en plusieurs étapes intermédiaires :

$$(\partial_t - Re^{-1}\Delta)\Delta_h\psi = \hat{\mathbf{e}}_z \cdot \nabla \times \mathbf{s} \Leftrightarrow \begin{cases} E\hat{f}_\psi &= \widehat{rhs}_\psi \\ \Delta_h\hat{\psi} &= \hat{f}_\psi \end{cases} \quad (18)$$

et

$$(\partial_t - Re^{-1}\Delta)\Delta\Delta_h\phi = -\hat{\mathbf{e}}_z \cdot \nabla \times \nabla \times \mathbf{s} \Leftrightarrow \begin{cases} E\hat{f}_\phi &= \widehat{rhs}_\phi \\ \Delta\hat{f}_\phi &= \hat{g}_\phi \\ \Delta_h\hat{\phi} &= \hat{f}_\phi \end{cases} \quad (19)$$

où la notation $E, r\widehat{hs}$ apparaît après avoir discrétisé les équations en temps utilisant un schéma implicite de premier ordre (Euler) pour les termes linéaires et explicite de deuxième ordre (Adams-Bashforth) pour les termes non-linéaires :

$$\begin{aligned} E\widehat{f}_\psi &\equiv (\mathbb{1} - \Delta t R e^{-1} \Delta) \widehat{f}_\psi(r, z; t + \Delta t) \\ r\widehat{hs}_\psi &\equiv \widehat{f}_\psi(r, z; t) + \frac{\Delta t}{2} \widehat{\mathbf{e}}_z \cdot \nabla \times (3\mathbf{s}(r, z; t) - \mathbf{s}(r, z; t - \Delta t)) \\ E\widehat{g}_\phi &\equiv (\mathbb{1} - \Delta t R e^{-1} \Delta) \widehat{g}_\phi(r, z; t + \Delta t) \\ r\widehat{hs}_\phi &\equiv \widehat{g}_\phi(r, z; t) - \frac{\Delta t}{2} \widehat{\mathbf{e}}_z \cdot \nabla \times \nabla \times (3\mathbf{s}(r, z; t) - \mathbf{s}(r, z; t - \Delta t)) \end{aligned}$$

La notation avec "chapeau" (ex. $\widehat{\psi}$) signifie que la quantité représente une transformé de Fourier d'une fonction. Les équations (18)-(19) peuvent être résolues indépendamment pour chacun des modes de Fourier car les opérateurs différentiels ne couplent pas des modes de Fourier.

Certaines conditions aux limites peuvent être imposées directement aux étapes correspondant aux problèmes de Poisson ou de Helmholtz. Pour cela nous utilisons une méthode classique dite *méthode τ* (voir section 5.2). Toutes les conditions (notamment les conditions couplées) qui ne peuvent pas être imposées directement par la méthode- τ sont imposées en utilisant la technique de *matrice d'influence*. L'idée de base de cette méthode est de trouver une forme de conditions aux bords du type Dirichlet (qui peuvent être imposées directement par la méthode τ) équivalentes aux conditions originales.

Matrice d'influence

Afin de donner une idée sur le principe de la méthode de matrice d'influence on peut considérer un problème générique suivant :

$$\mathcal{L}f = g \quad ; \quad \mathcal{B}f|_{\partial} = \beta \quad (20)$$

où \mathcal{L} est un opérateur différentiel (ex. $\mathcal{L} \equiv E\Delta\Delta_h$), f est une solution recherchée (ex. $f \equiv \widehat{\phi}$) et g est le membre droit de l'équation (ex. $g \equiv r\widehat{hs}_\phi$). L'expression $\mathcal{B}f|_{\partial} = \beta$ correspond à des conditions aux bords trop compliquées pour pouvoir les satisfaire par la méthode τ (ex. conditions (11)-(12)).

Il est possible de trouver une fonction σ telle que le système suivant ait la même solution que (??) :

$$\mathcal{L}f = g \quad ; \quad \mathcal{D}f|_{\partial} = \sigma \quad (21)$$

L'opérateur \mathcal{D} agissant aux bords ne correspond plus aux conditions originales données par \mathcal{B} mais il a l'avantage que les conditions qu'il définit peuvent être imposées par la méthode τ . Afin de trouver la distribution des valeurs aux bords σ assurant l'équivalence entre (20) et (21) nous décomposons la solution f en deux parties – la solution particulière f^p et la solution homogène f^h :

$$f = f^p + f^h$$

satisfaisant à :

$$\mathcal{L}f^p = g \quad ; \quad \mathcal{D}f^p|_{\partial} = 0, \quad (22a)$$

$$\mathcal{L}f^h = 0 \quad ; \quad \mathcal{B}f^h|_{\partial} = \beta - \mathcal{B}f^p|_{\partial} \quad (22b)$$

où la solution particulière f^p assure la satisfaction de l'équation $\mathcal{L}f = g$ et la solution homogène f^h a comme but d'assurer la satisfaction des conditions aux bords $\mathcal{B}f|_{\partial} = \beta$. La méthode de matrice d'influence, qui nous permet de déterminer f^h , est une forme discretisée de la méthode de *fonction de Green*. Supposons que nous pourrions trouver une fonction de Green homogène $G^h(\mathbf{x}; \mathbf{x}')$ satisfaisant

$$\mathcal{L}G^h(\mathbf{x}; \mathbf{x}') = 0 \quad ; \quad \mathcal{B}G^h(\mathbf{x}; \mathbf{x}')|_{\mathbf{x}''} = \delta(\mathbf{x}'' - \mathbf{x}') \quad (23)$$

où les opérateurs \mathcal{L} , \mathcal{B} utilisent la différentiation par rapport à la variable \mathbf{x} . Dans ce cas la solution homogène f^h aurait la forme suivante:

$$f^h(\mathbf{x}) = \oint_S G^h(\mathbf{x}; \mathbf{x}') (\beta(\mathbf{x}') - \mathcal{B}f^p(\mathbf{x})|_{\mathbf{x}'}) da' \quad (24)$$

Il est aussi difficile de trouver G^h à partir de (23) que f^h directement à partir de (22b). L'avantage de G^h par rapport à f^h est que G^h ne dépend pas du temps et peut donc être déterminé une seule fois. La fonction f^h doit être déterminée à chaque pas de temps. Il existe une méthode analogue pour déterminer f^h sans calculer G^h explicitement. Il s'agit de trouver à la place de G^h une *fonction test* $T(\mathbf{x}; \mathbf{x}')$ satisfaisant

$$\mathcal{L}T(\mathbf{x}; \mathbf{x}') = 0 \quad ; \quad \mathcal{D}T(\mathbf{x}; \mathbf{x}')|_{\mathbf{x}''} = \delta(\mathbf{x}'' - \mathbf{x}') \quad (25)$$

La fonction $T(\mathbf{x}; \mathbf{x}')$ peut être facilement déterminée car les conditions aux bords dans (25) sont données par l'opérateur \mathcal{D} , donc ils sont imposable par la méthode τ . On montre dans la section 5.4.2 que la solution f^h peut être écrite comme:

$$f^h(\mathbf{x}) = \oint_S T(\mathbf{x}; \mathbf{x}') \sigma(\mathbf{x}') da' \quad (26)$$

où σ est donne par

$$\sigma(\mathbf{x}'') = \oint_S I^{-1}(\mathbf{x}''; \mathbf{x}') (\beta(\mathbf{x}') - \mathcal{B}f^p(\mathbf{x})|_{\mathbf{x}'}) da' \quad (27)$$

où $I(\mathbf{x}''; \mathbf{x}') \equiv \mathcal{B}T(\mathbf{x}; \mathbf{x}')|_{\mathbf{x}''}$ est une *fonction d'influence* qui correspond à la matrice d'influence dans une formulation discrète. Dans une simulation numérique les étapes correspondant aux (22a), (27) et (26) sont effectués à chaque pas de temps et les étapes (25) et $I \rightarrow I^{-1}$, qui sont les plus coûteuses en termes du temps de calcul, peuvent (et doivent) être effectuées une seule fois pendant la phase de pré-traitement.

Les détails de la construction de la matrice d'influence pour le problème (10)-(12) sont exposés dans la section 5.4.2. Dans la section 5.4.3 nous discutons le problème de l'inversibilité de la matrice d'influence : nous proposons une méthode de régularisation basée sur une décomposition en valeurs singuliers (SVD). Nous développons aussi une méthode de préconditionnement nécessaire pour diminuer le nombre de conditionnement \mathcal{C}_I . Pour la matrice correspondant à la résolution spatiale $(N = 96) \times (K = 192)$ cette méthode nous permet de réduire \mathcal{C}_I de $O(10^{20})$ à $O(10^8)$.

Validation du solveur de Stokes

Afin de valider la partie implicite du solveur (sans terme non-linéaire – équations de Stokes) avant de tester le cas complet (équations de Navier-Stokes) nous avons comparé les résultats numériques obtenus par le code avec la solution analytique. Pour les modes de Fourier $m = \{0,1,2\}$ nous avons trouvé une forme polynomiale de $\hat{\psi}_{poly}$, $\widehat{rhs}_{\psi}^{poly}$, $\hat{\phi}_{poly}$, $\widehat{rhs}_{\phi}^{poly}$ satisfaisant aux équations (18)-(19) et aux conditions aux bords (12)-(12). Posant $\widehat{rhs}_{\psi} \equiv \widehat{rhs}_{\psi}^{poly}$, $\widehat{rhs}_{\phi} \equiv \widehat{rhs}_{\phi}^{poly}$, nous avons calculé numériquement $\hat{\psi}$ et $\hat{\phi}$ et nous les avons comparé avec les solutions exactes $\hat{\psi}_{poly}$ et $\hat{\phi}_{poly}$. La figure 4 présente l'erreur relative définie comme :

$$\epsilon_{\psi} = \frac{\sup |\hat{\psi} - \hat{\psi}_{poly}|}{\sup |\hat{\psi}_{poly}|} ; \quad \epsilon_{\phi} = \frac{\sup |\hat{\phi} - \hat{\phi}_{poly}|}{\sup |\hat{\phi}_{poly}|}$$

Nous constatons que dans le cas d'une solution polynomiale, l'erreur est d'ordre $O(10^{-14})$ pour ϵ_{ψ} et d'ordre $O(10^{-12})$ pour ϵ_{ϕ} , ce qui est très près de la précision machine qui est d'ordre $O(10^{-15})$. Pour tester la satisfaction des équations pour un problème de Stokes, nous avons étudié l'erreur définie comme :

$$\epsilon_{eq_{\psi}} = \frac{\sup |E\Delta\hat{\psi} - \widehat{rhs}_{\psi}|}{\sup |\widehat{rhs}_{\psi}|} ; \quad \epsilon_{eq_{\phi}} = \frac{\sup |E\Delta\hat{\phi} - \widehat{rhs}_{\phi}|}{\sup |\widehat{rhs}_{\phi}|}$$

L'erreur relative de satisfaction des équations représenté sur la figure 4 (pour le mode de Fourier $m = 0$) est d'ordre $O(10^{-10})$ – $O(10^{-7})$ pour $\hat{\psi}$. Pour le potentiel poloïdal ϕ cette erreur est d'ordre $O(10^{-10})$ dans l'intérieur de la domaine et d'ordre $O(10^{-4})$ – $O(10^{-1})$ près des bords. Dans les sections 4.6 et 5.5 nous expliquons que la grande erreur près de la paroi pour le potentiel $\hat{\phi}$ est une conséquence d'une singularité dans les coins du cylindre de la solution du problème de Stokes et non pas de l'imprécision de la méthode numérique. Concernant

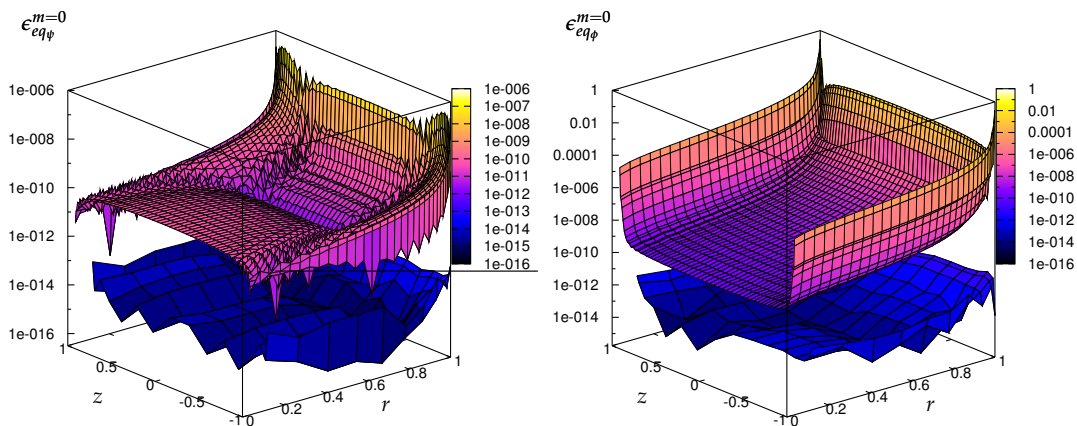


Figure 4: L'erreur de satisfaction des équations pour le mode de Fourier $m = 0$, après 100 itérations du solveur de Stokes. Résolution utilisée : $K = 64$, $N = 32$. **À gauche** : (surface en haut) $\epsilon_{eq_{\psi}}^{m=0}$ pour le problème de Stokes, (surface en bas) $\epsilon_{\psi}^{m=0}$ pour la solution polynomiale; **À droite** : (surface en haut) $\epsilon_{eq_{\phi}}^{m=0}$ pour le problème de Stokes, (surface en bas) $\epsilon_{\phi}^{m=0}$ pour la solution polynomiale.

la convergence de la méthode nous observons une bonne convergence exponentielle (voir fig. 5) ce qui prouve que le comportement singulier dans les coins du cylindre ne se reporte pas sérieusement sur la convergence de la méthode.

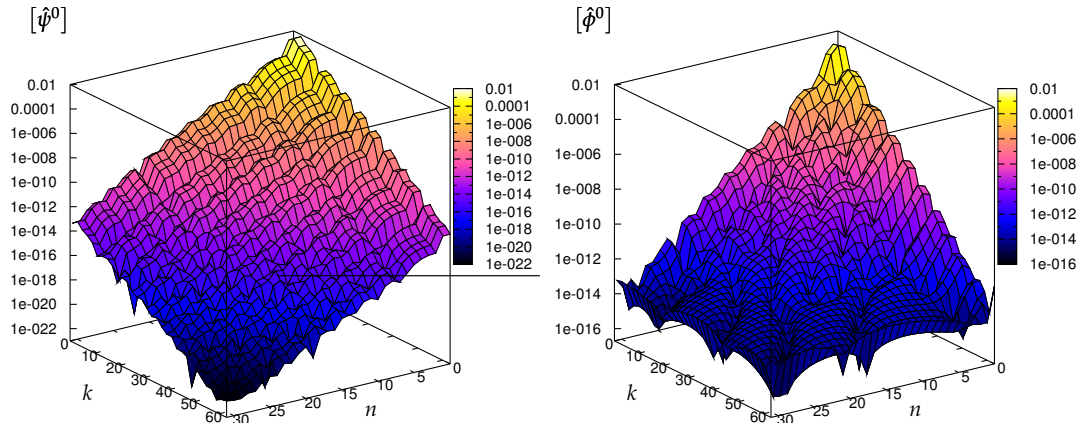


Figure 5: Coefficients spectraux pour le mode de Fourier $m = 0$, après 100 pas de temps du solveur de Stokes (pas de terme non-linéaire). Résolution utilisée : $K = 64$, $N = 32$. À gauche : $[\hat{\psi}^0]_{k,n}$; À droite : $[\hat{\phi}^0]_{k,n}$.

Vers un solveur MHD

Les équations (13) décrivant l'évolution du champ magnétique à l'intérieur du cylindre peuvent être résolues utilisant une méthode analogue à celle appliquée au cas hydrodynamique (Navier-Stokes). La résolution des équations à l'extérieur (vide) et la satisfaction des conditions de continuité à la paroi entre les champs magnétiques interne et externe présentent un nouveau défi. Dans la section 5.6 nous proposons une nouvelle méthode basée sur l'accordement du champ magnétique interne avec la solution externe dont la forme analytique est connue. Cette méthode permet de trouver la solution interne satisfaisant aux conditions de continuité (14)-(15) sans déterminer la solution externe explicitement.

L'idée de base

Dans le vide, à cause de l'absence de courants électriques, le champ magnétique \mathbf{B}^{vac} est irrotationnel et donc peut être représenté par le gradient d'un potentiel² scalaire ϕ^{vac} :

$$\nabla \times \mathbf{B}^{vac} = 0 \quad \Rightarrow \quad \mathbf{B}^{vac} = \nabla \phi^{vac}$$

Prenant en compte que le champ magnétique est solénoïdal ($\nabla \cdot \mathbf{B} = 0$) nous en déduisons que le potentiel ϕ^{vac} est une fonction harmonique satisfaisant à

$$\Delta \phi^{vac} = 0$$

²Ceci est vrai pour un domaine simplement connexe

avec les conditions aux bords du cylindre données par (14)-(15) et une condition aux limites à l'infini $\phi^{vac}(\mathbf{x} \rightarrow \infty) = 0$. On sait qu'une telle solution peut être représentée dans une base spectrale constituée des harmoniques sphériques décrivant la dépendance angulaire.

$$\phi^{vac} = \sum_l \sum_{-l \leq m \leq l} \hat{\phi}_{lm}^{vac} \rho^{-(l+1)} Y_{lm}(\zeta, \theta) \quad (28)$$

La dépendance radiale ρ est fixée pour chacune des harmoniques sphériques et n'introduit donc pas des nouveaux degrés de liberté à la solution. La forme donnée par (28) est exprimée en coordonnées sphériques (voir fig. 6). Il est alors nécessaire d'effectuer un changement des coordonnées pour pouvoir relier la solution interne avec la solution externe. Dans un problème discret, le nombre ($L \times M$) de ces degrés de liberté est le même que le nombre $2(K \times N) \times M$ des degrés de liberté d'une solution intérieure (ψ_B, ϕ_B) évaluée aux bords et correspond au nombre de points de bord. Le problème se réduit alors au problème de satisfaction des conditions aux bords couplées imposées sur la solution interne (ψ_B, ϕ_B) . La technique de la matrice d'influence peut être employée pour satisfaire ces conditions. Dans la section 5.6 nous présentons les détails de la construction de la matrice d'influence pour le champ magnétique et nous expliquons comment la solution extérieure peut être éliminée du schéma de résolution dans une étape de pré-traitement de la simulation. L'implémentation de la méthode décrite dans la section 5.6 fera l'objet d'une future étude.

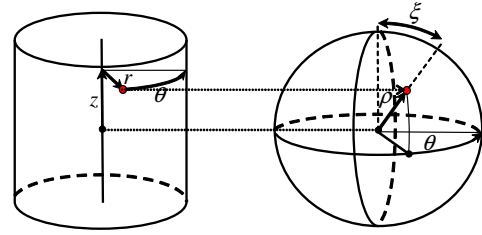


Figure 6: Illustration de changement des coordonnées : $\mathbf{x}(r, \theta, z) \mapsto \mathbf{x}(\rho, \theta, \zeta)$.

Stabilité/Validation

Dans le chapitre 6 nous complétons la présentation de la méthode spectrale par la discussion des problèmes concernant l'évaluation du terme non-linéaire. Nous présentons aussi les arguments pour le choix de la méthode d'intégration en temps la mieux adaptée au problème considéré.

Évaluation du terme non-linéaire

Étant donné que nos équations potentielles (10) sont obtenues après avoir pris le rotationnel où le double rotationnel de l'équation de Navier-Stokes, le terme non-linéaire $\mathbf{s} \equiv (\mathbf{u} \cdot \nabla) \mathbf{u}$ peut être remplacé par $\mathbf{s} \equiv \boldsymbol{\omega} \times \mathbf{u}$ (où $\boldsymbol{\omega} \equiv \nabla \times \mathbf{u}$) car $\nabla \times [(\mathbf{u} \cdot \nabla) \mathbf{u}] = \nabla \times [\boldsymbol{\omega} \times \mathbf{u}]$. L'évaluation du terme non-linéaire fait appel à des produits de fonctions. Ces produits correspondent dans l'espace spectral à des convolutions de fonctions. Nous utilisons l'approche pseudo-spectral qui consiste à effectuer des dérivations dans l'espace spectral et des produits des fonctions dans l'espace physique. Le coût de calcul de la convolution est comparable au coût de la transformation spectral \leftrightarrow physique effectuée dans un cas d'une méthode pseudo-spectral. Vu que l'évaluation du terme non-linéaire représente une partie très coûteuse en temps de calcul il est important de l'optimiser. L'évaluation du terme $\boldsymbol{\omega} \times \mathbf{u}$ est plus économique que celle de

$(\mathbf{u} \cdot \nabla)\mathbf{u}$ parce qu'elle nécessite la transformation de 9 et non pas de 15 champs scalaires entre les espaces spectral et physique.

Régularité

Le terme non-linéaire n'est pas calculé avec la même précision que les termes linéaires à cause du phénomène de doublement³ des fréquences spectrales. Dans les codes spectraux, des fréquences apparaissant dans le terme non-linéaire qui sont supérieures à la fréquence maximale représentable à une résolution spectrale donnée ne sont pas retenues. Dans la section 6.1 nous proposons une méthode d'évaluation du terme non-linéaire qui préserve sa régularité dans le sens de la condition (16), même en présence des erreurs de troncature. Dans une formulation potentielle (10) les termes non-linéaires sont :

$$s_\psi \equiv \hat{\mathbf{e}}_z \cdot \nabla \times \mathbf{s} = \frac{1}{r} [\partial_r r s_\theta - \partial_\theta s_r]$$

$$s_\phi \equiv -\hat{\mathbf{e}}_z \cdot \nabla \times \nabla \times \mathbf{s} = -\frac{1}{r} [\partial_r r s_r + \partial_\theta s_\theta] + \Delta_h s_z$$

L'utilisation des routines effectuant la transformation physique \rightarrow spectral assure par construction la régularité de \mathbf{s} au sens de condition (16). La régularité des s_ψ et s_ϕ impose néanmoins sur \mathbf{s} des conditions encore plus sévère : les termes $[\partial_r r s_\theta - \partial_\theta s_r]$ et $[\partial_r r s_r + \partial_\theta s_\theta]$ doivent être divisible par r . Ceci est d'autant plus difficile que aucun des termes $\partial_r r s_\theta$, $\partial_\theta s_r$, $\partial_r r s_r$ et $\partial_\theta s_\theta$ est a priori divisible par r séparément. Analytiquement, les contributions singulières $O(\frac{1}{r})$ présentes dans ces termes s'annulent une fois que leurs combinaisons données par (29) sont évaluées. Dans l'évaluation numérique du terme non-linéaire elles ne s'annulent pas à cause des erreurs de troncature commises pour chacun des termes. Nous démontrons dans la section 6.1 que la régularité de s_ψ et s_ϕ peut être assurée en effectuant toutes les opérations singulières dans l'espace physique.

Intégration temporelle

Le choix du schéma d'intégration en temps influence fortement la stabilité du code. Les couches limites présentes dans l'écoulement de von Kármán dans un cylindre fini peuvent être très fines pour des valeurs du nombre de Reynolds plus élevées. Les fines structures correspondant aux modes spectraux de haute fréquence spatiale peuvent, après leur amplification par le terme non-linéaire, déstabiliser la simulation. Il est donc nécessaire d'utiliser un schéma temporel qui amortit les haute fréquences spatiales. Nous avons choisi le schéma implicite du premier ordre (Euler) car entre tous les schéma inconditionnellement stable (A-stable) il amortit les hautes fréquences le plus fortement. Pour les termes non-linéaires nous utilisons le schéma de Adams-Bashforth (du seconde ordre). Pour résumer, la discrétisation temporelle Euler/Adams-Bashforth de l'équation de Navier-Stokes s'écrit comme :

$$(\mathbb{1} - \epsilon \Delta)\mathbf{u}(t + \Delta t) = \mathbf{u}(t) + \frac{\Delta t}{2} (3\mathbf{s}(t) - \mathbf{s}(t - \Delta t))$$

³Le produit des deux fonction ayant une fréquence spectrale k a une fréquence $2k$

ce qui en formulation potentielle donne :

$$(\mathbb{1} - \epsilon\Delta)\Delta_h\psi(t + \Delta t) = \Delta_h\psi(t) + \frac{\Delta t}{2} [3s_\psi(t) - s_\psi(t - \Delta t)]$$

$$(\mathbb{1} - \epsilon\Delta)\Delta\Delta_h\phi(t + \Delta t) = \Delta\Delta_h\phi(t) + \frac{\Delta t}{2} [3s_\phi(t) - s_\phi(t + \Delta t)]$$

Les valeurs du pas de temps Δt et de la résolution spatiale $M \times K \times N$ typiquement utilisées dans le code sont résumées dans le tableau 1 en fonction de nombre de Reynolds.

Re	configuration	Δt	résolution ($M \times K \times N$)
< O(500)	2D	0.05 - 0.1	$1 \times 32 \times 16$
500 - 1000	2D	0.02 - 0.05	$1 \times 64 \times 32$
1000 - 3000	2D	0.01 - 0.02	$1 \times 96 \times 48$
3000 - 5000	2D	0.005 - 0.01	$1 \times 128 \times 64$
5000 - 10000	2D	0.001 - 0.0025	$1 \times 180 \times 90$
< O(500)	3D	0.04 - 0.1	$8 \times 64 \times 32$
500 - 1000	3D	0.01 - 0.04	$16 \times 80 \times 40$
1000 - 3000	3D	0.025 - 0.01	$32 \times 100 \times 60$
3000 - 5000	3D	0.001 - 0.0025	$(64-96) \times 128 \times 80$

Table 1: Valeurs typiques du pas de temps Δt et de la résolution spatiale pour des configurations différentes.

Cas-test/Convergence

Nous avons validé notre solveur de Navier-Stokes en 2D et 3D sur des cas-test bien documentés dans la littérature. La configuration axisymétrique a été testée d'abord dans une configuration rotor-stator à $Re = 1850$ (écoulement stationnaire) avec une hauteur $h = 2$. Nous avons comparé les valeurs numériques de $u_\theta(r = 0)$ avec les résultats de Daube [17] et nous avons observé un très bon accord. Cet écoulement subit une bifurcation de Hopf vers un état oscillant à $Re \approx 2600$. Concernant la fréquence de ces oscillations (mesurée à $Re = 2800$), nous avons retrouvé un bon accord entre notre résultat et ceux de Daube [17], Speetjens [81] et Gelfgat *et al.* [29]. Le code tri-dimensionnel a été testé dans une configuration rotor-stator où, pour un rapport d'aspect $h = 3.5$, nous avons trouvé que le premier mode bifurquant correspondait à un mode de fréquence azimutale $m = 3$ et à une valeur critique du nombre de Reynolds $Re_c = 2116$. Ce résultat diffère de moins de 1% de celui de Gelfgat *et al.* [29] ($Re_c = 2131$).

Concernant la convergence spatiale du solveur de Navier-Stokes en formulation potentielle nous observons une convergence exponentielle très légèrement dégradée du fait de la singularité dans les coins du cylindre (voir fig. 7).

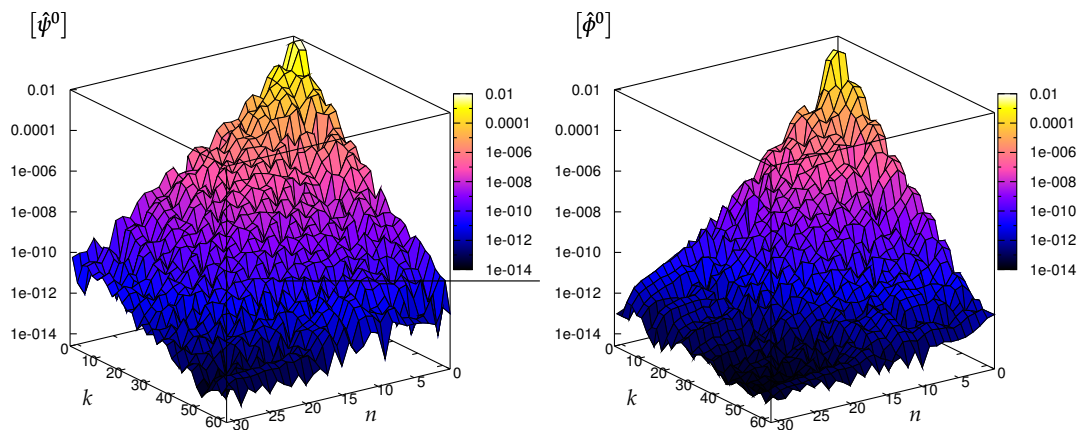


Figure 7: Coefficients spectraux pour $m = 0$, après 100 pas de temps du solveur Navier-Stokes ($Re = 750$, $\Delta t = 0.01$). Résolution utilisée : $K = 64$, $N = 32$. À gauche : $[\psi^0]$; À droite : $[\phi^0]$.

Applications et perspectives

Dans le chapitre 7 nous présentons les résultats préliminaires concernant une étude de la bifurcation turbulente et de la turbulence axisymétrique. Le contenu présentée dans ce chapitre peut être aussi considéré comme une présentation des perspectives pour de futurs travaux.

Bifurcation turbulente

Nous nous intéressons à un phénomène découvert récemment d'une bifurcation entre deux états turbulents dans l'écoulement de von Kármán (Marié [54], Ravelet *et al.* [74]). Expérimentalement, dans la situation à $Re \approx 10^5$ où un seul disque entraîne le fluide, l'écoulement est turbulent et sa moyenne temporelle correspond à une grande cellule toroïdale. Dans la situation où les deux disques sont en contra-rotation rapide, deux formes de l'écoulement moyen peuvent être observées: avec une seule ou deux cellules toroïdales. La structure est choisie pour le système dépend de la manière dont l'écoulement a été préparée. Figure 8 présente qualitativement un diagramme de la "bifurcation" entre ces deux états, où le paramètre de contrôle est la différence des couples mesurés expérimentalement. Une des raisons pour lesquelles cette transition est très intéressante est que l'état "bifurquant" correspond à un champ moyenné en temps et non pas à un champ instantané. Cette transition a un caractère statistique et n'est pas une bifurcation au sens de la théorie des systèmes dynamiques. Il est important de noter que cette transition a été observée uniquement lorsque l'entraînement de l'écoulement a été aidé par des pales courbées (voir fig. 9) collées aux disques tournants. Un des effets importants créé par les pales est que l'intensité de l'écoulement poloïdal par rapport à l'écoulement toroïdal aug-

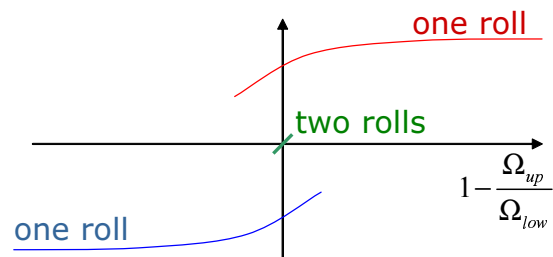


Figure 8: Boucle d'hysteresis pour le paramètre de bifurcation (représentation qualitative).

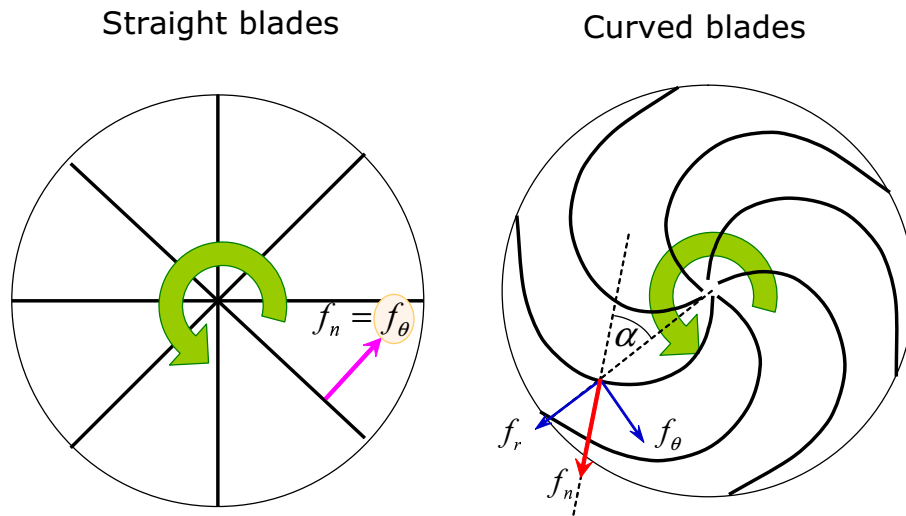


Figure 9: Modèle schématique des pales droites et courbées. Vecteurs correspondant aux forces avec lesquelles les pales forcent le fluide.

mente d'environ 10% pour les disques lisses (sans pale) à environ 70% pour le forçage avec les pales. Le premier but de notre étude numérique est de s'approcher au maximum avec notre simulation numérique à la configuration expérimentale c'est-à-dire de modéliser les pales expérimentales et ainsi d'améliorer le rapport poloïdal/toroïdal. La transition turbulente, bien visible à $Re = O(10^5)$, peut être aussi observée à $Re \approx 5000$, ce qui rend le problème accessible aux simulations numériques.

L'implémentation des parois internes correspondant aux vraies pales dans un code spectral est impossible. Nous modélisons l'effet des pales en introduisant une force en volume axisymétrique qui, en s'adaptant au cours du temps, imite la force exercée sur le fluide par les vraies pales. Cette force *inertielle* a pour but d'éviter que le fluide ait une composante de vitesse perpendiculaire à la surface des pales (non-pénétration de la surface des pales). Nous avons choisi la forme de cette fonction phénoménologiquement comme :

$$\mathbf{f}_\theta = f_n \sin(\alpha) \hat{\mathbf{e}}_\theta \quad (31a)$$

$$\mathbf{f}_r = f_n \cos(\alpha) \hat{\mathbf{e}}_r \quad (31b)$$

$$\mathbf{f}_n = f_n \hat{\mathbf{e}}_n = f_n \zeta(z) [(r\Omega(r) - u_\theta^{\text{axi}}) \sin(\alpha) - u_r^{\text{axi}} \cos(\alpha)]^3 \hat{\mathbf{e}}_n \quad (31c)$$

où $\Omega(r)$ décrit la vitesse azimutale des disques régularisés, $\zeta(z)$ est une fonction limitant cette force inertielle aux voisinage des disques et f_n est un coefficient scalaire contrôlant l'intensité de ce forçage.

Jusqu'à présent nous avons testé uniquement les pales droites ($\alpha = \pi/2$). Dans la section 7.1 nous comparons les écoulements obtenus dans des simulations avec seulement le forçage visqueux imposé par les disques lisses avec ceux obtenus dans les mêmes configurations mais avec l'ajout d'un forçage inertiel assuré par les disques avec les pales droites. Nos résultats montrent que la force en volume adaptative peut reproduire qualitativement certains des effets de vraies pales expérimentales. Notamment, nous avons observé l'amplification de l'intensité

de l'écoulement poloïdal. Dans une simulation axisymétrique le rapport poloïdal/toroïdal a changé de $\approx 13\%$ à $\approx 45\%$ grâce à l'utilisation du forçage inertiel. Dans une simulation tri-dimensionnelle ce rapport a passé de $\approx 13\%$ à $\approx 27\%$. Nous espérons que, en augmentant l'intensité du forçage, nous pourrions approcher encore plus la valeur expérimentale de 70%.

Turbulence axisymétrique

Pour la turbulence en deux dimensions cartésiennes, il existe une description statistique des propriétés de ces écoulements et des quantités conservées par l'écoulement. Le but du projet de N. Leprovost, B. Dubrulle, P. H. Chavanis et R. Monchaux ([45, 44, 60]) est d'établir une description analogue pour la turbulence axisymétrique dans une géométrie cylindrique.

Il peut être démontré que, pour un écoulement axisymétrique d'un fluide parfait (dont l'évolution est décrite par l'équation d'Euler) en absence de bords et de forçage, il existe une relation entre les deux fonctions de courant, toroïdale σ et poloïdale η , qui satisfont aux relations suivantes :

$$\sigma = F(\eta), \quad (32a)$$

$$-\Delta_* \eta = \xi = \frac{F(\eta)}{2y} F'(\eta) + g(\eta). \quad (32b)$$

où f et g sont des fonctions inconnues. Les deux fonctions de courant correspondent à l'écoulement le plus probable (qui est stationnaire et axisymétrique). Dans cette configuration, plusieurs quantités intégrales sont conservées au cours du temps : l'énergie, l'hélicité, la circulation et les Casimirs.

Le but de notre projet numérique est de vérifier si ces prédictions théoriques s'appliquent aussi à l'écoulement turbulent d'un fluide visqueux à haut Reynolds. Il est aussi intéressant de vérifier comment les quantités conservées par un fluide parfait sont dissipées au cours du temps dans un écoulement visqueux. Les observations expérimentales réalisées par Monchaux *et al.* [60] montrent que dans l'écoulement de von Kármán en contra-rotation à $Re = O(10^5)$ la relation (32a) semble s'appliquer pour la partie intérieure (c.à.d. éloignée des bords du cylindre) de l'écoulement et peut être écrite :

$$F(\eta) \approx a_1 \eta + a_3 \eta^3 \quad (33)$$

Dans la section 7.2 nous étudions la relation entre σ et η dans le cas d'un écoulement où l'axisymétrie est imposée et aussi dans le cas d'un écoulement tri-dimensionnel turbulent moyenné en temps. Nous constatons que même si la relation $\sigma = F(\eta)$ entre les deux fonctions de courant n'est pas strictement satisfaite on peut néanmoins observer une trace de cette dépendance pour la partie de l'écoulement éloignée des bords. Nous retrouvons que l'écoulement satisfait qualitativement à (33) ce qui est en accord avec les observations expérimentales (voir fig. 10).

Conclusions

Nous avons développé une approche numérique originale permettant la résolution des équations de la magnétohydrodynamique dans une géométrie cylindrique en formulation potentielle (décomposition *poloïdale-toroïdale*). Cette méthode assure la nature solénoïdale des champs

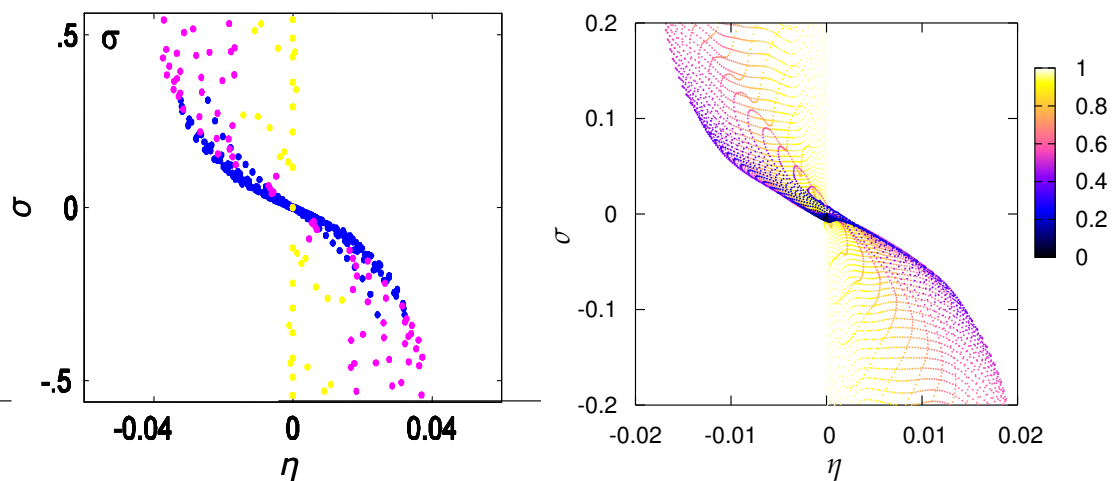


Figure 10: Scatterplot de $\sigma(\eta)$. L'échelle des couleurs indique la distance entre le point et le centre du cylindre $d(r,z) \equiv \max\{r, |z|\}$. **À gauche** : Mesures expérimentales dans le glycérol, $Re = 2000$, turbine avec des pales; **À droite** : Simulation numérique $Re = 3000$, écoulement moyenné en temps, simulation tri-dimensionnelle avec un forçage inertiel (pales), agrandissement de la région intérieure ($d \ll 1$).

de vitesse et magnétique par construction. Nous utilisons la technique de la *matrice d'influence* pour satisfaire aux conditions limites et aux conditions de continuité du champ magnétique à la paroi du cylindre. La matrice d'influence nous permet aussi d'éviter le calcul du champ magnétique externe à chaque pas de temps de la simulation.

Le solveur hydrodynamique a été validé sur des cas bien documentés dans la littérature (configuration rotor-stator 2D et 3D). Nous avons aussi comparé les résultats numériques avec une solution analytique pour un cas particulier de la solution polynomiale du problème de Stokes. Le code possède la propriété de convergence spectrale. Il a été parallélisé utilisant le protocole MPI afin de pouvoir effectuer des simulations très coûteuses de la turbulence tri-dimensionnelle.

Le code a ensuite été appliqué à deux problèmes concernant la turbulence dans la géométrie cylindrique : la *bifurcation turbulente* et la turbulence axisymétrique. Les résultats obtenus sont en bon accord qualitatif avec les observations expérimentales et sont encourageants pour l'obtention d'un accord quantitatif. La perspective la plus importante pour le code est son extension aux problèmes magnétiques (implémentation de la matrice d'influence magnétique).

Chapter 1

Introduction

1.1 Motivation

The earth's magnetic field is believed to be one of the indispensable elements that make life possible on our globe. This invisible shield protecting us from destructive radiation of ionized particles ejected by our sun seems to be produced by a very complicated, meta-stable and time-dependent mechanism. Several changes in the field's polarity have occurred, which can be deduced from geological observations of magnetization of rocks. Astronomical observations show that there exist planets and satellites (Mercury, Ganymede) which have their own magnetic field, similar to the earth's dipolar field. Evidence for topologically more complicated fields has been reported for gas giants (Jupiter, Saturn, Uranus and Neptune) as well as stars and galaxies. Probably the most impressive effects of the rapidly evolving magnetic field can be observed on the sun's surface in the form of spectacular protuberances.

All these observations suggest that the magnetic field is generated in a dynamical process. This fact, together with other physical arguments, convinced the scientific community that the magnetic field of celestial objects cannot be generated by a kind of solid magnet situated in the kernel. In the beginning of the 20th century, Larmor [42] suggested that the magnetic fields of the earth and other celestial bodies could result from a self-sustained *dynamo*, by which flow of a conducting fluid would generate a magnetic field which would in turn act on the flow. Most of the research which followed this prediction has been theoretical, and, later numerical, and has focused on a spherical geometry, for reasons of both mathematical simplicity and geophysical relevance.

There is currently a major international research effort to create an experimentally self-sustained fluid dynamo. In 2001 the first two working dynamos were reported by Gailitis *et al.* [26] at Riga and by Steglitz & Müller [82] at Karlsruhe. Experimental realizations of the dynamo effect have been performed in very constraining and topologically complicated geometries. There are several reasons for this, including the fact that physically the most natural, spherical shape is very difficult to deal with experimentally. Astrophysical theories of the dynamo effect assume that intense convection coupled with rotation is responsible for creating the necessary flow structures. For reasons of limited scale of experimental setups, it is very difficult to implement a convection-driven dynamo. The Riga and Karlsruhe experiments are implemented in rather complex variants of cylindrical geometry and include mechanical

forcing of the flow. The VKS (von Kármán Sodium) experiment performed in Cadarache (see Bourgoïn *et al.* [9]) also belongs to this family of dynamo experiments. In contrast to the Riga or Karlsruhe experiments, where periodization in one of the spatial directions was necessary, the geometry is a finite cylinder which is much simpler and topologically equivalent to a sphere. The magnetic effect observed in the VKS configuration, while not comparable to the geo- or astro- physical models, can be produced by a more natural, i.e. confined and not periodized, flow allowing a rich behavior and the feedback of the magnetic field on the flow¹. The reader can find more details concerning the VKS configuration in section 1.4.

Just as for many experimental investigations, there exists a need for performing a numerical simulation of the problem in order to obtain a better understanding of the complicated behavior of coupled velocity and magnetic fields in a turbulent regime as well as to compute quantities that for technical reasons cannot be measured experimentally.

From these arguments arises our motivation to develop and implement a numerical method which is well suited to modeling the configuration of the VKS experiment.

Numerical method

Paradoxically, a numerical simulation of a flow in a simple finite-cylinder geometry is much harder to implement than an equivalent method for topologically complicated geometries of the Riga or Karlsruhe experiments. From the computational point of view, modeling cylindrical flows which are periodic in the axial direction is a completely different and much easier problem than for a finite domain. Performing a numerical simulation of the dynamo effect in a configuration corresponding to the VKS experiment represents a challenging task, consisting of developing a method for solving the magnetohydrodynamic equations resulting from the Maxwell and Navier-Stokes equations in the finite cylinder geometry. This problem presents several important difficulties that must be addressed in order to ensure physical and mathematical consistency.

- The geometry of the problem while topologically simple, is difficult to handle correctly because of geometrical singularities which appear in the mathematical formulation of the problem formulated in cylindrical coordinates (axis and corners). The regularity of the solution must be ensured by a suitable method in order to achieve acceptable stability and convergence properties. We take special care of this problem by using a regular basis of radial polynomials developed by Matsushima & Marcus [58] satisfying the regularity conditions at the cylinder axis. Concerning the corner singularity which emerges from the discontinuity of the boundary conditions for the velocity at the contact point between rotating cylinder bases and immobile mantle, we treat this problem by applying regularization of the boundary conditions.
- Another kind of problem is ensuring the incompressibility of the velocity field and, even more important, the solenoidal character of the magnetic field (non-existence of magnetic monopoles). Imposing these constraints is far from trivial and requires employing sophisticated and complex techniques. They can be divided into two categories: those that

¹In the Riga and Karlsruhe experiments, the flow structures producing the dynamo are imposed by the boundaries without letting the flow reorganize itself freely under the influence of the magnetic field.

impose $\nabla \cdot \mathbf{u} = \nabla \cdot \mathbf{B} = 0$ (to some accuracy) at each time step of the simulation and those which represent velocity and magnetic fields by intermediate variables in such a way that \mathbf{u} and \mathbf{B} are divergence-free by construction. Each of these approaches has its difficulties, advantages and drawbacks. We consider in this work the second methodology by performing the decomposition of solenoidal fields into poloidal and toroidal scalar potentials. This approach, first formulated by Marques [55] for the periodic Couette flow and further applied in [56] to linear stability of Rayleigh-Bénard convection in finite cylinder, has to our knowledge never been implemented for time-evolution of a three-dimensional flow in a finite cylinder.

- The last problem we underline is the formulation and imposition in the numerical algorithm of the boundary condition for the magnetic field. The difficulty emerges from the fact that the magnetic field in the problem considered is not limited to the finite domain. An external magnetic field satisfying the asymptotic condition $\mathbf{B}(r \rightarrow \infty) \sim \frac{1}{r^3}$ at infinity must additionally match the internal field at the boundary. This is a particularly difficult problem for the spectral method we want to use in our solver because, for this class of discretization, splitting of the computational domain between two regions – internal and external (a non-simply-connected domain) – is not obvious². We propose a novel method for determining the internal field satisfying the matching condition with the external field without extending the domain beyond the finite cylinder and without solving for the external field. This method, formulated for spectral methods, can be applied under the condition that the external medium is a vacuum. In this work, mathematical and algorithmic details are given, without being implemented in a numerical code. This task can be considered as a perspective for the future, extending the working hydrodynamic code. A quite general method for non-spectral methods was proposed by Iskakov *et al.* [38]. Both approaches can be seen as numerical implementations of Green functions method commonly used in analytical electrostatics. From the mathematical and technical point of view they are, however, very different.

In this work we limit ourselves to the development of the hydrodynamic code using a method which can be applied in the future also to the fully coupled hydromagnetic problem. However, in addition to presenting a detailed methodology for the Navier-Stokes solver in potential formulation using the poloidal-toroidal decomposition, we prepare the theoretical and algorithmic background for including the magnetic field in future versions of the numerical code. The most important contribution of this work is developing and validating an algorithm for solving time-dependent, three-dimensional Navier-Stokes equations in finite cylindrical geometry ensuring the incompressibility of the field by using the potential formulation. From the technical point of view this study addresses the problem of satisfying high differential order, coupled boundary conditions by means of the *influence matrix* method, and can be considered as a contribution to this class of numerical methods. A first step toward future extension of the code to hydromagnetic problems has been made. A novel algorithm for satisfaction of the matching conditions for the magnetic field at the cylinder boundary has been

²One could consider use of the spectral element method or, for example, a mixed spectral / finite element approach.

proposed. The method is based on extending the influence matrix protocol already used for the hydrodynamic problem. Additionally it was our ambition to implement a highly accurate, pseudo-spectral code preserving the regularity properties of the mathematical formulation by correct handling of the coordinate system singularities.

In the following sections we present the outline of this thesis followed by the introductory material concerning the magnetohydrodynamic equations and the dynamo effect.

1.2 Outline of this thesis

This thesis consists of two parts: the first, presenting a mathematical description of the problem investigated completed by a brief overview of the state of art in the relevant research fields, and the second containing the details of the numerical method.

Chapter 1 – Introduction In addition to the introductory matter already exposed, we present the Maxwell and Navier-Stokes equations which lead to the equations of magnetohydrodynamics to which we will often refer in the further parts of this text. This is also necessary for explaining a general mechanism of the dynamo effect described at the end of this chapter.

Part I : System description

Chapter 2 – The von Kármán flow After discussing the state of the art concerning numerical studies relevant for this problem we present the mathematical model corresponding to the configuration investigated. The equations are presented in dimensionless form and the set of hydrodynamic and magnetic equations is defined together with the specification of the corresponding boundary conditions.

Chapter 3 – Poloidal-toroidal decomposition Here we communicate the motivation for using a potential approach for satisfying the divergence-free constraint. The current approach is briefly compared against other possible methods. This introductory discussion is followed by the details of translation of the equations of magnetohydrodynamics into the potential poloidal-toroidal formulation. A new set of equations is derived, together with the associated boundary conditions. The evidence for the *compatibility condition* is demonstrated. Advantages and drawbacks of the potential formulation are discussed.

Part II : Numerical method – Spectral solver

Chapter 4 – Spectral discretization In this chapter we explain the spatial discretization technique used in our spectral solver, paying special attention to the singular aspects of the polar coordinates. The regular polynomials are introduced together with more standard Fourier and Chebyshev spectral bases. The approach undertaken for regularizing the singular boundary conditions in cylinder corners is presented.

Chapter 5 – Spectral solver Here we present the method for solving the discretized Navier-Stokes equations in poloidal-toroidal formulation. Apart from describing the classical τ -method in one and three directions we expose the methodology for solving high-order differential equations by the *multi-step* algorithm. The following material presents the *influence matrix* technique employed for imposing the boundary condition. We also demonstrate the equivalence between the classical *Green functions* method and the influence matrix approach. This chapter is completed by necessary tests and convergence analysis of the linear Stokes-flow solver. After general conclusions concerning the algorithm we present at the theoretical and practical level a novel method for satisfaction of the matching conditions for the magnetic field. This method is explained by referring to the influence matrix protocol discussed before.

Chapter 6 – Stability/Validation We propose the method for stable evaluation of the nonlinear term and ensuring its regularity even in the presence of errors typically introduced by methods of evaluation of the nonlinear term by the *pseudo-spectral* approach (transformation, truncation and aliasing errors). We follow by presenting the semi-implicit time integration scheme well suited for the problem at hand. Validation of the hydrodynamic code followed by discussion of the method is presented at the end of this chapter.

Chapter 7 – Applications of the code to a few problems concerning turbulence in cylindrical geometry are presented in this chapter. These are *decaying turbulence* in axisymmetric cylindrical flows and adaptation of the spectral code to study the *global bifurcation* recently discovered by Marié [54] and Ravelet *et al.* [74]. A method for modeling the effect of interior boundaries (blades situated at rotating cylinder bases) through the introduction of *self-adapting* volume forces is described. Both of these preliminary studies can be considered as a presentation of perspectives for future work.

Chapter 8 – Concluding remarks Conclusions concerning work presented throughout this thesis are underlined and the possible perspectives for future applications of the method and of the numerical code are stated in this chapter.

1.3 Magnetohydrodynamic equations

In this section we introduce the basic equations of electrodynamics – the Maxwell equations and the Navier-Stokes equations for incompressible fluids. Taking these two descriptions as a base we derive the equations of magnetohydrodynamics which include coupling between magnetic and velocity fields.

1.3.1 Maxwell equations

The time evolution of magnetic and electric fields is described by the Maxwell equations [39, 75]

$$\nabla \times \mathbf{E} = -\frac{\partial \mathbf{B}}{\partial t} \quad (1.1a)$$

$$\nabla \times \mathbf{H} = \mathbf{j} + \frac{\partial \mathbf{D}}{\partial t} \quad (1.1b)$$

$$\nabla \cdot \mathbf{D} = \chi \quad (1.1c)$$

$$\nabla \cdot \mathbf{B} = 0 \quad (1.1d)$$

where \mathbf{E} and $\mathbf{H} \equiv \mathbf{B}/\mu$ denote electrical and magnetic fields, $\mathbf{D} = \epsilon\mathbf{E}$ and \mathbf{B} are electrical and magnetic induction fields and χ and \mathbf{j} are densities of electric free charges and currents. Quantities μ and ϵ denote magnetic permeability and dielectric constant³. The first equation (1.1a) is Faraday's law of induction. The second (1.1b) is Ampere's law. Equations (1.1c,d) are Gauss's laws for electricity and magnetism. The first of them is a generalization of Coulomb's law and the second one expresses the non-existence of magnetic monopoles.

Quasi-steady approximation

In this work we will consider the *quasi-steady approximation* i.e. a situation when the displacement current $\partial_t \mathbf{D}$ can be neglected. This choice can be justified by comparing the characteristic time scales of the problem. It can be seen from (1.1a) that

$$|\mathbf{E}| \approx \frac{\mathcal{L}}{\mathcal{T}} |\mathbf{B}|$$

and then, comparing the terms in (1.1b) gives

$$\frac{|\partial_t \mathbf{D}|}{|\nabla \times \mathbf{H}|} \approx \frac{\epsilon |\mathbf{E}| / \mathcal{T}}{|\mathbf{B}| / (\mu \mathcal{L})} \approx \frac{|\mathbf{E}| \mathcal{L}}{c^2 \mathcal{T} |\mathbf{B}|} \approx \left(\frac{\mathcal{L}}{c \mathcal{T}} \right)^2 \ll 1 \quad (1.2)$$

where c is the light speed in the considered medium, \mathcal{L} and \mathcal{T} are characteristic length scale (typically the system dimension) and the characteristic time scale which can be understood as the time needed for an information characteristic for a particular problem to propagate from one point of the system to another. Since in this work we are interested with magnetohydrodynamics at the laboratory scale without taking into account the electromagnetic radiation then

³In general, $\mu \equiv \mu(\mathbf{x})$ and $\epsilon \equiv \epsilon(\mathbf{x})$ are tensors that express a linear relation between two vector fields. We will, however, make the assumption that $\mu = \text{const}$ and $\epsilon = \text{const}$ are scalars describing homogeneous properties of media considered.

the characteristic information corresponds to the flow velocity $|\mathbf{u}| \approx \mathcal{L}/T$. For non-relativistic flows ($|\mathbf{u}| \ll c$) (1.2) demonstrates that the displacement current $\partial_t \mathbf{D}$ influences the system very little. More complete discussion of the Maxwell equation in a magnetohydrodynamical context is provided by Roberts [75]. Therefore, equation (1.1b) can now be reduced to:

$$\nabla \times \mathbf{H} = \mathbf{j} \quad (1.3)$$

For a conductor of electrical conductivity σ , moving with the velocity \mathbf{u} , the current density can be written as:

$$\mathbf{j} = \sigma(\mathbf{E} + \mathbf{u} \times \mathbf{B}) \quad (1.4)$$

which is effectively the generalization of Ohm's law. The contribution $\chi \mathbf{u}$ to \mathbf{j} , coming from free charges convected by the fluid, can be neglected in the *quasi-steady approximation* (see Roberts [75]). Equations (1.3) and (1.4) will be used later for eliminating the current density \mathbf{j} from the Maxwell equations.

Boundary conditions

In view of future applications it is necessary to explain the boundary conditions between two physically different electromagnetic regimes. In practical situations we are often interested in a magnetically sensitive fluid of a finite volume surrounded by some other medium. Since the equations or constants such as μ , ϵ , σ in neighboring domains can be different because of different physical properties, it is necessary to define boundary conditions which would ensure the correct matching between the solutions. Mathematical idealization of boundaries (i.e. considering them as two-dimensional surfaces) can often represent a spatial singularity over the global domain and therefore an integral formulation is needed to evaluate the fields on them. It can be shown by integrating Maxwell's equations (1.1) over infinitesimally small volumes and circuits placed on surfaces separating two possibly different physical regions (see Jackson [39], Roberts [75]) that the following relations are satisfied:

$$[\hat{\mathbf{n}} \times \mathbf{E}] = 0 \quad (1.5a)$$

$$[\hat{\mathbf{n}} \times \mathbf{H}] = \begin{cases} 0 & \text{if } \sigma < \infty \\ \mathbf{J}_s & \text{if } \sigma \rightarrow \infty \end{cases} \quad (1.5b)$$

$$[\hat{\mathbf{n}} \cdot \mathbf{B}] = 0 \quad (1.5c)$$

$$[\hat{\mathbf{n}} \cdot \mathbf{D}] = Q_s \quad (1.5d)$$

$$[\hat{\mathbf{n}} \cdot \mathbf{j}] = 0 \quad (1.5e)$$

where $[\cdot]$ measures the discontinuity at a boundary i.e. the difference between values obtained for a given expression by evaluating limits going from the opposite sides of the surface.

Conditions (1.5) are mutually dependent. For unsteady fields the solenoidal character of \mathbf{B} (1.1d) follows from Faraday's law (1.1a). Therefore, because (1.5a) is obtained from (1.1a) and (1.5c) from (1.1d) then (1.5c) is a consequence of (1.1a). For equations (1.5b) and (1.5e) we have a similar situation: because $\nabla \cdot \mathbf{j} = 0$ can be deduced from (1.1b) therefore (1.5e) follows from (1.5b). Concerning equation (1.5d), it can be considered as a definition of the surface charges Q_s so, it does not act as a condition on \mathbf{D} . In summary the complete and minimal set of

conditions for a general non-steady case can be reduced to four scalar conditions imposed on the tangential components of electric and magnetic field. Additionally, after assuming that the media considered are not ferromagnetic and that their conductivity is finite⁴ we can write:

$$[\hat{\mathbf{n}} \times \mathbf{E}] = 0 \quad (1.6a)$$

$$[\hat{\mathbf{n}} \times \mathbf{B}] = 0 \quad (1.6b)$$

The above system of equations implies that

$$[\mathbf{B}] = 0 \quad (1.7)$$

but the reverse implication does not hold. However, if the surrounding medium is a vacuum then, because of absence of electric currents, the magnetic field satisfies

$$\nabla \times \mathbf{B}^{vac} = 0 \quad \Rightarrow \quad \mathbf{B}^{vac} = \nabla \phi^{vac} \quad (1.8)$$

and by using (1.1d) we show that

$$\Delta \phi^{vac} = 0 \quad (1.9)$$

In this context we can regard (1.5c) as defining $\hat{\mathbf{n}} \cdot \nabla \phi^{vac}$ over the boundary. If additionally the surrounding vacuum extends to infinity, there generally exists a condition that $\mathbf{B} \rightarrow 0$ as the distance $R \rightarrow \infty$. In such a case, given that the magnetic potential ϕ^{vac} satisfies the Laplace equation with Neumann boundary conditions, the *uniqueness theorem* for the solutions to Laplace's equation tells us that ϕ^{vac} can be determined up to a constant. This implies that a unique \mathbf{B}^{vac} can be found. Knowledge of the solution in the vacuum fixes through (1.6b) the two tangential components of \mathbf{B} on the boundary, conditioning the solution in the non-vacuum regime. Therefore a unique \mathbf{B} can be found without solving for \mathbf{E} . A more rigorous demonstration will be provided in section 3.6. The sufficient boundary conditions for determining \mathbf{B} are then

$$[\mathbf{B}] = 0$$

$$\mathbf{B} \xrightarrow{R \rightarrow \infty} 0$$

1.3.2 Navier-Stokes equations

The dynamics of fluid flow is described by the Navier-Stokes equations. In the particular case of an incompressible Newtonian fluid, they can be presented in the following form:

$$\frac{\partial \mathbf{u}}{\partial t} + (\mathbf{u} \cdot \nabla) \mathbf{u} = -\frac{1}{\rho} \nabla p + \frac{1}{\rho} \mathbf{f} + \nu \Delta \mathbf{u} \quad (1.11a)$$

$$\nabla \cdot \mathbf{u} = 0 \quad (1.11b)$$

where ρ is the fluid density, ν is the kinematic viscosity and \mathbf{f} denotes volume forces. In the presence of the magnetic field, the Lorentz force can act on an electrically conducting fluid with the electric current distribution \mathbf{j} :

$$\mathbf{f} = \mathbf{j} \times \mathbf{B}. \quad (1.12)$$

The Coulomb force $\chi \mathbf{E}$ can be neglected here because of the *quasi-steady approximation* (see Roberts [75]).

⁴When conductivity is infinite, a boundary layer model must be introduced to define adequate boundary conditions (see Roberts [75] for more detailed discussion)

1.3.3 Magnetohydrodynamics equations

When a conducting fluid is moving in the presence of a magnetic field, the contribution of $\sigma \mathbf{u} \times \mathbf{B}$ in (1.4) must be taken into account. The coexistence of the electric currents and the magnetic field implies that the volume forces (1.12) must be considered in the Navier-Stokes equations (1.11). In such a case the Maxwell equations together with the Navier-Stokes equations could already be considered as the equations of magnetohydrodynamics. However, since magnetohydrodynamics mostly concerns the interaction between the fluid flow and the magnetic field then it is better to eliminate all other variables which are of less interest for a hydro-magnetic problem. For identifying the influence of the magnetic field on the fluid, it is natural to choose (1.3) rather than (1.4) as the definition of \mathbf{j} , because the fluid velocity \mathbf{u} is not present in (1.3):

$$\mathbf{j} = \frac{1}{\mu} \nabla \times \mathbf{B} \quad (1.13)$$

Deriving (1.13) from (1.3) we supposed that $\mu = \text{const}$ is homogeneous and therefore it can be moved in front of $\nabla \times$. By combining (1.13) with (1.12) we can express the volume force in terms of the magnetic field only

$$\mathbf{f} = \frac{1}{\mu} (\nabla \times \mathbf{B}) \times \mathbf{B}. \quad (1.14)$$

Using (1.11b) this force can be decomposed into the *magnetic pressure* and the *magnetic convective term*⁵:

$$\mathbf{f} = \frac{1}{\mu} (\mathbf{B} \cdot \nabla) \mathbf{B} - \nabla \frac{B^2}{2\mu} \quad (1.15)$$

Substituting (1.15) into (1.11a) leads to the following form of the Navier-Stokes equation:

$$\frac{\partial \mathbf{u}}{\partial t} + (\mathbf{u} \cdot \nabla) \mathbf{u} = -\frac{1}{\rho} \nabla \left(p + \frac{B^2}{2\mu} \right) + \frac{1}{\rho\mu} (\mathbf{B} \cdot \nabla) \mathbf{B} + \nu \Delta \mathbf{u} \quad (1.16)$$

The influence of the fluid motion on the magnetic field is related to the generation of the electric currents (1.4) through the effect of induction. Substituting (1.4) into (1.13) and taking the curl of the expression obtained gives us:

$$\nabla \times (\sigma \mathbf{E}) + \nabla \times (\sigma \mathbf{u} \times \mathbf{B}) = \frac{1}{\mu} \nabla \times \nabla \times \mathbf{B} \quad (1.17)$$

By using $\nabla \times \nabla \times = \nabla(\nabla \cdot \mathbf{B}) - \Delta \mathbf{B}$ together with (1.1d) and after expressing \mathbf{E} in terms of \mathbf{B} using (1.1a) and assuming that $\sigma = \text{const}$ we can write (1.17) as

$$-\sigma \frac{\partial \mathbf{B}}{\partial t} + \sigma \nabla \times (\mathbf{u} \times \mathbf{B}) = -\frac{1}{\mu} \Delta \mathbf{B} \quad (1.18)$$

⁵The adjective "convective" is used by analogy with the form of the hydrodynamic convective term $(\mathbf{u} \cdot \nabla) \mathbf{u}$. The term $(\mathbf{B} \cdot \nabla) \mathbf{B}$ corresponds to the contribution of the magnetic stress tensor acting in the direction of the magnetic field. The *magnetic pressure* term $B^2/2\mu$ corresponds to the contribution along the direction of a surface element across which the magnetic tensor is acting, and in this sense behaves as a pressure.

Summarizing, the system of the magnetohydrodynamic equations can be written in the following form:

$$\left\{ \begin{array}{l} \frac{\partial \mathbf{u}}{\partial t} + (\mathbf{u} \cdot \nabla) \mathbf{u} = -\frac{1}{\rho} \nabla \left(p + \frac{B^2}{2\mu} \right) + \frac{1}{\rho\mu} (\mathbf{B} \cdot \nabla) \mathbf{B} + \nu \Delta \mathbf{u}, \\ \frac{\partial \mathbf{B}}{\partial t} = \nabla \times (\mathbf{u} \times \mathbf{B}) + \frac{1}{\mu\sigma} \Delta \mathbf{B}, \\ \nabla \cdot \mathbf{u} = 0, \\ \nabla \cdot \mathbf{B} = 0. \end{array} \right. \quad \begin{array}{l} (1.19a) \\ (1.19b) \\ (1.19c) \\ (1.19d) \end{array}$$

1.4 Dynamo effect

The *dynamo effect* is the process of self-sustained generation of a permanent magnetic field through the mechanism of mutual interaction between the flow of electrically conducting medium and the induced magnetic field. This process is represented by the term $\nabla \times (\mathbf{u} \times \mathbf{B})$ in (1.19b). If one neglects the retro action of the magnetic field on the velocity field (the configuration of the *kinematic dynamo* problem) then the eigenvalues of the operator $\mathbf{B} \mapsto \nabla \times (\mathbf{u} \times \mathbf{B}) + Rm^{-1} \Delta \mathbf{B}$ with positive real part define the critical magnetic Reynolds number Rm_c corresponding to the threshold of the kinematic dynamo. The existence of such eigenvalues depend on the boundary conditions imposed on \mathbf{B} , its topology, and also on the form of the particular fluid flow. These conditions were extensively studied theoretically and resulted in the following *anti-dynamo* theorems specifying the conditions under which the dynamo cannot exist. According to Busse [12] and Proctor [73], these constraints can be divided into three categories:

- i Bounding theorems: Lower bounds on magnetic Reynolds numbers or related quantities that are necessary for amplifying magnetic fields,
- ii Structures and symmetries of magnetic fields that cannot be generated by the dynamo process (among them *Cowling's Theorem*, demonstrated in 1934, which is probably the most famous),
- iii Structures and symmetries of velocity fields that cannot be dynamos (e.g. Toroidal Theorem).

We recall here the most important anti-dynamo theorems corresponding to cases ii and iii:

ii magnetic field

- **Cowling's Theorem:** (Cowling [16])
An axisymmetric magnetic field cannot be sustained through a dynamo effect
This theorem was further extended to problems of time-dependent magnetic and velocity fields as well as to compressible flows having nonuniform but axisymmetric distribution of the electrical conductivity.
- **Second Cowling's Theorem:** (Cowling [16])
A magnetic field independent of one of the Cartesian coordinates cannot be sustained through a dynamo effect

iii velocity field

- **Toroidal Theorem:** (Elsasser [23], Bullard & Gellman [11])
A purely toroidal flow cannot sustain a magnetic field through a dynamo effect.
- **Plane flow:**
A plane flow cannot produce a dynamo effect.
- **Radial flow:** (Namikawa & Matsushita [61])
A compressible radial flow of a form $\mathbf{u} = f(\mathbf{x})\hat{\mathbf{e}}_r$ (having only the spherical radial component) cannot produce a dynamo effect.

These findings have essential importance for theoretical, experimental and numerical studies of the dynamo effect. The Cowling theorems challenged Larmor's hypothesis of a dynamo-generated magnetic field since the measured Earth's magnetic field is almost axisymmetric. It took almost a quarter of a century until Backus [1] and Herzenberg [34] demonstrated mathematically that nonaxisymmetric fields could indeed be generated.

Table 1.1 presents the recapitulation of known conditions for the existence of homogeneous dynamos.

properties	of magnetic field	of velocity field
axisymmetry	NO	YES
purely toroidal	NO	NO
purely poloidal	NO(?)	YES
helical symmetry	YES	YES

Table 1.1: Summary of the symmetry properties of the magnetic and velocity fields conditioning the existence of homogeneous dynamos.

Several models of dynamos, not necessarily spherical, have been created and for some of them, experimental confirmation is also available. We mention here some of these dynamo models:

Solid-body dynamos The Bullard dynamo is the simplest of existing solid-body models. The metallic disk rotating around its axis is put inside a coil whose contacts are connected: one to disk's origin and the second to its periphery. This system, being extremely simple, has been much studied theoretically. We assign to the solid-dynamo class also the configuration of Lowes & Wilkinson [51] which in 1963 has proved experimentally to produce a dynamo. This is a mixed, solid-fluid dynamo, where the fluid motion plays an important role but the dynamo action is essentially dependent on the magnetic susceptibility of solid components used in the experiment and therefore cannot be considered to be generated by the flow itself only.

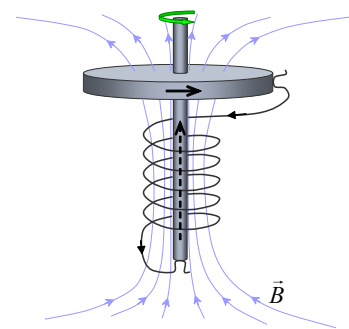


Figure 1.1: Bullard dynamo.

Periodic G.O. Roberts dynamo This configuration consist of a periodic flow independent of the vertical coordinate z , defined as $\mathbf{u} = \sin(y)\mathbf{e}_x + \sin(x)\mathbf{e}_y + (\cos(x) - \cos(y))\mathbf{e}_z$. While the flow is two-dimensional, it can induce and sustain a magnetic field dependent on z . The experimental realization of this model, performed at Karlsruhe, consists of a flow pumped through a system of alternating upstream and downstream oriented tubes enclosed in a helically shaped canal forcing an external helical flow. Such an unnaturally forced flow corresponds to the aforementioned mathematical form. The dynamo action in this configuration was first reported in 2000 by Steglitz & Müller [82]. It is worth mentioning that this kind of dynamo model is essentially laminar.

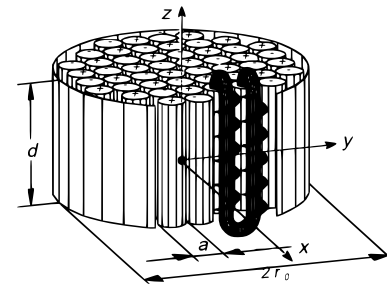


Figure 1.2: Model of the Roberts-type Karlsruhe experiment (Steglitz & Müller [83]).

Ponomarenko Dynamo The Ponomarenko [71] flow is, similarly to the Karlsruhe configuration, an example of a constrained dynamo with helical symmetry. Figure 1.3 shows a schematic model of the Riga experiment implementing the Ponomarenko-type dynamo. A propeller forces the helical flow in liquid sodium pumping it through a cylindrical tube. The returning flow is confined to a thin shell surrounding the cylinder. The whole vessel is surrounded by an immobile layer of liquid sodium. The dynamo action in this experiment was reported in 2000 (see Gailitis *et al.* [26]).

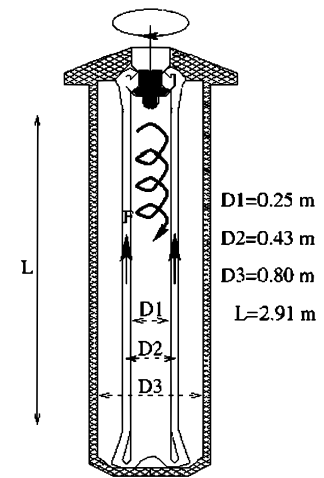


Figure 1.3: Schematic model of the Ponomarenko-type dynamo of Riga experiment (Gailitis *et al.* [26]).

Both working experiments (Riga and Karlsruhe) confirmed that a helical flow can be qualified as *dynamo-friendly*. This is because helical fields (both the velocity and the magnetic field) suffer from no constraints imposed by the anti-dynamo theorems (see table 1.1).

von Kármán configuration – VKS The configuration in which we are interested in this study is that of the VKS (von Kármán Sodium) experiment performed at Cadarache (Bourgoin *et al.* [9]). The configuration is a finite cylinder of aspect ratio $\frac{\text{height}}{\text{radius}} \approx 2$ filled with liquid sodium. The flow is forced by counter-rotating disks situated near the cylinder bases (see figure 1.4). This flow is called the *von Kármán swirling flow* and can produce, for high Reynolds numbers, a turbulent flow of strong helicity. In contrast to the previously described models and experimental setups, this configuration is expected to produce a turbulence-driven

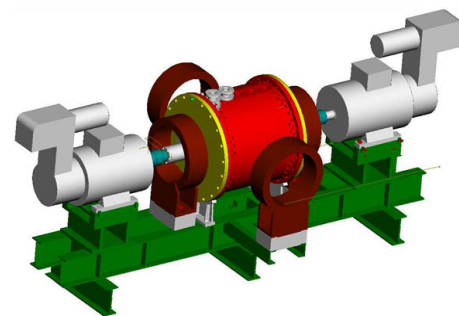


Figure 1.4: Model of the von Kármán Sodium (VKS) Cadarache experiment (Bourgoin *et al.* [9]).

dynamo through a complex mechanism of magnetic induction called the α - Ω effect. This kind of flow is very much less constrained by the boundaries and allows the free development of a retro-acting effect of the Lorentz force on the flow. No dynamo action has been observed up to now in this configuration, but a strong magnetic induction has been measured by Bourgoin *et al.* [9]. A new experiment called VKS2, capable of reaching higher magnetic Reynolds numbers, is currently being studied. There is a chance that dynamo action will be observed in this second setup.

Spherical dynamos Similarly to the VKS's finite cylinder configuration, the spherical geometry is weakly constraining. The experimental setups of Maryland (see Shew *et al.* [79]) and Wisconsin (see Forest *et al.* [25]) are examples of homogeneous dynamo models implemented in the spherical geometry. The helicity of the flow is produced by forcing it using internal propellers and by rotating the spherical vessel around its vertical axis. Additionally, convective forces supporting the mechanical forcing are produced by a system of heating and cooling boundaries. No dynamo has been reported up to this date in the Wisconsin experiment and the Maryland experiment is currently under construction.

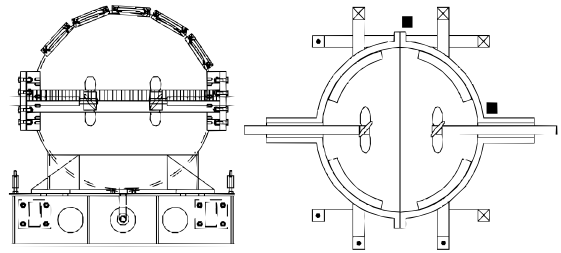


Figure 1.5: Schematic models of spherical dynamo experiments. Left: Wisconsin (Forest *et al.* [25]). Right: Maryland (Shew *et al.* [79])

Mechanism of induction

To understand how amplification of a magnetic field can be achieved in the configuration of the VKS experiment, it is necessary to consider two classical effects of induction: the Ω -effect and the α -effect. We present here only a brief, qualitative graphical explanation of these mechanisms. The most important fact is that lines of magnetic field can be deflected by the flow of fluid of finite conductivity. The bigger the magnetic Reynolds number the more pronounced is this effect.

Ω -effect In the first stage, an initial, e.g. vertical, magnetic field is tilted by a shear flow as it is shown on figure 1.6. This effect creates an induced magnetic field perpendicular to the original one. This effect cannot guarantee a dynamo by itself since the necessary condition is that the induced field have the same direction as the initial one.

α -effect In the second stage, the α -effect creates, from the horizontal magnetic field obtained through the Ω -effect, a secondary vertical induced field. This new field can ensure amplification of the initial field having the same orientation. The α -effect, introduced in 1955 by Parker [68], is far more complicated than the Ω -effect. It can appear in a flow of non-zero helicity (translation + rotation). This effect can be produced by non-axisymmetric, helical fluctuations of the velocity field. Since the mean flow in the VKS configuration is axisymmetric the α -effect

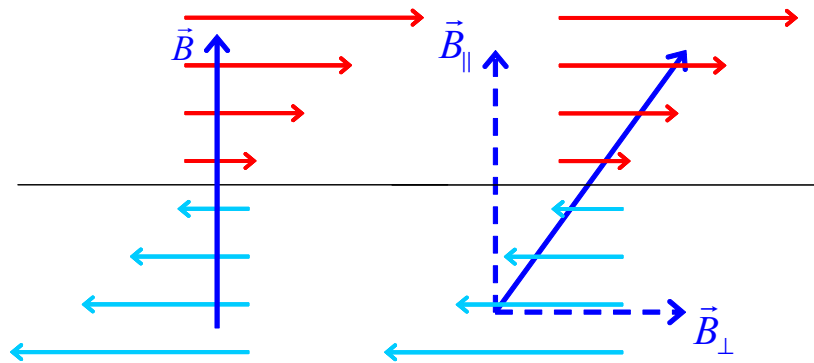


Figure 1.6: A graphical explanation for the Ω -effect. A new induced magnetic field \mathbf{B}_\perp (horizontal dashed arrow), is created from an initial field \mathbf{B} (thick vertical arrow). Horizontal arrows represent the velocity field.

can appear here only in a turbulent regime. This is very different from the Karlsruhe and Riga configurations where the dynamo effect is produced by the mean flow, which can be considered laminar, and not by fluctuations. A graphical interpretation is provided on figure 1.7.

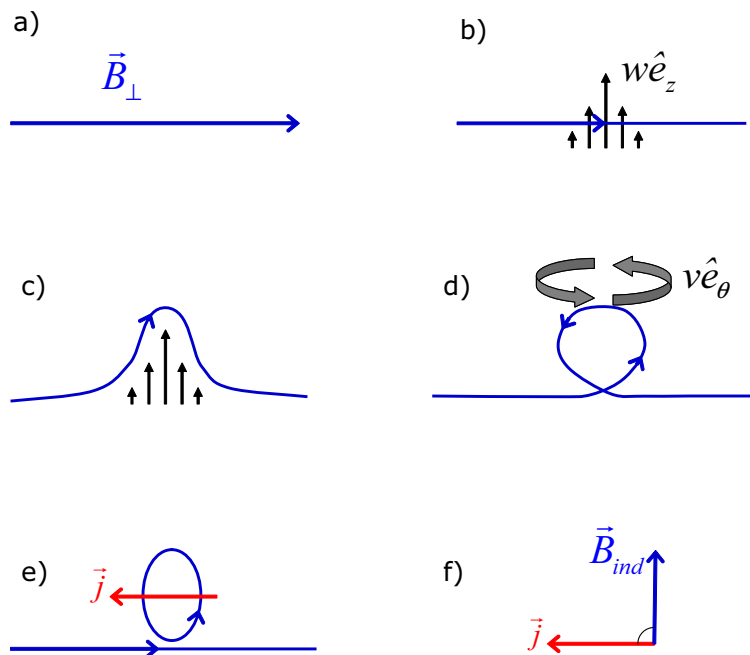


Figure 1.7: A graphical explanation for the α -effect. A secondary induced magnetic field \mathbf{B}_{ind} is created from \mathbf{B}_\perp (\mathbf{B}_\perp being induced through the Ω -effect: see fig. 1.6). The direction of the magnetic field generated by electrical currents \mathbf{j} is the same as that of the initial field \mathbf{B} (see fig. 1.6).

The von Kármán swirling flow has the capacity to produce both the Ω and α effects since the shear flow is generated by counter-rotating disks. The *Ekman pumping* creates a poloidal flow which, together with the toroidal component of velocity, results in flow having non-zero helicity.

1.4.1 Concluding remarks

The material presented in this section gives an idea about the difficulty in realization of both experimental and numerical study of a liquid dynamo. From the numerical point of view, the anti-dynamo theorems very much complicate the task, since they exclude axisymmetric as well as two-dimensional and plane flows. This means that a successful numerical simulation of the dynamo effect must be three-dimensional. Additionally, interaction between the velocity and magnetic fields requires ensuring the full coupling of these two variables in a numerical algorithm. All attempts to impose an ad-hoc velocity field (e.g. provided by experimental measurements or purely hydrodynamic simulations) which is the main idea of kinematic-dynamo approximation cannot reveal the self-sustaining character of a true dynamo effect.

Several numerical codes have been developed. Some of these simulate the kinematic dynamo and others treat the coupled problem. In spherical geometry, probably the most famous example of successful simulation of the dynamo effect is that of Glatzmaier & Roberts [31] corresponding to the Earth's dynamo model. For this configuration, the authors even observed a magnetic polarity reversal which is known to have occurred many times in the Earth's history. In cylindrical geometry, periodicity in the axial direction can be assumed in some type of dynamo (e.g. Ponomarenko or Taylor-Couette dynamo). An example of a numerical code solving a fully coupled problem in such geometry is that of Willis & Barenghi [89] applied to Taylor-Couette dynamo. The Roberts dynamo has been realized experimentally in Karlsruhe and was also simulated numerically using a kinematic dynamo code by Tilgner [85]. In this problem periodicity was imposed in two spatial directions.

The finite cylinder geometry seems to be the most difficult to implement since its only periodic direction is the angular one. Decoupling of the boundary conditions, by using spherical harmonics, can be used in the spherical geometry but cannot be used directly in the finite cylinder geometry. At present there exists no numerical code capable of solving the fully coupled hydromagnetic problem in this configuration. Implementing of the numerical method described throughout this thesis and proposing a method of extending it to the magnetohydrodynamic problem are the foundation for a three-dimensional magnetohydrodynamic solver in the finite cylinder geometry.

Part I

System description

Chapter 2

The von Kármán flow

2.1 Brief overview of studies

To situate this work in a more general context we will provide a brief overview of studies concerning the cylindrical von Kármán flow.

2.1.1 History

Open system The von Kármán flow owes its name to T. von Kármán who in 1921 introduced the problem of the flow in the semi-infinite domain bounded by a single rotating disk (see von Kármán [41]). He demonstrated that it is possible to solve the Navier-Stokes problem by using a similarity transformation leading to a system of two coupled nonlinear ordinary differential equations. The solutions to this system are called *self-similar*. One of the first solutions in this configuration was numerical, provided in 1934 by Cochran [14] who showed the characteristic effect of centrifugal *Ekman pumping* due to the rotation of the disk. The study was further advanced by Bödewadt [4] who found another self-similar solution for the fluid in solid-body rotation in contact with an infinite stationary disk. Batchelor [3], in 1951, extended the problem to the flow confined between two infinite rotating disks. In addition to the disk rotation ratio s , he introduced a new control parameter: the Reynolds number Re based on the gap between the disks. He did not, however, solve the problem explicitly, but provided instead some predictions concerning the nature of this flow. A number of solutions has been found since by analytical and numerical means – we also mention here the studies by Stewartson [84] and Zandbergen & Dijkstra [91].

The von Kármán flow controlled by these two parameters (s, Re) proved to have a rich variety of qualitatively different accessible states even before the transition to turbulence.

Finite system The first numerical study concerning disks of finite radius were performed in 1965 by Pearson [70] and followed by Brady & Durlofsky [10] who in 1987 provided asymptotic numerical results for configurations with disks of large but finite radii. Brady & Durlofsky [10] were able to simulate both open and free-slip configurations, in which lateral sidewalls were either absent or constrained only the radial component of velocity. Their results, supported also by earlier experimental and numerical observations by Dijkstra & van Hejst [20], proved

that the end conditions influence the flow over the entire domain and not only the end region. The confined flow in the counter-rotating configuration ($s < 0$) has proved to be quite different from the self-similar solutions mainly due to the separation of the boundary layer (near the disks) and the interior shear layer situated between two regions of opposite azimuthal velocities.

2.1.2 Stability analysis

The von Kármán flow in finite cylinder geometry is a very rich flow. The variation of three control parameters ($Re, s, \Gamma \equiv \frac{\text{height}}{\text{radius}}$) allows for an impressively large spectrum of qualitatively different solutions (even in a laminar regime). Defined in a simple geometry, this configuration is especially interesting for exploring the influence of its symmetries on the flow and transitions that it can undergo. From the computational point of view, the $SO(2)$ symmetry (azimuthal rotational symmetry) of the equations and the boundary conditions describing this fully three-dimensional flow can be efficiently exploited. This is also a reason for why this configuration is extensively studied in the context of transition to complex and turbulent flows. All these properties of the von Kármán flow, which is increasingly considered as one of the classical configurations, explain the constant interest of the scientific community in further exploring its complex behavior.

Chronologically, the first studies were devoted to the stability of the axisymmetric flows (mainly because of computational limitations). In the rotor-stator configuration, *vortex breakdown* forming characteristic recirculation bubbles was observed by number of authors (Lugt & Abboud [52], Daube & Sorensen [18], Lopez [46], Daube [17]). This now very well documented configuration became a benchmark for testing axisymmetric codes. Following Lopez & Shen [48], Speetjens [81] and a number of other authors, we will validate our method in the axisymmetric configuration by reproducing the stationary state at $Re = 1800$ and, for $Re = 2800$, the non-stationary, oscillating flow, for which we will compare the bifurcation threshold and the oscillation frequency against previous findings. The increasing computational power of modern computers has made it possible to study three-dimensional instabilities. Breaking of axisymmetry has become the subject of several studies, of which we can mention these of Gauthier *et al.* [28], Gelfgat *et al.* [29], Blackburn & Lopez [7], Lopez *et al.* [50] and Nore *et al.* [64]. Instabilities can be of different types: boundary-layer instabilities – leading to propagating spirals – or circular vortices (Gauthier *et al.* [27]), or shear layer instabilities ($s < 0$) – from which arise rotating waves – or funnel-like vortices observed by Lopez *et al.* [49]. Many other phenomena have been observed for different sets of (Re, s, Γ) such as negative spirals (Gauthier *et al.* [27]) or modulated traveling waves and heteroclinic cycles (Nore *et al.* [65, 64, 63]).

Three-dimensional instability precedes the axisymmetric one for $\Gamma < 1.6$ and $\Gamma > 2.8$. We have selected as the test problem for validating our code in three dimensions, a configuration with ($s = -1, \Gamma = 3.5, Re = 2150$), where the flow takes the form of a helical spiral. In section 6.3.2 we compare our results with those of Lopez *et al.* [47] and Gelfgat *et al.* [29].

2.1.3 Turbulence

Apart from the analysis of the stability of laminar von Kármán flows there exist a number of interesting phenomena that can be observed in the turbulent regime. The cylindrical geometry is very well suited for studying the properties of turbulent flows subjected to strong symmetry constraints. For example, according to the Taylor-Proudman theorem, sufficiently rapid rotation causes a flow to be independent of the direction of the rotation axis. In this regime one can expect to observe two-dimensional turbulence. This was recently explored by Swinney *et al.* [2, 40]. A related problem concerns laws describing decaying two-dimensional turbulence, which has been investigated mainly in Cartesian geometry (e.g. Yin [90]). However, decaying two-dimensional turbulence in a system with $SO(2)$ symmetry is still not very well understood. Some results have been provided by Leprovost [44]. One of the future plans for our code will be further investigation of this problem.

Still in the context of turbulent von Kármán flow, Marié [54] and Ravelet *et al.* [74] have recently discovered a very interesting instability, arising in a highly turbulent flow ($Re \approx 10^6$) in a counter-rotating configuration ($s < 0$). In this transition, a two-cell mean flow, with a shear layer at the cylinder mid-plane, undergoes switching to a one-cell mean flow with the shear layer next to the disk rotating with lower frequency. This bifurcation has a purely statistical behavior and is still very little understood. According to Ravelet *et al.* [74] this transition can also be observed for moderate values of Reynolds number $Re \approx 5000$ – a regime accessible to our numerical simulations. In chapter 7 we discuss the present state of our project to investigate this turbulent bifurcation numerically.

2.2 Mathematical model

2.2.1 System description

The flow configuration we are interested in uses an electrically conducting fluid of kinematic viscosity ν and density ρ . The container is a cylindrical vessel whose two bases can rotate with direction and speed given by Ω_+ et Ω_- (fig. 2.1). The indices $+$ and $-$ correspond to disks situated at $+h/2$ and $-h/2$ where h is the height of the cylinder. The lateral boundary is immobile. Non-dimensioning lengths by the radius R , we can redefine h to be the height-to-radius aspect ratio. The magneto-hydrodynamical properties of the fluid and of the surrounding vacuum were defined in section 1.3. We recall here equations (1.19) describing this configuration

$$\left\{ \begin{array}{l} \frac{\partial \mathbf{u}}{\partial t} + (\mathbf{u} \cdot \nabla) \mathbf{u} = -\frac{1}{\rho} \nabla \left(p + \frac{B^2}{2\mu} \right) + \frac{1}{\rho\mu} (\mathbf{B} \cdot \nabla) \mathbf{B} + \nu \Delta \mathbf{u}, \\ \frac{\partial \mathbf{B}}{\partial t} = \nabla \times (\mathbf{u} \times \mathbf{B}) + \frac{1}{\mu\sigma} \Delta \mathbf{B}, \\ \nabla \cdot \mathbf{u} = 0, \\ \nabla \cdot \mathbf{B} = 0. \end{array} \right. \quad \begin{array}{l} (2.1a) \\ (2.1b) \\ (2.1c) \\ (2.1d) \end{array}$$

This system of equations has a unique solution when completed by appropriate boundary conditions which are no-slip for the velocity field (2.2a,b) and continuity between internal and

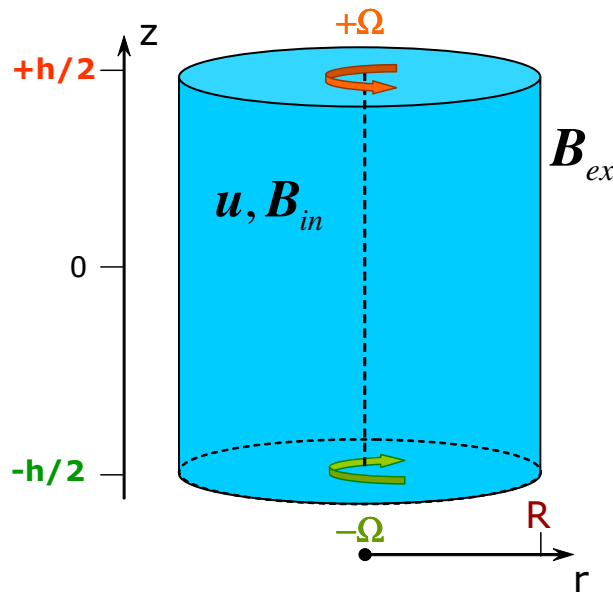


Figure 2.1: Schematic model of the cylindrical von Kármán configuration.

external parts of the magnetic field (2.2c) (see sections 1.3.1 and 3.6 for discussion of the continuity conditions):

$$\left\{ \begin{array}{l} \mathbf{u}|_{r=R} = 0, \\ \mathbf{u}|_{z=\pm\frac{h}{2}} = r\Omega_{\pm}\hat{\mathbf{e}}_{\theta}, \\ [\mathbf{B}]_{\partial} = 0, \\ \mathbf{B}|_{(r,z)\rightarrow\infty} = 0. \end{array} \right. \quad \begin{array}{l} (2.2a) \\ (2.2b) \\ (2.2c) \\ (2.2d) \end{array}$$

In the above equations the symbol ∂ represents the entire domain boundary. The notation $|_{\partial}$, $|_{r=R}$, $|_{z=\pm\frac{h}{2}}$ denote evaluation at a specified boundary and $[\cdot]_{\partial}$ measures the discontinuity at the boundary¹. One can notice that the velocity conditions (2.2) lead to a discontinuity at the cylinder corners; we will address this problem in section 4.6.

¹Discontinuity is measured as a difference between values obtained for a given expression by evaluating limits going from different directions (i.e. inside and outside the cylinder). See section 1.3.1 for a discussion of the boundary conditions.

2.2.2 Dimensionless equations

The system of equations (2.1) can be made dimensionless using the following scales:

$$\begin{aligned} \mathbf{u} : \mathcal{U} &\Rightarrow \mathbf{u}^* = \frac{\mathbf{u}}{\mathcal{U}} \\ \mathbf{B} : \mathcal{B} &\Rightarrow \mathbf{B}^* = \frac{\mathbf{B}}{\mathcal{B}} \\ \mathbf{r} : \mathcal{L} &\Rightarrow \mathbf{r}^* = \frac{\mathbf{r}}{\mathcal{L}} \\ t : \mathcal{T} &\Rightarrow t^* = \frac{t}{\mathcal{T}} \\ p : \mathcal{P} &\Rightarrow p^* = \frac{p}{\mathcal{P}} \end{aligned}$$

The characteristic units of velocity \mathcal{L} and of length \mathcal{U} can be taken to be one of the geometric lengths and the imposed velocity of the boundaries, respectively. There still remains a free choice for the time scale however – the candidates are: $\mathcal{T} = \mathcal{L}/c$, $\mathcal{T} = \mathcal{L}/\mathcal{U}$ or $\mathcal{T} = \mu\sigma\mathcal{L}^2$. From fastest to slowest time scales – \mathcal{L}/c is the characteristic time scale of propagation of electromagnetic waves, \mathcal{L}/\mathcal{U} is the characteristic time of advection by the fluid flow and finally, $\mathcal{T} = \mu\sigma\mathcal{L}^2$ is the characteristic time of diffusion of the magnetic field in the considered conducting media. For our purposes the most natural choice is the advective scale because it is also the characteristic time for the purely hydrodynamic problem with forcing which we will consider in this thesis. Therefore we define the characteristic time scale as

$$\mathcal{T} = \mathcal{L}/\mathcal{U}.$$

Once this choice has been made we can write the dimensionless form of (2.1b)

$$\frac{\mathcal{U}\mathcal{B}}{\mathcal{L}} \frac{\partial \mathbf{B}^*}{\partial t^*} = \frac{\mathcal{U}\mathcal{B}}{\mathcal{L}} \nabla^* \times (\mathbf{u}^* \times \mathbf{B}^*) + \frac{\mathcal{B}}{\mu\sigma\mathcal{L}^2} \Delta^* \mathbf{B}^*, \quad (2.3)$$

and after simplifying:

$$\frac{\partial \mathbf{B}^*}{\partial t^*} = \nabla^* \times (\mathbf{u}^* \times \mathbf{B}^*) + \frac{1}{Rm} \Delta^* \mathbf{B}^* \quad (2.4)$$

where $Rm = \mu\sigma\mathcal{L}\mathcal{U}$ is the magnetic Reynolds number which represents the ratio between intensities of magnetic advection and diffusion. The bigger the value of Rm , the more the magnetic field is influenced by the flow. One can notice that the magnetic scale \mathcal{B} is no longer present in (2.4). This is because equation (2.4) is linear in \mathbf{B}^* so that the solution to it can be arbitrarily scaled. Therefore we will choose the magnetic scale \mathcal{B} along with the nondimensionalization for the Navier-Stokes equation (2.1a):

$$\frac{\mathcal{U}}{\mathcal{T}} \frac{\partial \mathbf{u}^*}{\partial t^*} + \frac{\mathcal{U}^2}{\mathcal{L}} (\mathbf{u}^* \cdot \nabla^*) \mathbf{u}^* = -\frac{1}{\rho\mathcal{L}} \nabla^* \cdot \left(\mathcal{P} p^* + \frac{\mathcal{B}^2 \mathbf{B}^{*2}}{2\mu} \right) + \frac{\mathcal{B}^2}{\rho\mu\mathcal{L}} (\mathbf{B}^* \cdot \nabla^*) \mathbf{B}^* + \frac{\nu\mathcal{U}}{\mathcal{L}^2} \Delta^* \mathbf{u}^* \quad (2.5)$$

Using the characteristic scales listed below

$$\begin{aligned} \mathcal{T} &= \mathcal{L}/\mathcal{U} \\ \mathcal{B} &= \sqrt{\mu\rho\mathcal{U}} \\ \mathcal{P} &= \rho\mathcal{U}^2 \end{aligned}$$

we obtain the dimensionless form of (2.1a)

$$\frac{\partial \mathbf{u}^*}{\partial t^*} + (\mathbf{u}^* \cdot \nabla^*) \mathbf{u}^* = -\nabla^* \left(p^* + \frac{B^{*2}}{2} \right) + (\mathbf{B}^* \cdot \nabla^*) \mathbf{B}^* + \frac{1}{Re} \Delta^* \mathbf{u}^* \quad (2.6)$$

where $Re = \frac{\mathcal{L}\mathcal{U}}{\nu}$ is the Reynolds number which represents the ratio between characteristic scales of advective/inertial and viscous effects. In the absence of the magnetic field, if Re is small, the flow behaves more like Stokes viscous flow. If Re is large then the flow approaches ideal fluid dynamics governed by the Euler equation.

To simplify notation, we will not retain the $*$ superscript denoting dimensionless variables. From here we will use only dimensionless variables by default.

2.2.3 Equations of magnetohydrodynamics

Here we present the complete system of equations of magnetohydrodynamics (2.1) in dimensionless form and under the assumptions made in the previous section concerning characteristic time and spatial scales of the configuration we will consider:

$$\left\{ \begin{array}{l} \frac{\partial \mathbf{u}}{\partial t} + (\mathbf{u} \cdot \nabla) \mathbf{u} = -\nabla \left(p + \frac{B^2}{2} \right) + (\mathbf{B} \cdot \nabla) \mathbf{B} + \frac{1}{Re} \Delta \mathbf{u}, \\ \frac{\partial \mathbf{B}}{\partial t} = \nabla \times (\mathbf{u} \times \mathbf{B}) + \frac{1}{Rm} \Delta \mathbf{B}, \\ \nabla \cdot \mathbf{u} = 0, \\ \nabla \cdot \mathbf{B} = 0. \end{array} \right. \quad \begin{array}{l} (2.7a) \\ (2.7b) \\ (2.7c) \\ (2.7d) \end{array}$$

The boundary conditions have the same form as previously given in (2.2) except for the cylinder radius which is now fixed to $R = 1$.

$$\left\{ \begin{array}{l} \mathbf{u}|_{r=1} = 0, \\ \mathbf{u}|_{z=\pm \frac{h}{2}} = r\Omega_{\pm} \hat{\mathbf{e}}_{\theta}, \\ [\mathbf{B}]_{\partial} = 0, \\ \mathbf{B}|_{(r,z) \rightarrow \infty} = 0. \end{array} \right. \quad \begin{array}{l} (2.8a) \\ (2.8b) \\ (2.8c) \\ (2.8d) \end{array}$$

We should have dropped Ω_{\pm} in (2.8) since we already selected \mathcal{U} for the velocity scale but, because we will need it to regularize the boundary conditions (requiring $\Omega \equiv \Omega(r) \approx 1$), we will keep this dimensionless parameter.

Chapter 3

Poloidal-toroidal decomposition

3.1 Motivation

One of the most difficult numerical problems presented by the three-dimensional incompressible Navier-Stokes equations is that we must solve simultaneously for \mathbf{u} and p but all the conditions – the boundary conditions and incompressibility – are imposed only on the velocity field while none are defined for the pressure. This is because the pressure in the incompressible formulation is not a real physical quantity because it lacks thermodynamic meaning. The pressure serves only to counterbalance the nonlinear term which is the source of the divergence in the Navier-Stokes equations. The lack of boundary conditions for the pressure is sometimes treated by the ad-hoc introduction of some pressure boundary condition, notably in the family of methods based on *projection-diffusion* schemes. There are two main approaches to solving the Navier-Stokes equations without formulating any fictitious boundary conditions for the pressure field. The first method is to solve for (\mathbf{u}, p) fields (e.g. [86, 47]) or (\mathbf{u}, ω) (e.g. [78, 17, 33, 81]) using a *Green function* formalism, which in a discrete implementation has the name of *influence matrix* or *capacitance matrix* method. Another approach is to express the velocity in terms of other variables in such a manner that the divergence-free condition is satisfied by construction. The *potential methods* belong to this second category and rely on the existence of a vector potential for an arbitrary solenoidal field \mathbf{F} which is equivalent to Stoke's theorem:

$$\nabla \cdot \mathbf{F} = 0 \quad \Leftrightarrow \quad \mathbf{F} = \nabla \times \mathbf{A}$$

where the vector potential \mathbf{A} can be determined up to the gradient of an arbitrary scalar function.

The *scalar potential method* is another example of construction of a divergence-free field. By setting $\mathbf{A} \equiv \psi \hat{\mathbf{e}} + \nabla \times (\phi \hat{\mathbf{e}})$ we obtain the *poloidal*(ϕ)-*toroidal*(ψ) *decomposition* of a solenoidal field \mathbf{F}

$$\mathbf{F} = \nabla \times (\psi \hat{\mathbf{e}}) + \nabla \times \nabla \times (\phi \hat{\mathbf{e}})$$

where $\hat{\mathbf{e}}$ denotes a unit vector. This representation includes an additional gauge freedom for the choice of ψ and ϕ which we will examine in the following sections. It is clear that using one of the above representations, the $\nabla \cdot \mathbf{u} = 0$ condition is satisfied because of $\nabla \cdot \nabla \times (\cdot) = 0$. The proof of existence of such potentials for an arbitrary solenoidal field can be found in [55].

To understand where the name *poloidal-toroidal* comes from, consider a finite geometry with a rotational symmetry like a sphere or a cylinder. In the cylindrical case of interest to us, we arbitrarily fix the unit vector $\hat{\mathbf{e}} = \hat{\mathbf{e}}_z$ to be parallel to the cylinder axis (while in the spherical case one would fix $\hat{\mathbf{e}} = \hat{\mathbf{e}}_r$). The names poloidal-toroidal correspond to two main field line structures present in an axisymmetric field. Example structures are schematically represented on figure 3.1 showing basic flow structures in cylindrical von Kármán flow with counter-rotating disks. The toroidal flow corresponds to motion with only azimuthal velocity. Poloidal flow contains, in an axisymmetric case, radial and axial components of the velocity and generally forms recirculation rolls in the $r \times z$ plane. For a non-axisymmetric configuration, the two potentials have no clear associations with simple topological structures.

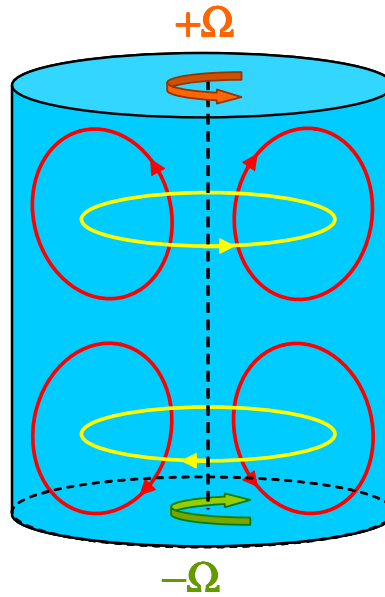


Figure 3.1: Two main topological flow structures in a case of counter-rotating disks: red (dark) – poloidal flow lines, yellow (light) – toroidal flow lines.

3.2 Poloidal-toroidal decomposition and the gauge freedom

We now introduce the *poloidal-toroidal decomposition* of the velocity and magnetic induction fields:

$$\mathbf{u} = \nabla \times (\psi_u \hat{\mathbf{e}}_z) + \nabla \times \nabla \times (\phi_u \hat{\mathbf{e}}_z), \quad (3.1a)$$

$$\mathbf{B} = \nabla \times (\psi_B \hat{\mathbf{e}}_z) + \nabla \times \nabla \times (\phi_B \hat{\mathbf{e}}_z). \quad (3.1b)$$

The components of the velocity are:

$$u_r = \frac{1}{r} \partial_\theta \psi_u + \partial_z \partial_r \phi_u, \quad (3.2a)$$

$$u_\theta = -\partial_r \psi_u + \frac{1}{r} \partial_z \partial_\theta \phi_u, \quad (3.2b)$$

$$u_z = -\Delta_h \phi_u. \quad (3.2c)$$

One important thing to notice is that this formulation contains a gauge freedom for the choice of $\psi_u, \psi_B, \phi_u, \phi_B$. The way to identify the gauge freedom is to find the class of solutions satisfying homogeneous problems $\mathbf{u} = 0$ and $\mathbf{B} = 0$. This leads to:

$$\begin{aligned} \mathbf{u}^{hom} = 0 &= \nabla \times (\psi^{hom} \hat{\mathbf{e}}_z) + \nabla \times \nabla \times (\phi^{hom} \hat{\mathbf{e}}_z) \\ 0 &= \nabla \times (\psi^{hom} \hat{\mathbf{e}}_z) + \nabla (\nabla \cdot (\phi^{hom} \hat{\mathbf{e}}_z)) - \Delta (\phi^{hom} \hat{\mathbf{e}}_z) \\ 0 &= \hat{\mathbf{e}}_z \times \nabla_h \psi^{hom} + \nabla \partial_z \phi^{hom} - (\Delta \phi^{hom}) \hat{\mathbf{e}}_z \\ 0 &= \hat{\mathbf{e}}_z \times \nabla_h \psi^{hom} + \nabla_h \partial_z \phi^{hom} - (\Delta_h \phi^{hom}) \hat{\mathbf{e}}_z \end{aligned}$$

↓

$$\hat{\mathbf{e}}_z \times \mathbf{u} = 0 \quad \Rightarrow \quad \hat{\mathbf{e}}_z \times \nabla_h \psi^{hom} = -\nabla_h \partial_z \phi^{hom} \quad (3.3a)$$

$$\hat{\mathbf{e}}_z \cdot \mathbf{u} = 0 \quad \Rightarrow \quad \Delta_h \phi^{hom} = 0 \quad (3.3b)$$

where $\nabla_h = \nabla - \partial_z \hat{\mathbf{e}}_z$, $\Delta_h = \Delta - \partial_z^2$ and the upper index hom denotes potentials corresponding to a homogeneous vector field. By (3.3b) the *poloidal potential* ϕ is determined up to a harmonic function on each domain slice perpendicular to $\hat{\mathbf{e}}_z$. Therefore the gauge freedom for the choice of the *poloidal potential* ϕ can be stated as:

$$\phi \sim \phi + \phi^{hom} \quad ; \quad \Delta_h \phi^{hom} = 0 \quad (3.4)$$

Once the choice for ϕ^{hom} is made, using (3.3a), ψ^{hom} can be determined up to an arbitrary function of the vertical coordinate z . Therefore the *toroidal potentials* $\psi_u, \psi_B \equiv \psi$ inherit the same gauge freedom:

$$\psi \sim \psi + h(z) \quad (3.5)$$

The existence of ψ^{hom} satisfying (3.3a) for all ϕ^{hom} satisfying (3.3b) is ensured through the Stokes theorem in two dimensions:

$$\begin{aligned} \nabla \times (3.3b) = 0 &\Rightarrow \Delta_h \partial_z \phi^{hom} = 0 \Rightarrow \nabla_h \cdot (\nabla_h \partial_z \phi^{hom}) = 0 \Rightarrow \\ &\Rightarrow \exists \psi^{hom} ; -\nabla_h (\partial_z \phi^{hom} \hat{\mathbf{e}}_z) = \nabla \times \psi^{hom} \hat{\mathbf{e}}_z \\ &\quad \downarrow \\ &\quad (3.3a) \end{aligned}$$

3.3 Potential form of the MHD equations

Substituting (3.1) into (2.7) results in equations whose linear parts couple three fields (ψ_u, ϕ_u, p) and two fields (ψ_B, ϕ_B). Because of the semi-implicit numerical approach which we intend to use for time integration, the separation of variables in the linear parts of equations (2.7) is essential. It is easy to accomplish this decoupling given that the $\hat{\mathbf{e}}_z$ components of the successive

curls of a vector field $\mathbf{F} = \nabla \times (\psi \hat{\mathbf{e}}_z) + \nabla \times \nabla \times (\phi \hat{\mathbf{e}}_z)$ have simple expressions:

$$\hat{\mathbf{e}}_z \cdot \mathbf{F} = -\Delta_h \phi, \quad (3.6a)$$

$$\hat{\mathbf{e}}_z \cdot \nabla \times \mathbf{F} = -\Delta_h \psi, \quad (3.6b)$$

$$\hat{\mathbf{e}}_z \cdot \nabla \times \nabla \times \mathbf{F} = \Delta \Delta_h \phi. \quad (3.6c)$$

and that, for a divergence-free field $\nabla \cdot \mathbf{F} = 0$, the Laplace operator Δ commutes with the $\nabla \times$ operator:

$$\nabla \times \Delta \mathbf{F} = \Delta \nabla \times \mathbf{F} \quad (3.7)$$

We will use (3.7), (3.6) to separate the potentials in the linear parts of equations (2.7a) and (2.7b).

$$\hat{\mathbf{e}}_z \cdot \nabla \times (\partial_t - Re^{-1}\Delta) \mathbf{u} = -(\partial_t - Re^{-1}\Delta) \Delta_h \psi_u \quad (3.8a)$$

$$\hat{\mathbf{e}}_z \cdot \nabla \times \nabla \times (\partial_t - Re^{-1}\Delta) \mathbf{u} = (\partial_t - Re^{-1}\Delta) \Delta \Delta_h \phi_u \quad (3.8b)$$

$$\hat{\mathbf{e}}_z \cdot (\partial_t - Rm^{-1}\Delta) \mathbf{B} = -(\partial_t - Rm^{-1}\Delta) \Delta_h \phi_B \quad (3.9a)$$

$$\hat{\mathbf{e}}_z \cdot \nabla \times (\partial_t - Rm^{-1}\Delta) \mathbf{B} = -(\partial_t - Rm^{-1}\Delta) \Delta_h \psi_B \quad (3.9b)$$

We can now write equations (2.7) in potential form:

$$(\partial_t - Re^{-1}\Delta) \Delta_h \psi_u = \hat{\mathbf{e}}_z \cdot \nabla \times \mathbf{s}_u \quad (3.10a)$$

$$(\partial_t - Re^{-1}\Delta) \Delta \Delta_h \phi_u = -\hat{\mathbf{e}}_z \cdot \nabla \times \nabla \times \mathbf{s}_u \quad (3.10b)$$

$$(\partial_t - Rm^{-1}\Delta) \Delta_h \phi_B = \hat{\mathbf{e}}_z \cdot \mathbf{s}_B \quad (3.11a)$$

$$(\partial_t - Rm^{-1}\Delta) \Delta_h \psi_B = \hat{\mathbf{e}}_z \cdot \nabla \times \mathbf{s}_B \quad (3.11b)$$

where

$$\mathbf{s}_u \equiv (\mathbf{u} \cdot \nabla) \mathbf{u} - (\mathbf{B} \cdot \nabla) \mathbf{B} \quad (3.12a)$$

$$\mathbf{s}_B \equiv -\nabla \times (\mathbf{u} \times \mathbf{B}) \quad (3.12b)$$

One can notice that the pressure p is no longer present in potential equations (3.10) corresponding to the original equations (2.7a) written in primitive variables, because we took the curl of the Navier-Stokes equation (2.7a). This is justified because the pressure is no longer necessary when its only task is to introduce an additional degree of freedom necessary for satisfying the divergence-free constraint, which, for the poloidal-toroidal representation (3.1), is already satisfied by construction.

3.4 Compatibility condition

3.4.1 Equivalence of potential and primitive variable formulation

Up to now we have not proved the equivalence between the potential and primitive variable formulations. Since we took the curl of equations (2.7a) and (2.7b) they gained an additional

degree of freedom which we must fix in such a way that these equations in potential form (3.10-3.11) define the same velocity \mathbf{u} and magnetic field \mathbf{B} as the original MHD equations (2.7).

We will first write (2.7) in a compact form, which will let us use a common form for (3.10) and (3.11):

$$\begin{aligned} \underbrace{(\partial_t - Re^{-1}\Delta)\mathbf{u} + \mathbf{s}_u}_{\mathbf{f}_u} &= -\nabla(p + B^2/2) \\ \mathbf{f}_u &= -\nabla(p + B^2/2) \\ \mathbf{g}_u \equiv \nabla \times \mathbf{f}_u &= 0 \end{aligned} \quad (3.13a)$$

$$\begin{aligned} \underbrace{(\partial_t - Rm^{-1}\Delta)\mathbf{B} + \mathbf{s}_B}_{\mathbf{g}_B} &= 0 \\ \mathbf{g}_B &= 0 \end{aligned} \quad (3.13b)$$

where we used a basic rule of potential theory:

$$\mathbf{f} = \nabla p \quad \Leftrightarrow \quad \nabla \times \mathbf{f} = 0 \quad (3.14)$$

Then we can write side by side the primitive variable formulation (2.7) and potential formulation (3.10), (3.11) using $\mathbf{g} \equiv \mathbf{g}_u, \mathbf{g}_B$:

$$\begin{array}{cc} \text{primitive variables} & \text{potential formulation} \\ \mathbf{g} = 0 & \Rightarrow \left\{ \begin{array}{l} \hat{\mathbf{e}} \cdot \mathbf{g} = 0 \\ \hat{\mathbf{e}} \cdot \nabla \times \mathbf{g} = 0 \end{array} \right. \end{array}$$

where $\hat{\mathbf{e}}$ is a unit vector ($\hat{\mathbf{e}} = \hat{\mathbf{e}}_z$ for (3.10)-(3.11)).

We will now prove that, for \mathbf{g} defined over a simply connected domain Ω , the potential and primitive variable formulations are equivalent if additional conditions (3.15c) and (3.15d) are satisfied:

$$\mathbf{g} = 0 \quad \Leftrightarrow \quad \left\{ \begin{array}{l} \hat{\mathbf{e}} \cdot \mathbf{g} = 0 \quad \text{in } \Omega \quad (3.15a) \\ \hat{\mathbf{e}} \cdot \nabla \times \mathbf{g} = 0 \quad \text{in } \Omega \quad (3.15b) \\ \nabla \cdot \mathbf{g} = 0 \quad \text{in } \Omega \quad (3.15c) \\ \hat{\mathbf{n}} \cdot \mathbf{g} = 0 \quad \text{on } \partial\Omega_h \quad (3.15d) \end{array} \right.$$

where $\hat{\mathbf{n}}$ is the normal vector to the boundary, and $\partial\Omega_h$ is the boundary of slices $\Omega_h \subset \Omega$ perpendicular to $\hat{\mathbf{e}}$. The rightwards implication of (3.15) is obvious, and the leftwards implication of (3.15) is proved as follows:

$$\left. \begin{array}{l} 0 = \hat{\mathbf{e}} \cdot \mathbf{g} \\ 0 = \hat{\mathbf{e}} \cdot \nabla \times \mathbf{g} \end{array} \right\} \Rightarrow \mathbf{g} = \nabla_h \kappa \left. \begin{array}{l} \nabla \cdot \mathbf{g} = 0 \\ \frac{\partial \kappa}{\partial n} = 0 \text{ on } \partial\Omega_h \end{array} \right\} \Rightarrow \Delta_h \kappa = 0 \left. \right\} \Rightarrow \kappa = \kappa_0(e) \Rightarrow \mathbf{g} = 0 \quad (3.16)$$

where the subscript h restricts differential operators to the directions perpendicular to $\hat{\mathbf{e}}$, which we shall call horizontal, e denotes the coordinate corresponding to $\hat{\mathbf{e}}$, which we call vertical, and the two-dimensional version of (3.14) has been used.

Condition (3.15c) is satisfied for \mathbf{g}_u defined in (3.13a) because $\mathbf{g} \equiv \nabla \times \mathbf{f}_u$ and for \mathbf{g}_B defined in (3.13b) because of (2.7d). The boundary condition (3.15d), which we shall call the *compatibility condition*, ensuring equivalence of both formulations, has a quite intuitive meaning as the normal projection of the original equations on the boundary. This permits the system, which has lost some information by taking the curl, to preserve some information about the original equations. Condition (3.15d) is sufficient but not unique – other boundary conditions ensuring (3.15) can exist. Discussion of the compatibility condition for a general domain (not restricted to simply-connected domains) can be found in [55].

Axisymmetric case

We will now specialize the above discussion to the cylindrical geometry where we shall choose $\hat{\mathbf{e}} \equiv \hat{\mathbf{e}}_z$ and $\hat{\mathbf{n}} \equiv \hat{\mathbf{e}}_r$. What we want to demonstrate is that for axisymmetric fields the compatibility condition (3.15d) is not necessary to guarantee the identity (3.15). This is because we can deduce $\Delta_h \kappa(r, z) = 0 \Rightarrow \kappa = \kappa_0(z)$ from (3.16) without specifying $\frac{\partial \kappa}{\partial n} = 0$ at the boundary $r = 1$:

$$\begin{aligned} \Delta_h \kappa(r, z) = \frac{1}{r} \partial_r r \partial_r \kappa(r, z) = 0 &\Rightarrow \kappa(r, z) = a_0(z) \ln(r) + \kappa_0(z) = \kappa_0(z) \\ &\Downarrow \\ \mathbf{g} = \nabla_h \kappa = \partial_r \kappa &\Rightarrow \partial_r \kappa_0 = \mathbf{g} = 0 \end{aligned} \quad (3.17)$$

where $a_0(z) = 0$ because of regularity constraints at the axis $r = 0$. We will use this property for defining the boundary conditions for the axisymmetric Fourier mode in section 5.3.

3.4.2 Hydrodynamic compatibility condition

We will now write the compatibility condition (3.15d) for the hydrodynamic problem in potential variables with $\hat{\mathbf{e}} \equiv \hat{\mathbf{e}}_z$, $\hat{\mathbf{n}} \equiv \hat{\mathbf{e}}_r$ and $\partial \Omega_h \equiv (r = 1)$:

$$\begin{aligned} 0 = \hat{\mathbf{e}}_r \cdot \mathbf{g}_u = \hat{\mathbf{e}}_r \cdot \nabla \times \mathbf{f}_u &= \hat{\mathbf{e}}_r \cdot \nabla \times ((\partial_t - Re^{-1} \Delta) \mathbf{u} + \mathbf{s}_u) = \\ &= \left(\frac{1}{r} \partial_\theta \hat{\mathbf{e}}_z - \partial_z \hat{\mathbf{e}}_\theta \right) \cdot ((\partial_t - Re^{-1} \Delta) \mathbf{u} + \mathbf{s}_u) \end{aligned} \quad (3.18)$$

Because derivatives ∂_θ and ∂_z act in directions parallel to the boundary $r = 1$, they vanish for all terms in \mathbf{f}_u which are zero at this boundary (i.e. \mathbf{u} and \mathbf{s}_u). Therefore the compatibility condition (3.18) for the velocity takes the following form:

$$\left(\frac{1}{r} \partial_\theta \hat{\mathbf{e}}_z - \partial_z \hat{\mathbf{e}}_\theta \right) \cdot \Delta \mathbf{u} = 0$$

The $\hat{\mathbf{e}}_\theta$ and $\hat{\mathbf{e}}_z$ components of the vector Laplacian have the following form:

$$\hat{\mathbf{e}}_\theta \cdot \Delta \mathbf{u} = \left(\Delta - \frac{1}{r^2} \right) u_\theta + \frac{2}{r^2} \partial_\theta u_r \quad (3.19a)$$

$$\hat{\mathbf{e}}_z \cdot \Delta \mathbf{u} = \Delta u_z \quad (3.19b)$$

After substituting (3.2) into (3.19) and fixing the gauge freedom (3.4) via $\phi_u|_{r=1} = 0$, the potential form of the compatibility condition can be written as:

$$\partial_{rz}^2 \Delta_h \psi_u - \frac{1}{r} \partial_\theta \Delta \Delta_h \phi_u = 0 \quad \text{at } r = 1 \quad (3.20)$$

3.4.3 Magnetic compatibility condition

For the magnetic field in potential formulation, the *magnetic compatibility condition* (3.15d) can be derived in an analogous way as for the velocity:

$$\hat{\mathbf{e}}_r \cdot \mathbf{g}_B = \hat{\mathbf{e}}_r \cdot \left((\partial_t - Rm^{-1} \Delta) \mathbf{B} + \mathbf{s}_B \right) = 0$$

but contrary to the velocity, the magnetic field does not vanish on the boundary so $\partial_t \mathbf{B} \neq 0$. As for the nonlinear term \mathbf{s}_B defined in (3.12b), it vanishes at the boundary because $\mathbf{u}|_{r=1} = 0$ ¹.

$$\hat{\mathbf{e}}_r \cdot \left(\partial_t - Rm^{-1} \Delta \right) \mathbf{B} = 0$$

In polar coordinates the radial component of the vector Laplace operator has the following form

$$\hat{\mathbf{e}}_r \cdot \Delta \mathbf{B} = \left(\Delta - \frac{1}{r^2} \right) B_r - \frac{2}{r^2} \partial_\theta B_\theta \quad (3.21)$$

Using (3.21) and substituting the potential form of B_r and B_θ analogous to (3.2) we obtain the potential form of the magnetic compatibility condition:

$$\left(\partial_t - \frac{1}{Rm} \left(\Delta - \frac{1}{r^2} \right) \right) \underbrace{\left(\frac{1}{r} \partial_\theta \psi_B + \partial_r \partial_z \phi_B \right)}_{B_r} - \frac{1}{Rm} \frac{2}{r^2} \partial_\theta \underbrace{\partial_r \psi_B}_{B_\theta} = 0 \quad \text{at } r = 1 \quad (3.22)$$

where the gauge was fixed via $\phi_B|_{r=1} = 0$ in order to simplify the expression for B_θ .

3.5 Hydrodynamic boundary conditions

We consider here the case of non-slip boundary conditions for velocity given by (2.8a,b). In potential variables these conditions can be written as follows:

At $r = 1$:

$$\underbrace{\frac{1}{r} \partial_\theta \psi_u + \partial_z \partial_r \phi_u}_{u_r} = 0, \quad (3.23a)$$

$$\underbrace{-\partial_r \psi_u + \frac{1}{r} \partial_z \partial_\theta \phi_u}_{u_\theta} = 0, \quad (3.23b)$$

$$\underbrace{-\Delta_h \phi_u}_{u_z} = 0. \quad (3.23c)$$

¹Since the expression $\hat{\mathbf{e}}_r \cdot \nabla \times (\mathbf{u} \times \mathbf{B})|_{r=1}$ does not involve normal derivatives of \mathbf{u} which may not be zero at $r = 1$, therefore the condition $\mathbf{u}|_{r=1} = 0$ is sufficient to guarantee $\mathbf{s}_B|_{r=1} = 0$

At $z = \pm \frac{h}{2}$:

$$\frac{1}{r} \partial_\theta \psi_u + \partial_z \partial_r \phi_u = 0, \quad (3.24a)$$

$$-\partial_r \psi_u + \frac{1}{r} \partial_z \partial_\theta \phi_u = r \Omega_\pm, \quad (3.24b)$$

$$-\Delta_h \phi_u = 0. \quad (3.24c)$$

As we discussed in section 3.2, there exists additional freedom for choosing ψ_u and ϕ_u : the gauge freedom. By fixing

$$\phi_u(r=1) = 0 \quad (3.25)$$

we can further simplify (3.23b):

$$\begin{aligned} \phi_u(r=1) = 0 \quad \Rightarrow \quad \partial_\theta \phi_u = \partial_z \phi_u = 0 \quad \text{at } r=1 \\ \Downarrow \\ \partial_r \psi_u = 0 \quad \text{at } r=1 \end{aligned} \quad (3.26a)$$

It is also possible to simplify (3.24a,b). The gauge freedom $\phi_u(r=1) = 0$ together with (3.24c) results in the Laplace equation on a horizontal disk with homogeneous boundary conditions. Such a problem has only the zero solution so we have:

$$\phi_u(z = \pm h/2) = 0 \quad (3.27)$$

Now we rewrite equation (3.24a) as

$$0 = \frac{1}{r} \partial_\theta \psi_u + \partial_z \partial_r \phi_u = r \left[-\frac{1}{r} \partial_\theta \left(\frac{-\psi_u}{r} \right) + \frac{1}{r} \partial_r r \left(\frac{\partial_z \phi_u}{r} \right) \right] = r \hat{\mathbf{e}}_z \cdot \nabla \times \left(\frac{-\psi_u}{r} \hat{\mathbf{e}}_r + \frac{\partial_z \phi_u}{r} \hat{\mathbf{e}}_\theta \right)$$

so, using (3.14), on each horizontal disk there exists a scalar potential $f(r, \theta)$ such that

$$\frac{-\psi_u}{r} \hat{\mathbf{e}}_r + \frac{\partial_z \phi_u}{r} \hat{\mathbf{e}}_\theta = \nabla_h f = \partial_r f \hat{\mathbf{e}}_r + \frac{1}{r} \partial_\theta f \hat{\mathbf{e}}_\theta \quad \Rightarrow \quad \begin{cases} \psi_u = -r \partial_r f \\ \partial_z \phi_u = \partial_\theta f \end{cases} \quad (3.28)$$

On the other hand we can now write

$$r \Omega_\pm = -\partial_r \psi_u + \frac{1}{r} \partial_\theta \partial_z \phi_u = \partial_r r \partial_r f + \frac{1}{r} \partial_\theta^2 f = r \Delta_h f$$

but from (3.27) and $\partial_z \phi_u = \partial_\theta f$ follows $\partial_\theta f(r=1, \theta) = 0 \Rightarrow f(r=1, \theta) = f_0$, so we have

$$r \Delta_h f = \Omega_\pm \quad \text{with } f(r=1, \theta) = f_0 \quad (3.29a)$$

$$\Downarrow \\ f = f_0 + \frac{\Omega_\pm \pi}{2} (r^2 - 1)$$

Then using (3.28) we can write the conditions equivalent to (3.24a,b):

$$\left. \begin{aligned} \psi_u = -r \partial_r f &= -\frac{\Omega_\pm \pi r^2}{2} \\ \partial_z \phi_u = \partial_\theta f &= 0 \end{aligned} \right\} \quad \text{at } z = \pm \frac{h}{2}$$

Equations (3.10) have five Laplacians acting in the horizontal directions and three acting in the vertical directions. Thus five conditions should be imposed on the lateral boundary and three at each cylinder disk. The number of conditions (3.24) imposed on $z = \pm h/2$ matches, however the no-slip conditions (3.23) imposed on $r = 1$ give us only three of five conditions needed. One of the two remaining conditions is the gauge freedom (3.25) that we already used for simplifying the no-slip conditions. The second is the compatibility condition (3.20) for the hydrodynamic potential problem. Therefore the complete system of boundary conditions is

$$\left. \begin{aligned} r^{-1}\partial_{\theta}\psi_u + \partial_z\partial_r\phi_u &= 0 & (3.30a) \\ \partial_r\psi_u &= 0 & (3.30b) \\ -\Delta_h\phi_u &= 0 & (3.30c) \\ \phi_u &= 0 & (3.30d) \\ \partial_{rz}^2\Delta_h\psi_u - \frac{1}{r}\partial_{\theta}\Delta\Delta_h\phi_u &= 0 & (3.30e) \end{aligned} \right\} \text{ at } r = 1$$

$$\left. \begin{aligned} \psi_u &= -\frac{\Omega_{\pm}\pi r^2}{2} & (3.31a) \\ \partial_z\phi_u &= 0 & (3.31b) \\ -\Delta_h\phi_u &= 0 & (3.31c) \end{aligned} \right\} \text{ at } z = \pm\frac{h}{2}$$

3.6 Magnetic boundary conditions

While equations (3.11) for the magnetic induction are of lower differential order than those for the velocity (3.10), the corresponding magnetic boundary conditions are more problematic. The magnetic field is not specified on the boundary but must instead satisfy the matching rules defined at the surface between two different regimes (see section 1.3.1).

3.6.1 General case

For the time-dependent fields in a non-ferromagnetic medium of finite electrical conductivity, the complete set of boundary conditions is defined in (1.6) and results in four scalar conditions. We recall these equations here:

$$[\hat{\mathbf{n}} \times \mathbf{E}] = 0 \quad (3.32a)$$

$$[\hat{\mathbf{n}} \times \mathbf{B}] = 0 \quad (3.32b)$$

If no further assumptions concerning the nature of the magnetic field can be made on either side of the boundary then the equations describing the two physically distinct regimes have form (2.7) and differ only in their dimensionless parameters Re and Rm . Since equation (3.32a) refers to the electric field \mathbf{E} which we already eliminated from the MHD equations, we now need to relate the condition imposed on \mathbf{E} and the potentials ψ_B, ϕ_B . This can be done by

deriving conditions for the magnetic vector potential \mathbf{A} instead of the electric field. There exists a direct relation between the magnetic vector potential satisfying

$$\mathbf{B} = \nabla \times \mathbf{A} \quad (3.33)$$

and the poloidal-toroidal decomposition (3.1b) into the scalar potentials ψ_B and ϕ_B :

$$\mathbf{B} = \nabla \times \mathbf{A} = \nabla \times (\psi_B \hat{\mathbf{e}}_z + \nabla \times (\phi_B \hat{\mathbf{e}}_z)), \quad (3.34)$$

so we have

$$\mathbf{A} = \psi_B \hat{\mathbf{e}}_z + \nabla \times (\phi_B \hat{\mathbf{e}}_z). \quad (3.35)$$

Equation (3.33) defines the magnetic vector potential up to a gradient of an arbitrary scalar potential ϕ^A

$$\mathbf{A} \sim \mathbf{A} + \nabla \phi^A$$

On the other hand from (1.1a) we have

$$\nabla \times \mathbf{E} = -\frac{\partial \mathbf{B}}{\partial t} \Rightarrow \nabla \times \left(\mathbf{E} + \frac{\partial \mathbf{A}}{\partial t} \right) = 0 \Rightarrow \mathbf{E} = -\frac{\partial \mathbf{A}}{\partial t} - \nabla \phi^E$$

where ϕ^E in the stationary problem corresponds to the electrostatic potential satisfying $\Delta \phi^E = \chi/\epsilon$ and in a non-stationary case depends on the form of \mathbf{A} . Due to the gauge freedom for the choice of \mathbf{A} , it is legitimate to set $\phi^E = 0$ but one can prefer to preserve this degree of freedom for other purposes. Fixing it would fix also the gauge for ψ_B and ϕ_B which can be used to simplify the boundary conditions as was done for the velocity conditions in section 3.5. Therefore the continuity condition (3.32a) is equivalent to

$$\left[\hat{\mathbf{n}} \times \frac{\partial \mathbf{A}}{\partial t} \right] = - \left[\hat{\mathbf{n}} \times \nabla \phi^E \right].$$

We can require $[\phi^E] = 0$ without fixing the gauge freedom for ϕ^A completely². Then we can write

$$\left[\hat{\mathbf{n}} \times \frac{\partial \mathbf{A}}{\partial t} \right] = 0.$$

If the magnetic vector potential \mathbf{A} satisfy $[\hat{\mathbf{n}} \times \mathbf{A}] = 0$ at some initial time (which we can always suppose), for the non-stationary problem, the continuity of $\partial_t [\hat{\mathbf{n}} \times \mathbf{A}]$ is equivalent to the continuity of $[\hat{\mathbf{n}} \times \mathbf{A}]$. To summarize, we shall write the boundary conditions for the magnetic field and the magnetic vector potential as:

$$[\hat{\mathbf{n}} \times \mathbf{A}] = 0 \Leftrightarrow [\hat{\mathbf{n}} \times \mathbf{E}] = 0 \quad (3.36a)$$

$$[\hat{\mathbf{n}} \times \mathbf{B}] = 0 \quad (3.36b)$$

Now the continuity conditions (3.36) can be translated into the conditions for magnetic scalar

²Fixing $[\phi^E]$ means only that we can specify it only on a single side of the boundary.

potentials. On the lateral boundary $r = 1$, $\hat{\mathbf{n}} = \hat{\mathbf{e}}_r$, using (3.36) together with (3.34) and (3.35) we obtain at $r = 1$:

$$[\hat{\mathbf{e}}_r \times \mathbf{A}] = 0 \Leftrightarrow \begin{cases} [A_\theta] = 0 & \Leftrightarrow [\partial_r \phi_B] = 0 \\ [A_z] = 0 & \Leftrightarrow [\psi_B] = 0 \end{cases} \quad (3.37a)$$

$$[\hat{\mathbf{e}}_r \times \mathbf{B}] = 0 \Leftrightarrow \begin{cases} [B_\theta] = 0 & \Leftrightarrow [-\partial_r \psi_B + \frac{1}{r} \partial_z \partial_\theta \phi_B] = 0 \\ [B_z] = 0 & \Leftrightarrow [-\Delta_h \phi_B] = 0 \end{cases} \quad (3.37b)$$

Similarly, at the top and bottom disks $z = \pm \frac{h}{2}$, $\hat{\mathbf{n}} = \hat{\mathbf{e}}_z$ we have

$$[\hat{\mathbf{e}}_z \times \mathbf{A}] = 0 \Leftrightarrow \begin{cases} [A_r] = 0 & \Leftrightarrow [\frac{1}{r} \partial_\theta \phi_B] = 0 \\ [A_\theta] = 0 & \Leftrightarrow [\partial_r \phi_B] = 0 \end{cases} \quad (3.38a)$$

$$[\hat{\mathbf{e}}_z \times \mathbf{B}] = 0 \Leftrightarrow \begin{cases} [B_r] = 0 & \Leftrightarrow [\frac{1}{r} \partial_\theta \psi_B + \partial_z \partial_r \phi_B] = 0 \\ [B_\theta] = 0 & \Leftrightarrow [-\partial_r \psi_B + \frac{1}{r} \partial_z \partial_\theta \phi_B] = 0 \end{cases} \quad (3.38b)$$

Are these conditions sufficient to define a well-posed problem? Equations (3.11) have two Laplacians acting in the vertical direction and four Laplacians acting in the horizontal direction. This means that four conditions must be given on the lateral cylinder boundary and two conditions on each of the two disks. The four conditions given by (3.32) or (3.36) are not sufficient, however. This is because they involve an additional unknown field, the external field outside the cylinder. We can define the external magnetic problem in the same manner as we defined the internal problem in (3.11):

$$(\partial_t - Rm_{ex}^{-1} \Delta) \Delta_h \phi^{B_{ex}} = \hat{\mathbf{e}}_z \cdot \mathbf{s}^{B_{ex}} \quad (3.39a)$$

$$(\partial_t - Rm_{ex}^{-1} \Delta) \Delta_h \psi^{B_{ex}} = \hat{\mathbf{e}}_z \cdot \nabla \times \mathbf{s}^{B_{ex}} \quad (3.39b)$$

Considering two different regimes (\mathbf{B} and \mathbf{B}_{ex}) requires twice as many conditions as a single-regime system.

We shall note however that the poloidal-toroidal formulation has the gauge freedom which allows us to arbitrarily set both internal and external potentials $\phi_B, \phi^{B_{ex}}$ at the boundary as we already did for the velocity potential ϕ_u in (3.25). This would give two additional equations. Additionally, fixing the gauge freedom for the poloidal potentials simplifies the boundary conditions. Setting in (3.37b)

$$\phi_B|_{r=1} = \phi^{B_{ex}}|_{r=1} = 0 \quad (3.40)$$

leads to the following simplifications at $r = 1$:

$$\left[-\partial_r \psi_B + \frac{1}{r} \partial_z \partial_\theta \phi_B \right] = 0 \Rightarrow [\partial_r \psi_B] = 0$$

and using (3.40) in (3.38b) gives at $z = \pm \frac{h}{2}$:

$$\left. \begin{aligned} \left[\frac{1}{r} \partial_\theta \psi_B + \partial_z \partial_r \phi_B \right] &= 0 \\ \left[-\partial_r \psi_B + \frac{1}{r} \partial_z \partial_\theta \phi_B \right] &= 0 \end{aligned} \right\} \Rightarrow [\partial_z \phi_B] = 0, \quad [\psi_B] = 0 \quad (3.41)$$

$$(3.42)$$

These simplifications can be derived by repeating the same procedure as for the boundary conditions for the velocity (see. section 3.5) and using the ability to differentiate jump condition in the directions tangent (but not normal) to the surface. The last two missing conditions needed to complete the system (3.11), (3.39a) are the magnetic compatibility condition (3.22) for both internal and external fields. Finally the complete system of boundary conditions for the magnetic potentials at the boundary between two different conducting fluids has the following form:

$$\left. \begin{aligned}
 & \left. \begin{aligned}
 & [-\partial_r \psi_B] = 0 \\
 & [\psi_B] = 0 \\
 & [\partial_r \phi_B] = 0 \\
 & [-\Delta_h \phi_B] = 0 \\
 & \phi_B = 0 \\
 & \phi^{B_{ex}} = 0
 \end{aligned} \right\} r = 1 \\
 & \left. \begin{aligned}
 & \left(\partial_t - Rm^{-1} (\Delta - r^{-2}) \right) \left(r^{-1} \partial_\theta \psi_B + \partial_r \partial_z \phi_B \right) - Rm^{-1} 2r^{-2} \partial_\theta \partial_r \psi_B = 0 \\
 & \left(\partial_t - Rm_{ex}^{-1} (\Delta - r^{-2}) \right) \left(r^{-1} \partial_\theta \psi^{B_{ex}} + \partial_r \partial_z \phi^{B_{ex}} \right) - Rm_{ex}^{-1} 2r^{-2} \partial_\theta \partial_r \psi^{B_{ex}} = 0
 \end{aligned} \right\} \\
 & \left. \begin{aligned}
 & [\psi_B] = 0 \\
 & [\partial_z \phi_B] = 0 \\
 & \phi_B = 0 \\
 & \phi^{B_{ex}} = 0
 \end{aligned} \right\} z = \pm \frac{h}{2}
 \end{aligned} \right\}$$

3.6.2 Conductor/vacuum configuration

The case when the fluid of finite electric conductivity is restricted to a finite volume (here a cylinder) and is surrounded by vacuum is of special importance to us, because it models well the experimental configuration of the VKS experiment. As it was already explained in section 1.3.1, the boundary condition for the magnetic field can be simplified. We recall that the external magnetic field in vacuum satisfies

$$\nabla \times \mathbf{B}^{vac} = 0 \quad \Rightarrow \quad \mathbf{B} = \nabla \phi^{vac}$$

In this case the continuity of all three components of the magnetic field are sufficient conditions to uniquely determine both the internal and external fields. The equations describing the internal field are given in (3.11) while the external problem is reduced to

$$\Delta \phi^{vac} = 0 \quad (3.45)$$

Equations (3.11) and (3.45) contain five Laplacians acting in the horizontal direction and three acting in the vertical direction. Continuity of the magnetic field at the boundary gives us three scalar conditions:

$$[\mathbf{B}] = 0 \quad \Rightarrow \quad \left\{ \begin{aligned}
 & B_r = B_r^{vac} \quad \Rightarrow \quad \frac{1}{r} \partial_\theta \psi_B + \partial_r (\partial_z \phi_B - \phi^{vac}) = 0 \quad (3.46a) \\
 & B_\theta = B_\theta^{vac} \quad \Rightarrow \quad -\partial_r \psi_B + \frac{1}{r} \partial_\theta (\partial_z \phi_B - \phi^{vac}) = 0 \quad (3.46b) \\
 & B_z = B_z^{vac} \quad \Rightarrow \quad -\Delta \phi_B + \partial_z (\partial_z \phi_B - \phi^{vac}) = 0 \quad (3.46c)
 \end{aligned} \right.$$

The magnetic potential ϕ^{vac} corresponds to the potentials $\psi^{B_{ex}}$ and $\phi^{B_{ex}}$ used in the previous subsection. It defines the external magnetic field \mathbf{B}_{ex} in vacuum. Since the relation between these variables is indirect, the equations and boundary conditions for the configuration with the vacuum as the external medium must be derived independently from the general formulation. Instead of the gauge choice (3.40), we can choose ϕ_B in a way to satisfy

$$(\partial_z \phi_B - \phi^{vac})|_{r=1} = 0 \quad (3.47)$$

Then the complete system of boundary conditions, including the magnetic compatibility condition (3.22), takes the following form:

At $r = 1$, we have

$$[B_r] = 0 \Rightarrow \frac{1}{r} \partial_\theta \psi_B + \partial_r (\partial_z \phi_B - \phi^{vac}) = 0 \quad (3.48a)$$

$$[B_\theta] = 0 \Rightarrow \partial_r \psi_B = 0 \quad (3.48b)$$

$$[B_z] = 0 \Rightarrow \Delta \phi_B = 0 \quad (3.48c)$$

$$gauge \Rightarrow \partial_z \phi_B - \phi^{vac} = 0 \quad (3.48d)$$

$$magnetic\ compatibility\ condition \Rightarrow (\partial_t - Rm^{-1} (\Delta - r^{-2})) (r^{-1} \partial_\theta \psi_B + \partial_r \partial_z \phi_B) + Rm^{-1} \frac{2}{r^3} \partial_z \partial_\theta \phi_B = 0 \quad (3.48e)$$

where the form of the magnetic compatibility condition (3.22) was altered by a different choice of the gauge condition (3.48d) and simplified using (3.48b).

At $z = \pm h/2$, conditions (3.46) remain unchanged. In section 5.6 we will explain how to numerically solve (3.11) with the boundary conditions (3.46).

3.7 Discussion

3.7.1 Advantages/disadvantages

A natural question that the reader could ask about the idea of the toroidal-poloidal decomposition is: What are the advantages of this approach over the traditional primitive variables or velocity-vorticity formulations? Some reasons can be outlined:

- The first reason for using a potential formulation is to satisfy the incompressibility constraint which is difficult to accomplish by non-potential methods.
- There is no need to solve for the hydrodynamic pressure since it has been completely removed from potential equations.
- The induction equation (2.7b), contrary to the Navier-Stokes equation (2.7a), does not contain a pressure term, which is used in the primitive variable formulation for imposing the divergence-free condition. For this reason some algorithms introduce a fictitious pressure term. In the toroidal-poloidal formulation the magnetic field is solenoidal by construction.

- Because all operators in potential equations (3.10) and (3.11) act on scalar fields, the Poisson solver needed for implementing a semi-implicit scheme for time integration is simpler. In contrast, vector operators like $\Delta \mathbf{F}$ couple the components of the vector field and diagonalization of the corresponding Poisson problem requires the introduction of redefined variables (see [86] or [69] for an adequate methodology).
- Single type of spectral expansion can be used for scalar potentials. For vector fields each component has different type of radial / azimuthal expansion; see the discussion in section 4.4.

Of course there is always a price to pay for removing serious problem, here the incompressibility constraint. A new difficulty has appeared in the potential formulation: equations (3.10) and (3.11) are of higher differential order than the equivalent equations (2.7) and the associated boundary conditions are far more complex: some of them couple the potentials and are of high differential order (e.g. compatibility conditions). Imposing such complicated conditions requires sophisticated methods. The *influence matrix* technique is the method of choice when complex and possibly coupled boundary conditions must be satisfied, but, as the reader will see in section 5.4, proves to be quite difficult to implement.

In the primitive variable formulation, solving for the pressure field requires a method which is similar to the influence matrix approach. Taking this into account, the primitive variable and potential formulations can be considered comparable in terms of technical difficulty.

3.7.2 Concluding remarks

In this chapter we have introduced a potential formulation of the magnetohydrodynamic equations (2.7), where the poloidal-toroidal decomposition of the solenoidal vector fields \mathbf{u} and \mathbf{B} has been used to impose the divergence-free constraint. According to the physical model studied, the appropriate boundary conditions (2.8) have been stated in their potential form and simplified. In particular, the necessity for imposing the compatibility condition, ensuring equivalence between the primitive variable and the poloidal-toroidal description, has been explained and a possible form of this condition has been given for both velocity and magnetic fields (see section 3.4). The MHD equations (3.10) and (3.11) in the scalar potential form define four equations whose linear parts are decoupled. This greatly simplifies the numerical method used for solving the system when a semi-implicit time integration scheme is performed. We recall that the original vector equations (2.7), written in cylindrical coordinates, couple components of the vector fields.

Notation concerning the velocity and magnetic potentials introduced in this chapter will be widely used in the following chapters. The numerical method explained in this thesis is focused on solving the equations in the form given by (3.10) and (3.11) with boundary conditions stated in (3.30), (3.31), (3.46) and (3.48). We assemble here all of these equations and boundary conditions:

Hydrodynamic problem:

$$(\partial_t - Re^{-1}\Delta)\Delta_h\psi_u = \hat{\mathbf{e}}_z \cdot \nabla \times \mathbf{s}_u \quad (3.49a)$$

$$(\partial_t - Re^{-1}\Delta)\Delta\Delta_h\phi_u = -\hat{\mathbf{e}}_z \cdot \nabla \times \nabla \times \mathbf{s}_u \quad (3.49b)$$

$$\mathbf{s}_u \equiv (\mathbf{u} \cdot \nabla)\mathbf{u} - (\mathbf{B} \cdot \nabla)\mathbf{B} \quad (3.49c)$$

Boundary conditions:

$$r^{-1}\partial_\theta\psi_u + \partial_z\partial_r\phi_u = 0 \quad (3.50a)$$

$$\partial_r\psi_u = 0 \quad (3.50b)$$

$$-\Delta_h\phi_u = 0 \quad (3.50c)$$

$$\phi_u = 0 \quad (3.50d)$$

$$\partial_{rz}^2\Delta_h\psi_u - \frac{1}{r}\partial_\theta\Delta\Delta_h\phi_u = 0 \quad (3.50e)$$

$$\psi_u = -\frac{\Omega_\pm\pi r^2}{2} \quad (3.51a)$$

$$\partial_z\phi_u = 0 \quad (3.51b)$$

$$-\Delta_h\phi_u = 0 \quad (3.51c)$$

Magnetic problem (conductor/vacuum):

$$(\partial_t - Rm^{-1}\Delta)\Delta_h\phi_B = \hat{\mathbf{e}}_z \cdot \mathbf{s}_B \quad (3.52a)$$

$$(\partial_t - Rm^{-1}\Delta)\Delta_h\psi_B = \hat{\mathbf{e}}_z \cdot \nabla \times \mathbf{s}_B \quad (3.52b)$$

$$\mathbf{s}_B \equiv -\nabla \times (\mathbf{u} \times \mathbf{B}) \quad (3.52c)$$

$$\Delta\phi^{vac} = 0 \quad (3.52d)$$

Boundary conditions:

$$\frac{1}{r}\partial_\theta\psi_B + \partial_r(\partial_z\phi_B - \phi^{vac}) = 0 \quad (3.53a)$$

$$\partial_r\psi_B = 0 \quad (3.53b)$$

$$\Delta\phi_B = 0 \quad (3.53c)$$

$$\partial_z\phi_B - \phi^{vac} = 0 \quad (3.53d)$$

$$\left(\partial_t - Rm^{-1}(\Delta - r^{-2})\right)\left(r^{-1}\partial_\theta\psi_B + \partial_r\partial_z\phi_B\right) + Rm^{-1}\frac{2}{r^3}\partial_z\partial_\theta\phi_B = 0 \quad (3.53e)$$

$$\frac{1}{r}\partial_\theta\psi_B + \partial_r(\partial_z\phi_B - \phi^{vac}) = 0 \quad (3.54a)$$

$$-\partial_r\psi_B + \frac{1}{r}\partial_\theta(\partial_z\phi_B - \phi^{vac}) = 0 \quad (3.54b)$$

$$\Delta_h\phi_B + \partial_z\phi^{vac} = 0 \quad (3.54c)$$

Part II

Numerical method – Spectral solver

Chapter 4

Spectral discretization

4.1 Introduction

There exist two main categories of numerical methods used for solving partial derivatives. The difference between them is essentially the way the differential expressions are evaluated. In the first category are *local methods*, sometimes called *finite precision* or *fixed precision* methods and to this class belong techniques like finite difference/volume/elements. Spectral methods represent the second family, called *global* or *spectral precision* methods.

We present in this chapter a brief and definitely not comprehensive comparison of both classes together with arguments playing a role for the choice of a method best suited to our needs. The necessary introduction of spatial discretization models in all three dimensions $\hat{\mathbf{e}}_r, \hat{\mathbf{e}}_\theta, \hat{\mathbf{e}}_z$ is presented in this chapter while paying special attention to the various singularity issues of a cylindrical coordinate system of finite size.

4.1.1 Local methods

The adjective "local" means that to evaluate an expression containing differential operators at a given point, only its neighborhood (fixed number of points situated in its proximity) is taken into account. These methods are characterized by an algebraic convergence, i.e. the error ϵ of approximation of an exact solution by the discrete solution decays with a fixed order D :

$$\epsilon \sim N^{-D},$$

where N is the spatial resolution of the method. Local methods are also sometimes called *finite precision* methods.

4.1.2 Spectral precision

For this class of methods, a truncated series of orthogonal functions is used to represent the solution. In this sense, one should no longer think of spatial discretization in terms of partitioning the computational domain into some number of points/volumes/elements. In spectral methods the solution is decomposed in a basis of orthogonal functions appropriate for a given geometry and problem specificity. The solution is uniquely represented by the *spectral coefficients* of the weighted sum of basis functions. For spectral methods the analytical rules for

differentiating the basis functions imply how the coefficients defining the solution should be transformed under differentiation. Because each basis function is defined over the global domain, spectral methods are called global. In other words, knowledge of the whole solution is needed to evaluate a differential expression in a single point.

The most important advantage of spectral methods is their spatial convergence property. For an infinitely differentiable solution, these techniques have an exponential convergence i.e.

$$\epsilon \sim \exp(-N)$$

where N is the number of basis functions used for representing a solution. This means that the convergence of a spectral method is always faster than that of a method converging as any finite power of N . This is the reason why these methods are sometimes said to be of *infinite precision*.

Singularity and spectral methods

As was mentioned in the introduction, exponential convergence is possible under the condition that the solution is C^∞ . When the function has only m continuous derivatives the general theory of polynomial approximation predicts that the order of a spectral method becomes algebraic:

$$\epsilon \sim N^{-(m+\delta)}$$

where δ does not depend on m . Therefore, in practice, spectral methods are advantageous mainly for problems where the solution is regular, or the singularity can in some way be eliminated or damped.

4.1.3 Advantages and limitations of spectral methods

As it is not the subject of this work to make a comprehensive comparison of different discretization approaches, we outline only the most important advantages and drawbacks of local and spectral methods in order to justify the choice we have made for the numerical method.

local methods

algebraic convergence
no geometry restrictions
less susceptible to singularities

spectral methods

exponential convergence (less resolution is needed)
only simple geometries are permitted
singularities deteriorate convergence
(one should note however that singularities often reduce the convergence of spectral methods to the level that local methods have without singularities)

Because the geometry of the investigated problem is quite simple (finite cylinder) the use of spectral methods seems natural. Moreover, since the numerical code is intended to be used for studying three-dimensional turbulent hydromagnetic flows, high spatial precision makes it possible to reduce the resolution needed for performing computationally expensive simulations. In the following sections we will define the spectral basis appropriate for the cylindrical geometry.

4.2 Azimuthal direction

It is natural to use the Fourier basis for representing a function's angular dependence. Let $f(\theta)$ be periodic over the interval $\theta \in [0, 2\pi]$. The truncated Fourier-series approximation can be stated as:

$$f(\theta) \approx \sum_{m=-\lfloor \frac{M}{2} \rfloor}^{\lfloor \frac{M}{2} \rfloor} \hat{f}^m e^{im\theta},$$

where M is the azimuthal resolution and $\lfloor \frac{M}{2} \rfloor$ denotes the largest integer smaller than $\frac{M}{2}$. Quantity $\lfloor \frac{M}{2} \rfloor$ correspond to the number of Fourier modes (for the circular domain it corresponds to the maximal angular frequency which can be represented by this approximation) and \hat{f}^m are spectral coefficients of the expansion of f in the Fourier basis. The symbol $\hat{\cdot}$ indicates that the quantity is related to the spectral space.

Since we will solve the Navier-Stokes and induction equations using a pseudo-spectral method, evaluation of nonlinear terms requires the use of collocation points. The product of functions in *physical space* corresponds to the convolution of their spectral transforms $\widehat{fg} = \hat{f} * \hat{g}$, but for evaluating nonlinear terms it is easier to perform this in physical space using discrete function values $f^l \equiv f(\theta_l)$ evaluated at Gauss quadrature abscissas¹:

$$\theta_l = \frac{2\pi l}{M} \quad ; \quad l = 0 \dots M-1. \quad (4.1)$$

Additionally, if $f : \mathbb{R} \rightarrow \mathbb{R}$, then coefficients \hat{f}^m corresponding to negative m can be determined from those with positive m because of the relation $\hat{f}^{-m} = \overline{\hat{f}^m}$, where $\overline{\cdot}$ denotes complex conjugate. We then have:

$$f(\theta) \approx \sum_{m=0}^{\lfloor \frac{M}{2} \rfloor} \hat{f}^m e^{im\theta} + \sum_{m=1}^{\lfloor \frac{M}{2} \rfloor} \overline{\hat{f}^m} e^{-im\theta}. \quad (4.2)$$

This series can be further split into even and odd modes whose spectral coefficients are real numbers

$$f(\theta_l) = \hat{f}^0 + 2 \sum_{m=1}^{\lfloor \frac{M}{2} \rfloor} \Re(\hat{f}^m) \cos(m\theta_l) - 2 \sum_{m=1}^{\lfloor \frac{M-1}{2} \rfloor} \Im(\hat{f}^m) \sin(m\theta_l), \quad (4.3)$$

where $\hat{f}^0 \in \mathbb{R}$ and if M is an even number then $\hat{f}^{\lfloor M/2 \rfloor} \in \mathbb{R}$. It can be seen that the number of real spectral coefficients $\{\hat{f}^0, \Re(\hat{f}^m), \Im(\hat{f}^m)\}$ in the above expression is the same as the number of collocation points M . Therefore the dimensions of spectral and physical spaces in the sense of number of degrees of freedom are the same. When solving differential equations, the most important property of trigonometric functions is that they are eigenfunctions of differential operators. In a discrete representation, differential operators in Fourier space take the form of a diagonal matrix:

$$g = \partial_\theta f \quad \Leftrightarrow \quad \hat{g}^{m'} = im\delta_m^{m'} \hat{f}^m \quad \Leftrightarrow \quad \hat{g}^m = im\hat{f}^m.$$

¹This is equivalent to computing the convolution under the condition that *dealiasing* is used in order to avoid casting of high frequencies to the low ones having extrema at the same collocation points. See Canuto *et al.* [13] for more details.

This property is the basis of a very important characteristic of numerical methods built around the spectral Fourier expansion: each of the Fourier modes can be treated separately, i.e. the Fourier modes are decoupled.

Fourier mode separation

The consequence of the diagonal form of differential operators is that for an expression that is linear in θ , all operations can be performed separately on each of Fourier modes. In fact they can be further decomposed into even and odd modes represented only by real coefficients. Let us take as an example a three dimensional Poisson problem stated for $f : \mathbb{R} \rightarrow \mathbb{R}$ and $g : \mathbb{R} \rightarrow \mathbb{R}$:

$$\Delta f(r, \theta, z) = g(r, \theta, z). \quad (4.4)$$

According to what we said about separability of mode-decomposed functions, this equation is equivalent to a system of M separate 2D Poisson problems:

$$\begin{aligned} \Delta^0 \hat{f}^0(r, z) &= \hat{g}^0(r, z), \\ &\vdots \\ \Delta^m \Re(\hat{f}^m(r, z)) &= \Re(\hat{g}^m(r, z)), \\ \Delta^m \Im(\hat{f}^m(r, z)) &= \Im(\hat{g}^m(r, z)), \\ &\vdots \\ \Delta^{M-1} \hat{f}^{M-1}(r, z) &= \hat{g}^{M-1}(r, z) \end{aligned}$$

where $\Delta^m \equiv \frac{1}{r} \partial_r r \partial_r - \frac{m^2}{r^2} + \partial_z^2$ and the Fourier transform $f(r, \theta, z) \xrightarrow{\mathcal{F}} \hat{f}^m(r, z)$ was applied to both sides of (4.4). This property not only reduces the computational cost of the solver, but also allows for quite straightforward parallelization, since each of these 2D Poisson problems can be executed by a separate process. This advantage should not be underestimated, since the Poisson solver is often in practice the crucial and time consuming part of an elliptic PDE solver.

4.3 Axial direction

Because in the vertical direction z the finite cylindrical domain has two boundaries (upper and bottom disks), then Chebyshev polynomials can be successfully employed for the spectral basis. The Chebyshev polynomials are defined as follows:

$$\mathcal{T}_k(z) = \cos(k \arccos(z)) \quad (4.5)$$

where k is the polynomial order. This polynomial basis is orthogonal on the interval $[-1, 1]$ over a weight $(1 - z^2)^{-\frac{1}{2}}$.

The spectral approximation of function $f(z)$ defined over the range $[-h/2, h/2]$ can be written as:

$$f(z) \approx \sum_{k=0}^{K-1} \hat{f}_k \mathcal{T}_k\left(\frac{2z}{h}\right)$$

where K denotes the axial resolution and $K - 1$ is the polynomial order of the Chebyshev approximation.

Chebyshev-Gauss grid

The abscissas of the associated Gauss quadrature for Chebyshev polynomials are defined as follows:

$$z_k = \cos\left(\frac{\pi(k + \frac{1}{2})}{K}\right) \quad ; \quad k = 0, 1, \dots, K - 1. \quad (4.6)$$

The *min-max* property

The Chebyshev polynomials are widely used in spectral collocation methods because of their excellent approximation properties. In fact, they are nearly the same as the *min-max polynomials* which, among polynomials of the same degree, have the smallest maximum deviation from the approximated function (see Press *et al.* [72]). This property makes it possible to significantly minimize the number of spectral coefficients used to represent the approximated function to a given precision.

Differential operator

There exist simple recursive formulas for evaluating values and derivatives of functions represented by Chebyshev series. They can be derived from the relation:

$$\mathcal{T}_{k+1} = 2z\mathcal{T}_k(z) - \mathcal{T}_{k-1}(z) \quad ; \quad k \geq 1$$

Spectral coefficients of the derivative $g(z) = \partial_z f(z)$ are given by the following formula:

$$\begin{aligned} \hat{g}_k &= \hat{g}_{k+2} + \frac{4}{h}(k+1)\hat{f}_{k+1} \quad ; \quad k = K-2, K-1, \dots, 0 \\ \hat{g}_K &= \hat{g}_{K-1} = 0 \end{aligned}$$

from which we can deduce the matrix form of the differential operator ∂_z which is:

$$Z_{k',k} = \begin{cases} 2k & \text{if } (k > k' \text{ and } k + k' \text{ is odd}) \\ 0 & \text{otherwise} \end{cases}$$

and for ∂_z^2 we have

$$Z_{k',k}^2 = \begin{cases} k(k^2 - k'^2) & \text{if } (k > k' + 1 \text{ and } k + k' \text{ is even}) \\ 0 & \text{otherwise} \end{cases}$$

Both $Z_{k',k}$ and $Z_{k',k}^2$ are scattered upper triangular matrices. For example, matrix $Z_{k',k}^2$ is of the following form (X^e and X^o denote non-null elements multiplying either even or odd coeffi-

icients \hat{f}_k):

$$\begin{bmatrix} 0 & 0 & X^e & 0 & X^e & 0 & X^e & 0 \\ & 0 & 0 & X^o & 0 & X^o & 0 & X^o \\ & & 0 & 0 & X^e & 0 & X^e & 0 \\ & & & 0 & 0 & X^o & 0 & X^o \\ & & & & 0 & 0 & X^e & 0 \\ & & & & & 0 & 0 & X^o \\ & & & & & & 0 & 0 \\ & & & & & & & 0 \end{bmatrix}$$

and can be further easily decomposed into a triangular block matrix by performing even/odd separation of rows and columns.

$$\left[\begin{array}{cccc|cccc} 0 & X^e & X^e & X^e & & & & \\ & 0 & X^e & X^e & & & & \\ & & 0 & X^e & & & & \\ & & & 0 & & & & \\ \hline & & & & 0 & X^o & X^o & X^o \\ & & & & & 0 & X^o & X^o \\ & & & & & & 0 & X^o \\ & & & & & & & 0 \end{array} \right]$$

We will use this matrix organization later for optimizing the 2D spectral Poisson solver.

4.4 Radial direction

4.4.1 Regularity condition

The radial direction is quite different in nature from both the azimuthal and axial directions because the associated spectral basis must take into account the coordinate singularity at the origin $r = 0$. A regularity condition should be respected by functions representing the radial dependence in polar coordinates. The role of this condition is to guarantee that a spectrally represented function is C^∞ in its entire domain including the origin. The non-satisfaction of the regularity condition can, for some problems, deteriorate the accuracy and convergence of spectral method since the solution can contain contributions which are non-analytic at the coordinate origin. In some situations it is observed that the non-regular spectral solution can be

affected by different types of spurious modes². For finite-difference methods, spurious waves oscillating from point to point called *two-delta* or *sawtooth* were reported by Colonius [15] and Vichnevetsky & Bowle [88]. For pseudo-spectral methods, high-frequency spurious modes occupying the entire domain can appear. Additionally, the grid clustering around the origin often strongly affect the scheme's CFL criterion restricting the maximal time step of a semi-implicit or explicit time integration. The problem does not exist in Cartesian coordinate system – in two dimensions an arbitrary continuous function can be represented by a series of monomials $x^i y^j$:

$$f(x, y) = \sum_{i=0}^{\infty} \sum_{j=0}^{\infty} \hat{f}_{ij} x^i y^j.$$

However, when a function of polar coordinates (r, θ) is represented by Fourier polynomials in angular direction \hat{e}_θ , there exist relations between the azimuthal modes indexed by m and the parity and order of polynomials representing the radial dependence on r . The proper way of defining such a series is:

$$f(r, \theta) = \sum_{m=-\infty}^{\infty} \sum_{\substack{n=m \\ n+m \text{ is even}}}^{\infty} \hat{f}_n^m r^n e^{im\theta}. \quad (4.7)$$

The relations in (4.7) between n and m can be derived by performing a transformation from Cartesian to polar coordinates on a 2D monomial $x^i y^j$.

Singular effects – graphical interpretation

It is useful to graphically explain some of the effects of the polar coordinate singularity, since it is sometimes not so intuitive to qualitatively understand how violation of regularity conditions can affect results obtained.

All singular contributions to a function defined as

$$f(r, \theta) = \sum_{m=-\infty}^{\infty} \sum_{n=0}^{\infty} \hat{f}_n^m r^n e^{im\theta}$$

can be identified analytically by determining the non-differentiable terms which are either of polynomial order incompatible with the corresponding Fourier mode, or have a polynomial order of the wrong parity.

Parity relation (n + m even) On the left of figure 4.1 we show a graphical interpretation of the effect of parity mismatch between radial and azimuthal functions. When an odd radial function is combined with an even function of angle, as for $f(r, \theta) = r$, the corresponding indices $m = 0$ and $n = 1$ do not satisfy relations given in (4.7) which leads to a nondifferentiable function at $r = 0$. The function becomes perfectly regular when considering $f(r, \theta) = r^2$, since $m = 0$ and $n = 2$ satisfy the regularity condition (see fig. 4.1-right).

²Here it should be noted that these "spurious modes" are due to the singularity at the origin, which results from the polar coordinate representation. In general, there is no reason to consider the coordinate origin as a physically special point.

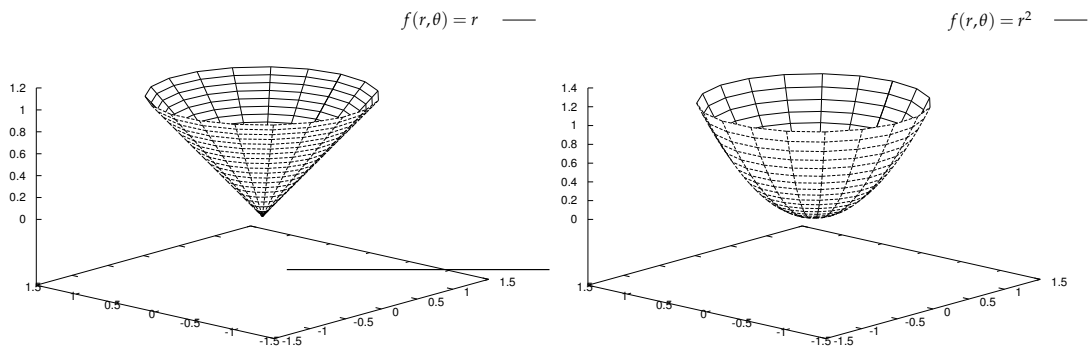


Figure 4.1: Coordinate singularity effects: Parity mismatch. Left: $f(r, \theta) = r$; Right: $f(r, \theta) = r^2$

Polynomial order ($n \geq m$) When the parity of the radial function is that of the parity of the corresponding Fourier mode but the polynomial order does not satisfy $n \geq m$ then another kind of singularity can be observed. On figure 4.2-left it can be seen that depending on the

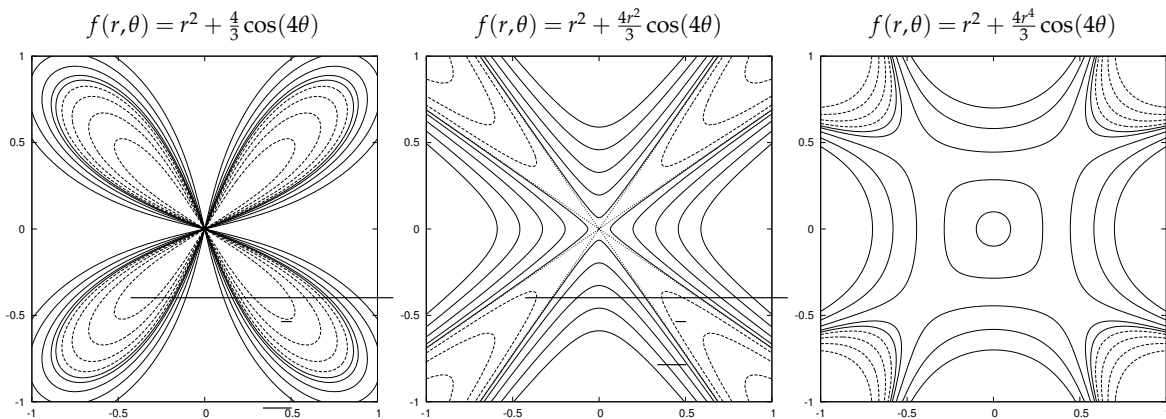


Figure 4.2: Coordinate singularity effects. Left: discontinuity of value; Middle: discontinuity of Laplacian; Right: regular function

direction θ along which the origin $r = 0$ is approached, the function $f(r \rightarrow 0, \theta) \rightarrow f_{r=0}(\theta)$ takes different values, becoming undefined at the coordinate origin. When the polynomial order in the radial direction is higher but not yet sufficiently high then the function is continuous but not infinitely differentiable at the origin (see figure 4.2-middle). The function becomes analytical beginning from $n = m$ (see figure 4.2-right) when the angle-dependent contributions are sufficiently damped.

Clustering at $r = 0$ It is important to attenuate successive frequencies when approaching the coordinate origin in order to avoid an excessive clustering of smaller and smaller spatial scales. On the left of figure 4.3 we show a situation where all azimuthal modes are combined with the same radial polynomial r^2 . On the right, the regular situation is presented where the clustering effect is no longer present.

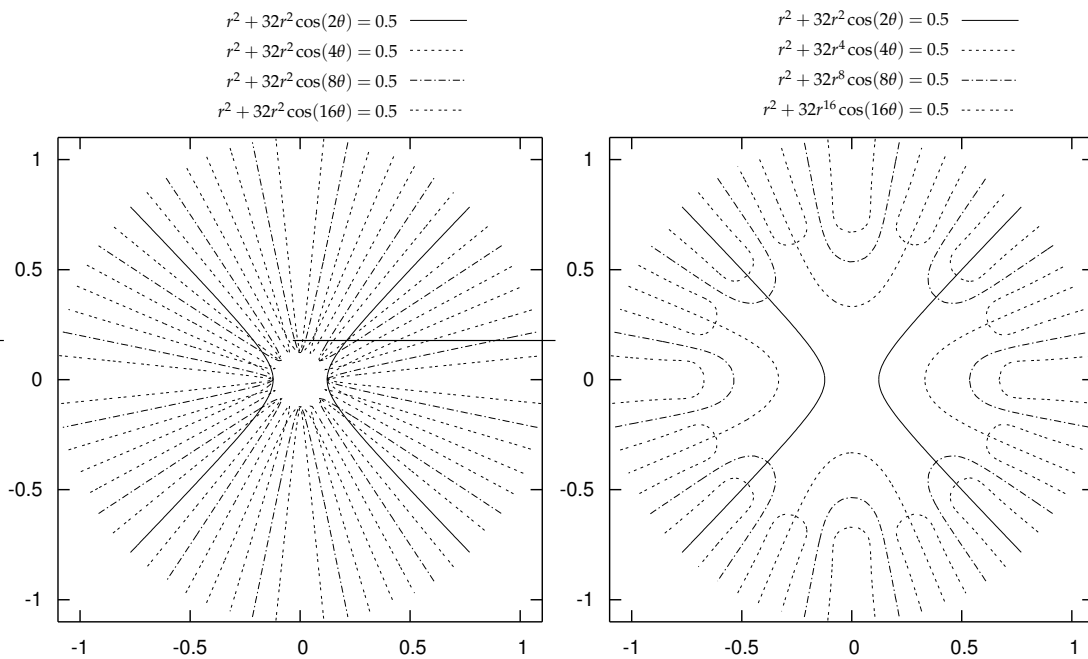


Figure 4.3: Clustering effect – contours of $f^m(r, \theta) = 0.5$. Left: $f^m(r, \theta) = r^2 + 32r^2 \cos(m\theta)$; Right: $f^m(r, \theta) = r^2 + 32r^m \cos(m\theta)$

4.4.2 Regularization of an arbitrary spectral basis

The easiest way of imposing the correct parity and order for radial polynomials would be using the monomial basis: $\hat{f}^m(r) = \sum_i \hat{f}_i r^{m+2i}$. Monomial basis is, however, numerically very ill-conditioned and cannot be used. Correct parity of radial functions defined over $r \in [0, 1]$ can be achieved by even or odd Chebyshev polynomials defined over $r \in [-1, 1]$ but used only for $r \geq 0$. This approach was implemented by several authors (see [86, 48, 56, 81]). A commonly used approach for dealing with coordinate singularity due to the order mismatch is regularization (i.e. suppression) of few low-order modes in the radial direction in order to ensure $(n \geq m)$. Typically Chebyshev polynomials are used, accompanied by some additional axis conditions guaranteeing the $\mathcal{C}^{n \ll \infty}$ class³ for the approximated function. It is unclear how the partial satisfaction of regularity conditions can affect the solution to a particular problem. Trying to impose the regularity conditions for more or all radial modes by imposing increasingly many conditions, generally leads, for iterative schemes for time integration, to ill-conditioned solvers or severe time step restrictions (see Matsushima & Marcus [58]). This is because transformation of Chebyshev polynomials to the monomial basis, in which the regularity conditions can be imposed, is very ill-conditioned.

In finite difference, volume or element methods it is the clustering effect rather than coordinate singularity which affects the solution. Non-polar grids can be used as a remedy in this case. This prohibits, however, mixed algorithms using a Fourier expansion in the periodic (azimuthal) direction and treating the radial direction by a non-spectral method.

³In practice usually $2 \leq n \leq 4$.

4.4.3 Regular basis of radial polynomials

In this work we will use, following Matsushima & Marcus [58], a polynomial basis which preserves the C^∞ property of approximated functions in polar coordinates and yet is numerically well-conditioned. These polynomials $\mathcal{Q}_n^m(\alpha, \beta; r)$ are defined by the singular Sturm-Liouville equation

$$\left(\frac{(1-r^2)^{1-\alpha}}{r^\beta} \frac{d}{dr} \left((1-r^2)^\alpha r^\beta \frac{d}{dr} \right) - \frac{|m|(|m| + \beta - 1)}{r^2} + n(n + 2\alpha + \beta - 1) \right) \mathcal{Q}_n^m(\alpha, \beta; r) = 0, \quad (4.8)$$

defined over $r \in [0, 1]$ with $0 \leq |m| \leq n$, where $\alpha \in [0, 1]$ and β is a positive integer. With the special choice of $\alpha = 1, \beta = 1$, $\mathcal{Q}_n^m(1, 1; r)$ are related to Legendre and shifted Jacobi polynomials used by Leonard & Wray [43]. The n order polynomials $\mathcal{Q}_n^m(\alpha, \beta; r)$ associated with the m Fourier mode have the following expression

$$\mathcal{Q}_n^m(\alpha, \beta; r) \equiv \sum_{p=0}^{\frac{n-|m|}{2}} \frac{(-1)^{p+\frac{n-|m|}{2}} \Gamma\left(\frac{n+|m|+\gamma-1}{2} + p\right) \Gamma\left(\frac{2|m|+\beta+1}{2}\right)}{p! \left(\frac{n-|m|}{2} - p\right)! \Gamma\left(\frac{2|m|+\beta+1}{2} + p\right) \Gamma\left(\frac{2|m|+\gamma-1}{2}\right)} r^{|m|+2p}, \quad (4.9)$$

with $\gamma = 2\alpha + \beta$ and Γ is the gamma function⁴. $\mathcal{Q}_n^m(\alpha, \beta; r)$ are complete and orthogonal with respect to the weight function

$$w(\alpha, \beta; r) \equiv \frac{r^\beta}{(1-r^2)^{1-\alpha}}.$$

so that the inner product is

$$\int_0^1 \mathcal{Q}_n^m(\alpha, \beta; r) \mathcal{Q}_{n'}^m(\alpha, \beta; r) w(\alpha, \beta; r) dr = I_n^m(\alpha, \beta) \delta_{nn'}$$

The normalized basis function $\Phi_n^m(\alpha, \beta; r)$ can be defined as

$$\Phi_n^m(\alpha, \beta; r) \equiv \frac{1}{\sqrt{I_n^m(\alpha, \beta)}} \mathcal{Q}_n^m(\alpha, \beta; r) \quad (4.10)$$

There exist recurrence formulas for evaluating $\mathcal{Q}_n^m(\alpha, \beta; r) \equiv \mathcal{Q}_n^m(r)$ as well as the integration constants $I_n^m(\alpha, \beta) \equiv I_n^m$ in a number of operations proportional to $n - |m|$. The formulas can be found in [58] and in Appendix A. An arbitrary radial function $\hat{f}^m(r)$ associated with Fourier mode m can be decomposed in the basis of polynomials $\Phi_n^m(\alpha, \beta; r) = \Phi_n^m(r)$:

$$\hat{f}^m(r) \approx \sum_{\substack{n=|m| \\ n+m \text{ is even}}}^{\begin{matrix} 2(N-1) \text{ if } m \text{ is even} \\ 2N-1 \text{ if } m \text{ is odd} \end{matrix}} \hat{f}_n^m \Phi_n^m(r) \quad (4.11)$$

where N denotes the spatial resolution in radial direction (number of collocation points) and $2(N-1), 2N-1$ correspond to the polynomial orders for even and odd modes m respectively. We define \hat{N} – the polynomial order of spectral expansion in radial direction:

$$\hat{N} \equiv \hat{N}(N, m) = \begin{cases} 2(N-1) & m \text{ is even} \\ 2N-1 & m \text{ is odd} \end{cases} \quad (4.12)$$

⁴An extension of the factorial to complex and real number arguments.

so that, $\hat{f}^m(r) \sim O(r^{\hat{N}})$. Notation $\hat{f}^m(r)$ represents a Fourier transform of a real function $f(r, \theta)$ in the sense of transform given in (4.3). To obtain the spectral coefficients \hat{f}_n^m from the original function $f(r, \theta)$, first the fast Fourier transform can be used to determine $\hat{f}^m(r)$ and then the inverse of (4.11) can be stated as

$$\hat{f}_n^m = \int_0^1 \hat{f}^m(r) \Phi_n^m(r) w(r) dr. \quad (4.13)$$

The Gauss quadrature formula for (4.13) is then

$$\hat{f}_n^m = \int_0^1 \hat{f}^m(r) \Phi_n^m(r) w(r) dr = \sum_{i=0}^{N-1} \hat{f}^m(r_i) \Phi_n^m(r_i) w_i + \epsilon. \quad (4.14)$$

Points $\{r_i\}$ are the abscissas of the quadrature and ϵ is the error of the formula ($\epsilon = 0$ if $\hat{f}^m(r) \Phi_n^m(r)$ is of order less than or equal to $2(N-1)$). For a given m the corresponding radial expansion is defined by $N - \lfloor \frac{m}{2} \rfloor$ coefficients $\{f_n^m; n = m, m+2, \dots, \hat{N}\}$.

4.4.4 Differential operators

To construct the Poisson solver, two generic operators acting in the \hat{e}_r direction must be defined. These are

$$r\partial_r, \quad r^2 \quad (4.15)$$

Other operators used along with the Poisson solver are

$$\frac{1}{r^2}, \quad \frac{1}{r} \partial_r r \partial_r \equiv \frac{1}{r^2} (r\partial_r)^2 \quad (4.16)$$

and can be constructed from (4.15). All these operators preserve parity.

Recursive formulas

The recurrence relations defining the way in which spectrally represented functions are altered by applying to them the operators (4.15) were derived by Matsushima & Marcus [58]. In general these relations can be written for a generic operator \mathcal{H} as

$$\begin{aligned} g(r, \theta) = \mathcal{H}f(r, \theta) &\Rightarrow \hat{g}_n^m = \hat{\mathcal{H}}^m(n, n') \hat{f}_{n'}^m \\ &\Updownarrow \\ \sum_{\substack{n'=n-2l \\ n+m \text{ even}}}^{n+2u} \hat{\mathcal{L}}^m(n, n') \hat{g}_{n'}^m &= \sum_{\substack{n'=n-2l' \\ n+m \text{ even}}}^{n+2u'} \hat{\mathcal{R}}^m(n, n') \hat{f}_{n'}^m; \quad n = |m|, 2|m|, \dots, \hat{N} \end{aligned} \quad (4.17)$$

where $\hat{\mathcal{L}}^m(n, n') \equiv [\hat{\mathcal{L}}^m]_i^j$ and $\hat{\mathcal{R}}^m(n, n') \equiv [\hat{\mathcal{R}}^m]_i^j$ with $i = \frac{n'-|m|}{2}$, $j = \frac{n-|m|}{2}$; $i, j = 0, \dots, \hat{N} - \lfloor \frac{m}{2} \rfloor - 1$ are banded matrices defining the matrix operator $\hat{\mathcal{H}}^m(n, n') \equiv [\hat{\mathcal{H}}^m]_i^j$ in the following sense:

$$[\hat{\mathcal{L}}^m]_i^j [\hat{g}^m]^i = [\hat{\mathcal{R}}^m]_i^j [\hat{f}^m]^i \Rightarrow [\hat{\mathcal{H}}^m] = ([\hat{\mathcal{L}}^m])^{-1} [\hat{\mathcal{R}}^m] \quad (4.18)$$

The existence of recurrence relations has an important consequence: acting with such an operator on a vector can be done in $O((d^{\mathcal{L}} + d^{\mathcal{R}})(N - \lfloor \frac{m}{2} \rfloor))$ operations. The quantities $d^{\mathcal{L}} \approx l + u$

and $d^{\mathcal{R}} \approx l' + u'$ are the number of all non-zero diagonals in banded matrices $[\hat{\mathcal{L}}^m]$ and $[\hat{\mathcal{R}}^m]$ and l, l', u, u' are the numbers of their sub-/super- diagonals. For small values of $d^{\mathcal{L}}, d^{\mathcal{R}}$, this can significantly improve performance compared with the case when a full matrix $[\mathcal{H}]$ is used with the operation count $O\left(\left(N - \lfloor \frac{m}{2} \rfloor\right)^2\right)$. In table 4.1 we stated the numbers l, l', u, u' corresponding to the matrix operators (4.15)-(4.16)⁵ and to some of their combinations. A similar

Operator	\mathcal{L}			\mathcal{R}		
	1	u	$d^{\mathcal{L}}$	l'	u'	$d^{\mathcal{R}}$
$r\partial_r$	0	1	2	0	1	2
r^2	0	0	1	1	1	3
$\frac{1}{r^2}$	1	1	3	0	0	1
$(r\partial_r)^2$	0	2	3	0	2	3
$(r\partial_r)^2 - m^2$	0	2	3	0	2	3
$(r\partial_r)^2 + \lambda r^2$	1	3	5	0	2	3

Table 4.1: Numbers of lower (l, l') and upper (u, u') diagonals in the left and right matrices $[\hat{\mathcal{L}}^m]$ and $[\hat{\mathcal{R}}^m]$.

decomposition into banded left and right matrices $[\mathcal{L}]$ and $[\mathcal{R}]$ is possible for a quite large class of differential operators acting on various polynomial expansions. Tuckerman [87] shows a systematic way to construct such matrices and recursion relations.

4.5 Discretization in 3D

To synthesize what we have presented in the preceding sections we shall define the spectral discretization we use in cylindrical coordinates. The following formula applies to scalar functions defined over $(r, \theta, z) \in [0, 1] \times [0, 2\pi] \times [-\frac{h}{2}, \frac{h}{2}]$:

$$f(r, \theta, z) \approx \sum_{m=-\lfloor \frac{M}{2} \rfloor}^{\lfloor \frac{M}{2} \rfloor} \sum_{k=0}^{K-1} \sum_{\substack{n=|m| \\ n+m \text{ even}}}^{\hat{N}} \hat{f}_{kn}^m e^{im\theta} \mathcal{Q}_n^m(r) \mathcal{T}_k\left(\frac{2z}{h}\right) \quad (4.19)$$

where \hat{f}_{kn}^m are complex coefficients and \mathcal{T}_k and \mathcal{Q}_n^m are defined by (4.5) and (4.9). We can write (4.19) also as:

$$f(r, \theta, z) \approx \sum_{m=-\lfloor \frac{M}{2} \rfloor}^{\lfloor \frac{M}{2} \rfloor} \sum_{k=0}^{K-1} \sum_{\eta=0}^{N-\lfloor \frac{m}{2} \rfloor-1} [\hat{f}^m]_{k\eta} e^{im\theta} \mathcal{Q}_{m+2\eta}^m(r) \mathcal{T}_k\left(\frac{2z}{h}\right) \quad (4.20)$$

where coefficients $\{\hat{f}_{kn}^m\}$ were replaced by their matrix representation $[\hat{f}^m]_{k\eta}$.

Since we are interested only in real functions, using trigonometric formulation like that given in (4.3) is more appropriate.

⁵The recurrence relation for the $\frac{1}{r^2}$ operator is numerically unstable: tri-diagonal LU decomposition without pivoting can be used instead.

4.6 Boundary condition regularization

The boundary conditions defined in (2.2) present a singularity in the azimuthal component of velocity u_θ at $r = 1$, $z = \pm \frac{h}{2}$ since the upper and bottom disks rotate while the lateral boundary remains steady. The boundary conditions can be restated as

$$u_\theta|_{r=1}(\theta, z) = 0 \quad \text{and} \quad u_\theta|_{z=\pm \frac{h}{2}}(r, \theta) = \pm r\Omega_\pm,$$

where Ω_\pm is the angular velocity of the disks situated at $z = \pm \frac{h}{2}$ measured in $\frac{\text{rad}}{\text{s}}$. It is clear that such conditions are contradictory, i.e. discontinuous at the corner points. From the mathematical point of view, a solution to a PDE with a finite number of singular points presents no problem and does not prohibit existence of a solution smooth everywhere except at these special points. However, in numerical schemes this problem should be treated with special care. As we already mentioned, spectral methods do not converge exponentially for a non-regular solution. This is because series of smooth functions, which is the case of most spectral decompositions, cannot converge *uniformly* to a singular or discontinuous solution. If nothing is done to prevent it, one should expect to observe the *Gibbs phenomenon* causing spurious oscillations propagating into the whole domain and not confined to the neighborhood of the singularity. For local methods the situation is different: the singularity problem is less severe here since it may concern only a close neighborhood of the singular point (typically the characteristic length is on the order of the grid interval). Finite volume methods have additionally the advantage of a local integral formulation and therefore the discontinuity presents an even less serious problem for them. However in some cases (e.g. Georgiu *et al.* [30]), spurious oscillations can contaminate the solution in the entire domain. In the problem of solutocapillary instabilities studied by Martin-Witkowski & Walker [57], the authors were required to explicitly filter the solution to achieve a acceptable convergence. Additionally, local methods are known to have much higher numerical diffusion or dispersion⁶.

4.6.1 Overview of singularity treatment techniques

We will present here a very brief overview of approaches addressing the singularity problem concentrating on applications to spectral methods. We should differentiate between

- techniques having as an aim recovering the convergence of a method without claiming to capture the mathematically exact solution of the singular problem,
- those which approach the exact solution to the singular problem,
- and those which try to employ a physically justified model which is no longer singular.

Filters

The first class is the singularity filters. The local methods belong to this group because they filter the effect of the singularity at the smallest available scale preventing in many cases its

⁶Whether the scheme is dissipative or dispersive depends on its spatial order parity. Even orders are more diffusive while the odd ones increase dispersion.

propagation to the rest of the computational domain. Spectral methods on the other hand must use an explicit filtering. A filter can be implemented by approximating the Heaviside-like functions defining the solution at the boundary by a steep but smooth profile. For a cylinder with rotating bases, the singular boundary conditions are:

$$u_\theta|_{r=1}(z) = 0 \quad , \quad u_\theta|_{z=\pm\frac{h}{2}}(r) = \begin{cases} r\Omega_\pm & \text{if } r < 1 \\ 0 & \text{otherwise} \end{cases} \quad (4.21)$$

or, equivalently, as

$$u_\theta|_{r=1}(z) = \begin{cases} 0 & \text{if } -\frac{h}{2} < z < \frac{h}{2} \\ \Omega_\pm & z = \pm\frac{h}{2} \end{cases} \quad , \quad u_\theta|_{z=\pm\frac{h}{2}}(r) = r\Omega_\pm. \quad (4.22)$$

We can regularize boundary condition (4.21) by replacing it by the following one:

$$u_\theta|_{z=\pm\frac{h}{2}}(r) = r(1 - r^\mu)\Omega_\pm \quad (4.23)$$

where μ is an arbitrary but reasonably large even integer (e.g. $\mu = 10$). Another choice is to regularize the velocity on the lateral boundary by approximating (4.22) by:

$$u_\theta|_{r=1}(z) = \left(\frac{2z}{h}\right)^\mu \times \begin{cases} \Omega_+ & \text{if } z \geq 0 \\ \Omega_- & \text{if } z < 0 \end{cases} \quad (4.24)$$

The system with boundary conditions (4.23) and (4.24) no longer defines the same problem as (4.21) or (4.22), but has the advantage of being almost regular. It is not yet perfectly regular since, even with stationary corner conditions (i.e. without discontinuity of the velocity), it can still be proved (Moffatt [59]) that higher order derivatives are singular. In fact, the analytic solution for the vorticity contains the term $O(r^{1.74\dots})$ meaning that the second derivative in r diverges at the corner. The consequence is that even continuous boundary conditions lead to a singular solution due to the singularity of the geometry. In practice this singularity is qualified as *weak* and usually does not prevent the solution from converging exponentially⁷.

Still, an important question can be asked: Can one be sure that regularizing the boundary conditions at an *ad hoc* selected scale does not affect the properties of global large-scale flow? The answer to this question, but concerning solid state mechanics, is known as the *Saint-Venant principle* [76]. One of many existing formulations is that of Solomon [80]. The principle states that

"a system of forces statically equivalent to zero, applied to a portion of the boundary, of diameter comparable with the smallest of the body's dimensions, produces displacements, deformations and tensions considerable only at distances comparable with this diameter".

Several works are focused on formulating and determining the applicability of a similar statement concerning fluid dynamics applications. A recent review can be found in Horgan [37] and seems to justify validity of this idea.

⁷Convergence can, however, be deteriorated slightly for some resolutions when successive *Moffatt rolls* appear but are not yet well-captured by the representable spatial scales (see Nguyen [62]). This "weak" singularity can be more severe if a numerical method requires the solution to be $C^{\geq 4}$.

Singularity subtraction The main idea of this approach is to decompose the solution into a regular unknown part and an a priori known analytic form of the singular solution valid in the neighborhood of the corner. Then, only the regular part must be treated by a numerical algorithm. The feedback of the local singular solution on the numerical one can be filtered down to the scales representable by the spatial resolution. The main advantage of this method is that it recovers the convergence of the scheme and approaches at the same time the mathematically exact solution. This method was introduced in [77] for a driven cavity problem. An application of this approach to injection of fluid into a cylindrical channel was presented by Botella & Peyret [8]. The results obtained using this kind of method are generally of high precision and often provide a benchmark for a particular problem. The main drawback of this approach is that it requires knowledge of the solution near the singular point. For a 2D driven cavity problem, the nature of the singularity was given by [19] and Moffatt [59] for a Stokes flow. This task becomes more difficult when considering inertial (Navier-Stokes) flows and, for many configurations, the solution is unknown. Additionally, for 3D flows, determining an analytical solution becomes extremely difficult (see Hills & Moffatt [35]). Finally the problem of physical mechanism is still not addressed by this class of methods. There is no reason to expect these techniques to model the microscopic behavior of a real fluid in the neighborhood of the corner. The filter-based methods can sometimes be better suited for a particular application, especially if some experimental data can help to adjust the a priori unknown scale of filtering.

Physically motivated methods Since this subject extends far beyond the interests of this work, we only briefly mention here some ideas for physically justified treatments of singular conditions. The natural way of thinking would point to methods from *molecular dynamics*. These are well suited for this kind of problem since they reflect the microscopic nature of the fluid at the smallest scales. However, for several reasons, these methods are very hard to adapt to problems containing both large and small scales. Application to non steady flows is also problematic here. Several continuous (macroscopic) approaches have been proposed as a compromise between a continuous and a molecular description. These all introduce a spatially limited physical effect which effectively removes the singularity. We should mention here methods based on the variable slippage as well as the surface viscosity or dynamic surface tension applicable to free-surface problems. A comprehensive review of physically justified models, as well as other regularization techniques, is provided by Nguyen [62].

4.6.2 Boundary velocity regularization

In this work we use singularity filtering by replacing the original Dirichlet boundary conditions on the top and bottom disks by a function satisfying continuous boundary conditions (see figure 4.4-left). We justify this choice by the fact that we are not interested in finding the solution to the singular problem. In experimental setups like VKS, the boundary conditions are not discontinuous: The forcing is not obtained by rotating the lids, but rather by rotating blades of diameter smaller than that of the cylinder, placed near the upper and bottom bases. We define

a regularized profile for $u_\theta|_{z=\pm\frac{h}{2}}$ as follows:

$$u_\theta|_{z=\pm\frac{h}{2}}(r) = \pm r \underbrace{\left(1 - e^{-\frac{r-1}{\delta}}\right)}_{\Omega_\pm(r)} \quad (4.25)$$

This form is similar to (4.23) but allows control of the steepness of the profile by varying δ . In practice, we use $0.005 < \delta < 0.05$. This function differs by more than 10% from that defined in (2.2b) only on a small range, approximately $1 - 2\delta \lesssim r < 1$ (see fig. 4.6.2). As was shown by Lopez & Shen [48], for comparing with results obtained using different methods and for benchmark purposes it is enough to use a small $\delta \approx 0.005$ if sufficient spectral resolution is used to represent such a steep profile. Another reason to prefer (4.25) over (4.23) is that, for

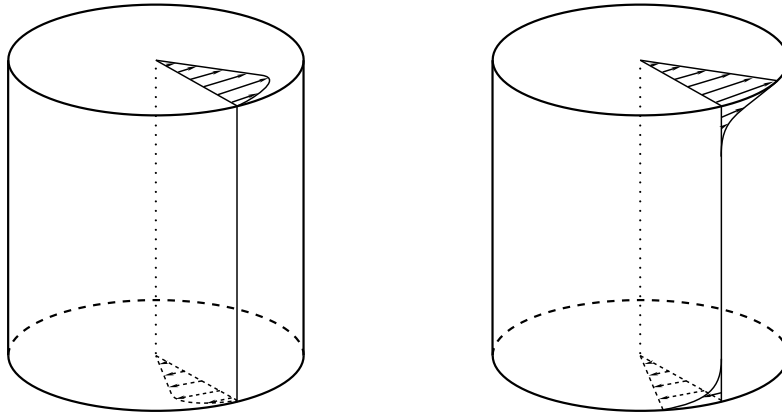


Figure 4.4: Regularized profile used for elimination of the discontinuous boundary conditions at the cylinder corners. Left – regularization on upper and bottom disks: $u_\theta|_{z=\pm\frac{h}{2}}(r) = r \left(1 - e^{-\frac{r-1}{\delta}}\right)$. Right – regularization on lateral cylinder's mantle: $u_\theta|_{r=1}(z) = \Omega_+ e^{-(1-\frac{2z}{h})/\delta} + \Omega_- e^{-(1+\frac{2z}{h})/\delta}$, $u_\theta|_{z=\pm\frac{h}{2}}(r) = r\Omega_\pm$

a given order \hat{N} of the polynomial approximation, (4.25) results in the much steeper profile than that corresponding to (4.23) with $\mu = \hat{N} - 1$ (see figure 4.6). Once we have changed $\Omega_\pm \equiv \text{const.} \rightarrow \Omega_\pm(r)$, the boundary condition (3.51a) for the toroidal potential ψ_u must be updated together with (4.25). Since the boundary conditions are axisymmetric, we can determine ψ_u by solving (3.51a) with $\partial_\theta \psi_u = 0$:

$$\partial_r \psi_u|_{z=\pm\frac{h}{2}}(r) = r\Omega_\pm(r) \quad \Rightarrow \quad \psi_u|_{z=\pm\frac{h}{2}}(r) = \frac{1}{2}r^2 + \delta(\delta - r)e^{-\frac{r-1}{\delta}} + \underbrace{\delta^2 e^{-\frac{1}{\delta}}}_{\approx 0}. \quad (4.26)$$

where the integration constant was fixed in order to satisfy $\psi_u|_{z=\pm\frac{h}{2}}(r=0) = 0$. Note that the last term in (4.26) can be considered negligible⁸ for typically used values of δ . The inconvenient aspect of using a non-polynomial profile is that the error of satisfaction of the boundary and axis conditions by a spectral polynomial approximation of (4.26) can be non-negligible (see figure 4.6). In order to numerically obtain a spectral representation of $\psi_u|_{z=\pm\frac{h}{2}}(r)$ defined in

⁸For $\delta < 0.03$ we have $\delta^2 e^{-\frac{1}{\delta}} < 10^{-17}$ which is below a machine's double precision round-off error $O(10^{-15})$.

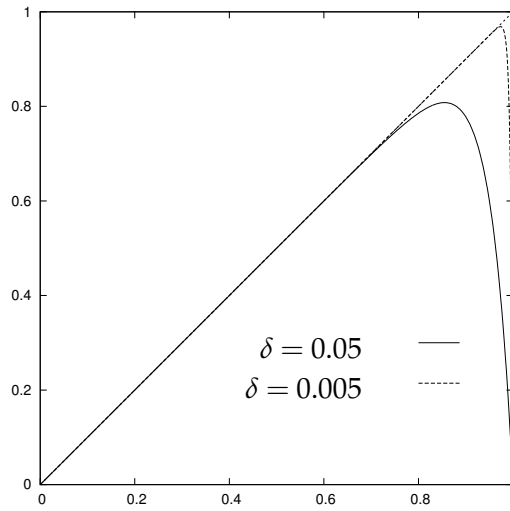


Figure 4.5: Example of regularized profiles for $u_\theta|_{z=\pm\frac{h}{2}}(r) = r\left(1 - e^{-\frac{r-1}{\delta}}\right)$.

(4.26) satisfying at the same time $\psi_u|_{z=\pm\frac{h}{2}}(r=0) = \partial_r\psi_u|_{z=\pm\frac{h}{2}}(r=0) = \partial_r\psi_u|_{z=\pm\frac{h}{2}}(r=1) = 0$ with machine precision, one can use the following procedure:

- 1) Project (4.25) on a regular radial basis of odd polynomials corresponding to the $m = 1$ Fourier mode (see (4.11)). This should be performed using Gauss-Radau collocation points (which include the boundary point).
- 2) Integrate the approximation obtained by applying $-\int_0^r dr$ in the spectral space and represent the result in the basis of the radial polynomials corresponding to $m = 0$.

Another possible choice for regularizing the boundary conditions is to apply a filter to the lateral boundary while keeping the velocity profile on the upper and bottom disk unchanged (see figure 4.4-right):

$$u_\theta|_{r=1}(z) = \Omega_+ e^{-(1-\frac{2z}{h})/\delta} + \Omega_- e^{-(1+\frac{2z}{h})/\delta}, \quad (4.27a)$$

$$u_\theta|_{z=\pm\frac{h}{2}}(r) = r\Omega_\pm, \quad (4.27b)$$

This kind of regularization is similar to that of Lopez & Shen [48]. The corresponding boundary conditions for $\psi_u|_{r=1}(z)$ can be obtained by applying $-\int_0^1 dr$ to (4.27):

$$\psi_u|_{r=1}(z) = -r\Omega_+ e^{-(1-\frac{2z}{h})/\delta} - r\Omega_- e^{-(1+\frac{2z}{h})/\delta},$$

$$\psi_u|_{z=\pm\frac{h}{2}}(r) = -\frac{r^2\Omega_\pm}{2}.$$

Note on the minimal spatial resolution

Regularization of the boundary condition imposes a lower bound on the spectral resolution – the spectral approximation must be able to represent the regularization profiles smoothly. In consequence, trying to approach the solution of a singular problem by setting a very steep

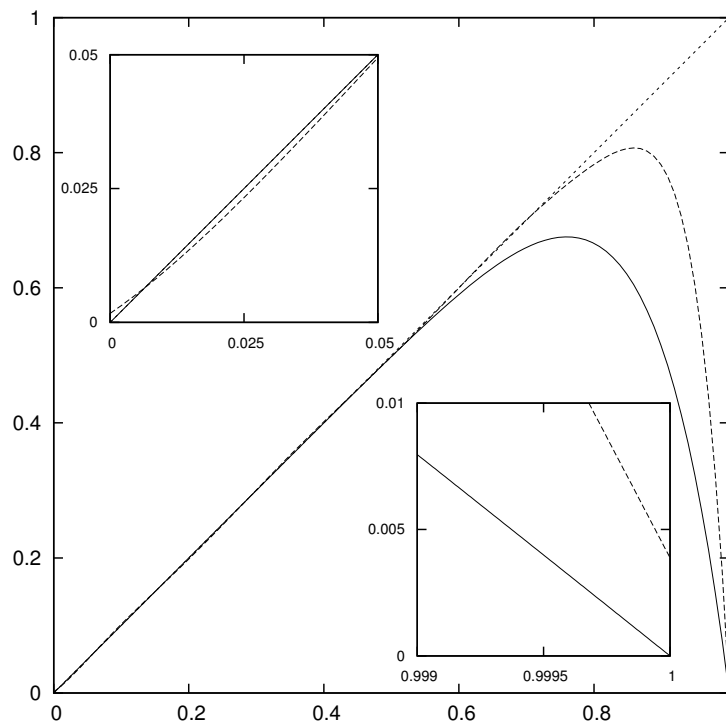


Figure 4.6: **Main graph:** Comparison between regular profiles represented by polynomials of order $O(r^9)$. Solid line: $u_\theta|_{z=\pm\frac{h}{2}}(r) = r(1 - r^8)$; Dashed line: $u_\theta|_{z=\pm\frac{h}{2}}(r) \approx r\left(1 - e^{\frac{r-1}{\delta}}\right)$. **Sub-graphs:** Zoom on the sensitive points shows that a polynomial approximation of a non-polynomial profile does not satisfy required boundary conditions at $r = 0$ and $r = 1$.

profile increases considerably the spatial resolution required. Additionally, Lopez & Shen [48] observed that the actual resolution should be approximately twice the minimal resolution sufficient for representing the regularization profiles. This is because the nonlinear term produces modes of twice as high frequency as those necessary for describing the boundary condition.

Chapter 5

Spectral solver

5.1 Introduction

This chapter presents the numerical method for solving the Navier-Stokes equation for the incompressible fluid in toroidal-poloidal variable formulation. The material exposed throughout this chapter represents the main contribution of this thesis.

We will start by formulating one- and two- dimensional Poisson/Helmholtz solvers (for axial and radial directions). We will follow by deriving the methodology for solving the high order elliptic/parabolic problem resulting from the Stokes equation in potential formulation using the Poisson solvers. Before presenting the influence matrix method for satisfaction of the boundary conditions we will discuss an analytic analogue of this technique – the Green function method. Analysis of the precision and convergence properties of the linear Stokes solver will be provided. Finally we will describe a method for solving the magnetic problem in the conductor-vacuum configuration.

5.2 Poisson solver

We will present in this section an algorithm for solving the Poisson equation:

$$\Delta f = g \quad ; \quad \mathcal{B}f|_{\partial} = \beta \quad (5.1)$$

where \mathcal{B} is the boundary condition operator ($\mathcal{B} \equiv \mathbb{1}$ for Dirichlet boundary conditions and $\mathcal{B} \equiv \frac{\partial}{\partial n}$ for Neumann boundary conditions). The method will also be applied to solve Helmholtz systems:

$$(\Delta + \lambda)f = g \quad ; \quad \mathcal{B}f|_{\partial} = \beta \quad (5.2)$$

Helmholtz problems appear in semi-implicit time integration schemes, where an equation of type $(\partial_t - Re^{-1}\Delta)f = g$ is discretized in time as follows

$$\frac{f^{i+1} - f^i}{\Delta t} - Re^{-1}\Delta f^{n+1} = g^n$$
$$\overbrace{(\mathbb{1} - \underbrace{\Delta r Re^{-1} \Delta}_{\epsilon})}^E f^{n+1} = f^n + \Delta t g^n$$

Here the first-order implicit Euler scheme was used for f and the first-order explicit Euler scheme for g .

We will present first the methodology called the τ -method for solving a one dimensional version of (5.1) or (5.2). The extension of this method to two dimensions using the *partial diagonalization* technique will be presented in section 5.2.2.

5.2.1 τ method – one dimension

The Poisson equation (5.1) is known to have a unique solution if appropriate (Dirichlet or Neumann¹) boundary conditions are specified on each of the domain boundaries.

In a discrete spectral representation, where differential operators are represented by matrices and functions by vectors of spectral coefficients, equations (5.1) and (5.2) can be written in matrix-vector form:

$$[\mathbf{L}][f] = [g] \quad ; \quad [\mathbf{B}][f] = [\beta] \quad (5.3)$$

where $[\mathbf{L}]$ denotes the differential operator's matrix corresponding to the Poisson operator ($\mathcal{L} \equiv \partial_x^2$) or to the Helmholtz operator ($\mathcal{L} \equiv \partial_x^2 + \lambda$) and $[f]$ and $[g]$ are column vectors of spectral coefficients and $[\mathbf{B}]$ is a matrix corresponding to the boundary condition operator \mathcal{B} . As an example, for $[f]$ the expansion coefficients of $f(x)$ in the basis of Chebyshev polynomials \mathcal{T} we would have:

$$\begin{aligned} f(x_i) &= \sum_j \mathcal{T}_j(x_i) f_j \quad \equiv \quad [\mathbf{T}]_{ij} [f]_j \quad \equiv \quad [\mathbf{T}][f] \\ (\mathcal{B}f)|_{x_i} &= \sum_j (\mathcal{B}\mathcal{T}_j)|_{x_i} f_j \quad \equiv \quad [\mathcal{B}\mathbf{T}]_{ij} [f]_j \quad \equiv \quad [\mathbf{B}][f] \end{aligned}$$

Poisson problem ($\lambda = 0$): In this situation, the operator $\mathcal{L} \equiv \partial_x^2$, which has a non-trivial kernel, corresponds to a singular matrix $[\mathbf{L}]$ (the last two rows are zero). In order for (5.3) to have a solution it is necessary that $[g]$ satisfy the compatibility/solvability condition which can be generally written as:

$$\ker([\mathbf{L}]^\dagger) \perp [g] \quad (5.4)$$

Here, (5.4) implies that the last two coefficients of $[g]$ must be zero. This expresses the fact that g , which is defined as a second derivative of f , must be two orders lower in polynomial degree. Thus system defined by the matrix $[\mathbf{L}] = [\partial_x^2]$ has a unique solution only if additional conditions² on f are specified. These conditions can be imposed by replacing the last two rows in $[\mathbf{L}]$ by the boundary condition matrix $[\mathbf{B}]$ and the last two coefficients in $[g]$ by the boundary values $[\beta]$. The system obtained, which we will identify by an additional overbar, can be solved by a standard Gaussian elimination

$$\overline{[\mathbf{L}]} [f] = \overline{[g]} \quad \Leftrightarrow \quad \begin{bmatrix} \mathbf{L}_{lo} \\ \mathbf{B} \end{bmatrix} \begin{bmatrix} f \end{bmatrix} = \begin{bmatrix} g \\ \beta \end{bmatrix} \quad (5.5)$$

¹For Neumann boundary conditions, the solution is determined up to a constant

²The number of conditions that can be imposed is equal to the dimension of the nullspace of the differential operator: for ∂_x^2 , two conditions can be imposed.

The subscript $_{lo}$ denotes the low-frequency part of a quantity. If g does not satisfy (5.4) (i.e. the last two coefficients are non-zero), then we can still solve the system by modifying $[\mathbf{L}]$ and $[g]$ but at the price of losing the information contained in the two highest-frequency modes. The consequence is that we commit an error τ defined via

$$\overline{[\mathbf{L}]} [f] = \overline{[g]} \quad \Rightarrow \quad [\mathbf{L}] [f] = [g] + [\tau]$$

where $[\tau]$ is a vector containing only the two highest frequencies. This method of solving an incompatible system is known as the τ -method.

Helmholtz problem ($\lambda \neq 0$): A similar situation occurs if operator $\mathcal{L} \equiv \partial_x^2 + \lambda$ is used in (5.5). However in this case, the resulting matrix $[\mathbf{L}]$ has a null kernel and can be inverted without specifying any additional boundary or solvability conditions. Trying to impose the boundary conditions would result in an overdetermined system. Applying the τ -method by applying the modifications to $[\mathbf{L}]$ and $[g]$

$$[\mathbf{L}] \rightarrow \overline{[\mathbf{L}]} \quad \text{and} \quad [g] \rightarrow \overline{[g]}$$

produces the τ error, regardless of the form of $[g]$.

The good property of the τ -method is that the error of the solution vector $[f]$ (which should not be confused with the high-frequency τ -error of satisfaction of the equation) is distributed among all frequencies.

Schur decomposition

It is possible to solve for the low-frequency part f_{lo} of the solution f separately from the high frequencies. This can be done by performing the Schur decomposition of a matrix for which the last rows have been replaced by the boundary conditions. System (5.5) can be written in the following form:

$$\left[\begin{array}{c|c} \mathbf{L}'_{lo} & \mathbf{L}'_{hi} \\ \hline \mathbf{B}_{lo} & \mathbf{B}_{hi} \end{array} \right] \begin{bmatrix} f_{lo} \\ f_{hi} \end{bmatrix} = \begin{bmatrix} g_{lo} \\ \beta \end{bmatrix} \quad (5.6)$$

The equations for each of the blocks can be written as follows:

$$[\mathbf{L}'_{lo}] [f_{lo}] + [\mathbf{L}'_{hi}] [f_{hi}] = [g_{lo}] \quad (5.7a)$$

$$[\mathbf{B}_{lo}] [f_{lo}] + [\mathbf{B}_{hi}] [f_{hi}] = [\beta] \quad (5.7b)$$

These can be rewritten in a form giving the equation for $[f_{lo}]$ and the formula for determining $[f_{hi}]$ once $[f_{lo}]$ is known:

$$\underbrace{\left([\mathbf{L}'_{lo}] - [\mathbf{L}'_{hi}] [\mathbf{B}_{hi}]^{-1} [\mathbf{B}_{lo}] \right)}_{[\mathbf{L}^*]} [f_{lo}] = \underbrace{[g_{lo}] - [\mathbf{L}'_{hi}] [\mathbf{B}_{hi}]^{-1} [\beta]}_{[g^*]}$$

$$\Downarrow$$

$$[f_{lo}] = [\mathbf{L}^*]^{-1} [g^*]$$

$$[f_{hi}] = [\mathbf{B}_{hi}]^{-1} ([\beta] - [\mathbf{B}_{lo}] [f_{lo}]) \quad (5.8)$$

The matrix $[\mathbf{L}^*]$ is an approximation of the operator of the boundary value Laplace/Poisson problem, which differs from the discrete approximation of the differential expression corresponding to $[\partial_x^2]$. Without boundary conditions, matrix $[\mathbf{L}] \leftrightarrow \Delta$ has only null eigenvalues. The operator $[\overline{\mathbf{L}}]$, while defining a correct Poisson problem (5.5), does not have a spectrum similar to that of the Laplacian, since for \mathbf{B} corresponding to Dirichlet boundary conditions its spectrum contain positive and complex eigenvalues. In contrast to $[\overline{\mathbf{L}}]$, the $[\mathbf{L}^*]$ matrix has a spectrum which approximates the spectrum of the ∂_x^2 operator

$$Sp([\mathbf{L}^*]) \approx Sp(\partial_x^2) = -k^2 \quad ; \quad k = 0, \dots, \infty$$

with $-k^2$ being the eigenvalue corresponding to the eigenmode of frequency k . This is also the appropriate operator to use when considering the diagonalization technique for solving a two-dimensional problem.

Even/odd separation

As we already mentioned in section 4.3 it is possible to separate the even and odd Chebyshev coefficients and the corresponding matrix elements in order to make the matrix block-diagonal. This reduces the computational cost associated with performing matrix operations on vectors of Chebyshev coefficients. After permuting rows and columns of operator $[\mathbf{D}_z^2] \leftrightarrow \partial_z^2$ we can write the one-dimensional Poisson boundary value problem (5.3) as follows:

$$\left[\begin{array}{cccc|cccc} 0 & X^e & X^e & X^e & & & & \\ & 0 & X^e & X^e & & & & \\ & & 0 & X^e & & & & \\ B^e & B^e & B^e & B^e & & & & \\ \hline & & & & 0 & X^o & X^o & X^o \\ & & & & & 0 & X^o & X^o \\ & & & & & & 0 & X^o \\ & & & & B^o & B^o & B^o & B^o \end{array} \right] \begin{bmatrix} f_{lo}^e \\ f_{lo}^e \\ f_{lo}^e \\ f_{hi}^e \\ f_{lo}^o \\ f_{lo}^o \\ f_{lo}^o \\ f_{hi}^o \end{bmatrix} = \begin{bmatrix} g_{lo}^e \\ g_{lo}^e \\ g_{lo}^e \\ \beta^e \\ f_{lo}^o \\ f_{lo}^o \\ f_{lo}^o \\ \beta^o \end{bmatrix} \quad (5.9)$$

where subscripts $^e, ^o$ stand for even and odd coefficients respectively. The even and odd boundary conditions $[B^e], [B^o]$ can be defined as follows:

$$\begin{aligned} [B]^e &= \frac{1}{2} ([\mathbf{B}]_+ + [\mathbf{B}]_-) & \beta^e &= \frac{1}{2} ([\beta]_+ + [\beta]_-) \\ [B]^o &= \frac{1}{2} ([\mathbf{B}]_+ - [\mathbf{B}]_-) & \beta^o &= \frac{1}{2} ([\beta]_+ - [\beta]_-) \end{aligned}$$

where the $_+$ and $_-$ subscripts denote rows of \mathbf{B} evaluating boundary values at $+1$ and -1 . This system is equivalent to two completely separate equations:

$$\begin{aligned} \overline{[\mathbf{L}]}^e [f]^e &= \overline{[g]}^e \\ \overline{[\mathbf{L}]}^o [f]^o &= \overline{[g]}^o \end{aligned}$$

Each of these two systems can be solved by Schur decomposition.

5.2.2 Partial diagonalization method – two/three dimensions

In two dimensions the spectral coefficients representing solutions can be written in a matrix form $f(r, z) \leftrightarrow [\mathbf{f}]_{kn}$ where the column direction (indexed by $k \in [0, K - 1]$) corresponds to $\hat{\mathbf{e}}_z$ and the row direction (indexed by $n \in [0, N - 1]$) corresponds to $\hat{\mathbf{e}}_r$. Using this notation we can write the two-dimensional discrete version of Poisson equation (5.1) as

$$[\mathbf{f}] [\mathbf{D}_r^2]^T + [\mathbf{D}_z^2] [\mathbf{f}] = [\mathbf{g}] \quad ; \quad [\mathbf{B}_z] [\mathbf{f}] = [\beta_z], \quad [\mathbf{f}] [B_r] = [\beta_r] \quad (5.11)$$

We consider a full cylinder (and not the cylindrical shell) for which the regularity at the cylinder axis replaces one of the boundary conditions. In this case, there are two boundary conditions to satisfy in the $\hat{\mathbf{e}}_z$ direction and only one in the radial direction $\hat{\mathbf{e}}_r$: thus $[\mathbf{B}_z]$ and $[\beta_z]$ are matrices of size $2 \times K$ and $2 \times N$ while $[c_r], [\beta_r]$ are vectors of dimensions N and K).

In cylindrical geometry it is possible to decompose a three-dimensional problem into a set of decoupled two-dimensional problems, one for each of the Fourier modes, since differential operators in the azimuthal direction are diagonal in Fourier space (see section 4.2). We can then write a matrix form of the three dimensional Poisson equation as

$$[\mathbf{f}] \left(\underbrace{[\mathbf{D}_r^2]^T - m^2 [\mathbf{R}^{-2}]^T}_{\frac{1}{r} \partial_r r \partial_r - \frac{m^2}{r^2}} + \underbrace{[\mathbf{D}_z^2]}_{\partial_z^2} \right) [\mathbf{f}] = [\mathbf{g}]. \quad (5.12)$$

We introduce the Helmholtz operator \mathcal{H}_λ^m defined as follows:

$$\mathcal{H}_\lambda^m \equiv \frac{1}{r} \frac{\partial}{\partial r} r \frac{\partial}{\partial r} - \frac{m^2}{r^2} + \lambda \quad \leftrightarrow \quad [\mathbf{H}_\lambda^m]. \quad (5.13)$$

Then equation (5.12) can be written in the following form

$$[\mathbf{f}] [\mathbf{H}_0^m]^T + [\mathbf{D}_z^2] [\mathbf{f}] = [\mathbf{g}] \quad (5.14)$$

Equation (5.14) cannot be solved directly because operators $[\mathbf{D}_z^2]$ and $[\mathbf{H}_0^m]^T$ are placed on different sides of $[\mathbf{f}]$. The standard technique for solving such an equation is to diagonalize one or both matrices, which transforms a two-dimensional problem into a set of one-dimensional problems or even a set of scalar equations (see Canuto *et al.* [13]). We prefer a partial diagonalization approach, where only one matrix (we shall choose $[\mathbf{D}_z^2]$) diagonalized and then, a set of $M \times (K - 2)$ one-dimensional problems must be solved in the remaining direction $\hat{\mathbf{e}}_r$. In order to be able to perform the diagonalization, we must first transform the $[\mathbf{D}_z^2]$ operator using the previously discussed Schur decomposition. The operator $[\mathbf{D}_z^{*2}]$ (of size $(K - 2) \times (K - 2)$) constructed in this way has the boundary conditions incorporated and its spectrum approximates that of the continuous problem (5.1) with boundary conditions.

Let us denote $[\mathbf{W}]$ the diagonalization matrix (i.e. the matrix whose columns are the eigenvectors) and $[\Lambda]$ the diagonal matrix of the eigenvalues $\lambda = \{\lambda_0, \lambda_1, \dots, \lambda_{K-3}\}$ of the $[\mathbf{D}_z^{*2}]$ operator:

$$[\mathbf{D}_z^{*2}] = [\mathbf{W}]^{-1} [\Lambda] [\mathbf{W}]$$

Then (5.14) can be transformed as follows

$$\begin{aligned} [\mathbf{f}] [\mathbf{H}_0^m]^T + [\mathbf{W}]^{-1} [\Lambda] [\mathbf{W}] [\mathbf{f}] &= [\mathbf{g}^*] \\ [\mathbf{W}] [\mathbf{f}] [\mathbf{H}_0^m]^T + [\Lambda] [\mathbf{W}] [\mathbf{f}] &= [\mathbf{W}] [\mathbf{g}^*] \\ \widetilde{[\mathbf{f}]} [\mathbf{H}_0^m]^T + [\Lambda] \widetilde{[\mathbf{f}]} &= \widetilde{[\mathbf{g}^*]} \\ \widetilde{[\mathbf{f}]}_k \left([\mathbf{H}_0^m]^T + \lambda_k [\mathbf{1}] \right) &= \widetilde{[\mathbf{g}^*]}_k, \quad k = 0, \dots, K - 3 \\ \widetilde{[\mathbf{f}]} [\mathbf{H}_\lambda^m]^T &= \widetilde{[\mathbf{g}^*]} \end{aligned} \quad (5.15)$$

where $\widetilde{[\mathbf{f}]} = [\mathbf{W}] [\mathbf{f}]$ and $\widetilde{[\mathbf{g}^*]} = [\mathbf{W}] [\mathbf{g}^*]$. Linear system (5.15) must be solved for each Fourier mode m and for each eigenvalue λ (in total $M \times (K - 2)$ one-dimensional equations).

For a given m , the expression in (5.15) is a shorthand for the following sequence of $(K - 2)$ one-dimensional equations, each of size N :

$$\begin{aligned} \widetilde{[\mathbf{f}]}_0 [\mathbf{H}_{\lambda_0}^m]^T &= \widetilde{[\mathbf{g}^*]}_0 \\ \widetilde{[\mathbf{f}]}_1 [\mathbf{H}_{\lambda_1}^m]^T &= \widetilde{[\mathbf{g}^*]}_1 \\ &\vdots \\ \widetilde{[\mathbf{f}]}_{K-3} [\mathbf{H}_{\lambda_{K-3}}^m]^T &= \widetilde{[\mathbf{g}^*]}_{K-3} \end{aligned}$$

Note that diagonalization of $[\mathbf{D}_z^2]$ need be performed only once for the entire simulation, in a preprocessing step, separately for even $[\mathbf{D}_z^{*2}]^e$ and odd $[\mathbf{D}_z^{*2}]^o$ blocks of the second derivative matrix (5.9). Once $\widetilde{[\mathbf{f}]}$ is found, the final solution vector $[\mathbf{f}]$ can be found by applying $[\mathbf{W}]^{-1}$:

$$[\mathbf{f}] = [\mathbf{W}]^{-1} \widetilde{[\mathbf{f}]} \quad (5.16)$$

5.2.3 Solving the Helmholtz equation – τ -method in radial direction

If one decides to impose the boundary conditions through the τ -method and perform diagonalization in the axial direction, then the general method described using the example of the Chebyshev polynomials should be optimized for treating the radial direction in order to take advantage of the partial (and not full) diagonalization. Generally, the direction requiring lower spatial resolution, is treated by diagonalizing the corresponding operator. This is because this leads to an algorithm where at each step of the time iteration loop multiplying by the diagonalization matrix is necessary. In our problem, the spatial resolution typically used in the axial direction is not smaller than in the radial direction. However, since the even and odd blocks of the axial Laplacian ∂_z^2 (see (5.9)) can be diagonalized independently, the cost of multiplying of a single Fourier mode by the diagonalization matrix, which is block-diagonal, can be reduced to $2(N - \lfloor \frac{m}{2} \rfloor) (\frac{K}{2} - 1)^2$ operation. Diagonalization performed in the radial direction would require $K((N - \lfloor \frac{m}{2} \rfloor) - 1)^2$ operations. Therefore, for configurations with $K < 2(N - \lfloor \frac{m}{2} \rfloor)$, diagonalization in the axial direction is justified³. For a problem discretized with spectral resolution $M \times K \times N$ the algorithm has a computational cost of $O(M \times K^2 \times N)$ operations. We must then solve $M \times (K - 2)$ one-dimensional Poisson problems, each of size $N - \lfloor \frac{m}{2} \rfloor$, where M, K, N are the azimuthal, axial and radial directions respectively. If a recursion relation of size $d \ll N$ exist⁴ for this Poisson problem, its solution requires only $O(d \times N)$ operations (see section 4.4.4). Solution of the Poisson problem in three dimensions, thus requires $O(M \times K \times N \times d)$ operations, which is less than the cost of multiplying the system by the diagonalization matrix.

Band-diagonal matrix formulation

Let us consider the following Helmholtz problem:

$$\mathcal{H}_\lambda f = g \quad (5.17)$$

with the Helmholtz operator \mathcal{H} defined in (5.13). This differential equation, which appears in the two-dimensional formulation of the Poisson solver based on the partial diagonalization method, can be written using operators r^2 and $r\partial_r$, for which there exist simple recursive formulas (see appendix A)

$$\begin{aligned} \frac{1}{r} \frac{\partial}{\partial r} r \frac{\partial}{\partial r} - \frac{m^2}{r^2} + \lambda &= \frac{1}{r^2} ((r\partial_r)^2 - m^2 + \lambda r^2) \\ &\Downarrow \\ r^2 \mathcal{H}_\lambda f = r^2 g &\Leftrightarrow \mathcal{L}_\lambda f = \mathcal{R} r^2 g \end{aligned}$$

³For high angular resolution, where $M \lesssim N$, the diagonalization in the radial direction can be optimal.

⁴In fact, recursive formulas corresponding to the banded-matrix formulation of an ODE problem in one dimension can be derived for a large class of spectral approximations, among them Chebyshev or Legendre polynomials. For detailed description of a methodology for defining the banded-matrix formulation for differential operator see Tuckerman [87].

where \mathcal{L}_λ and \mathcal{R} are the left and right operators defining $r^2\mathcal{H}_\lambda$ in the sense of equation (4.17). In matrix notation, the Helmholtz problem in the radial direction can be stated as follows

$$[\mathbf{L}][f'] = \underbrace{[\mathbf{R}][r^2]}_{[\mathbf{Q}]}[g] \quad (5.18)$$

where prime superscript in f' means that no boundary conditions have yet been imposed on the system. The correct way of imposing the boundary conditions $]f|_\partial = \beta$ on (5.18) is the following:

$$\begin{aligned} [\mathbf{Q}]^{-1}[\mathbf{L}][f] &= [g] + \tau_1[\delta_{i,N-1}] & \Leftrightarrow & \overline{[\mathbf{Q}]^{-1}[\mathbf{L}]}[f] = \overline{[g]} \\ [B] \cdot [f] &= \beta \end{aligned} \quad (5.19)$$

where the horizontal bar means that the boundary conditions have been incorporated into the matrices and corresponding right-hand-sides according to definition (5.5). The above formulation is not equivalent to the following one

$$\begin{aligned} [\mathbf{L}][f] &= [\mathbf{Q}][g] + \tau_1[\delta_{i,N-1}] & \Leftrightarrow & \overline{[\mathbf{L}]}[f] = [\mathbf{Q}]\overline{[g]} \\ [B] \cdot [f] &= \beta \end{aligned} \quad (5.20)$$

which is easier to implement but, according to Matsushima & Marcus [58], leads to large errors near the boundary and therefore should not be used. The matrix $[\mathbf{Q}]$ is penta-diagonal but its inverse $[\mathbf{Q}]^{-1}$ is a dense matrix. In order to take an advantage of the banded-matrix formulation it is necessary to express the solution $[f] = \overline{[\mathbf{Q}^{-1}\mathbf{L}]^{-1}}\overline{[g]}$ in terms of a corrected solution to the system $[\mathbf{L}][f] = [\mathbf{Q}]\overline{[g]}$. The linear system defined by the matrix $[\mathbf{L}]$ can be solved efficiently using the LU-decomposition since, for a banded matrix, the LU-factors are also band-diagonal.

The derivation of this algorithm is the following:

$$\begin{aligned} \overline{[\mathbf{Q}]^{-1}[\mathbf{L}]}[f] &= \overline{[g]} \\ [\mathbf{Q}]\overline{[\mathbf{Q}]^{-1}[\mathbf{L}]}[f] &= [\mathbf{Q}]\overline{[g]} \\ \begin{bmatrix} \mathbf{Q} \end{bmatrix} \begin{bmatrix} \mathbf{Q}^{-1}\mathbf{L} \\ B \end{bmatrix} [f] &= \begin{bmatrix} \mathbf{Q} \end{bmatrix} \begin{bmatrix} g \\ \beta \end{bmatrix} \\ \begin{bmatrix} \mathbf{Q} \end{bmatrix} \left(\begin{bmatrix} \mathbf{Q}^{-1}\mathbf{L} \\ 0 \\ B-x \end{bmatrix} \right) [f] &= \begin{bmatrix} \mathbf{Q} \end{bmatrix} \begin{bmatrix} g \\ \beta \end{bmatrix} \quad ; \quad [x]_i \equiv [\mathbf{Q}^{-1}\mathbf{L}]_{N-1,i} \\ \underbrace{([\mathbf{L}] + [\mathbf{Q}]_{i,N-1} \otimes [B-x])}_{[\mathbf{L}']} [f] &= [\mathbf{Q}]\overline{[g]} \end{aligned} \quad (5.21a)$$

where we assumed that $m = 0$ to simplify the notation: $(N - \lfloor \frac{m}{2} \rfloor) - 1 \rightarrow N - 1$. For $m \neq 0$ expression $(N - \lfloor \frac{m}{2} \rfloor) - 1$ should be substituted in place of $N - 1$.

Sherman-Morison-Woodbury formula It is possible to express $[\mathbf{L}']^{-1}$ using $[\mathbf{L}]^{-1}$. The Sherman-Morrison-Woodbury (SMW) theorem (see Golub & van Loan [32] for a proof) states that if a matrix \mathbf{A} is altered by a perturbation \mathbf{a} such that $\mathbf{A} \rightarrow \mathbf{A} + \mathbf{a} \equiv \mathbf{A}'$, and if the perturbation is of the form $\mathbf{a} \equiv \mathbf{v} \otimes \mathbf{w} \equiv \mathbf{v}\mathbf{w}^T$ then its inverse can be written as:

$$\mathbf{A}'^{-1} = \mathbf{A}^{-1} - (\mathbf{A}^{-1}\mathbf{v})(\mathbb{1} + \mathbf{w}^T\mathbf{A}^{-1}\mathbf{v})^{-1}(\mathbf{w}^T\mathbf{A}^{-1})$$

Applying this formula to (5.21a) gives

$$[f] = \left([\mathbf{L}]^{-1} - \frac{[\mathbf{L}]^{-1}[\mathbf{Q}]_{i,N-1} \otimes [B-x][\mathbf{L}]^{-1}}{1 - [B-x][\mathbf{L}]^{-1}[\mathbf{Q}]_{i,N-1}} \right) [\mathbf{Q}][\bar{g}] \quad (5.22)$$

It can be shown by performing straightforward simplification of (5.22) that the solution vector $[f]$ can be written as

$$[f] = [f'] + \tau[G] \quad ; \quad \tau \equiv \frac{\beta - [B] \cdot [f']}{[B] \cdot [G]} \quad (5.23)$$

with $[f'] \equiv [\mathbf{L}]^{-1}[\mathbf{Q}][\bar{g}]$ and $[G] \equiv [\mathbf{L}]^{-1}[\mathbf{Q}]_{i,N-1}$. The formula stated in (5.23) requires $O(N)$ operations assuming that all matrix operations are performed taking into account the band-diagonal structure of $[\mathbf{L}]$ and $[\mathbf{Q}]$.

Stable algorithm

The formulation (5.23) is, however, numerically instable for large N since the dominant element of each row of matrix $[\mathbf{L}]$ is situated on the first super-diagonal. In order to derive a stable algorithm it is necessary to perform a cyclic permutation $[\mathbf{P}]$ of rows of $[\mathbf{L}]$ such that $[\mathbf{P}][\mathbf{L}] \equiv [\mathbf{L}^P]$:

$$\begin{aligned} [\mathbf{L}^P]_{i+1,j} &= [\mathbf{L}]_{i,j} \quad ; \quad i = 0, \dots, N-2 \\ [L^P]_{0,j} &= [L]_{N-1,j} \end{aligned}$$

Since the first row of the matrix $[\mathbf{L}^P]$ breaks its penta-diagonal structure then it is necessary to apply once again the SMW technique in order to compute $[\mathbf{L}^P]^{-1}$ efficiently. Let $[\overline{\mathbf{L}^P}]$ be the matrix defined as follows:

$$\begin{bmatrix} \mathbf{L}^P \end{bmatrix} \longrightarrow \begin{bmatrix} a \\ \mathbf{L}^P \end{bmatrix} \equiv [\overline{\mathbf{L}^P}]$$

where a is an arbitrary value whose order of magnitude is that of the diagonal values of $[\overline{\mathbf{L}^P}]$. The matrix $[\overline{\mathbf{L}^P}]$ defined in this way is penta-diagonal (2 sub- and 2 super- diagonals) and diagonally dominant, ensuring stable inversion. Inserting the SMW formula expressing $[\mathbf{L}]$ in terms of $[\overline{\mathbf{L}^P}]$ in (5.22) leads to the formulation of Matsushima & Marcus [58], for which the solution $[f]$ can be written as

$$[f] = [f''] + \tau_1[G_1] + \tau_2[G_2] \quad (5.24)$$

where $[f''] \equiv (\overline{[\mathbf{L}^P]})^{-1} [y^P]$ and $[y^P] \equiv [\mathbf{P}][\mathbf{Q}][g]$. Vectors $[G_1]$ and $[G_2]$ are defined as

$$[G_1] \equiv (\overline{[\mathbf{L}^P]})^{-1} [\mathbf{P}][Q]_{i,N-1} \quad ; \quad [G_2] \equiv (\overline{[\mathbf{L}^P]})^{-1}_{i,0} \quad (5.25)$$

Coefficients τ_1, τ_2 are given by the following formulas:

$$\begin{aligned} \tau_1 &\equiv \left((y_0^P - [F] \cdot [f'']) ([B] \cdot [G_2]) - ([F] \cdot [G_2]) (\beta - [B] \cdot [f'']) \right) / \xi \\ \tau_2 &\equiv - \left((y_0^P - [F] \cdot [f'']) ([B] \cdot [G_1]) - ([F] \cdot [G_1] - Q_{N-1,N-1}) (\beta - [B] \cdot [f'']) \right) / \xi \end{aligned}$$

with

$$\xi \equiv ([F] \cdot [G_1] - Q_{N-1,N-1}) ([B] \cdot [G_2]) - ([F] \cdot [G_2]) ([B] \cdot [G_1])$$

and $[F]$ denotes the last row of $[\mathbf{L}]$.

5.3 High order PDE solver

The two-dimensional Poisson solver described in the preceding section is an essential tool for solving the Navier-Stokes problem. We will use it for numerically solving the potential equations (3.49) with the boundary conditions (3.50), (3.51) where we have replaced (3.51a) by its regularized form (4.26). To simplify the notation we will drop the u subscript denoting quantities related to the velocity:

$$\psi \equiv \psi_u, \quad \phi \equiv \phi_u, \quad \mathbf{s} \equiv \mathbf{s}_u, \quad \text{etc.}$$

This notation will hold unless it is redefined explicitly. We then have:

$$(\partial_t - Re^{-1}\Delta)\Delta_h\psi = \underbrace{\hat{\mathbf{e}}_z \cdot \nabla \times \mathbf{s}}_{s_\psi} \quad (5.27a)$$

$$(\partial_t - Re^{-1}\Delta)\Delta\Delta_h\phi = \underbrace{-\hat{\mathbf{e}}_z \cdot \nabla \times \nabla \times \mathbf{s}}_{s_\phi} \quad (5.27b)$$

together with

$$r^{-1}\partial_\theta\psi + \partial_z\partial_r\phi = 0 \quad (5.28a)$$

$$\partial_r\psi = 0 \quad (5.28b)$$

$$-\Delta_h\phi = 0 \quad (5.28c)$$

$$\phi = 0 \quad (5.28d)$$

$$\partial_{rz}^2\Delta_h\psi - \frac{1}{r}\partial_\theta\Delta\Delta_h\phi = 0 \quad (5.28e)$$

$$\psi = \int_0^r r\Omega_\pm(r)dr \quad (5.29a)$$

$$\partial_z\phi = 0 \quad (5.29b)$$

$$-\Delta_h\phi = 0 \quad (5.29c)$$

In (5.29), $\Omega_{\pm}(r) = 1 - e^{\frac{r-1}{\delta}}$ and therefore from (4.26) we have

$$\int_0^r r\Omega_{\pm}(r)dr \cong \frac{1}{2}r^2 + \delta(\delta - r)e^{\frac{r-1}{\delta}}.$$

The appropriate way to solve such multi-Laplacian differential equations is to construct a multi-step scheme involving solutions to the ordinary Poisson problem. A classical illustration of this idea is the two-dimensional Navier-Stokes problem in streamfunction formulation.

5.3.1 2D Navier-Stokes in streamfunction formulation

We will take a look at this example because it is in many points similar to our problem. We consider a 2D incompressible flow $\mathbf{u}(x,y) \equiv (u(x,y), v(x,y))$ in Cartesian coordinates represented by its streamfunction Ψ satisfying

$$\mathbf{u} = \nabla \times \Psi \hat{\mathbf{e}}_z \Leftrightarrow \begin{cases} u = -\partial_y \Psi \\ v = \partial_x \Psi \end{cases} \quad (5.30)$$

and related to the vorticity ω through the following relation

$$\Delta \Psi = -\omega \quad \text{with} \quad \omega = \hat{\mathbf{e}}_z \cdot \nabla \times \mathbf{u}. \quad (5.31)$$

The flow defined by (5.30) is divergence-free by construction. The first step for deriving the equation for Ψ is to take $\hat{\mathbf{e}}_z \cdot \nabla \times$ of the Navier-Stokes equations obtaining

$$(\partial_t - \nu \Delta)\omega = -(\mathbf{u} \cdot \nabla)\omega \quad \text{with} \quad \mathbf{u}|_{\partial} = 0, \quad (5.32)$$

where we specified no-slip boundary conditions. After replacing \mathbf{u} and ω by their expressions (5.30) and (5.31) we obtain the pure streamfunction formulation:

$$(\partial_t - \nu \Delta)\Delta \Psi = \{\Psi, \Delta \Psi\} \quad \text{with} \quad \begin{cases} \Psi|_{\partial} = 0 \\ \frac{\partial \Psi}{\partial \mathbf{n}}|_{\partial} = 0 \end{cases}. \quad (5.33)$$

where $\{f, g\} = \frac{\partial f}{\partial x} \frac{\partial g}{\partial y} - \frac{\partial f}{\partial y} \frac{\partial g}{\partial x}$ is the Poisson bracket. In order to solve (5.32) or (5.33) we need first to introduce a time integration scheme. Let us consider an implicit method for the diffusive, linear term and explicit for the advective, nonlinear term.

$$\frac{\omega^{n+1} - \omega^n}{\Delta t} = \nu \Delta \omega^{n+1} - (\mathbf{u}^n \cdot \nabla)\omega^n$$

which leads to the following (\mathbf{u}, ω) formulation

$$\underbrace{(\mathbb{1} - \epsilon \Delta)}_E \omega^{n+1} = \underbrace{\omega^n - \Delta t (\mathbf{u}^n \cdot \nabla)\omega^n}_{s^n} \quad \text{with} \quad \mathbf{u}^{n+1}|_{\partial} = 0, \quad (5.34)$$

or the equivalent Ψ formulation:

$$\underbrace{(\mathbb{1} - \epsilon \Delta)}_E \Delta \Psi^{n+1} = \underbrace{\Delta \Psi^n + \Delta t \{\Psi^n, \Delta \Psi^n\}}_{-s^n} \quad \text{with} \quad \begin{cases} \Psi^{n+1}|_{\partial} = 0 \\ \frac{\partial \Psi^{n+1}}{\partial \mathbf{n}}|_{\partial} = 0 \end{cases}. \quad (5.35)$$

where $\epsilon \equiv \nu \Delta t$. The difficult point about both (5.34) and (5.35) is satisfaction of the boundary conditions. In (5.34) the problem is that all constraints are imposed on the velocity field and none are defined for the vorticity. This is because there is no physical boundary conditions that ω should respect. This kind of indirect boundary condition cannot be implemented directly by the τ -method. One could think that the situation is much simpler for (5.35), since all boundary conditions (5.33) are defined for the same variable Ψ and moreover, they are of standard Dirichlet and Neumann type. Unfortunately, the matrix corresponding to the fourth order operator $E\Delta$ with the last four rows replaced by the boundary conditions stated in (5.33) has several spurious⁵ eigenvalues which do not correspond to physical growth rates of any of the solutions to (5.33).

The remedy to this problem is the *influence matrix* method which we will discuss in detail in section 5.4. In this approach we solve the following successive Poisson problems

$$Ef = s^n \quad f|_{\partial} = b \quad (5.36a)$$

$$\Delta\Psi^{n+1} = f \quad \Psi^{n+1}|_{\partial} = 0 \quad (5.36b)$$

which no longer correspond to (5.35), since we arbitrarily set Dirichlet boundary conditions for f . However, this system can be solved directly by using the τ -method, without generating spurious modes. The key idea of the *influence matrix* method is the following statement:

There exist $\mathbf{b} = \mathbf{b}(s^n)$ such that the solutions Ψ^{n+1} to (5.36) and to (5.35) are the same.

The *influence matrix* technique gives the recipe for finding the correct b .

5.3.2 Multi-Poisson solver

Since the Navier-Stokes equations in the poloidal-toroidal variables are, in many respects, similar to the streamfunction formulation discussed above, we will apply the same logic while developing the multi-step resolution methodology for (5.27). Because they are treated differently, we prefer to present separately the equations for the axisymmetric Fourier mode $m = 0$ and for situations with $m \neq 0$. Since the problems for different Fourier modes are decoupled, we shall simplify the notation by using $\hat{f} \equiv \hat{f}^m$ to refer to the Fourier component under consideration.

⁵Here it is important that the operator $E\Delta \leftrightarrow (\mathbb{1} - \Delta t\nu\Delta)\Delta$ involves a discrete time evolution over the time interval Δt . The important difference between E and Δ is that E does not need any boundary conditions in order to be invertible which is not the case for Δ . Therefore substituting some rows of operator E involving the time evolution is much more delicate since it alters not only spatial modes but also the associated growth rates. The spurious modes can grow while iterating such a system, making the solver unstable. The operator E is known to support imposing of only one boundary condition.

Axisymmetric mode ($m = 0$)

The axisymmetric parts of equations (5.27) in multi-step formulation, after applying the Fourier transformation, can be stated for $\hat{\psi}$ as follows:

$$E\hat{f}_\psi = \widehat{rhs}_\psi \quad ; \quad \begin{cases} \hat{f}_\psi|_{z=\pm\frac{h}{2}} = \hat{\sigma}_{f_\psi}(r) & \Leftrightarrow \hat{\psi}|_{z=\pm\frac{h}{2}} = \int_0^r r\hat{\Omega}_\pm(r)dr \\ \int_0^1 \hat{f}_\psi r dr = 0 & \Leftrightarrow \partial_r \hat{\psi}|_{r=1} = 0 \end{cases} \quad (5.37a)$$

$$\Delta_h \hat{\psi} = \hat{f}_\psi \quad ; \quad \hat{\psi}|_{r=0} = 0 \quad (5.37b)$$

and for $\hat{\phi}$:

$$E\hat{g}_\phi = \widehat{rhs}_\phi \quad ; \quad \hat{g}_\phi|_{\partial} = \hat{\sigma}_{g_\phi} \Leftrightarrow \begin{cases} \partial_{rz}^2 \hat{\phi}|_{r=1} = 0 \\ \partial_z \hat{\phi}|_{z=\pm\frac{h}{2}} = 0 \end{cases} \quad (5.38a)$$

$$\Delta \hat{f}_\phi = \hat{g}_\phi \quad ; \quad \hat{f}_\phi|_{\partial} = 0 \quad \Leftrightarrow \Delta_h \hat{\phi}|_{\partial} = 0$$

$$\Delta_h \hat{\phi} = \hat{f}_\phi \quad ; \quad \hat{\phi}|_{r=1} = 0 \quad (5.38b)$$

where $\Delta \equiv (\frac{1}{r}\partial_r r \partial_r + \partial_z^2)$, $\Delta_h \equiv (\frac{1}{r}\partial_r r \partial_r)$, $E \equiv (\mathbb{1} - \epsilon\Delta)$ and $\epsilon \equiv Re^{-1}\Delta t$. Once the operator $(\partial_t - Re^{-1}\Delta)$ is replaced with $E \equiv (\mathbb{1} - \epsilon\Delta)$ the meaning of the corresponding right-hand-sides $\hat{s}_\psi, \hat{s}_\phi$ also change: they now denote the $\hat{\mathbf{e}}_z$ component of curl and double curl of the nonlinear term according to (3.49c) but they also contain the terms coming from the implicit time discretization evaluated at the preceding time step. For the first-order implicit Euler scheme the new $\{\hat{s}_\psi, \hat{s}_\phi\} \mapsto \{\widehat{rhs}_\psi, \widehat{rhs}_\phi\}$ is defined by the following expression

$$E\{\Delta_h \hat{\psi}, \Delta \Delta_h \hat{\phi}\}^{t+\Delta t} = \underbrace{\Delta t \{\hat{s}_\psi, \hat{s}_\phi\}^{t+\Delta t} + \{\Delta_h \hat{\psi}, \Delta \Delta_h \hat{\phi}\}^t}_{\{\widehat{rhs}_\psi, \widehat{rhs}_\phi\}} \quad (5.39)$$

While presenting the boundary conditions we used the " \Leftrightarrow " symbol to indicate the corresponding, **but not always equivalent**, original boundary conditions given in (5.28) and (5.29). The Dirichlet boundary conditions defined by the boundary values $\hat{\sigma}_{f_\psi}$ (5.37a) and $\hat{\sigma}_{g_\phi}$ (5.38a) remain unknown at this stage. They will be determined later using the influence matrix technique in such a way as to satisfy the actual boundary conditions stated on the right of the " \Leftrightarrow " symbol. The reason why the conditions $\hat{\psi}|_{z=\pm\frac{h}{2}} = \int_0^r r\hat{\Omega}_\pm(r)dr$ and $\partial_z \hat{\phi}|_{z=\pm\frac{h}{2}} = 0$ cannot be imposed directly on $\hat{\psi}$ in (5.37b) and on $\hat{\phi}$ in (5.38b) is that the operator $\Delta_h \equiv \frac{1}{r}\partial_r r \partial_r$ does not contain ∂_z^2 and so no vertical condition ($z = \pm\frac{h}{2}$) can be added to the corresponding equations.

One can notice that the *compatibility condition* (5.28e) is not present in (5.37) and (5.38). The reason for this is that the axisymmetric fields in potential variables do not require any additional boundary conditions in order to be compatible with the original primitive-variable formulation (see section 3.4.1 for the proof).

Neumann boundary conditions for axisymmetric modes The identity $\int_0^1 \hat{f}_\psi r dr = 0 \Leftrightarrow \partial_r \hat{\psi}|_{r=1} = 0$ in (5.37a) is not trivial and needs to be explained. Similarly, the origin of the new condition $\hat{\psi}|_{r=0} = 0$ in (5.37b) is not clear. The property that the Neumann boundary condition $\partial_r \hat{\psi}|_{r=1} = 0$

imposed on the axisymmetric mode $\hat{\psi}$ must be translated into an integral condition on \hat{f}_ψ is characteristic of the Poisson equation in polar coordinates. To illustrate this, we consider the following equation in two dimensions:

$$\Delta f \equiv \left(\frac{1}{r} \partial_r r \partial_r - \frac{1}{r^2} \partial_\theta^2 \right) f = g \quad (5.40)$$

The scalar functions f, g can be decomposed simultaneously into Fourier ($f(r, \theta) \xrightarrow{\mathcal{F}} \hat{f}^m(r)$) and polynomial ($\hat{f}^m(r) \rightarrow \hat{f}_n^m$) bases respecting the regularity rules explained in section 4.4.1:

$$f(r, \theta) = \sum_{m=-\infty}^{\infty} \sum_{\substack{n=m \\ n+m \text{ even}}}^{\infty} \hat{f}_n^m r^n \mathbf{e}^{im\theta}$$

$$g(r, \theta) = \sum_{m=-\infty}^{\infty} \sum_{\substack{n=m \\ n+m \text{ even}}}^{\infty} \hat{g}_n^m r^n \mathbf{e}^{im\theta}$$

Substituting the above expansion into (5.40) gives

$$\sum_{m=-\infty}^{\infty} \sum_{\substack{n=m \\ n+m \text{ even}}}^{\infty} (n^2 - m^2) \hat{f}_n^m r^{n-2} \mathbf{e}^{im\theta} = \sum_{m=-\infty}^{\infty} \sum_{\substack{n=m \\ n+m \text{ even}}}^{\infty} \hat{g}_n^m r^n \mathbf{e}^{im\theta} \quad (5.41)$$

resulting for a given m in the following system of relations between coefficients $\hat{f}_{n+2} \equiv \hat{f}_{n+2}^m$ and $\hat{g}_n \equiv \hat{g}_n^m$:

$$0(2m+0)\hat{f}_m = 0 \quad (5.42a)$$

$$2(2m+2)\hat{f}_{m+2} = \hat{g}_m \quad (5.42b)$$

$$4(2m+4)\hat{f}_{m+4} = \hat{g}_{m+2} \quad (5.42c)$$

$$6(2m+6)\hat{f}_{m+6} = \hat{g}_{m+4} \quad (5.42d)$$

$$\vdots$$

$$(n^2 - m^2)\hat{f}_n = \hat{g}_{n-2} \quad (5.42e)$$

$$\vdots$$

One can see that the coefficient \hat{f}_m cannot be determined from (5.42a) and another condition must be added. This is of course not surprising – the Laplacian requires one condition per boundary in order to be invertible. Let us consider imposing the Dirichlet boundary condition $\hat{f}(r=1) = \hat{\sigma}$:

$$\hat{f}_m + \hat{f}_{m+2} + \hat{f}_{m+4} + \hat{f}_{m+6} + \dots = \hat{\sigma} \quad (5.43)$$

It is clear that the above condition determines \hat{f}_m . Now, we look at the Neumann boundary condition $\partial_r \hat{f}(r=1) = \hat{\sigma}$

$$m\hat{f}_m + (m+2)\hat{f}_{m+2} + (m+4)\hat{f}_{m+4} + (m+6)\hat{f}_{m+6} + \dots = \hat{\sigma} \quad (5.44)$$

This determines \hat{f}_m only if $m > 0$. Moreover, for $m = 0$, (5.44) is inconsistent with (5.42). Substituting (5.42) into (5.44) with $m = 0$ we obtain the solvability condition that \hat{g}_n must satisfy in order to define a well-posed problem:

$$\frac{\hat{g}_0^0}{2} + \frac{\hat{g}_2^0}{4} + \frac{\hat{g}_4^0}{6} + \frac{\hat{g}_6^0}{8} + \dots = \hat{\sigma}^0 \quad (5.45)$$

which can also be written as:

$$\int_0^1 \hat{g}^0(r) r dr = \hat{\sigma}^0 \quad (5.46)$$

This condition is a particular case of a solvability/compatibility condition for a general domain:

$$\int g dv = \int \Delta f dv = \int \nabla f \cdot \hat{\mathbf{n}} ds \quad (5.47)$$

which written for the unit disk $r \leq 1$ gives

$$\int_0^1 r dr \int_0^{2\pi} d\theta g = \int_0^{2\pi} d\theta \partial_r f \quad (5.48)$$

For non-axisymmetric Fourier modes, the integrals on either side of (5.48) vanish.

Therefore, the conclusion is that for the axisymmetric modes, the right-hand-side of the Poisson equation with Neumann boundary conditions must satisfy the solvability condition. In other words, the condition imposed on a normal derivative of \hat{f} must be turned into an integral condition on \hat{g} . The remaining degree of liberty \hat{f}_0^0 can be fixed by imposing an arbitrary Dirichlet condition on $\hat{f}^0(r = r_0)$.

We can apply this consideration to the Neumann boundary condition $\partial_r \hat{\psi}^0|_{r=1} = 0$ defined in (5.37a). This condition must be replaced by the compatibility condition $\int_0^1 \hat{f}_\psi^0 r dr = 0$ corresponding to (5.46). We fix the remaining degree of freedom by requiring $\hat{\psi}^0|_{r=0} = 0$ in (5.37b).

Non-axisymmetric modes

The multi-step resolution scheme for non-axisymmetric modes $\hat{\psi}$ can be written as follows:

$$E \hat{f}_\psi = \widehat{rhs}_\psi \quad ; \quad \hat{f}_\psi|_{\partial} = \hat{\sigma}_{f_\psi} \Leftrightarrow \begin{cases} (\hat{\psi})|_{z=\pm \frac{h}{2}} = 0 \\ (-\frac{im}{r} \hat{\psi} + \partial_z \partial_r \hat{\phi})|_{r=1} = 0 \end{cases} \quad (5.49a)$$

$$\Delta_h \hat{\psi} = \hat{f}_\psi \quad ; \quad \partial_r \hat{\psi}|_{r=1} = 0 \quad (5.49b)$$

and for $\hat{\phi}$:

$$E \hat{g}_\phi = \widehat{rhs}_\phi \quad ; \quad \hat{g}_\phi|_{\partial} = \hat{\sigma}_{g_\phi} \Leftrightarrow \begin{cases} (\partial_z \hat{\phi})|_{z=\pm \frac{h}{2}} = 0 \\ (\partial_{rz}^2 \Delta_h \hat{\psi} - \frac{im}{r} \Delta \Delta_h \hat{\phi})|_{r=1} = 0 \end{cases} \quad (5.50a)$$

$$\Delta \hat{f}_\phi = \hat{g}_\phi \quad ; \quad \hat{f}_\phi|_{\partial} = 0 \Leftrightarrow \Delta_h \hat{\phi}|_{\partial} = 0 \quad (5.50b)$$

$$\Delta_h \hat{\phi} = \hat{f}_\phi \quad ; \quad \hat{\phi}|_{r=1} = 0 \quad (5.50c)$$

where $\Delta \equiv (\frac{1}{r} \partial_r r \partial_r - \frac{m^2}{r^2} + \partial_z^2)$, $\Delta_h \equiv (\frac{1}{r} \partial_r r \partial_r - \frac{m^2}{r^2})$ and $E \equiv (1 - \epsilon \Delta)$. The boundary conditions written on the right of braces are the actual ones and are supposed to be satisfied using the

influence matrix method which will give us $\hat{\sigma}_{f_\psi}$ and $\hat{\sigma}_{g_\phi}$. Here it should be mentioned that since, for non-axisymmetric modes the conditions (5.28a) and (5.28e) cannot be decoupled, they cannot be imposed separately on $\hat{\psi}$ and $\hat{\phi}$. The reason for which we assigned arbitrarily these coupled conditions to (5.49a) and (5.50a) is to show that the number of the equations and of the boundary conditions matches.

5.4 Influence matrix

This is a powerful tool which can be used to satisfy very complicated boundary conditions, even those coupling several functions. This technique is a discrete analogue of the Green functions method used in analytic calculations (especially in electromagnetic problems). While the general concept is classic, in practice the influence matrix method is not very well known and by consequence is relatively rarely implemented in numerical algorithms. To understand the reason why this method is considered unusual, it is necessary to go into the details of practical implementation. This can give an idea about the level of difficulty, robustness and computational cost of this approach. Before exposing the whole methodology, we prefer to present the general idea on a classic example from electrostatic theory. We believe that the influence matrix method can be better or more intuitively understood by showing the analogy between this technique and the Green functions method applied to a simple physical problem.

5.4.1 Green function method

We will base our presentation on the formulation of Jackson [39]. Let us consider a finite volume V bounded by the surface S . Let ρ be the electric charge density inside the volume V . The electric scalar potential Φ can be determined for this system from the Poisson equation

$$\Delta\Phi = -\frac{\rho}{\epsilon_0} \quad (5.51)$$

where ϵ_0 is the electrical permeability of vacuum. This equation must be completed by Dirichlet or Neumann boundary conditions in order to define a well-posed problem with a unique solution. The electric potential corresponding to a single isolated (in a vacuum) point charge q situated at position \mathbf{x}' has the following form

$$\Phi(\mathbf{x}) = \frac{1}{4\pi\epsilon_0} \frac{q}{|\mathbf{x} - \mathbf{x}'|} \quad (5.52)$$

and it can be verified that

$$\Delta\Phi = \frac{q}{4\pi\epsilon_0} \Delta\left(\frac{1}{|\mathbf{x} - \mathbf{x}'|}\right) = -\frac{\delta(\mathbf{x} - \mathbf{x}')}{\epsilon_0} q \quad (5.53)$$

where δ represents the Dirac distribution.

Principle of field superposition In order to obtain a solution for a continuous distribution $\rho(\mathbf{x})$ of charges surrounded by a vacuum, we use the principle of additivity of the electric

potential (which follows directly from additivity of charge and from the linear dependence between the charge density and the electric potential):

$$\Phi(\mathbf{x}) = \frac{1}{4\pi\epsilon_0} \int \frac{\rho(\mathbf{x}')}{|\mathbf{x} - \mathbf{x}'|} d^3x'. \quad (5.54)$$

The potential $\Phi(\mathbf{x})$ defined in (5.54) represents, however, only a particular solution which cannot satisfy arbitrarily imposed boundary conditions. This is because we have chosen to construct the solution for a continuous distribution of charges from a particular solution (5.52) corresponding to a point-source potential. In general there exists a class of functions $G(\mathbf{x}; \mathbf{x}')$ called *Green functions* satisfying

$$\Delta G(\mathbf{x}, \mathbf{x}') = -4\pi\delta(\mathbf{x} - \mathbf{x}') \quad (5.55)$$

where

$$G(\mathbf{x}; \mathbf{x}') = \frac{1}{|\mathbf{x} - \mathbf{x}'|} + G^h(\mathbf{x}, \mathbf{x}') \quad (5.56)$$

with homogeneous part G^h satisfying the Laplace equation

$$\Delta G^h(\mathbf{x}; \mathbf{x}') = 0. \quad (5.57)$$

General solution The general solution for Φ can be constructed from G by using *Green's second identity*:

$$\int_V (\phi\Delta\psi - \psi\Delta\phi) d^3x = \oint_S \left(\phi \frac{\partial\psi}{\partial n} - \psi \frac{\partial\phi}{\partial n} \right) da \quad (5.58)$$

from which, by substituting $\psi \rightarrow G(\mathbf{x}, \mathbf{x}')$ and $\phi \rightarrow \Phi(\mathbf{x}, \mathbf{x}')$, we obtain

$$\Phi(\mathbf{x}) = \frac{1}{4\pi\epsilon_0} \int_V \rho(\mathbf{x}') G(\mathbf{x}; \mathbf{x}') d^3x' + \frac{1}{4\pi} \oint_S \left(G(\mathbf{x}; \mathbf{x}') \frac{\partial\Phi}{\partial n'} - \Phi(\mathbf{x}') \frac{\partial G(\mathbf{x}; \mathbf{x}')}{\partial n'} \right) da' \quad (5.59)$$

Since the boundary values $\Phi(\mathbf{x}')$ and normal derivatives $\frac{\partial\Phi}{\partial n}$ are present in (5.59), we can ensure the satisfaction of either Dirichlet or Neumann boundary conditions by choosing G^h in such a way as to make the surface integral depend only on a single type of boundary condition. We will satisfy Dirichlet boundary conditions by choosing

$$G_D(\mathbf{x}; \mathbf{x}') = 0 \quad \text{for } \mathbf{x}' \text{ on } S \quad (5.60)$$

which implies the following form of solution:

$$\Phi(\mathbf{x}) = \frac{1}{4\pi\epsilon_0} \int_V \rho(\mathbf{x}') G_D(\mathbf{x}; \mathbf{x}') d^3x' - \frac{1}{4\pi} \oint_S \Phi(\mathbf{x}') \frac{\partial G_D(\mathbf{x}; \mathbf{x}')}{\partial n'} da' \quad (5.61)$$

and for Neumann boundary conditions we will require

$$\frac{\partial G_N(\mathbf{x}; \mathbf{x}')}{\partial n'} = -\frac{4\pi}{S} \quad \text{for } \mathbf{x}' \text{ on } S \quad (5.62)$$

which follows from the *Stokes theorem* for which we have

$$\oint_S \frac{\partial G}{\partial n'} da' = 4\pi \quad (5.63)$$

Thus, for Neumann boundary conditions the general solution takes the following form

$$\Phi(\mathbf{x}) = \langle \Phi \rangle_S + \frac{1}{4\pi\epsilon_0} \int_V \rho(\mathbf{x}') G_N(\mathbf{x}; \mathbf{x}') d^3x + \frac{1}{4\pi} \oint_S G_N(\mathbf{x}; \mathbf{x}') \frac{\partial \Phi}{\partial n'} da' \quad (5.64)$$

where $\langle \Phi \rangle_S$ is the average value of the potential over the whole surface.

Conclusions

This short classic demonstration shows a very important property of a solution written in terms of Green functions. The Green functions $G(\mathbf{x}; \mathbf{x}')$ do not formally depend on a particular distribution of charges on the surface S and satisfy simple boundary conditions. This means that for a given type of problem, regardless of the particular realization of the system, the solution can be written in terms of functions depending only on the geometry. This has an essential consequence for the influence matrix method – the Green functions for a given geometry can be found once and for all, and there is no need to determine them at each time step of a temporal integration (assuming that the properties of the boundary do not depend on time).

One can ask: What arguments allow us to think that the reasoning shown for the simple problem stated in (5.51) apply to the high order differential equations (5.27)? Not only are the equations different, but they are also time-dependent and the boundary conditions (5.28) and (5.29) are far more complex and cannot be qualified as being of Dirichlet or Neumann type. Although this is true, we should remember that the reason for which the Green function method works for Dirichlet and Neumann boundary condition is that the Poisson problem with this kind of boundary condition is well-posed. The principle of field superposition, on the other hand, is more general and follows from the linearity of equations. In our problem equations (5.27) follows from equation (2.7a) for the velocity \mathbf{u} for which all boundary conditions are of Dirichlet type and, therefore, correspond to the well-posed problem.

Additionally, when considering a single iteration of a semi-implicit time integration scheme, equation (2.7a) can be written as

$$\underbrace{(\mathbb{1} - \epsilon\Delta)}_E \mathbf{u}^{n+1} = \underbrace{\mathbf{u}^n + \mathbf{s} - \nabla \left(p + \frac{B^2}{2} \right)}_{RHS^n(\mathbf{u}, \mathbf{B})} \quad (5.65)$$

where the analogy with (5.51) can be written as $E \leftrightarrow \Delta$ and $\mathbf{u}^{n+1} \leftrightarrow \Phi$ and $RHS^n(\mathbf{u}, \mathbf{B}) \leftrightarrow -\frac{\rho}{\epsilon_0}$. Another difference is that operator E does not have the same formal properties as Δ , mainly because it has a trivial kernel while Δ does not. This would mean that E does not permit specifying the boundary conditions. This is, however, an artifact of discretization of the continuous problem. We know that operator $(\partial_t - Re^{-1}\Delta)$ requires both initial and boundary conditions, and for this reason we treat E in the same manner as Δ . Of course these are only qualitative arguments and in general the nonlinear Navier-Stokes equations cannot be compared to the Poisson problem⁶. We will however make a common assumption that we can treat a single

⁶Especially since the Navier-Stokes equation in three dimensions has not yet been proved to define a well-posed problem.

time step as a quasi-static situation with the right-hand-side $RHS^n(\mathbf{u}, \mathbf{B})$ independent of \mathbf{u}^{n+1} . This allows us to treat equation (5.65) for \mathbf{u} as well as equations (5.27) for (ψ, ϕ) as linear.

5.4.2 Discrete Green functions method – influence matrix

Before starting to translate the methodology presented for the electrostatic example into a discrete matrix formulation let us try to estimate the potential computational/storage cost of such an algorithm in a practical numerical implementation. We consider a discretized volume with collocation points situated at positions \mathbf{x}_i . We want to determine the solution $[\Phi]_i$ satisfying Dirichlet boundary conditions. The Green functions $G(\mathbf{x}_i; \mathbf{x}_j)$ can be represented by a matrix $[\mathbf{G}]_{ij}$ with $i, j \in 0 \dots N^3 - 1$, where N^3 is the total number of points in a three-dimensional computational domain and N represents the typical resolution along a single direction. The Green functions satisfy

$$\sum_i^{N^3-1} [\Delta]_{ki} [\mathbf{G}]_{ij} = [\delta]_{kj} \quad (5.66)$$

The notation $[\Delta]$ represents the matrix⁷ corresponding to the Laplace operator Δ . The solution vector $[\Phi]_i$ can then be constructed using the analogy to formula (5.61):

$$[\Phi]_i = \sum_k^{N^3-1} [\mathbf{G}]_{ik} [\rho]_k + \sum_l^{O(N^2)} [\partial_n \mathbf{G}]_{il} [\Phi]_{\partial}{}_l$$

where $O(N^2)$ indicates the order of magnitude of the total number of boundary points, which can differ depending on a particular geometry. Note that in three dimensions with $N = O(100)$, the total number of points can be of order of millions, making it impossible to compute and store $[\mathbf{G}]$ which would then be a matrix of dimension of order $O(10^6)$. This is the reason why in numerical algorithms the Green functions can be used only for satisfying the boundary conditions and not to calculate the whole solution. In order to compute the second sum in the above expression, only $O(N^2)$ Green functions are needed. This number corresponding to a two-dimensional domain is much smaller, but can still be on the order of several thousands. This may still seem too much to solve a three-dimensional problem thousands of times. However, if the geometry considered has at least one periodic dimension, then the Fourier transform can be used, and since this problem is linear, it can be solved separately for each of N Fourier modes. This means that instead of solving $O(N^2)$ three-dimensional problems one needs to solve $O(N^2)$ two-dimensional problems:

$$\forall m \quad \sum_i^{O(N^2)} [\Delta^m]_{ki} [\hat{\mathbf{G}}^m]_{il} = [\delta]_{kl} \quad ; \quad i = 0 \dots O(N^2), \quad k, l = 0 \dots O(N) \quad (5.67)$$

where $\hat{\mathbf{G}}^m$ are the Green functions used for satisfying the boundary conditions on the m^{th} Fourier mode. The dimension of the boundary of a single mode is $O(N)$. The total cost measured in number of operations of to compute $\hat{\mathbf{G}}^m$ for all Fourier modes is

$$(\text{number of Fourier modes}) \times (\text{number of boundary points per single mode}) \times (\text{cost of solution to 2D problem})$$

⁷Note that this is only formal notation – in practical implementations, in more than one dimension, an operator is never stored as a single matrix acting in all directions. Each spatial direction has an associated differential operator matrix of size equal to the resolution in this direction.

which gives us

$$O(N) \times O(N) \times O(N^3) = O(N^5)$$

Taking into account that a single step of time integration for a three-dimensional solution has complexity $O(N^4)$, we conclude that the overall cost of finding all necessary Green function for a three-dimensional problem in a geometry with at least one periodic dimension is comparable to the cost of $O(N)$ time iterations of the solver. This cost is acceptable.

The methodology

We will now describe the algorithm for satisfying the boundary conditions in a form which can be applied to our problem. We have already described in section 5.3 a multi-step solver capable of producing a solution under the condition that we know the boundary values $\hat{\sigma}_{f_\psi}$ and $\hat{\sigma}_{g_\phi}$. We will now derive the algorithm for finding these values.

For reasons of simplicity and generality we will present the methodology for a problem stated as follows

$$\mathcal{L}f = g \quad ; \quad (\mathcal{B}f)|_{\partial} = \beta \quad (5.68)$$

and we see that the above problem can be associated with (5.49) and (5.50) by substituting

$$\mathcal{L} \equiv \left\{ \begin{array}{c} E\Delta_h \\ E\Delta\Delta_h \end{array} \right\} \quad , \quad f \equiv \left\{ \begin{array}{c} \hat{\psi} \\ \hat{\phi} \end{array} \right\} \quad , \quad g \equiv \left\{ \begin{array}{c} \widehat{rhs}_\psi \\ \widehat{rhs}_\phi \end{array} \right\}$$

where the boundary conditions $(\mathcal{B}f)|_{\partial} = \beta$ would correspond to those indicated by braces in (5.49) and (5.50). We expect these boundary conditions to be equivalent to Dirichlet boundary conditions imposed on \hat{f}_ψ and \hat{g}_ϕ :

$$\left\{ \begin{array}{c} \hat{f}_\psi \\ \hat{g}_\phi \end{array} \right\} \Big|_{\partial} = \left\{ \begin{array}{c} \hat{\sigma}_{f_\psi} \\ \hat{\sigma}_{g_\phi} \end{array} \right\}$$

which can be written in terms of $\hat{\psi}$ and $\hat{\phi}$ as:

$$\underbrace{\left\{ \begin{array}{c} \Delta_h \\ \Delta\Delta_h \end{array} \right\}}_{\mathcal{D}} \left\{ \begin{array}{c} \hat{\psi} \\ \hat{\phi} \end{array} \right\} \Big|_{\partial} = \underbrace{\left\{ \begin{array}{c} \hat{\sigma}_{f_\psi} \\ \hat{\sigma}_{g_\phi} \end{array} \right\}}_{\sigma} \quad (5.69)$$

In (5.69), the boundary conditions defined by

$$\mathcal{D}f = \sigma \quad (5.70)$$

can be considered easy to impose because they correspond to Dirichlet boundary conditions imposed on \hat{f}_ψ and \hat{g}_ϕ . The existence of σ such that

$$\begin{array}{l} \mathcal{L}f = g \\ \mathcal{B}f|_{\partial} = \beta \end{array} \Leftrightarrow \begin{array}{l} \mathcal{L}f = g \\ \mathcal{D}f|_{\partial} = \sigma \end{array} \quad (5.71)$$

follows from the assumption that equation $\mathcal{L}f = g$ with the boundary conditions defined by \mathcal{B} or \mathcal{D} has a unique solution.

Now we can present the methodology for the influence matrix method applied to the generic problem (5.68). In order to separate the problem of satisfying the equation from that of satisfying the boundary condition, we decompose solution f into particular and homogeneous parts:

$$f = f^p + f^h \quad (5.72)$$

satisfying

$$\mathcal{L}f^p = g \quad ; \quad (\mathcal{D}f^p)|_{\partial} = 0 \quad (5.73a)$$

$$\mathcal{L}f^h = 0 \quad ; \quad (\mathcal{B}f^h)|_{\partial} = \beta - (\mathcal{B}f^p)|_{\partial} \quad (5.73b)$$

where the particular solution f^p satisfies the original inhomogeneous differential equation in (5.68) but with the arbitrary boundary conditions (5.73a), and the homogeneous solution f^h satisfies the related homogeneous differential equation with the actual boundary conditions from (5.68). It can be checked that $f = f^p + f^h$ satisfies both the equation and the boundary conditions given in (5.68).

We suppose that (5.73a) can be easily solved. The difficult task is to find f^h from (5.73b) because we do not yet know how to impose the boundary conditions involving operator \mathcal{B} . However, somewhat improved because f^h is responsible only for satisfying the boundary conditions and not for satisfying the original inhomogeneous differential equation stated in (5.68) with the right-hand-side g which varies from one timestep to another.

Now we can use the idea of *homogeneous Green functions*. Let $G^h(\mathbf{x}, \mathbf{x}')$ be defined as the solution to the following problem:

$$\mathcal{L}G^h(\mathbf{x}; \mathbf{x}') = 0 \quad ; \quad \mathcal{B}G^h(\mathbf{x}; \mathbf{x}')|_{\mathbf{x}''} = \delta(\mathbf{x}'' - \mathbf{x}') \quad (5.74)$$

where operators \mathcal{L} , \mathcal{B} involve differentiation and evaluation of variable \mathbf{x} and not \mathbf{x}' , $\mathbf{x}'' \in S$. The homogeneous solution f^h can be written as

$$f^h(\mathbf{x}) = \oint_S G^h(\mathbf{x}; \mathbf{x}') (\beta(\mathbf{x}') - \mathcal{B}f^p(\mathbf{x})|_{\mathbf{x}'}) da' \quad (5.75)$$

We now have a formula for f^h but we do not know G^h and one can argue that finding G^h is as difficult as finding f^h directly from (5.73b). This is true, but the essential difference is that G^h is completely independent of the boundary values β , the right hand side g and the particular solution f^p . This makes it possible to consider even a computationally expensive algorithm for finding G^h . Depending only on the operators \mathcal{L} and \mathcal{B} which do not change in time, G^h can be determined in the preprocessing stage of a numerical time-dependent simulation.

There exists an indirect way for determining f^h which, as we will see later, is equivalent to finding G^h . We introduce the *test function* $T(\mathbf{x}; \mathbf{x}')$ which is the solution to the following problem

$$\mathcal{L}T(\mathbf{x}; \mathbf{x}') = 0 \quad ; \quad \mathcal{D}T(\mathbf{x}; \mathbf{x}')|_{\mathbf{x}''} = \delta(\mathbf{x}'' - \mathbf{x}') \quad (5.76)$$

which we can solve because the boundary conditions given by operator \mathcal{D} can be imposed directly in our solver. It can be shown using (5.76) and (5.70) that function f^h can be written as the surface integral:

$$f^h(\mathbf{x}) = \oint_S T(\mathbf{x}; \mathbf{x}') \sigma(\mathbf{x}') da' \quad (5.77)$$

This definition involves the unknown distribution of boundary values σ which must be determined. By applying the boundary operator \mathcal{B} to both sides of (5.77) and by using the boundary condition stated in (5.73b) we obtain

$$\mathcal{B}f^h|_{\mathbf{x}''} = -\mathcal{B}f^p|_{\mathbf{x}''} + \beta(\mathbf{x}'') = \oint_S \underbrace{(\mathcal{B}T(\mathbf{x}; \mathbf{x}'))|_{\mathbf{x}''}}_{I(\mathbf{x}''; \mathbf{x}')} \sigma(\mathbf{x}') da' \quad (5.78)$$

where we defined a new function $I(\mathbf{x}''; \mathbf{x}')$, which we will call the *influence function*, depending only on the boundary points $\mathbf{x}', \mathbf{x}'' \in S$. The influence function $I(\mathbf{x}''; \mathbf{x}')$ obtained by evaluating

$$I(\mathbf{x}''; \mathbf{x}') = \mathcal{B}T(\mathbf{x}; \mathbf{x}')|_{\mathbf{x}''} \quad (5.79)$$

captures the influence of the choice of the test point \mathbf{x}' on the value of the boundary condition \mathcal{B} evaluated at \mathbf{x}'' .

In order to solve equation (5.78) for σ we introduce transformation \mathcal{I} defined as

$$\mathcal{I}[\sigma(\mathbf{x}'')] = \oint_S I(\mathbf{x}''; \mathbf{x}') \sigma(\mathbf{x}') da'. \quad (5.80)$$

We assume existence of the transformation \mathcal{I}^{-1} defined as

$$\mathcal{I}^{-1}[\rho(\mathbf{x}'')] = \oint_S I^{-1}(\mathbf{x}''; \mathbf{x}') \rho(\mathbf{x}') da' \quad (5.81)$$

which is the inverse of \mathcal{I} in the following sense:

$$\begin{aligned} \mathcal{I}^{-1} [\mathcal{I}[\sigma(\mathbf{x}'')]] &= \sigma(\mathbf{x}'') \\ &\Downarrow \\ \oint_S (I^{-1} * I)(\mathbf{x}''; \mathbf{x}') \sigma(\mathbf{x}') da' &= \sigma(\mathbf{x}'') \\ &\Downarrow \\ \oint_S \left(\oint_S I^{-1}(\mathbf{x}''; \mathbf{x}''') I(\mathbf{x}'''; \mathbf{x}') da''' \right) \sigma(\mathbf{x}') da' &= \sigma(\mathbf{x}'') \\ &\Downarrow \\ \oint_S I^{-1}(\mathbf{x}''; \mathbf{x}''') I(\mathbf{x}'''; \mathbf{x}') da''' &= \delta(\mathbf{x}'' - \mathbf{x}') \end{aligned}$$

We see that by construction I and I^{-1} satisfy

$$(I * I^{-1})(\mathbf{x}''; \mathbf{x}') = (I^{-1} * I)(\mathbf{x}''; \mathbf{x}') = \delta(\mathbf{x}'' - \mathbf{x}') \quad (5.82)$$

Applying \mathcal{I}^{-1} to both sides of (5.78) we finally obtain an expression for σ :

$$\begin{aligned}
 \mathcal{I}^{-1} \left[\oint_S I(\mathbf{x}''; \mathbf{x}') \sigma(\mathbf{x}') da' \right] &= \mathcal{I}^{-1} \left[\mathcal{B}f^h|_{\mathbf{x}''} \right] \\
 &\Downarrow \\
 \oint_S \underbrace{\left(I^{-1} * I \right)}_{\delta(\mathbf{x}'' - \mathbf{x}')} (\mathbf{x}''; \mathbf{x}') \sigma(\mathbf{x}') da' &= \mathcal{I}^{-1} \left[-\mathcal{B}f^p|_{\mathbf{x}''} + \beta(\mathbf{x}'') \right] \\
 &\Downarrow \\
 \sigma(\mathbf{x}'') &= \oint_S I^{-1}(\mathbf{x}''; \mathbf{x}') \left(-\mathcal{B}f^p|_{\mathbf{x}'} + \beta(\mathbf{x}') \right) da' \quad (5.83)
 \end{aligned}$$

where all the terms in integral (5.83), except for $\mathcal{B}f^p|_{\mathbf{x}'}$, can be calculated once in the preprocessing step of the simulation. The term $\mathcal{B}f^p|_{\mathbf{x}'}$ must be evaluated at each time step after determining f^p from (5.73a). Once σ is calculated, f^h can be obtained from (5.77) and the final solution $f = f^p + f^h$ is determined.

We can also solve for f without calculating f^h explicitly. Equivalence (5.71) justifies the following implicit definition of f .

$$\mathcal{L}f = g \quad ; \quad (\mathcal{D}f)|_{\partial} = \sigma \quad (5.84)$$

It is possible now to *a posteriori* determine the homogeneous Green function G^h . Substituting (5.83) into (5.77) gives:

$$\begin{aligned}
 f^h(\mathbf{x}) &= \oint_S T(\mathbf{x}; \mathbf{x}') \left[\oint_S I^{-1}(\mathbf{x}'; \mathbf{x}'') \left(-\mathcal{B}f^p|_{\mathbf{x}''} + \beta(\mathbf{x}'') \right) da'' \right] da' = \\
 &= \oint_S \left[\oint_S T(\mathbf{x}; \mathbf{x}') I^{-1}(\mathbf{x}'; \mathbf{x}'') da' \right] \left(-\mathcal{B}f^p|_{\mathbf{x}''} + \beta(\mathbf{x}'') \right) da''
 \end{aligned}$$

and by comparing with (5.75) G^h can be identified as

$$G^h(\mathbf{x}; \mathbf{x}') = \oint_S T(\mathbf{x}; \mathbf{x}'') I^{-1}(\mathbf{x}''; \mathbf{x}') da'' \quad (5.85)$$

Influence matrix

We are now ready to write the discrete version of the algorithm presented in the preceding paragraph – the *influence matrix* method. The algorithm can be divided into a few general steps, referring to formulas already presented.

Algorithmfor each m **Preprocessing**

1. $\forall \mathbf{x}' \in S$ solve (5.76) to find $T(\mathbf{x}; \mathbf{x}')$
2. Construct $I(\mathbf{x}; \mathbf{x}')$ from (5.79)
3. Construct $I^{-1}(\mathbf{x}; \mathbf{x}')$ from (5.82)

For each time step

4. Solve (5.73a) in order to obtain a particular solution f^p
5. Calculate $-\mathcal{B}f^p|_{\partial} + \beta$
6. Find σ from (5.83)
7. Solve (5.84) in order to obtain the final solution f

We will employ the following notation:

Types of fields

- $\hat{\psi}, \hat{\phi}$ Spectral representation of toroidal and poloidal potentials corresponding to the Fourier mode m solutions to (5.49)-(5.50) or (5.37)-(5.38).
- $\hat{\psi}^p, \hat{\phi}^p$ Particular solutions satisfying (5.49) or (5.37) with $\hat{\sigma}_{f_\psi} = 0$ and (5.50) or (5.38) with $\hat{\sigma}_{g_\phi} = 0$.
- $\hat{\psi}^h, \hat{\phi}^h$ Homogeneous solutions satisfying (5.49) or (5.37) with $\widehat{rhs}_\psi = 0$ and (5.50) or (5.38) with $\widehat{rhs}_\phi = 0$.
- $\hat{\psi}^t, \hat{\phi}^t$ Test functions which are solution to (5.49) and (5.50) or (5.37) and (5.38) with δ -type boundary values for $\hat{\sigma}_{f_\psi}$ and $\hat{\sigma}_{f_\phi}$ (the boundary condition will be explained later).

A one-index expression $[f]_\rho$ will denote a vector and two-index (and usually boldface) expression $[\mathbf{f}]_{\kappa\nu}$ will denote a matrix with κ indexing rows and ν indexing columns.

Indices and matrix/vector notation

- $[\hat{\psi}_s]_\rho \equiv [\hat{\psi}_s]_{\kappa\nu}$ Matrix of spectral coefficients in Fourier-Chebyshev-Radial basis.
- $\kappa \in [0, K-1]$ indexes Chebyshev modes (axial direction – $\mathcal{T}_\kappa(\frac{2z}{h})$)
- $\nu \in [0, N - \lfloor \frac{m}{2} \rfloor]$ indexes radial modes (radial direction – $\mathcal{Q}_\nu^m(r)$)
- $\rho \in [0, K(N - \lfloor \frac{m}{2} \rfloor) - 1]$ indexes all spectral coefficients corresponding to a given mode ($\rho = (\kappa(N - \lfloor \frac{m}{2} \rfloor) + \nu)$)
- $s \in \{e, o\}$ indicates whether even or odd part (regarding $\hat{\mathbf{e}}_z$ direction) of the field is referenced (also $s \in \{e = 0, o = 1\}$). Even (symmetric) and odd (anti-symmetric) parts are defined as follows: $\hat{f}_s(z) = \frac{\hat{f}(z) + (-1)^s \hat{f}(-z)}{2}$

$$\begin{aligned}
\langle \hat{\psi}^t \rangle_i^{j_s} &\equiv \left([\hat{\psi}^t]^{j_s} \right)_i \text{ Matrix of boundary values (still in spectral space)} \\
i \leftrightarrow \mathbf{x}'' &\text{ depending on its value, } i \text{ references a particular spectral coefficient} \\
&\text{ of a boundary function either on } (r = 1) \text{ or on } (z = \pm \frac{h}{2}) \\
i \in &\left\{ \overbrace{\{k_e\}, \{k_o\}}^k, \overbrace{\{n_e\}, \{n_o\}}^n \right\} \\
&\text{even on } r=1 \quad \text{odd on } r=1 \quad \text{symmetric on } z=\pm \frac{h}{2} \quad \text{antisymmetric on } z=\pm \frac{h}{2} \\
j_s \leftrightarrow \mathbf{x}' &\text{ identifies a test function obtained for } \delta\text{-type boundary conditions} \\
&\text{ specified for } j_s\text{'th spectral coefficient of a boundary function} \\
&\text{ for } \langle \hat{\psi}_s^{t,m=0} \rangle^{j_s} : j_s \in \{n_s\}, \quad \text{for } \langle \hat{\psi}_s^{t,m \neq 0} \rangle^{j_s} : j_s \in \{k_s\} \\
&\text{ for } \langle \hat{\phi}_s^t \rangle^{j_s} : j_s \in \{\{k_s\}, \{n_s\}\} \\
k_e &\text{ indicates an even coefficient of the Chebyshev expansion of boundary} \\
&\text{ values on } (r = 1) : k_e \in [0, \frac{K-1}{2}] \leftrightarrow [\hat{f}(r = 1)]_{2k_e} \\
k_o &\text{ indicates an odd coefficient of the Chebyshev expansion of boundary} \\
&\text{ values on } (r = 1) : k_o \in [\frac{K+1}{2}, K-1] \leftrightarrow [\hat{f}(r = 1)]_{2(k_o - \frac{K+1}{2})+1} \\
n_e &\text{ indicates a spectral coefficient of the radial expansion of boundary} \\
&\text{ values on } (z = \pm \frac{h}{2}) \text{ obtained for } z\text{-reflection symmetric} \\
&\text{ part of solution : } n_e \in [K, K + N - \lfloor \frac{m}{2} \rfloor - 1] \leftrightarrow \left[\frac{\hat{f}(z = +\frac{h}{2}) + \hat{f}(z = -\frac{h}{2})}{2} \right]_{(n_e - K)} \\
n_o &\text{ indicates a spectral coefficient of radial expansion of boundary} \\
&\text{ values on } (z = \pm \frac{h}{2}) \text{ obtained for } z\text{-reflection antisymmetric solution:} \\
&n_o \in [K + N - \lfloor \frac{m}{2} \rfloor, K + 2(N - \lfloor \frac{m}{2} \rfloor) - 1] \leftrightarrow \left[\frac{\hat{f}(z = +\frac{h}{2}) - \hat{f}(z = -\frac{h}{2})}{2} \right]_{(n_o - K - N + \lfloor \frac{m}{2} \rfloor + 1)}
\end{aligned}$$

We will use \mathbf{x} to represent either r or z in expressions that concern both variables. Similarly, i and j_s can reference rows or columns depending on context.

Step 1. The homogeneous solutions $[\hat{\psi}^h]$ and $[\hat{\phi}^h]$ can be decomposed into a basis of test solutions $[\hat{\psi}_s^t]^{j_s}$ and $[\hat{\phi}_s^t]^{j_s}$. The discrete analogue of (5.77) can be written as

$$\begin{aligned}
[\hat{\psi}^h] &= \sum_{s=\{e,o\}} \sum_{j_s} [\hat{\psi}_s^t]^{j_s} \\
[\hat{\phi}^h] &= \sum_{s=\{e,o\}} \sum_{j_s} [\hat{\phi}_s^t]^{j_s}
\end{aligned}$$

The first step is to construct the set of test solutions by choosing the δ -type boundary conditions for σ corresponding to (5.76). In the axisymmetric case $m = 0$ this can be done by substituting $\hat{\sigma}_{g_\phi} \equiv \delta(\mathbf{x}'' - \mathbf{x}')$ in (5.37) and (5.38) and for other modes $m \neq 0$ we will set $\hat{\sigma}_{f_\psi} \equiv \delta(\mathbf{x}'' - \mathbf{x}')$ in (5.49) and (5.50). The systems which one must solve in order to obtain the set of test solutions, according to the previously described notation, will have the following form:

Axisymmetric case $m = 0$:

$\hat{\psi}^t$:

$$\left[\widetilde{\hat{f}_\psi^t} \right]^{j_s} \left[-\epsilon \mathbf{H}_{\lambda - \frac{1}{\epsilon}} \right]^T = 0 \quad ; \quad \begin{cases} \langle \hat{f}_\psi^t \rangle_n^{j_s} = \delta_{n,j_s} \Leftrightarrow \hat{f}_\psi^t|_{z=\pm\frac{h}{2}}(r'') = \delta(r'' - r') \\ \langle \left[\hat{f}_\psi^t \right]^{j_s} \left[\int_0^1 r dr \right]^T \rangle_k = 0 \Leftrightarrow \int_0^1 \hat{f}_\psi^t r dr = 0 \end{cases} \quad (5.86a)$$

$$\left[\widetilde{\hat{\psi}^t} \right]^{j_s} \left[\mathbf{H}_0 \right]^T = \left[\widetilde{\hat{f}_\psi^{t*}} \right]^{j_s} \quad ; \quad \left(\left[\hat{\psi}^t \right]^{j_s} \right)_k^{r=0} = 0 \Leftrightarrow \hat{\psi}^t|_{r=0} = 0 \quad (5.86b)$$

where the notation $(\cdot)|_k^{r=0}$ denotes the k 'th coefficient of a quantity evaluated at $(r = 0)$.

$\hat{\phi}^t$:

$$\left[\widetilde{\hat{g}_\phi^t} \right]^{j_s} \left[-\epsilon \mathbf{H}_{\lambda - \frac{1}{\epsilon}} \right]^T = 0 \quad ; \quad \langle \hat{g}_\phi^t \rangle_i^{j_s} = \delta_{i,j_s} \Leftrightarrow \hat{g}_\phi^t|_{\partial}(\mathbf{x}'') = \delta(\mathbf{x}'' - \mathbf{x}') \quad (5.87a)$$

$$\left[\widetilde{\hat{f}_\phi^t} \right]^{j_s} \left[\mathbf{H}_\lambda \right]^T = \left[\widetilde{\hat{g}_\phi^{t*}} \right]^{j_s} \quad ; \quad \langle \hat{f}_\phi^t \rangle_i^{j_s} = 0 \Leftrightarrow \hat{f}_\phi^t|_{\partial} = 0 \quad (5.87b)$$

$$\left[\widetilde{\hat{\phi}^t} \right]^{j_s} \left[\mathbf{H}_0 \right]^T = \left[\widetilde{\hat{f}_\phi^{t*}} \right]^{j_s} \quad ; \quad \langle \hat{\phi}^t \rangle_k^{j_s} = 0 \Leftrightarrow \hat{\phi}^t|_{r=1} = 0 \quad (5.87c)$$

For a given j_s , these systems of linear matrix equations, which must be solved for each m , correspond to the three-dimensional Poisson solver based on the τ -method (see section 5.2.1) and the partial diagonalization technique described in section 5.2.2. The methodology for constructing matrices like $\left[\widetilde{\hat{\psi}^t} \right]^{j_s}$ or $\left[\widetilde{\hat{f}_\psi^{t*}} \right]^{j_s}$ was described in section 5.2.1. Note that the above matrix equations are defined only for the $K - 2$ eigenvalues $\lambda_k \in \{\lambda_0, \lambda_1, \dots, \lambda_{K-3}\}$ defined in (5.13). The two highest frequencies corresponding to $k = \{K - 1, K - 2\}$ can be obtained from (5.8) once the low frequency solutions $\left[\widetilde{\hat{\psi}^t} \right]^{j_s}$ and $\left[\widetilde{\hat{\phi}^t} \right]^{j_s}$ are known. The test solutions $\left[\hat{\psi}^t \right]^{j_s}$ and $\left[\hat{\phi}^t \right]^{j_s}$ can be obtained by applying the inverse transformation corresponding to (5.16). The methodology for constructing the Helmholtz operator $\left[\mathbf{H}_\lambda \right]$ was described in section 5.2.2. The time-step evolution operator $E \equiv (\mathbb{1} - \epsilon \Delta)$ can also be written using the Helmholtz operator $\left[-\epsilon \mathbf{H}_{\lambda - \frac{1}{\epsilon}} \right]$. The boundary conditions at $(z = \pm \frac{h}{2})$ specified to the right of the semicolons in (5.86-5.87) are imposed by the τ -method and are incorporated into the *-marked matrices obtained from Schur decomposition of matrix operators corresponding to ∂_z^2 . Boundary conditions at $(r = 1)$ are satisfied by replacing the last row in Helmholtz operators by the boundary condition vector and the last row in the right-hand-side matrix by the boundary values as was shown in (5.5).

Non-axisymmetric cases $m \neq 0$:

The procedure for obtaining the *tilde* \sim and *star* $*$ marked matrices as well as the Helmholtz matrices is the same as that described for the axisymmetric case.

The following matrix equations must be solved in order to obtain the test solution for $m \neq 0$:

$\hat{\psi}^t$:

$$\left[\widehat{f}_{\psi}^t \right]^{j_s} \left[-\epsilon \mathbf{H}_{\lambda - \frac{1}{\epsilon}} \right]^T = 0 \quad ; \quad \left\langle \widehat{f}_{\psi}^t \right\rangle_i^{j_s} = \delta_{i,j_s} \Leftrightarrow \hat{f}_{\psi}^t \Big|_{\partial}(\mathbf{x}'') = \delta(\mathbf{x}'' - z') \quad (5.88a)$$

$$\left[\widehat{\psi}^t \right]^{j_s} \left[\mathbf{H}_0 \right]^T = \left[\widehat{f}_{\psi}^{t*} \right]^{j_s} \quad ; \quad \left\langle \left[\widehat{\psi}^t \right]^{j_s} \left[\partial_r \right]^T \right\rangle_k = 0 \Leftrightarrow \begin{cases} \partial_r \hat{\psi}^t \Big|_{r=1} = 0 \\ \Downarrow \\ \hat{\psi}^t \Big|_{z=\pm \frac{h}{2}} = 0 \end{cases} \quad (5.88b)$$

The boundary conditions in (5.88a) and (5.88b) require some comments. One can notice that the test point z' and the corresponding index j_s concern only the ($r = 1$) boundary. This suggests that the test functions obtained for $\mathbf{x}' \equiv r'$ indexed by ($j_s \in \{n_s\}$) are forbidden since they should play no role in satisfaction of the boundary condition for the homogeneous function $\hat{\psi}^h$. Solutions $\hat{\psi}^t$ obtained for such boundary conditions would certainly contain non-zero values at the boundary ($z = \pm \frac{h}{2}$) and this would conflict with the boundary condition $\hat{\psi}^h \Big|_{z=\pm \frac{h}{2}} = 0$. It can be seen that all test functions corresponding to test points $\mathbf{x}' \equiv z'$ and indexes ($j_s \in \{k_s\}$) satisfy the $\hat{\psi}^t \Big|_{z=\pm \frac{h}{2}} = 0$ condition. This is because δ -type boundary conditions specified only at ($r = 1$) imply $\hat{f}_{\psi}^t \Big|_{z=\pm \frac{h}{2}} = 0$. Since the Poisson equation (5.88b) should be satisfied on each horizontal disk⁸, therefore on ($z = \pm \frac{h}{2}$) it actually corresponds to the Laplace equation with homogeneous Neumann boundary conditions which is known to have only constant solutions. However the only constant solution permitted for non-axisymmetric modes due to the regularity constraints is $\hat{\psi}^t \Big|_{z=\pm \frac{h}{2}}(r) = 0$ which is exactly the boundary conditions that $\hat{\psi}^h$ should satisfy. This implication is indicated at the right of equation (5.88b).

$\hat{\phi}^t$:

$$\left[\widehat{g}_{\phi}^t \right]^{j_s} \left[-\epsilon \mathbf{H}_{\lambda - \frac{1}{\epsilon}} \right]^T = 0 \quad ; \quad \left\langle \widehat{g}_{\phi}^t \right\rangle_i = \delta_{i,j_s} \Leftrightarrow \hat{g}_{\phi}^t \Big|_{\partial}(\mathbf{x}'') = \delta(\mathbf{x}'' - \mathbf{x}') \quad (5.89a)$$

$$\left[\widehat{f}_{\phi}^t \right]^{j_s} \left[\mathbf{H}_{\lambda} \right]^T = \left[\widehat{g}_{\phi}^{t*} \right]^{j_s} \quad ; \quad \left\langle \widehat{f}_{\phi}^t \right\rangle_i = 0 \Leftrightarrow \hat{f}_{\phi}^t \Big|_{\partial} = 0 \quad (5.89b)$$

$$\left[\widehat{\phi}^t \right]^{j_s} \left[\mathbf{H}_0 \right]^T = \left[\widehat{f}_{\phi}^{t*} \right]^{j_s} \quad ; \quad \left\langle \widehat{\phi}^t \right\rangle_k = 0 \Leftrightarrow \hat{\phi}^t \Big|_{r=1} = 0 \quad (5.89c)$$

The final solutions $[\hat{\psi}^t]$ and $[\hat{\phi}^t]$ can be obtained from $[\widehat{\psi}^t]^{j_s}$ and $[\widehat{\phi}^t]^{j_s}$ by applying the inverse transformation corresponding to (5.16)

Step 2. The influence matrix can be constructed after or in parallel with construction of the test functions $[\widehat{\psi}^t]^{j_s}$ and $[\widehat{\phi}^t]^{j_s}$. Once a test function is obtained we can evaluate the boundary operators on it. Of course, only those operators which correspond to the boundary conditions

⁸This is because $[\mathbf{H}_0]$ corresponds to Δ_h which does not contain ∂_z^2

that have not already been satisfied for the test functions⁹ must be used for building the influence matrix.

For the axisymmetric modes, these operators are written to the right of the Dirichlet σ -conditions in (5.37a) and (5.38a). In order to exploit the parity properties of the test solutions in z , we will use the even ($s' = e$) and odd ($s' = o$) combinations of the original boundary operators. We will use $\mathcal{B}_{s''}$ as a placeholder for the boundary operators of parity s'' . An operator can be qualified as even if it preserves parity (ex. $[\partial_z^2][f_s] = [(\partial_z^2 f)_s]$) and similarly, an operator can be qualified as odd if it changes the parity of a solution (ex. $[\partial_z][f_s] = [(\partial_z f)_{1-s}]$). In the definitions below, T^{j_s} stands for a test function of parity s corresponding to the j_s 'th test point. We shall employ the following notation to classify the even and odd combinations (identified by s') of boundary values obtained by applying an operator of parity s'' to a test function of parity s :

$$\begin{aligned}\langle \mathcal{B}_{s''} \rangle_{z=\pm\frac{h}{2}}^{s'} T^{j_s}(r, z) &\equiv \frac{(\mathcal{B}_{s''} T^{j_s})|_{z=\frac{h}{2}}(r) + (-1)^{s'} (\mathcal{B}_{s''} T^{j_s})|_{z=-\frac{h}{2}}(r)}{2} \equiv \langle \mathcal{B}_{s''} |^{s'} T \rangle_k^{j_s} \\ \langle \mathcal{B}_{s''} \rangle_{r=1}^{s'} T^{j_s}(r, z) &\equiv \frac{(\mathcal{B}_{s''} T^{j_s})|_{r=1}(z) + (-1)^{s'} (\mathcal{B}_{s''} T^{j_s})|_{r=1}(-z)}{2} \equiv \langle \mathcal{B}_{s''} |^{s'} T \rangle_n^{j_s}\end{aligned}$$

The following rules can be specified for $\langle \mathcal{B}_{s''} |^{s'} T \rangle^{j_s}$ quantities:

$$\begin{aligned}\langle \mathcal{B}_{s'} |^{s'} T \rangle_{n_{1-s}}^{j_s} &= 0 & \langle \mathcal{B}_{s'} |^{1-s'} T \rangle_{n_s}^{j_s} &= 0 \\ \langle \mathcal{B}_{s'} |^{s'} T \rangle_{k_{1-s}}^{j_s} &= 0 & \langle \mathcal{B}_{s'} |^{1-s'} T \rangle_{k_s}^{j_s} &= 0\end{aligned}$$

Using this notation we can write the matrix expression equivalent to (5.79):

$$\begin{aligned}\left\{ \begin{array}{c} [\mathbf{I}_\psi^0]^e \\ [\mathbf{I}_\psi^0]^o \end{array} \right\} &\equiv \left[\frac{\langle \mathbf{1} |^e \hat{\psi}^t \rangle_{n_e}^{j_s}}{\langle \mathbf{1} |^o \hat{\psi}^t \rangle_{n_o}^{j_s}} \right] = \left[\frac{\langle \mathbf{1} \rangle_{z=\pm\frac{h}{2}}^e}{\langle \mathbf{1} \rangle_{z=\pm\frac{h}{2}}^o} \right] \left[\hat{\psi}^t \right]^{j_s} \\ \left\{ \begin{array}{c} [\mathbf{I}_\phi^0]^e \\ [\mathbf{I}_\phi^0]^o \end{array} \right\} &\equiv \left[\frac{\langle \partial_{rz}^2 |^e \hat{\phi}^t \rangle_{k_e}^{j_s}}{\langle \partial_{rz}^2 |^o \hat{\phi}^t \rangle_{k_o}^{j_s}} \right] = \left[\frac{\langle \partial_{rz}^2 \rangle_{r=1}^e}{\langle \partial_{rz}^2 \rangle_{r=1}^o} \right] \left[\hat{\phi}^t \right]^{j_s} \\ &\quad \left[\frac{\langle \partial_z |^e \hat{\phi}^t \rangle_{n_e}^{j_s}}{\langle \partial_z |^o \hat{\phi}^t \rangle_{n_o}^{j_s}} \right] = \left[\frac{\langle \partial_z \rangle_{z=\pm\frac{h}{2}}^e}{\langle \partial_z \rangle_{z=\pm\frac{h}{2}}^o} \right] \left[\hat{\phi}^t \right]^{j_s}\end{aligned}$$

⁹It is necessary that such conditions be satisfied also by the particular solution at each timestep.

The influence matrix for the non-axisymmetric modes has the following structure:

$$[\mathbf{I}]^m \equiv \begin{bmatrix} \mathbf{I}^{m,e} & \\ \hline & \mathbf{I}^{m,o} \end{bmatrix} \equiv \begin{bmatrix} \mathbf{I}_{\psi}^{m,e} & \mathbf{I}_{\phi}^{m,e} & \\ \hline & & \mathbf{I}_{\psi}^{m,o} & \mathbf{I}_{\phi}^{m,o} \end{bmatrix}$$

Step 3. Writing equation (5.82) we have assumed that the inverse $\mathbf{I}^{-1}(\mathbf{x}''; \mathbf{x}')$ of the influence function $\mathbf{I}(\mathbf{x}''; \mathbf{x}')$ exists. In discrete formulation this would mean that for each $m \in [0, \hat{M}]$ the influence matrix $[\mathbf{I}]^m$ is invertible. In fact, this assumption is never met. The influence matrices are singular for several reasons. The first issue is geometric. The finite cylinder has corners at which both conditions, imposed on $(z = \pm \frac{h}{2})$ and $(r = 1)$, must be satisfied simultaneously. Some conditions are therefore redundant. In the situation when the test functions are selected by choosing the δ -conditions at the boundary in the spectral rather than physical space, the redundant conditions correspond to a particular combination of conditions evaluated for all test functions and cannot be easily identified. Moreover, the singularity of the influence matrix can also depend on the restriction of a discrete Poisson solver. Because of the τ -method used for satisfying the boundary conditions at each level of the multi-step solver, some solutions are not accessible or can be linearly dependent.

As an example we consider a test function $[\hat{\psi}^t]^{k_R}$ corresponding to the test point of the highest frequency in the \hat{e}_z direction. Such conditions lead to an intermediate test solution $[\hat{f}_{\psi}^t]^{k_R}$ which contains only the highest coefficients $[\hat{f}_{\psi}^t]_{\hat{K},n}^{k_R}$. These coefficients are replaced by the zero boundary values (τ -method) in the right-hand-side of the equation for $[\hat{\psi}^t]$, which becomes the Laplace equation with homogeneous Dirichlet (for $m = 0$) or Neumann (for $m \neq 0$) boundary conditions. Taking into account the regularity restrictions for the solutions corresponding to $m \neq 0$ we obtain the null solution corresponding to a null column in the influence matrix.

It is also possible that some rows of the influence matrix, corresponding to the highest frequencies evaluated at the boundary, are zero. This can occur when a boundary operator like ∂_z decreases the polynomial order of test functions. The number of null rows is not necessarily equal to the number of null columns, but the number of linearly independent rows is the same as the number of linearly independent columns.

The last class of singularity can be of numerical origin. Some boundary value distributions can be almost linearly dependent which can result in ill-conditioned influence matrix. Also, because some conditions incorporated in the influence matrix are of much higher differential order than others, the structure of the influence matrix is very inhomogeneous and a simple scaling does not necessarily improve the situation. The effect of numerical singularity is that the influence matrix, in addition to zero singular values corresponding to previously described effects, has some number of nearly zero singular values.

A remedy to the problems described above was proposed by Tuckerman [86] and consists of identifying the spurious and weakly (numerically) spurious combinations of test functions by diagonalizing the influence matrix. In this approach, one replaces the zero eigenvalues by an arbitrary value (say 1). The matrix obtained by this arbitrary manipulation of its spectrum becomes invertible. The idea behind this is that the eigenvectors corresponding to the zero eigenvalues play no role in satisfaction of the boundary conditions and can therefore be multiplied by an arbitrary value. This is of course true only under the condition that the linear system of equations defined by the singular matrix and the right-hand-side represents an under-determined problem. This in turn is possible only if the right-hand-side satisfies the compatibility condition (5.4). Because the particular solutions (constructed in step 4) are determined using the same multi-step solver that we used for the test functions and the same boundary operators are used for building the right-hand-side of the influence matrix problem (step 5.), there is *a priori* a good chance that this constructed right-hand-side vector satisfies the compatibility condition.

Step 4. The final solution can be written as the sum of particular and homogeneous solutions $f(\mathbf{x}) = f^p(\mathbf{x}) + f^h(\mathbf{x})$ (see (5.73a)) which can be stated for $\hat{\psi}$ and $\hat{\phi}^m$ as follows

$$\begin{aligned} [\hat{\psi}] &= [\hat{\psi}^p] + [\hat{\psi}^h] \\ [\hat{\phi}] &= [\hat{\phi}^p] + [\hat{\phi}^h] \end{aligned}$$

We will find the particular solution by choosing the homogeneous boundary conditions σ : In the axisymmetric case $m = 0$ we will choose $\hat{\sigma}_{g\phi} = 0$ in (5.37) and (5.38) and for other modes $m \neq 0$ we will set $\hat{\sigma}_{f\psi} = 0$ in (5.49) and (5.50). Thus the systems which one must solve for each m and λ in order to obtain the particular solution, in matrix notation will have the following form:

Axisymmetric case $m = 0$:

$\hat{\psi}^p$:

$$\overline{[\hat{f}_\psi^p]} \overline{[-\epsilon \mathbf{H}_{\lambda - \frac{1}{\epsilon}}]}^T = \overline{[rhs_\psi^*]} ; \left\{ \begin{array}{l} \langle \hat{f}_\psi^p \rangle_n = 0 \Leftrightarrow \hat{f}_\psi^p|_{z=\pm \frac{h}{2}} = 0 \\ \langle [\hat{f}_\psi^p] [\int_0^1 r dr]^T \rangle_k = 0 \Leftrightarrow \int_0^1 \hat{f}_\psi^p r dr = 0 \end{array} \right. \quad (5.91a)$$

$$\overline{[\hat{\psi}^p]} \overline{[\mathbf{H}_0]}^T = \overline{[\hat{f}_\psi^{p*}]} ; \langle \hat{\psi}^p \rangle_k = 0 \Leftrightarrow \hat{\psi}^p|_{r=0} = 0 \quad (5.91b)$$

$\hat{\phi}^p$:

$$\widetilde{[\hat{\mathcal{G}}_\phi^p]} \overline{[-\epsilon \mathbf{H}_{\lambda-\frac{1}{\epsilon}}]}^T = \overline{[\widehat{rhs}_\phi^*]} \quad ; \quad \langle \hat{\mathcal{G}}_\phi^p \rangle_i = 0 \Leftrightarrow \hat{\mathcal{G}}_\phi^p|_\partial = 0 \quad (5.92a)$$

$$\widetilde{[\hat{f}_\phi^p]} \overline{[\mathbf{H}_\lambda]}^T = \overline{[\hat{\mathcal{G}}_\phi^{p*}]} \quad ; \quad \langle \hat{f}_\phi^p \rangle_i = 0 \Leftrightarrow \hat{f}_\phi^p|_\partial = 0 \quad (5.92b)$$

$$\widetilde{[\hat{\phi}^p]} \overline{[\mathbf{H}_0]}^T = \overline{[\hat{f}_\phi^{p*}]} \quad ; \quad \langle \hat{\phi}^p \rangle_k = 0 \Leftrightarrow \hat{\phi}^p|_{r=1} = 0 \quad (5.92c)$$

Non-axisymmetric cases $m \neq 0$: $\hat{\psi}^p$:

$$\widetilde{[\hat{f}_\psi^p]} \overline{[-\epsilon \mathbf{H}_{\lambda-\frac{1}{\epsilon}}]}^T = \overline{[\widehat{rhs}_\psi^*]} \quad ; \quad \langle \hat{f}_\psi^p \rangle_i = 0 \Leftrightarrow \hat{f}_\psi^p|_\partial = 0 \quad (5.93a)$$

$$\widetilde{[\hat{\psi}^p]} \overline{[\mathbf{H}_0]}^T = \overline{[\hat{f}_\psi^{p*}]} \quad ; \quad \langle [\hat{\psi}^p] [\partial_r]^T \rangle_k = 0 \Leftrightarrow \begin{cases} \partial_r \hat{\psi}^p|_{r=1} = 0 \\ \downarrow \\ \hat{\psi}^p|_{z=\pm\frac{h}{2}} = 0 \end{cases} \quad (5.93b)$$

 $\hat{\phi}^p$:

$$\widetilde{[\hat{\mathcal{G}}_\phi^p]} \overline{[-\epsilon \mathbf{H}_{\lambda-\frac{1}{\epsilon}}]}^T = \overline{[\widehat{rhs}_\phi^*]} \quad ; \quad \langle \hat{\mathcal{G}}_\phi^p \rangle_i = 0 \Leftrightarrow \hat{\mathcal{G}}_\phi^p|_\partial = 0 \quad (5.94a)$$

$$\widetilde{[\hat{f}_\phi^p]} \overline{[\mathbf{H}_\lambda]}^T = \overline{[\hat{\mathcal{G}}_\phi^{p*}]} \quad ; \quad \langle \hat{f}_\phi^p \rangle_i = 0 \Leftrightarrow \hat{f}_\phi^p|_\partial = 0 \quad (5.94b)$$

$$\widetilde{[\hat{\phi}^p]} \overline{[\mathbf{H}_0]}^T = \overline{[\hat{f}_\phi^{p*}]} \quad ; \quad \langle \hat{\phi}^p \rangle_k = 0 \Leftrightarrow \hat{\phi}^p|_{r=1} = 0 \quad (5.94c)$$

The final solutions $[\hat{\psi}^p]$ and $[\hat{\phi}^p]$ can be obtained from $[\widehat{\psi}^p]$ and $[\widehat{\phi}^p]$ by applying the inverse transformation corresponding to (5.16).

Step 5. In order to obtain σ from (5.83) it is necessary to evaluate at each time step the difference between the boundary condition values obtained for the particular solution f^p and their desired values β . Using notation from step 2, we can write the vector corresponding to the expression $-\mathcal{B}f^p|_{x'} + \beta(x')$ in the following way:

Axisymmetric modes:

$$\left\{ \begin{array}{l} [Rhs_\psi^0]^e \\ [Rhs_\psi^0]^o \end{array} \right\} \equiv \frac{\left\langle \left(\int_0^r r \hat{\Omega}(r) dr \right) \Big| \begin{array}{l} e \\ o \end{array} - \mathbb{1} \Big| \hat{\psi}^p \right\rangle_{n_e}}{\left\langle \left(\int_0^r r \hat{\Omega}(r) dr \right) \Big| \begin{array}{l} e \\ o \end{array} - \mathbb{1} \Big| \hat{\psi}^p \right\rangle_{n_o}}$$

$$\left\{ \begin{array}{l} [Rhs_\phi^0]^e \\ [Rhs_\phi^0]^o \end{array} \right\} \equiv \frac{\left\langle -\partial_{rz}^2 \Big| \begin{array}{l} e \\ o \end{array} \hat{\phi}^p \right\rangle_{k_e}^{j_s}}{\left\langle -\partial_z \Big| \begin{array}{l} e \\ o \end{array} \hat{\phi}^p \right\rangle_{n_e}^{j_s}} \quad , \quad [Rhs]^0 \equiv \begin{array}{l} [Rhs_\psi^{0,e}] \\ [Rhs_\psi^{0,o}] \\ [Rhs_\phi^{0,e}] \\ [Rhs_\phi^{0,o}] \end{array}$$

Non-axisymmetric modes:

$$[Rhs]^m \equiv \begin{array}{l} [Rhs^{m,e}] \\ [Rhs^{m,o}] \end{array} \equiv \begin{array}{l} \frac{\left\langle -im \Big| \begin{array}{l} e \\ o \end{array} \hat{\psi}^p - \partial_{rz}^2 \Big| \begin{array}{l} e \\ o \end{array} \hat{\phi}^p \right\rangle_{k_e}}{\left\langle -\partial_{rz}^2 \Big| \begin{array}{l} e \\ o \end{array} \hat{f}_\psi^p + im\Delta \Big| \begin{array}{l} e \\ o \end{array} \hat{f}_\phi^p \right\rangle_{k_e}} \\ \frac{\left\langle -\partial_z \Big| \begin{array}{l} e \\ o \end{array} \hat{\phi}^p \right\rangle_{n_e}}{\left\langle -im \Big| \begin{array}{l} e \\ o \end{array} \hat{\psi}^p - \partial_{rz}^2 \Big| \begin{array}{l} e \\ o \end{array} \hat{\phi}^p \right\rangle_{k_o}} \\ \frac{\left\langle -\partial_{rz}^2 \Big| \begin{array}{l} e \\ o \end{array} \hat{f}_\psi^p + im\Delta \Big| \begin{array}{l} e \\ o \end{array} \hat{f}_\phi^p \right\rangle_{k_o}}{\left\langle -\partial_z \Big| \begin{array}{l} e \\ o \end{array} \hat{\phi}^p \right\rangle_{n_o}} \end{array}$$

Step 6. The boundary values $\hat{\sigma}_{f_\psi}$ and $\hat{\sigma}_{g_\phi}$ needed to solve (5.37), (5.38), (5.49) and (5.50) can be found by solving the following linear systems:

For the axisymmetric mode:

$$\begin{bmatrix} \mathbf{I}_\psi^{0,e} & & & \\ & \mathbf{I}_\psi^{0,o} & & \\ \hline & & \mathbf{I}_\phi^{0,e} & \\ & & & \mathbf{I}_\phi^{0,o} \end{bmatrix} \begin{bmatrix} \hat{\sigma}_{f_\psi}^{0,e} \\ \hat{\sigma}_{f_\psi}^{0,o} \\ \hat{\sigma}_{f_\psi}^{0,e} \\ \hat{\sigma}_{f_\psi}^{0,o} \end{bmatrix} = \begin{bmatrix} Rhs_\psi^{0,e} \\ Rhs_\psi^{0,o} \\ Rhs_\phi^{0,e} \\ Rhs_\phi^{0,o} \end{bmatrix} \quad (5.95)$$

For non-axisymmetric modes:

$$\begin{bmatrix} \mathbf{I}_\psi^{m,e} & \mathbf{I}_\phi^{m,e} & & \\ \hline & & \mathbf{I}_\psi^{m,o} & \mathbf{I}_\phi^{m,o} \end{bmatrix} \begin{bmatrix} \hat{\sigma}_{f_\psi}^{m,e} \\ \hat{\sigma}_{g_\phi}^{m,o} \\ \hat{\sigma}_{f_\psi}^{m,o} \\ \hat{\sigma}_{g_\phi}^{m,e} \end{bmatrix} = \begin{bmatrix} Rhs^{m,e} \\ \\ Rhs^{m,o} \\ \end{bmatrix} \quad (5.96)$$

Step 7. Finally the solutions $\hat{\psi}$ and $\hat{\phi}$ can be found by solving (5.37), (5.38), (5.49) and (5.50) with σ_{f_ψ} and σ_{g_ϕ} obtained in step 5.

Axisymmetric case $m = 0$:

$\hat{\psi}$:

$$\widetilde{[\hat{f}_\psi]} \overline{[-\epsilon \mathbf{H}_{\lambda-\frac{1}{\epsilon}}]}^T = \overline{[rhs_\psi^*]} ; \begin{cases} \langle \hat{f}_\psi \rangle_n = [\hat{\sigma}_{f_\psi}] \Leftrightarrow \hat{f}_\psi|_{z=\pm\frac{h}{2}} = \hat{\sigma}_{f_\psi} \\ \langle [\hat{f}_\psi] [\int_0^1 r dr]^T \rangle_k = 0 \Leftrightarrow \int_0^1 \hat{f}_\psi r dr = 0 \end{cases} \quad (5.97a)$$

$$\widetilde{[\hat{\psi}]} [\mathbf{H}]^T = \overline{[\hat{f}_\psi^*]} ; \langle \hat{\psi} \rangle_k = 0 \Leftrightarrow \hat{\psi}|_{r=0} = 0 \quad (5.97b)$$

$\hat{\phi}$:

$$\widetilde{[\hat{g}_\phi]} \overline{[-\epsilon \mathbf{H}_{\lambda-\frac{1}{\epsilon}}]}^T = \overline{[rhs_\phi^*]} ; \langle \hat{g}_\phi \rangle_i = [\hat{\sigma}_{g_\phi}] \Leftrightarrow \hat{g}_\phi|_{\partial} = \hat{\sigma}_{g_\phi} \quad (5.98a)$$

$$\widetilde{[\hat{f}_\phi]} [\mathbf{H}_\lambda]^T = \overline{[\hat{g}_\phi^*]} ; \langle \hat{f}_\phi \rangle_i = 0 \Leftrightarrow \hat{f}_\phi|_{\partial} = 0 \quad (5.98b)$$

$$\widetilde{[\hat{\phi}]} [\mathbf{H}]^T = \overline{[\hat{f}_\phi^*]} ; \langle \hat{\phi} \rangle_k = 0 \Leftrightarrow \hat{\phi}|_{r=1} = 0 \quad (5.98c)$$

Non-axisymmetric cases $m \neq 0$:

$\hat{\psi}$:

$$\widetilde{[\hat{f}_\psi]} \overline{[-\epsilon \mathbf{H}_{\lambda - \frac{1}{\epsilon}}]}^T = \overline{[\widehat{rhs}_\psi^*]} \quad ; \quad \langle \hat{f}_\psi \rangle_i = [\hat{\sigma}_{f_\psi}] \Leftrightarrow \hat{f}_\psi|_\partial = \hat{\sigma}_{f_\psi} \quad (5.99a)$$

$$\widetilde{[\hat{\psi}]} \overline{[\mathbf{H}]}^T = \overline{[\hat{f}_\psi^*]} \quad ; \quad \langle [\hat{\psi}] [\partial_r]^T \rangle_k = 0 \Leftrightarrow \begin{cases} \partial_r \hat{\psi}|_{r=1} = 0 \\ \downarrow \\ \hat{\psi}|_{z=\pm \frac{h}{2}} = 0 \end{cases} \quad (5.99b)$$

$\hat{\phi}$:

$$\widetilde{[\hat{g}_\phi]} \overline{[-\epsilon \mathbf{H}_{\lambda - \frac{1}{\epsilon}}]}^T = \overline{[\widehat{rhs}_\phi^*]} \quad ; \quad \langle \hat{g}_\phi \rangle_i = [\hat{\sigma}_{g_\phi}] \Leftrightarrow \hat{g}_\phi|_\partial = \hat{\sigma}_{g_\phi} \quad (5.100a)$$

$$\widetilde{[\hat{f}_\phi]} \overline{[\mathbf{H}_\lambda]}^T = \overline{[\hat{g}_\phi^*]} \quad ; \quad \langle \hat{f}_\phi \rangle_i = 0 \quad \Leftrightarrow \hat{f}_\phi|_\partial = 0 \quad (5.100b)$$

$$\widetilde{[\hat{\phi}]} \overline{[\mathbf{H}]}^T = \overline{[\hat{f}_\phi^*]} \quad ; \quad \langle \hat{\phi} \rangle_k = 0 \quad \Leftrightarrow \hat{\phi}|_{r=1} = 0 \quad (5.100c)$$

The final solutions $[\hat{\psi}]$ and $[\hat{\phi}]$ can be obtained from $\widetilde{[\hat{\psi}]}$ and $\widetilde{[\hat{\phi}]}$ by applying the inverse transformation corresponding to (5.16).

5.4.3 Towards an invertible influence matrix

Discussing the singular character of the influence matrix in the preceding section we mentioned that, according to Tuckerman [86] its inverse matrix can be diagonalized in order to identify the spurious modes corresponding to the zero (or almost zero) eigenvalues satisfying $\{\mu_i < \epsilon_\mu\}$. The threshold parameter ϵ_μ must be tuned experimentally. The singular eigenvectors, for a problem with the right-hand-sides given by (5.95)-(5.96) satisfying the compatibility condition (5.4), have no influence on the satisfaction of the boundary conditions incorporated in the influence matrix. Therefore, the zero eigenvalues can be replaced by arbitrary but non-zero values and then the inverse matrix can be obtained from the reciprocals of its corrected

spectrum $\{\mu^*\}$:

$$\begin{aligned} [\mathbf{I}] &= [\mathbf{W}] [\delta_{j,i}\mu_i] [\mathbf{W}]^{-1} \longrightarrow [\mathbf{W}] [\delta_{j,i}\mu_i^*] [\mathbf{W}]^{-1} = [\mathbf{I}^*] \\ \text{where } \mu_i^* &= \begin{cases} 1 & \text{if } |\mu_i| < \epsilon_\mu \\ \mu_i & \text{otherwise} \end{cases} \\ &\downarrow \\ [\mathbf{I}^*]^{-1} &= [\mathbf{W}] \begin{bmatrix} \delta_{j,i} \\ \mu_i^* \end{bmatrix} [\mathbf{W}]^{-1} \end{aligned} \quad (5.101)$$

where $[\mathbf{W}]$ is the diagonalizing matrix. Two conditions are necessary for this method to work:

- The influence matrix must be diagonalizable – a condition necessary for the existence of the regular matrix $[\mathbf{W}]$
- The eigenvalues satisfying $\mu_i < \epsilon_\mu$, corresponding to the spurious modes, must be clearly distinguishable from the other ones. This means that the difference between the smallest valid eigenvalues and the largest spurious eigenvalues must be much bigger than the difference between one small valid eigenvalue and another.

As an example let us consider the influence matrix corresponding to $m = 1$ and to the spatial resolution $(N = 96) \times (K = 192)$. The Reynolds number is $Re = 10000$ and the time step $\Delta t = 0.01$, which corresponds to $\epsilon^{-1} = \frac{Re}{\Delta t} = 10^6$. The magnitudes of the eigenvalues of the even block $[\mathbf{I}^{1,e}]$ of matrix $[\mathbf{I}^1]$ are presented on figure 5.1-left. It is not obvious how many singular values

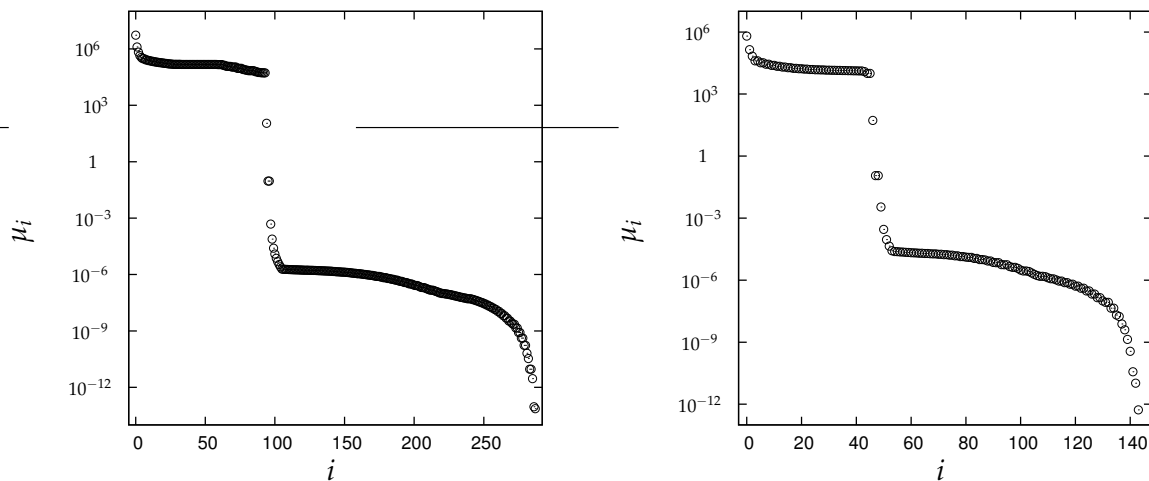


Figure 5.1: Magnitudes of eigenvalues $\{|\mu_i|\}$ of $[\mathbf{I}^{1,e}]$ ($m = 1$). Left: $(N = 96) \times (K = 192)$, $\epsilon^{-1} = \frac{Re}{\Delta t} = 10^6$; Right: $(N = 48) \times (K = 96)$, $\epsilon^{-1} = \frac{Re}{\Delta t} = 10^4$.

should be considered as spurious. One can propose the last two values 0.91×10^{-13} , $.72 \times 10^{-13}$ as they are the smallest ones and are both of the same order of magnitude. The problem is, however, more difficult: the same analysis performed for a different resolution $(N = 48) \times (K = 96)$ suggests that only the last singular eigenvalue may be considered spurious (see figure 5.1-right). The number of the spurious eigenvalues of the influence matrix should not depend

on the spectral resolution. It depends only on the geometry and on the kind of boundary conditions. The number of weakly spurious eigenvalues which appear in consequence of the finite machine accuracy can, however, differ from one resolution to another. Tests performed for several resolutions, modes m and values of ϵ^{-1} showed that the number of distinguishable spurious eigenvalues can vary from 1, for low spectral resolutions and small values of ϵ^{-1} , up to 4, for high resolutions or very big values of ϵ^{-1} .

Since the low-resolution problems are less susceptible to the numerical inaccuracy and do not suffer from weakly spurious modes, one can try to correct the same number of eigenvalues for all resolutions: e.g. if for a given mode m and for a low resolution only one spurious eigenvalue can be identified, then for all resolutions for this mode the smallest eigenvalue should be considered spurious. This approach leads, however, to an unstable solver, which for high resolutions suffers from high-frequency oscillations degrading the smoothness of the solution and affecting the stability of a time integration scheme. Trying to decrease the time step amplifies even more the weakly spurious modes by increasing the condition number of the influence matrix.

The number of lost meaningful digits in a numerical solution to a linear system defined by a matrix is approximately proportional to the decimal logarithm of its condition number. The eigenvalues presented on figure 5.1 correspond to a matrix with condition number $\mathcal{C}_{I^*} \equiv \frac{\max\{\mu_i^*\}}{\min\{\mu_i^*\}} \approx 10^{17}$ when the two smallest eigenvalues are set to 1. This means that the inverse matrix $[\mathbf{I}^{1,e}]$ can be significantly perturbed even by a numerical noise of order $O(10^{-15})$. It seems therefore necessary to choose the threshold parameter ϵ_μ in order to guarantee a reasonable conditioning of the influence matrix and not only to cut off the distinguishable eigenvalues/eigenmodes. This criterion was also adopted by Tuckerman [86] and Speetjens [81].

On the other hand, treating an increasing number of small eigenvalues as spurious as the resolution is increased leads to errors in satisfaction of the boundary conditions. If only one condition is incorporated in the influence matrix method, and if this condition is evaluated only on a single type of test function then there exists a simple interpretation of the weakly spurious modes and eigenvalues: if an eigenvalue becomes, for high resolutions, smaller than a threshold of acceptable matrix conditioning, then the corresponding mode plays almost no role in satisfaction of the boundary condition under the given machine accuracy. This does not necessarily mean that the system has lost some degrees of freedom, but rather that these degrees of freedom cannot be fixed by the test functions used for constructing the influence matrix. When more than one condition must be satisfied by the influence matrix method and different classes of test functions are used to build the matrix, then weakly spurious eigenvalues can appear because of bad scaling of the influence matrix. If this is the case, then even if a linear combination of the test functions satisfying all boundary conditions exists, it can be impossible to find by solving the linear system defined by the influence matrix. Speetjens [81] observed that for an *a priori* known (from analytic solution) distribution of the boundary values (corresponding to σ in (5.71)) the correct solution can be found by the solver for virtually all resolutions and values of ϵ^{-1} . If the influence matrix technique is used instead, the solver becomes conditionally stable with upper bound for ϵ^{-1} depending on the spectrum of the influence matrix and with the lower bound given by the CFL condition for the explicitly time-evolved nonlinear term. Our observations confirm those of Speetjens [81]. For example, for

resolution $(M = 8) \times (N = 48) \times (K = 96)$ the time integration of Stokes equation, performed using the first-order implicit Euler scheme, diverges for $\epsilon^{-1} > 10^5$ and $m > 0$. The axisymmetric mode $m = 0$ converges for all values of ϵ^{-1} . Our explanation for this is that the influence matrix for the axisymmetric mode $m = 0$ decouples the poloidal and toroidal test functions evaluating a single type of boundary condition per single type of test function (angular velocity at $z = \pm \frac{h}{2}$ on $\hat{\psi}^t$ and normal velocity on $\hat{\phi}^t$). In this situation, the argument that weakly spurious modes play no role in satisfaction of the boundary conditions is valid. For $m > 0$ all test functions are coupled via boundary conditions of different nature (e.g. compatibility condition). This leads to a very bad scaling of the influence matrix. Additionally we observed that for high resolutions the influence matrix for $m > 0$ is very poorly diagonalizable. This means that the diagonalization matrix $[\mathbf{W}]$ is very ill-conditioned for the inversion. We verified that some of the column vectors building $[\mathbf{W}]$ are almost linearly dependent.

Diagonalization vs SVD

We propose a slight modification to the procedure proposed by Tuckerman [86] consisting of replacing the diagonalization of the influence matrix by its singular value decomposition (SVD). The singular matrix can be regularized using the SVD by performing steps analogous to those from (5.101):

$$\begin{aligned}
 [\mathbf{I}] &= [\mathbf{U}] [\delta_{j,i} \gamma_i] [\mathbf{V}]^T \longrightarrow [\mathbf{U}] [\delta_{j,i} \gamma_i^*] [\mathbf{V}]^T = [\mathbf{I}^*] \\
 \text{where } \gamma_i^* &= \begin{cases} 1 & \text{if } |\gamma_i| < \epsilon_\gamma \\ \gamma_i & \text{otherwise} \end{cases} \\
 &\Downarrow \\
 [\mathbf{I}^*]^{-1} &= [\mathbf{V}] \begin{bmatrix} \delta_{j,i} \\ \gamma_i^* \end{bmatrix} [\mathbf{U}]^T
 \end{aligned} \tag{5.102}$$

where $[\mathbf{U}]$ and $[\mathbf{V}]$ are orthogonal matrices and $\{\gamma_i\}$ are the singular values which are real and positive.

The first thing to notice is that the process (5.102) makes use of the orthogonality of $[\mathbf{U}]$ and $[\mathbf{V}]$ i.e. $[\mathbf{U}]^{-1} = [\mathbf{U}]^T$ and $[\mathbf{V}]^{-1} = [\mathbf{V}]^T$. The singular value decomposition, in contrast to the eigenvalue decomposition, exists for all matrices (even those which are not diagonalizable) and is better conditioned than the diagonalization of a general matrix. On figure 5.2-left we present the singular values of the matrix for which norms of eigenvalues are presented on figure 5.1-left. It can be seen on figure 5.2-left that smallest singular value is better separated from the others than for eigenvalues (see fig. 5.1-left). The condition number of the influence matrix $[\mathbf{I}^*]$ regularized by correcting its last eigenvalue is, however, still very big: $\mathcal{C}_{I^*} \approx 10^{20}$. The main advantage of the SVD over diagonalization resides in the ability to apply it even to a very poorly diagonalizable matrices.

Scaling

The matrix condition number can be decreased by scaling. If scaling is performed by dividing each row by its norm, the condition number of the matrix can be significantly reduced, down to

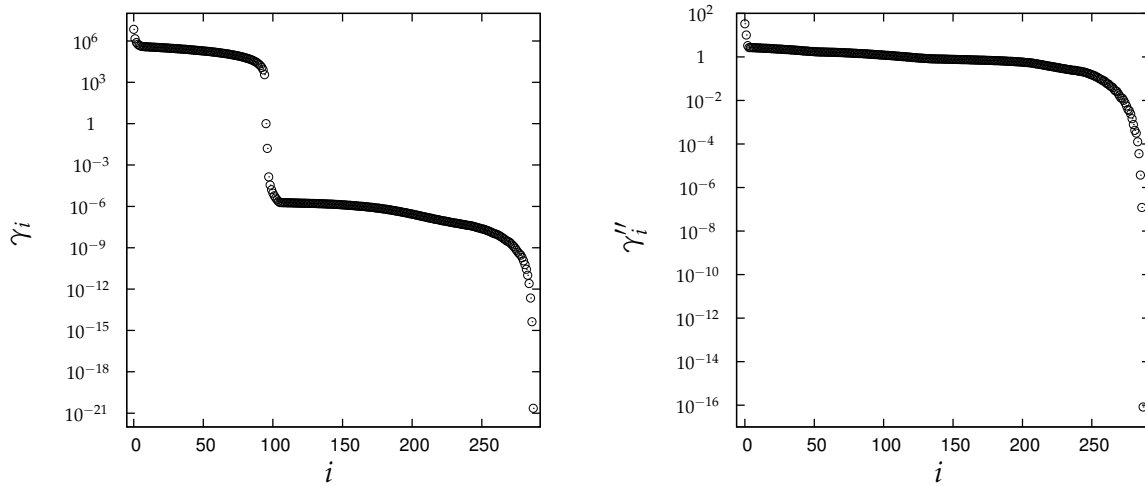


Figure 5.2: Singular values $\{\gamma_i\}$ ($\epsilon^{-1} = \frac{Re}{\Delta t} = 10^6$, $m = 1$, $(N = 96) \times (K = 192)$). Left: actual matrix $[\mathbf{I}^{1,e}]$. Right: scaled matrix $[\mathbf{I}^{1,e}]'' \equiv [\boldsymbol{\alpha}] [\mathbf{I}^{1,e}] [\boldsymbol{\beta}]$.

$\mathcal{C} = 10^{11}$. Additional scaling of columns does not significantly changes the condition number.

Further enhancing of the influence matrix is possible by scaling matrix blocks corresponding to different combinations of types of test functions and boundary conditions. The influence matrices $[\mathbf{I}^{p,m}]$ for $m > 0$ have 9 characteristic blocks corresponding to combinations of 3 classes of test functions ($\hat{\psi}^t$ and $\hat{\phi}^t$ selected for delta-type conditions at $r = 1$ and $\hat{\phi}^t$ selected for delta-type conditions at $z = \pm \frac{h}{2}$) and 3 different boundary conditions. The matrix norms b_{ji} of each of the blocks are:

$$[\mathbf{I}^{1,e}] = \begin{bmatrix} b_{11} = 10^7 & b_{12} = 1 & b_{13} = 1 \\ b_{21} = 10^{-2} & b_{22} = 10^{-5} & b_{23} = 10^{-5} \\ b_{31} = 0 & b_{32} = 10^{-5} & b_{33} = 10^{-4} \end{bmatrix} \quad (5.103)$$

The numbers were determined for the influence matrix corresponding to the resolution $(N = 96) \times (K = 192)$ and were provided to give a qualitative idea about differences between norms of different matrix blocks. We now wish to scale the block-rows and block-columns in such a way as to make the norms of the resulting scaled blocks b'_{ji} equal to one another.

$$[\boldsymbol{\alpha}] [\mathbf{I}^{p,m}] [\boldsymbol{\beta}] = \begin{bmatrix} \alpha_1 & 0 & 0 \\ 0 & \alpha_2 & 0 \\ 0 & 0 & \alpha_3 \end{bmatrix} \begin{bmatrix} b_{11} & b_{12} & b_{13} \\ b_{21} & b_{22} & b_{23} \\ 0 & b_{32} & b_{33} \end{bmatrix} \begin{bmatrix} \beta_1 & 0 & 0 \\ 0 & \beta_2 & 0 \\ 0 & 0 & \beta_3 \end{bmatrix} = \begin{bmatrix} b'_{11} & b'_{12} & b'_{13} \\ b'_{21} & b'_{22} & b'_{23} \\ 0 & b'_{32} & b'_{33} \end{bmatrix} \quad (5.104)$$

In general there exist no such $\{\alpha_i\}$ and $\{\beta_i\}$ satisfying $b_{11} = b_{12} = b_{13} = b_{21} = b_{22} = b_{23} = b_{32} = b_{33} = 1$. We can instead require

$$\begin{aligned}\alpha_1\beta_1b_{11} &= \alpha_2\beta_2b_{22} = \alpha_3\beta_3b_{33} = 1 \\ \alpha_2\beta_1b_{21} &= \alpha_1\beta_2b_{12} \\ \alpha_3\beta_1b_{31} &= \alpha_1\beta_3b_{13}\end{aligned}\tag{5.105}$$

The system (5.105) has an infinite number of possible solutions, from which we can select the following:

$$\begin{aligned}\alpha_1 &= \sqrt{\frac{b_{21}b_{32}b_{33}}{b_{11}b_{12}b_{23}}} & \alpha_2 &= \sqrt{\frac{b_{32}b_{33}}{b_{22}b_{23}}} & \alpha_3 &= 1 \\ \beta_1 &= \sqrt{\frac{b_{11}b_{23}}{b_{11}b_{21}b_{32}b_{33}}} & \beta_2 &= \sqrt{\frac{b_{23}}{b_{22}b_{32}b_{33}}} & \beta_3 &= \frac{1}{b_{33}}\end{aligned}\tag{5.106}$$

The influence matrix $[\mathbf{I}^{1,e}]$ scaled using (5.106) has the following structure:

$$[\mathbf{I}^{1,e}]' = \begin{bmatrix} b'_{11} = 1 & b'_{12} = 10^{-2} & b'_{13} = 10^{-2} \\ b'_{21} = 10^{-2} & b'_{22} = 1 & b'_{23} = 1 \\ b'_{31} = 0 & b'_{32} = 1 & b'_{33} = 1 \end{bmatrix}$$

and the condition number $C'_I \approx 10^{11}$. This condition number is the same as for a simple row or column scaling. However, if the block scaling is followed by row scaling, then the condition number obtained after correcting only the smallest singular value is further decreased down to $C''_I \approx 10^8$. The singular values of matrix $[\mathbf{I}^{1,e}]''$ scaled in this way are presented on figure 5.2-right. The condition number of each block of the influence matrix corresponding to $m = 0$ can be decreased by scaling its rows only.

Conclusions

The regularization of the influence matrix performed using SVD preceded by the scaling of the matrix blocks and rows¹¹ makes it possible to use the influence matrix method for high resolutions (e.g. $(M = 128) \times (K = 192) \times (N = 96)$). The same threshold for the condition number of the influence number can be used for all resolutions and values of ϵ^{-1} . This threshold was fixed in our numerical code to $C''_I < 10^{10}$, which means that all singular values γ''_s for

¹¹The order in which the scaling is performed is important: first the block-scaling and then the row scaling.

type of matrix	number of spurious values
$\left[\mathbf{I}_{\psi}^{0,p} \right]''$	2
$\left[\mathbf{I}_{\phi}^{0,p} \right]''$	3
$\left[\mathbf{I}^{0 < m < \lfloor \frac{M}{2} \rfloor, p} \right]''$	1
$\left[\mathbf{I}^{\lfloor \frac{M}{2} \rfloor, e} \right]''$	4
$\left[\mathbf{I}^{\lfloor \frac{M}{2} \rfloor, o} \right]''$	3

Table 5.1: Number of spurious modes for different types of matrix blocks building the scaled influence matrices $[\mathbf{I}^{m,p}]''$.

which $\frac{\max_i |\gamma_i''|}{\gamma_s''} \geq 10^{10}$ are treated as spurious or weakly spurious are set to an arbitrary non-zero value. The number of spurious modes identified does not depend on the spectral resolution. The influence matrices corresponding to the Fourier modes $m = 0$ and $m = \lfloor M/2 \rfloor$ have different number of spurious singular values. This is because their structures differ from those of the matrices corresponding to $0 < m < \lfloor M/2 \rfloor$. Table 5.4.3 presents numbers of spurious modes that can be identified for the different types of blocks comprising the influence matrices.

5.5 Tests - Stokes problem in 2D

In this section we present the validation of the implicit solver presented throughout this chapter. In order to isolate properties of the spectral solver from the specific problems concerning evaluation of the nonlinear term we consider the Stokes problem corresponding to equations (5.27) for which we choose $\mathbf{s} = 0$ (see definition of \mathbf{s} in (3.49c)). This methodology not only makes it possible to test the spectral solver independently from the pseudo spectral algorithm for evaluation of the nonlinear terms, but, in addition, the numerical solution can be compared against an analytic solution calculated for the linear problem. Let us consider a single step of an implicit, first-order Euler scheme, for a discrete time integration:

$$E\Delta_h\psi(t_{n+1}) = \underbrace{\Delta_h\psi(t_n)}_{rhs_{\psi}} \quad (5.107a)$$

$$E\Delta\Delta_h\phi(t_{n+1}) = \underbrace{\Delta\Delta_h\phi(t_n)}_{rhs_{\phi}} \quad (5.107b)$$

We are interested in finding an analytic polynomial solution corresponding to a single step of the iteration (5.107) assuming that rhs_{ψ} and rhs_{ϕ} can be considered independent of $\psi(t_{n+1})$ and $\phi(t_{n+1})$. With this assumption, rhs_{ψ} and rhs_{ϕ} no longer define a Stokes problem, but on the other hand, a polynomial solution to (5.107) can then exist.

5.5.1 Polynomial solutions

In order to (5.107) has a polynomial solution in addition to the boundary conditions (3.50)-(3.51) some additional, but not explicitly known, conditions must be satisfied by both the solution (ψ, ϕ) and the right-hand-side (rhs_ψ, rhs_ϕ) . To solve this problem a symbolic algorithm implemented in MapleTM was developed. The general idea is to treat the solution (ψ, ϕ) , as well as the the right-hand-side (rhs_ψ, rhs_ϕ) , as unknown functions having more degrees of freedom that it would be normally necessary for satisfaction of the equation (5.107) and the boundary conditions. The additional degrees of freedom of such an under-determined problem can be used for selecting the polynomial solution. We will present briefly this algorithm.

If the Fourier transform is applied to (5.107) then the solution can be found separately for each azimuthal mode. Let $\hat{\psi}_{poly} \equiv \hat{\psi}_{poly}^m(r, z)$, $\hat{\phi}_{poly} \equiv \hat{\phi}_{poly}^m(r, z)$ denote reference polynomial solutions corresponding to the Fourier mode m and satisfying (5.107) with the right hand sides $\widehat{rhs}_\psi^{poly}$, $\widehat{rhs}_\phi^{poly}$. We represent $\{\hat{\psi}_{poly}, \hat{\phi}_{poly}, \widehat{rhs}_\psi^{poly}, \widehat{rhs}_\phi^{poly}, \Omega_\pm^{poly}\}$ as monomial series of order $O(z^K r^{2N+m})$.

$$\begin{aligned} \hat{\psi}_{poly}(r, z) &= \sum_{n=0}^N \sum_{k=0}^K a_{kn} z^k r^{2n+m}, & \hat{\phi}_{poly}(r, z) &= \sum_{n=0}^N \sum_{k=0}^K b_{kn} z^k r^{2n+m} \\ \widehat{rhs}_\psi^{poly}(r, z) &= \sum_{n=0}^N \sum_{k=0}^K c_{kn} z^k r^{2n+m}, & \widehat{rhs}_\phi^{poly}(r, z) &= \sum_{n=0}^N \sum_{k=0}^K d_{kn} z^k r^{2n+m} \\ \Omega_+^{poly} &= -\Omega_-^{poly} = \sum_{n=0}^N e_n r^{2n+m} \end{aligned} \quad (5.108)$$

All these polynomials together represent a system of $4(N+1)(K+3)$ degrees of freedom. We expect that for sufficiently large N and K there exists a combination of $\{a_{kn}, b_{kn}, c_{kn}, d_{kn}, e_n\}$ for which functions (5.108) satisfy both the equations and the boundary conditions. After substituting (5.108) into (5.107) we obtain the underdetermined linear system of $2(N+1)(K+1)$ equations. Solving such a system produces a new reduced set of unfixed coefficients. Some of these free coefficients can be fixed by imposing on system $(\hat{\psi}_{poly}, \hat{\phi}_{poly}, \widehat{rhs}_\psi^{poly}, \widehat{rhs}_\phi^{poly}, \Omega_\pm^{poly})$ the boundary conditions. Finally, a solution satisfying both the equations and the boundary conditions can be identified. Such a solution can still have several degrees of freedom which can be fixed so as to limit, for instance, their polynomial order or to impose a particular symmetry. We are mainly interested in fixing a non-

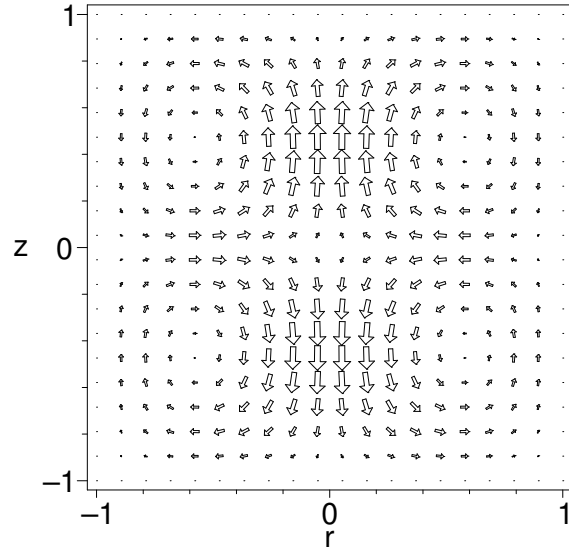


Figure 5.3: Axisymmetric mode $m = 0$. Poloidal component of the velocity $(\hat{u}_r^{poly}, \hat{u}_z^{poly})$.

trivial solution containing several frequencies and corresponding to a possibly realistic profile Ω_{\pm} . Here we present an example set of polynomials found for the axisymmetric mode ($m = 0$) by requiring $\Omega_{\pm}^{poly} = \pm(1 - r^6)$. The available degrees of freedom have been fixed in order to obtain a flow having two recirculation rolls separated by the mid-plane $z = 0$.

$$\hat{\psi}_{poly}(r, z) = \frac{1}{64}z(-30z^2 + 33z^4 + 5)r^8 - \frac{5}{48}z(z-1)(z+1)(5z^2-1)r^6 - \frac{1}{2}z^5r^2 \quad (5.109a)$$

$$\widehat{rhs}_{\psi}^{poly}(r, z) = -z(-690z^2 + 33z^4 + 185)r^6 + \frac{3}{4}z(-1970z^2 + 425 + 1609z^4)r^4 \quad (5.109b)$$

$$-60z(z-1)(z+1)(5z^2-1)r^2 - 40z^3 + 2z^5 \quad (5.109c)$$

$$\hat{\phi}_{poly}(r, z) = -\frac{1}{2}(r-1)^3(r+1)^3(z-1)^2(z+1)^2 * z \quad (5.109d)$$

$$\widehat{rhs}_{\phi}^{poly}(r, z) = -72z(5z^2 - 33)r^4 - 96z(3z^4 + 108 - 131z^2)r^2 + 1248z^5 \quad (5.109e)$$

$$+4344z - 6456z^3 \quad (5.109f)$$

The potentials $\hat{\psi}_{poly}$ and $\hat{\phi}_{poly}$ correspond to the following velocity:

$$\hat{u}_r^{poly} = -3r(z-1)(z+1)(5z^2-1)(r-1)^2(r+1)^2 \quad (5.110a)$$

$$\hat{u}_{\theta}^{poly}(r, z) = -\frac{1}{8}zr(r-1)(r+1)(-30r^4z^2 + 5r^4 + 33r^4z^4 + 8r^2z^4 + 8z^4) \quad (5.110b)$$

$$\hat{u}_z^{poly} = 6z(z-1)^2(z+1)^2(r-1)(r+1)(3r^2-1) \quad (5.110c)$$

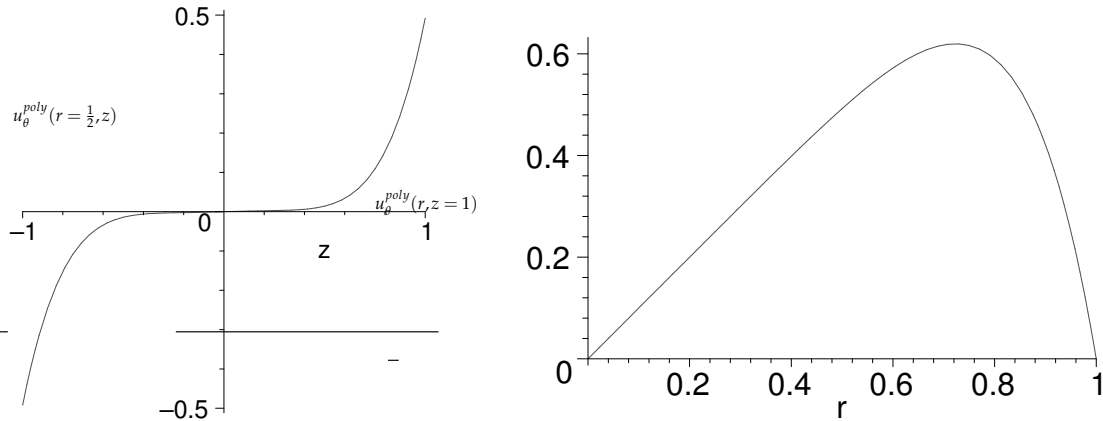


Figure 5.4: Axisymmetric mode $m = 0$. Left: Azimuthal velocity profile at $r = \frac{1}{2}$; Right: Azimuthal velocity profile at $z = h/2 = 1 : r\Omega_{+}^{poly} = r(1 - r^6)$.

Tests

Comparing analytic polynomial solutions with the numerically obtained ones has as its aim to validate the implementation of the multi-step solver. It is expected that for the polynomial right

hand sides $\widehat{rhs}_\psi = \widehat{rhs}_\psi^{poly}$ and $\widehat{rhs}_\phi = \widehat{rhs}_\phi^{poly}$ the solver should give correct solutions $\hat{\psi} = \hat{\psi}_{poly}$, $\hat{\phi} = \hat{\phi}_{poly}$ provided that sufficient spectral resolution is used. In this situation, no truncation error should be made by the τ -method. For a single Fourier mode, we define the relative error of a numerical solution $(\hat{\psi}, \hat{\phi})$ as

$$\epsilon_\psi \equiv \epsilon_\psi^m = \frac{\sup |\hat{\psi}^m - \hat{\psi}_{poly}^m|}{\sup |\hat{\psi}_{poly}^m|} \quad (5.111a)$$

$$\epsilon_\phi \equiv \epsilon_\phi^m = \frac{\sup |\hat{\phi}^m - \hat{\phi}_{poly}^m|}{\sup |\hat{\phi}_{poly}^m|} \quad (5.111b)$$

For all polynomial solutions which have been used in the validation process, we obtained numerical solutions whose relative errors were typically of order $O(10^{-14})$ and never exceeding $O(10^{-12})$ (see the bottom surfaces on figure 5.5). The error in satisfaction of the boundary conditions, which for a generic boundary operator \mathcal{B} and boundary values β we define as $\epsilon_{\mathcal{B}\phi} = \sup |\mathcal{B}\hat{\phi} - \beta|$, was of order $O(10^{-14})$.

This validation procedure was performed for several polynomial solutions corresponding to Fourier modes ranging from $m = 0$ to $m = 5$. Therefore we can conclude that for polynomial solutions our solver produces correct solutions to machine precision, which is a good argument for proving correctness of implementation of the equations and the boundary conditions in the poloidal-toroidal formulation. Of course, in real applications where the solutions are always truncated, this validation methodology is insufficient.

5.5.2 Non-polynomial case

If the right-hand-sides \widehat{rhs}_ψ^m and \widehat{rhs}_ϕ^m do not correspond to a polynomial solution or if the spectral solver resolution is insufficient to represent the polynomial solution without truncating some coefficients then the equations can no longer be satisfied exactly. The idea of the τ -method is to sacrifice satisfaction of the equations corresponding to the highest frequencies of the right-hand-side in favour of exact satisfaction of the boundary conditions. This approach is justified as long as the high frequencies in the right-hand-sides are small compared to the low frequencies. Spectral methods ensure this condition since the magnitude of the spectral coefficients of right-hand-sides arising during time integration of well-resolved fields should decay exponentially.

The situation for a multi-step solver using the τ -method for imposing the boundary conditions is slightly different. Since the intermediate solutions \hat{f}_ψ , \hat{g}_ϕ and \hat{f}_ϕ suffer from the τ -error distributed between all spectral coefficients the error committed by $(\hat{\psi}, \hat{\phi})$ is no longer restricted to the highest frequency equations, but is also present for lower frequency equations. However, when the error of satisfaction of the equations is computed in physical instead of in spectral space, one observes that the error is concentrated in the very close neighborhood of the boundaries, rapidly decaying with the distance from the boundaries (see figure 5.5-left). This behavior is similar to that observed for a standard one-step τ -solver. We define the error of

satisfaction of the equations as

$$\epsilon_{eq_\psi} = \frac{|E\Delta_h\hat{\psi} - \widehat{rhs}_\psi|}{\sup |\widehat{rhs}_\psi|}, \quad \epsilon_{eq_\phi} = \frac{|E\Delta_h\hat{\phi} - \widehat{rhs}_\phi|}{\sup |\widehat{rhs}_\phi|} \quad (5.112)$$

This error depends significantly on the right-hand-side functions \widehat{rhs}_ψ and \widehat{rhs}_ϕ . For completely arbitrary right-hand-sides, the boundary conditions can be very constraining and can lead to a nearly singular solution suffering from spurious oscillations. The maximal relative error (5.112), while still mainly restricted to the neighborhood of the boundaries, can then reach a level significantly higher than 100%. During time integration, however, when the right-hand-sides are calculated from the solution found at the previous timestep, the errors $\epsilon_{eq_\psi}, \epsilon_{eq_\phi}$ are considerably smaller. Typically¹², these errors are $O(0.01)$ for non-axisymmetric modes $\hat{\psi}^m$ and of order $O(0.1)$ for $\hat{\phi}^m$. For the axisymmetric mode $m = 0$ the maximal error of satisfaction of the equation for $\hat{\psi}^0$ is smaller, $O(10^{-6})$ on the boundaries and $O(10^{-10})$ for the internal points. This is much less than for $\hat{\phi}^0$, for which the error in cylinder corners reaches $O(1)$! There is an explanation for this. The axisymmetric poloidal flow defined by $\hat{\phi}^0$ describes a two-dimensional flow in a rectangular container with stationary walls. For this configuration, an analytic asymptotic solution for the flow near the container corners was provided by Moffatt [59]. This solution is not infinitely regular in the corner. The second derivative of the vorticity diverges¹³ which implies that the bi-Laplacian of the velocity also diverges at the domain corners. The error $\epsilon_{eq_\phi}^m$ (5.112) measures satisfaction of (5.27b) which corresponds to the axial component of the Laplacian of the Navier-Stokes equations. For exact solutions to the continuous two-dimensional Stokes problem this quantity must therefore diverge at the cylinder corners unlike the numerically computed value, which is forced to be finite and regular. This explains the high level of error for $\hat{\phi}^0$. The Stokes solutions in the proximity of the corners are also singular for three-dimensional flows (some analytic results have been provided by Hills & Moffatt [35]). This is the reason why, for the non-axisymmetric modes, we can observe the same corner singularity for both $\hat{\psi}^m$ and $\hat{\phi}^m$, which are coupled for $m \neq 0$ (see figure 5.6). Satisfaction of the Navier-Stokes equation at the corners is ensured since it follows from the satisfaction of the boundary condition, which our solver imposes to precision $O(10^{-14})$.

At the interior points, the relative error (5.112) for all Fourier modes very rapidly reaches a level of order $O(10^{-6})$ (at a distance of only two points away from the boundaries this error is $O(10^{-4})$). This proves that, for the multi-step solver, the non-satisfaction of the equations for low frequencies does not have severe consequences for the spatial distribution of the error in physical space.

On figure 5.5 we show the decimal logarithm of the relative error (5.112) for $\hat{\psi}^0$ and $\hat{\phi}^0$ evaluated in physical space. The errors represented on figure 5.5 are computed after 100 timesteps. The relative error for $m = 2$ is presented on figure 5.6. One should note that the errors that

¹²Here we consider only right-hand-sides obtained from time iteration performed without the nonlinear term. Generally, the nonlinear term introduces arbitrary components to the right-hand-side, due to the truncation errors as well as amplified high frequencies because of multiplication. In consequence, the right-hand-sides \widehat{rhs}_ψ and \widehat{rhs}_ϕ^m in the nonlinear solver can be weakly incompatible with the boundary conditions and can amplify the equation satisfaction error. We will consider these and other properties of the nonlinear solver in section 6.1.

¹³ $\omega \sim r^{1.74}..$

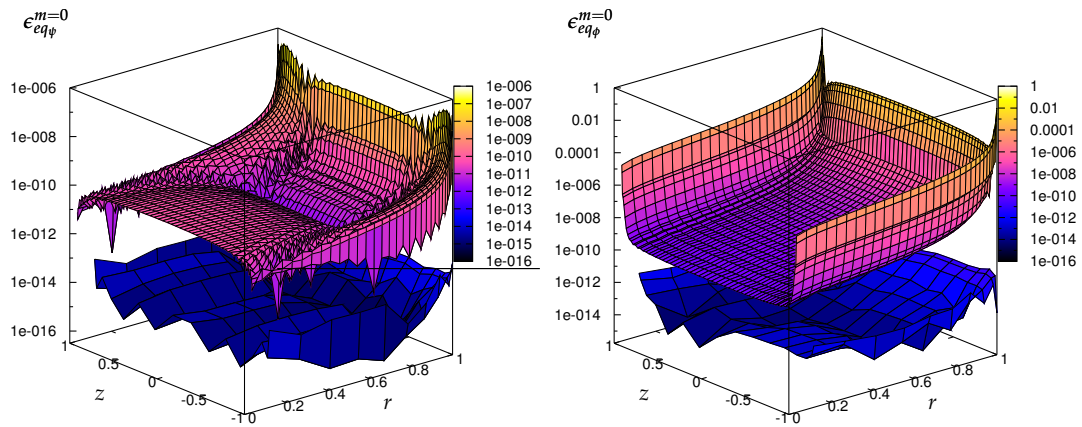


Figure 5.5: Error of satisfaction of equations for $m = 0$, after 100 time-iterations of a linear multi-step solver. Resolution used: $K = 64$, $N = 32$. **Left:** (upper surface) $\epsilon_{eq\psi}^{m=0}$ for Stokes problem, (bottom surface) $\epsilon_{eq\psi}^{m=0}$ for polynomial solution (5.109); **Right:** (upper surface) $\epsilon_{eq\phi}^{m=0}$ for Stokes problem, (bottom surface) $\epsilon_{eq\phi}^{m=0}$ for polynomial solution (5.109).

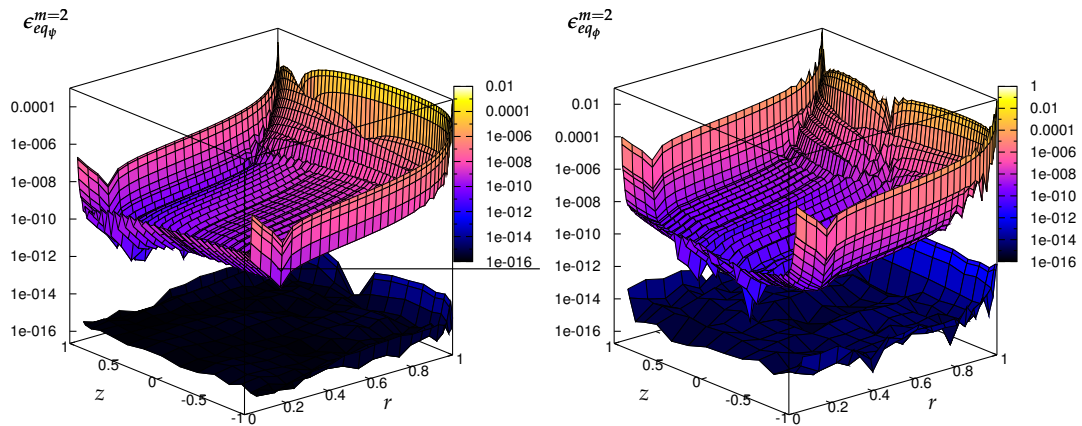


Figure 5.6: Error of satisfaction of equations for $m = 2$, after 100 time-iterations of a linear multi-step solver. Resolution used: $K = 64$, $N = 32$. **Left:** (upper surface) $\epsilon_{eq\psi}^{m=2}$ for Stokes problem, (bottom surface) $\epsilon_{eq\psi}^{m=2}$ for polynomial solution; **Right:** (upper surface) $\epsilon_{eq\phi}^{m=2}$ for Stokes problem, (bottom surface) $\epsilon_{eq\phi}^{m=2}$ for polynomial solution.

we are discussing represent quite severe criteria, since we analyze the satisfaction of the curl and double curl of the original Navier-Stokes equations governing the velocity. It should be expected that, for resolution $K = 64$, $N = 32$ the maxima of the high-frequency spectrum¹⁴ of the errors in satisfying the original Navier-Stokes equations would correspond to the maxima of $\epsilon_{eq\psi}^m$ and $\epsilon_{eq\phi}^m$ divided by coefficients of orders $O(64)$ and $O(64^2)$, respectively.

¹⁴These high-frequency errors correspond to errors situated near the boundary.

Spatial convergence

The important indicator of spatial convergence for spectral methods is the decay rate of high-frequency coefficients in the solution fields. For a well-behaved solver in the absence of volume and boundary singularities, the magnitude of spectral coefficients should decay rapidly¹⁵ with their frequency. On figures 5.7 and 5.8 we represent in logarithmic scale the spectral coefficients corresponding to a solution obtained after 100 timesteps of the linear (Stokes) solver. The spec-

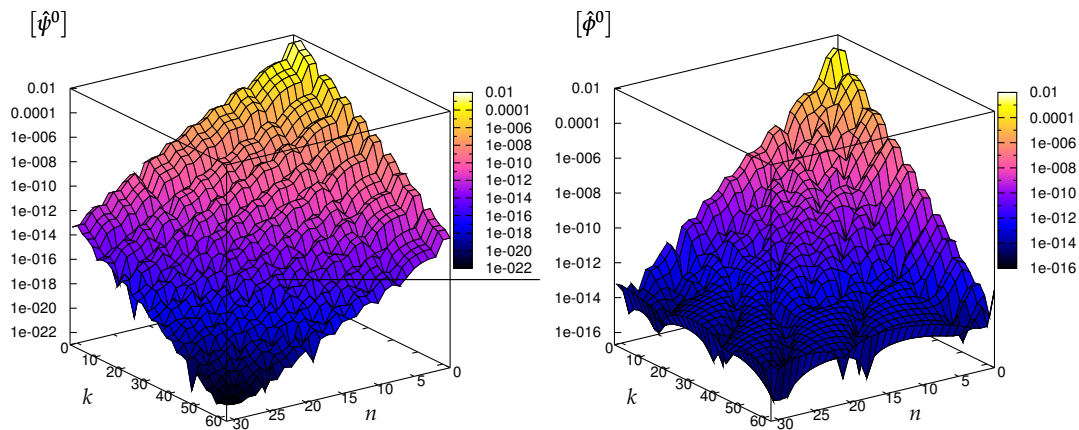


Figure 5.7: Spectral coefficients for $m = 0$, after 100 timesteps of a linear multi-step solver. Resolution used: $K = 64$, $N = 32$. Left: $[\hat{\psi}^0]$; Right: $[\hat{\phi}^0]$.

tral coefficients presented on figures 5.7, 5.8 were obtained by initializing the linear simulation with arbitrary spectral coefficients of low frequency (magnitude of initial coefficients $O(10^{-2})$). The spectral coefficients for the axisymmetric mode $\hat{\psi}^0$ behave correctly, showing exponential

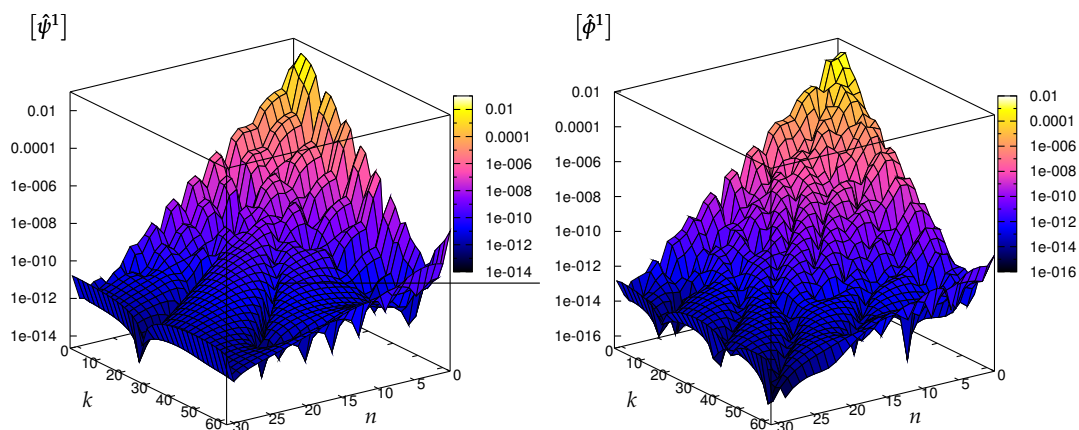


Figure 5.8: Spectral coefficients for $m = 1$, after 100 timesteps of a linear multi-step solver. Resolution used: $K = 64$, $N = 32$. Left: $[\hat{\psi}^1]$; Right: $[\hat{\phi}^1]$.

decay with frequency (figure 5.7-left). Convergence of other modes (figures 5.7-5.9) is not per-

¹⁵It is expected that for a laminar flow this decay rate should be exponential. The existence of thin boundary layers can significantly influence the convergence.

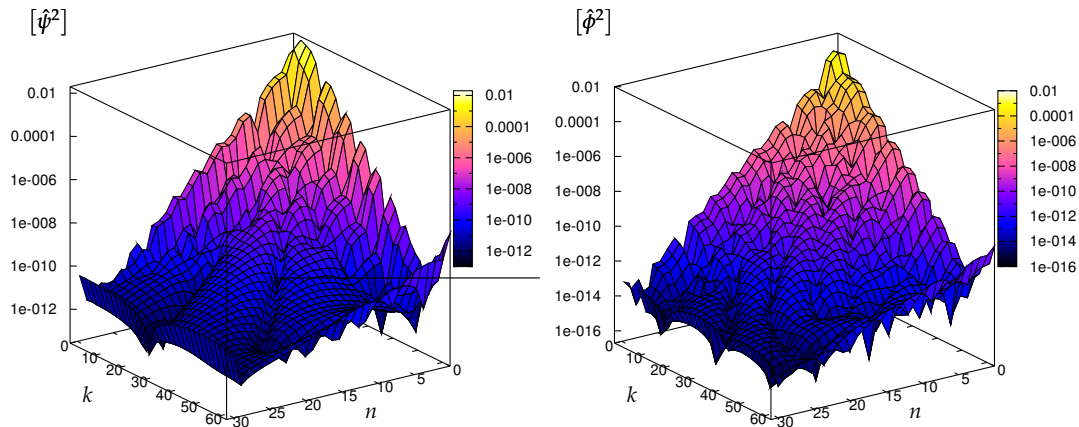


Figure 5.9: Spectral coefficients for $m = 2$, after 100 timesteps of a linear multi-step solver. Resolution used: $K = 64$, $N = 32$. Left: $[\hat{\psi}^2]$; Right: $[\hat{\phi}^2]$.

factly exponential (i.e. high frequency spectral coefficients seem not to decrease below a level $O(10^{-12})$). This can almost certainly be attributed to the existence of the corner singularities.

5.6 Towards an MHD solver

In this section we present a method for solving the magnetic equations (3.52) with the boundary conditions stated in (3.53)-(3.54). To our knowledge, at present, there exist no methods applicable to the spectral formulation in a finite cylinder. The main problem is due to the topologically different nature of the external region (vacuum) which is not simply-connected. Additionally the external domain is unbounded and extends to infinity which imposes use of a different class of spectral basis for representing the external solution. Finally, the internal boundary of the external region (a cylindrical hole) makes imposition of the boundary conditions very problematic¹⁶. A possible approach can be to define the induction equation in an integral formulation. The most important advantage is then that no boundary conditions must be specified. Using this formulation Dobler & Rädler [21] solved a stationary kinematic dynamo problem in cylindrical geometry and provided a mathematical formulation for a temporal eigenvalue problem¹⁷. A similar integro-differential formulation for finite-volume/boundary-element method was proposed by Isakov *et al.* [38]. Both methods can be seen as examples of the Green function method applied to a particular space-discretization.

We present here a method for solving the induction equation (2.7b) in the poloidal-toroidal formulation (3.52) in a configuration where the internal domain is a finite cylinder of finite conductivity and the external medium is a vacuum. This technique can also be considered as a variant of the Green function method, applied to a purely differential formulation.

¹⁶In spherical coordinates such a boundary (a spherical hole) is associated with a single (radial) variable. In cylindrical coordinates, imposition of the boundary conditions on an internal boundary (cylindrical hole), cannot be performed by standard spectral methods.

¹⁷The magnetic field is represented as $\mathbf{B}(\mathbf{x}, t) = \tilde{\mathbf{B}}(\mathbf{x})e^{\gamma t}$, with γ being a complex number.

5.6.1 External solution in vacuum

If the medium surrounding the cylinder is a vacuum, we will show that the external magnetic field can be expressed in terms of the internal field. For problems where the boundary conditions are imposed on a spherical boundary, this was demonstrated by Dudley & James [22]. However, if the boundary cannot be associated with a condition for a single variable (e.g. $r = R$), the problem becomes more complicated. We will present a numerical method for finding the internal solution independently from the external one, which can be determined *a posteriori* if needed.

We use spherical coordinates to express the external solution because, outside a cylinder of finite length, it must satisfy $\phi^{vac}(\rho \rightarrow \infty) \rightarrow 0$, where ρ is the spherical radius satisfying $\rho = r^2 + z^2$ (outside an infinitely long or axially periodic cylinder, cylindrical coordinates would be the natural choice). The general solution to $\Delta\phi^{vac} = 0$ satisfying this boundary condition is

$$\begin{aligned}\phi^{vac} &= \sum_l \sum_{-l \leq m \leq l} \hat{\phi}_{lm}^{vac} \rho^{-(l+1)} Y_{lm}(\xi, \theta) = \\ &= \sum_m e^{im\theta} \sum_{l \geq |m|} \hat{\phi}_{lm}^{vac} \rho^{-(l+1)} c_{lm} P_{lm}(\cos(\xi))\end{aligned}\quad (5.113)$$

$$\text{with } c_{lm} = \sqrt{\frac{2l+1}{4\pi} \frac{(l-m)!}{(l+m)!}}$$

where ξ is the polar angle and θ is the longitude. Functions $Y_{lm}(\xi, \theta)$ are the spherical harmonics describing the angular dependence of the solution and P_{lm} are the associated Legendre polynomials. The most important property of (5.113) is that for a given longitudinal mode m , the solution (5.113) has degrees of freedom associated only with its polar dependence on ξ . These degrees of freedom are counted by the single index l . The radial dependence of (5.113) is fixed! This means that in order to determine $\hat{\phi}_m^{vac}$ it is sufficient to specify its values on a one-dimensional boundary.

The shape of the boundary does not play any role – as long as the boundary is simply connected it can be parametrized. The conditions (3.53)-(3.54) specified at the cylinder boundaries $(r = 1, z) \cup (r, z = \pm \frac{h}{2})$, for a given m , are also one-dimensional. It is then possible to perform a coordinate change and establish a relation between the free coefficients $\hat{\phi}^{vac}$ and the boundary functions $(\hat{\psi}^B, \hat{\phi}^B)(\mathbf{x} \in (r = 1, z) \cup (r, z = \pm \frac{h}{2}))$ through the matching conditions (3.53)-(3.54). The relations between (r, z) and (ρ, ξ) are the following:

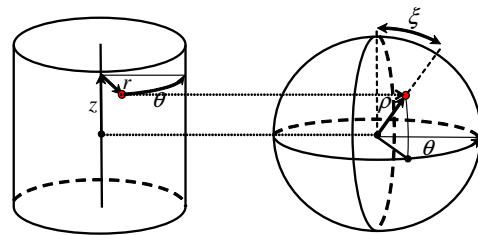


Figure 5.10: Illustration of coordinate mapping : $\mathbf{x}(r, \theta, z) \mapsto \mathbf{x}(\rho, \theta, \xi)$.

$$\begin{aligned}\rho^2 &= r^2 + z^2 & \tan \xi &= \frac{r}{z} \\ \sin \xi &= \frac{r}{\rho} & \cos \xi &= \frac{z}{\rho}\end{aligned}\quad (5.114)$$

A graphical description of both cylindrical and spherical coordinates is presented on figure 5.10. In order to express the differential expressions present in boundary conditions (3.53-3.54) we will need to write $\left. \frac{\partial \phi^{vac}}{\partial r} \right|_{z=\pm \frac{h}{2}}$ and $\left. \frac{\partial \phi^{vac}}{\partial z} \right|_{r=1}$ in terms of $\left. \frac{\partial \phi^{vac}}{\partial \rho} \right|_{\xi}$ and $\left. \frac{\partial \phi^{vac}}{\partial \xi} \right|_{\xi}$:

$$\begin{pmatrix} \frac{\partial}{\partial r} \\ \frac{\partial}{\partial z} \end{pmatrix} = \begin{pmatrix} \frac{\partial \rho}{\partial r} & \frac{\partial \xi}{\partial r} \\ \frac{\partial \rho}{\partial z} & \frac{\partial \xi}{\partial z} \end{pmatrix} \begin{pmatrix} \frac{\partial}{\partial \rho} \\ \frac{\partial}{\partial \xi} \end{pmatrix} \quad (5.115)$$

where the matrix elements can be evaluated by using (5.114)

$$\begin{aligned} \frac{\partial \rho}{\partial r} &= \frac{d\rho}{d\rho^2} \frac{\partial \rho^2}{\partial r} = \frac{r}{\rho} = \sin \xi & \frac{\partial \xi}{\partial r} &= \frac{d\xi}{d \tan \xi} \frac{\partial \tan \xi}{\partial r} = \cos^2 \xi \frac{1}{z} = \frac{z}{\rho^2} = \frac{\cos \xi}{\rho} \\ \frac{\partial \rho}{\partial z} &= \frac{d\rho}{d\rho^2} \frac{\partial \rho^2}{\partial z} = \frac{z}{\rho} = \cos \xi & \frac{\partial \xi}{\partial z} &= \frac{d\xi}{d \tan \xi} \frac{\partial \tan \xi}{\partial z} = -\cos^2 \xi \frac{r}{z^2} = -\frac{r}{\rho^2} = -\frac{\sin \xi}{\rho} \end{aligned} \quad (5.116)$$

Substituting (5.116) into (5.117) gives:

$$\begin{pmatrix} \frac{\partial}{\partial r} \\ \frac{\partial}{\partial z} \end{pmatrix} = \begin{pmatrix} \frac{r}{\rho} & \frac{z}{\rho^2} \\ \frac{z}{\rho} & -\frac{r}{\rho^2} \end{pmatrix} \begin{pmatrix} \frac{\partial}{\partial \rho} \\ \frac{\partial}{\partial \xi} \end{pmatrix} \quad (5.117)$$

We introduce functions $\{\hat{\phi}_l^Y\}$ defined as

$$\hat{\phi}_l^Y(\rho, \xi) \equiv \hat{\phi}_{lm}^Y(\rho, \xi) = \rho^{-(l+m+1)} c_{l+m,m} P_{l+m,m}(\cos(\xi)) \quad ; \quad l = 0, \dots, L-1 \quad (5.118)$$

so that, for a given Fourier mode $\hat{\phi}_m^{vac}$ of ϕ^{vac} , we have:

$$\hat{\phi}^{vac}(\rho, \xi) \equiv \hat{\phi}_m^{vac}(\rho, \xi) = \sum_{l=1}^{L-1} \hat{\phi}_l^{vac} \hat{\phi}_{lm}^Y(\rho, \xi) \quad (5.119)$$

The partial derivatives $\frac{\partial \phi^{vac}}{\partial r}$ and $\frac{\partial \phi^{vac}}{\partial z}$ present in (3.53)-(3.54) can be determined by evaluating $\frac{\partial \hat{\phi}_l^Y}{\partial r}$ and $\frac{\partial \hat{\phi}_l^Y}{\partial \xi}$ using (5.117):

$$\begin{aligned} \frac{\partial \hat{\phi}_l^Y}{\partial r} &= \frac{r}{\rho} \frac{\partial \hat{\phi}_l^Y}{\partial \rho} + \frac{z}{\rho^2} \frac{\partial \hat{\phi}_l^Y}{\partial \xi} \\ \frac{\partial \hat{\phi}_l^Y}{\partial z} &= \frac{z}{\rho} \frac{\partial \hat{\phi}_l^Y}{\partial \rho} - \frac{r}{\rho^2} \frac{\partial \hat{\phi}_l^Y}{\partial \xi} \end{aligned} \quad (5.120)$$

where $\frac{\partial \hat{\phi}_l^Y}{\partial \rho}$ and $\frac{\partial \hat{\phi}_l^Y}{\partial \xi}$, by using (5.118), can be written as:

$$\begin{aligned} \frac{\partial \hat{\phi}_l^Y}{\partial \rho} &= -\frac{l+m+1}{\rho} \hat{\phi}_l^Y = -(l+m) \rho^{-(l+m+2)} c_{l+m,m} P_{l+m,m}(\cos(\xi)) \\ \frac{\partial \hat{\phi}_l^Y}{\partial \xi} &= -\rho^{-(l+m+1)} c_{l+m,m} \underbrace{\sin(\xi)}_{r/\rho} P'_{l+m,m}(\cos(\xi)) \underbrace{\frac{1}{z}}_{z/\rho} \end{aligned} \quad (5.121)$$

Substituting (5.121) into (5.120) results in the following expressions

$$\frac{\partial \hat{\phi}_l^Y}{\partial r}(r, z) = c_{l+m, m} \rho^{-(l+m)} \left[-\frac{r}{\rho^3} ((l+m)\rho P_{l+m, m}(z/\rho) + z P'_{l+m, m}(z/\rho)) \right] \quad (5.122a)$$

$$\frac{\partial \hat{\phi}_l^Y}{\partial z}(r, z) = c_{l+m, m} \rho^{-(l+m)} \left[-\frac{1}{\rho^3} ((l+m)z\rho P_{l+m, m}(z/\rho) - r^2 P'_{l+m, m}(z/\rho)) \right] \quad (5.122b)$$

$$\rho \equiv \rho(r, z) = \sqrt{r^2 + z^2}$$

5.6.2 Continuity conditions

For simplicity, we will drop the B subscript, so that in this section we have:

$$\psi \equiv \psi_B, \quad \phi \equiv \phi_B, \quad \hat{\psi} \equiv \hat{\psi}_B, \quad \hat{\phi} \equiv \hat{\phi}_B$$

Before presenting the method for solving (3.52), we will further simplify the corresponding boundary conditions (3.53)-(3.54) by writing them in a form corresponding to the m 'th azimuthal Fourier mode:

$$im\hat{\psi} + r\partial_r(\partial_z\hat{\phi} - \hat{\phi}^{vac}) = 0 \quad (5.123a)$$

$$\partial_r\hat{\psi} = 0 \quad (5.123b)$$

$$\Delta\hat{\phi} = 0 \quad (5.123c)$$

$$\partial_z\hat{\phi} - \hat{\phi}^{vac} = 0 \quad (5.123d)$$

$$\left(\partial_t - Rm^{-1}(\Delta - r^{-2}) \right) \left(\frac{im}{r}\hat{\psi} + \partial_{rz}^2\hat{\phi} \right) + Rm^{-1}\frac{2im}{r^3}\partial_z\hat{\phi} = 0 \quad (5.123e)$$

at $r = 1$

$$im\hat{\psi} + r\partial_r(\partial_z\hat{\phi} - \hat{\phi}^{vac}) = 0 \quad (5.124a)$$

$$-r\partial_r\hat{\psi} + im(\partial_z\hat{\phi} - \hat{\phi}^{vac}) = 0 \quad (5.124b)$$

$$\Delta_h\hat{\phi} + \partial_z\hat{\phi}^{vac} = 0 \quad (5.124c)$$

at $z = \pm \frac{h}{2}$

Equations (5.123)-(5.124) can be further simplified by considering problems for $m =$ and $m \neq 0$ separately.

Axisymmetric case ($m = 0$)

For the axisymmetric mode, simplification is straightforward: by substituting $m = 0$ into (5.123)-(5.124) we obtain:

$$\partial_r(\partial_z\hat{\phi} - \hat{\phi}^{vac}) = 0 \quad (5.125a)$$

$$\partial_r\hat{\psi} = 0 \quad (5.125b)$$

$$\Delta\hat{\phi} = 0 \quad (5.125c)$$

$$\partial_z\hat{\phi} - \hat{\phi}^{vac} = 0 \quad (5.125d)$$

at $r = 1$

where the magnetic compatibility condition was dropped, since it is not necessary for the axisymmetric mode (see section 3.4.1 for explanations). At the top and bottom disks ($z = \pm \frac{h}{2}$) we have:

$$\left. \begin{aligned} \Delta_h \hat{\psi} = 0 & \quad \left\{ \begin{array}{l} \partial_r (\partial_z \hat{\phi} - \hat{\phi}^{vac}) = 0 \\ \hat{\psi} = 0 \quad \leftarrow \quad \partial_r \hat{\psi} = 0 \\ r^{-1} \partial_r r \partial_r \hat{\phi} + \partial_z \hat{\phi}^{vac} = 0 \end{array} \right. \quad \text{at } z = \pm \frac{h}{2} \end{aligned} \right\} \begin{array}{l} (5.126a) \\ (5.126b) \\ (5.126c) \end{array}$$

where the leftward implication in (5.126b) follows from the gauge choice for ψ which is determined up to an arbitrary function of coordinate z . We can therefore choose $\hat{\psi}(r=0, z) = 0$, which together with $\partial_r \hat{\psi} = 0$ implies $\hat{\psi} = 0$ at $z = \pm \frac{h}{2}$.

From (5.125)-(5.126) we conclude that for the axisymmetric mode, the toroidal ($\hat{\psi}$) and poloidal ($\hat{\phi}$) potentials are completely decoupled. This is analogous to the velocity potentials $\hat{\psi}_u$ and $\hat{\phi}_u$ whose axisymmetric components are also decoupled. The external solution $\hat{\phi}^{vac}$ is coupled only to $\hat{\phi}$.

Non-axisymmetric case ($m \neq 0$)

Boundary conditions at $r = 1$ remains in the form (5.123) while (5.124), corresponding to $z = \pm \frac{h}{2}$, can be further simplified. For $m \neq 0$ we can write

$$\partial_z \hat{\phi} - \hat{\phi}^{vac} = \frac{r}{im} \partial_r \hat{\psi} \quad \text{at } (r, z = \pm \frac{h}{2}) \cup (r = 1, z) \quad (5.127)$$

which follows directly from (5.124b) and (5.123b,d). We substitute (5.127) into (5.124a) obtaining:

$$0 = im \hat{\psi} + r \partial_r \left(\frac{r}{im} \partial_r \hat{\psi} \right) = \frac{r^2}{im} \Delta_h \hat{\psi} \quad \text{at } z = \pm \frac{h}{2} \quad (5.128)$$

Using (5.128) together with (5.123b) one can notice that $\hat{\psi}$ satisfies at $z = \pm \frac{h}{2}$ the Laplace equation with homogeneous Neumann conditions which for non-axisymmetric modes implies:

$$\hat{\psi} = 0 \quad \text{at } z = \pm \frac{h}{2} \quad (5.129)$$

Using (5.129) we can deduce from (5.124b) that

$$\partial_z \hat{\phi} - \hat{\phi}^{vac} = 0 \quad \text{at } z = \pm \frac{h}{2} \quad (5.130)$$

Therefore, the final set of continuity conditions at $z = \pm \frac{h}{2}$ can be written as:

$$\left. \begin{aligned} \Delta_h \hat{\psi} = 0 \quad \text{or} \quad \hat{\psi} = 0 \\ \partial_z \hat{\phi} - \hat{\phi}^{vac} = 0 \\ \Delta_h \hat{\phi} + \partial_z \hat{\phi}^{vac} = 0 \end{aligned} \right\} \quad \text{at } z = \pm \frac{h}{2} \quad \begin{array}{l} (5.131a) \\ (5.131b) \\ (5.131c) \end{array}$$

5.6.3 Multi-Poisson solver for induction equation

We will formulate the multi-step procedure for solving the induction equation in toroidal-poloidal formulation (3.52) with the boundary conditions specified in the preceding section. The formulation will be analogous to that presented for the hydrodynamic problem in section 5.3.2. We begin by redefining symbols E , \widehat{rhs}_ψ and \widehat{rhs}_ϕ as follows:

$$\begin{aligned} E &\equiv (\partial_t - Rm^{-1}\Delta) \\ \widehat{rhs}_\psi &\equiv \widehat{rhs}_{\psi_B} \equiv \hat{\mathbf{e}}_z \cdot \mathbf{s}_B \\ \widehat{rhs}_\phi &\equiv \widehat{rhs}_{\phi_B} \equiv \hat{\mathbf{e}}_z \cdot \nabla \times \mathbf{s}_B \\ \mathbf{s}_B &\equiv -\nabla \times (\mathbf{u} \times \mathbf{B}) \end{aligned}$$

Axisymmetric mode ($m = 0$):

For potential $\hat{\psi}$ we have:

$$E\hat{f}_\psi = \widehat{rhs}_\psi \quad ; \quad \begin{cases} \int_0^1 \hat{f}_\psi r dr = 0 \\ \hat{f}_\psi|_{z=\pm\frac{h}{2}} = 0 \end{cases} \Leftrightarrow \begin{cases} \partial_r \hat{\psi}|_{r=1} = 0 \\ \Delta_h \hat{\psi}|_{z=\pm\frac{h}{2}} = 0 \end{cases} \Leftrightarrow \begin{cases} \partial_r \hat{\psi}|_{r=1} = 0 \\ \partial_r \hat{\psi}|_{z=\pm\frac{h}{2}} = 0 \end{cases} \quad (5.132a)$$

$$\Delta_h \hat{\psi} = f_\psi \quad ; \quad \hat{\psi}|_{r=0} = 0 \quad (5.132b)$$

To the left of the semi-colon we have written the PDE and to the right we have written the boundary conditions which we will impose on this PDE.

For $\hat{\phi}$ we have:

$$E\hat{f}_\phi = \widehat{rhs}_\phi \quad ; \quad \hat{f}_\phi|_{\partial} = \hat{\sigma}_{f_\phi} \Leftrightarrow \begin{cases} (\hat{f}_\phi + \partial_z^2 \hat{\phi})|_{r=1} = 0 \\ (\hat{f}_\phi + \partial_z \hat{\phi}^{vac})|_{z=\pm\frac{h}{2}} = 0 \end{cases} \Leftrightarrow \begin{cases} \Delta \hat{\phi}|_{r=1} = 0 \\ (\Delta_h \hat{\phi} + \partial_z \hat{\phi}^{vac})|_{z=\pm\frac{h}{2}} = 0 \end{cases} \quad (5.133a)$$

$$\Delta_h \hat{\phi} = \hat{f}_\phi \quad ; \quad \hat{\phi}|_{r=1} = \hat{\sigma}_\phi \Leftrightarrow (\partial_z \hat{\phi} - \hat{\phi}^{vac})|_{r=1} = 0 \quad (5.133b)$$

and for coefficients $\hat{\phi}_l^{vac}$:

$$\Delta \hat{\phi}^{vac} = 0 \quad ; \quad \begin{cases} \hat{\phi}^{vac}(\rho \rightarrow \infty) = 0 \\ \partial_r (\partial_z \hat{\phi} - \hat{\phi}^{vac})|_{\partial} = 0 \end{cases} \quad (5.136)$$

We have written the equation (5.136) for $\hat{\phi}^{vac}$ in order to define a complete system of equations and boundary conditions, but this equation need not be solved, since the form of $\hat{\phi}^{vac}$ satisfying $\hat{\phi}^{vac}(\rho \rightarrow \infty) \rightarrow 0$ is known and given in (5.113). This leaves only the boundary conditions at the solid boundary ∂ that remain to be satisfied.

Non-axisymmetric modes ($m \neq 0$):

$$E\hat{f}_\psi = \widehat{rhs}_\psi \quad ; \quad \begin{cases} \hat{f}_\psi|_{r=1} = \hat{\sigma}_{f_\psi} \Leftrightarrow (im\hat{\psi} + r\partial_r(\partial_z\hat{\phi} - \hat{\phi}^{vac}) = 0)|_{r=1} \\ \hat{f}_\psi|_{z=\pm\frac{h}{2}} = 0 \Leftrightarrow \Delta_h\hat{\psi}|_{z=\pm\frac{h}{2}} = 0 \Leftrightarrow \partial_r\hat{\psi}|_{z=\pm\frac{h}{2}} = 0 \end{cases} \quad (5.137a)$$

$$\Delta_h\hat{\psi} = f_\psi \quad ; \quad \partial_r\hat{\psi}|_{r=1} = 0 \quad (5.137b)$$

$$E\hat{f}_\phi = \widehat{rhs}_\phi \quad ; \quad \hat{f}_\phi|_{\partial} = \hat{\sigma}_{f_\phi} \Leftrightarrow \begin{cases} (\hat{f}_\phi + \partial_z^2\hat{\phi})|_{r=1} = 0 \Leftrightarrow \Delta\hat{\phi}|_{r=1} = 0 \\ (\hat{f}_\phi + \partial_z\hat{\phi}^{vac})|_{z=\pm\frac{h}{2}} = 0 \Leftrightarrow (\Delta_h\hat{\phi} + \partial_z\hat{\phi}^{vac})|_{z=\pm\frac{h}{2}} = 0 \end{cases} \quad (5.138a)$$

$$\Delta_h\hat{\phi} = \hat{f}_\phi \quad ; \quad \hat{\phi}|_{r=1} = \hat{\sigma}_\phi \Leftrightarrow (\partial_z\hat{\phi} - \hat{\phi}^{vac})|_{r=1} = 0 \quad (5.138b)$$

$$\Delta\hat{\phi}^{vac} = 0 \quad ; \quad \begin{cases} \hat{\phi}^{vac}(\rho \rightarrow 0) = 0 \\ (\partial_t - Rm^{-1}(\Delta - r^{-2}))(\frac{im}{r}\hat{\psi} + \partial_r\partial_z\hat{\phi}) + \\ + Rm^{-1}\frac{2im}{r^3}\partial_z\hat{\phi} = 0 \end{cases} \quad (5.139)$$

It can seem strange that the magnetic compatibility condition, which concerns essentially the internal solution only, is specified in (5.139) as a boundary condition for $\hat{\phi}^{vac}$. The fact that we have written this condition in (5.139) does not mean that it is imposed on $\hat{\phi}^{vac}$ alone. The compatibility condition as well as the conditions defined by $\hat{\sigma}_{f_\psi}$, $\hat{\sigma}_{f_\phi}$ and $\hat{\sigma}_\phi$ are coupled and must be imposed by the influence matrix technique. The reason for writing these boundary conditions next to the differential equations (5.137)-(5.139) of the multi-step solver is to show that the total number of the boundary conditions matches the differential order of the equations. Only these boundary conditions which are explicitly written for $\hat{\psi}$ and $\hat{\phi}$ (without using $\hat{\sigma}$) can be imposed directly (by the τ -method) at the indicated level of the multi-step procedure.

5.6.4 Influence matrix for the magnetic problem

The boundary conditions specified by $\hat{\sigma}_{f_\psi}$, $\hat{\sigma}_\phi$ in (5.133), (5.137), (5.138) and also those from (5.136) and (5.139) must be imposed by the influence matrix technique discussed in section 5.4 for the Stokes solver.

Main idea Before applying this methodology to the magnetic problem we recall briefly the key idea, which is a decomposition of the solutions ϕ , ψ into homogeneous and particular parts. The homogeneous solutions (ϕ^h , ψ^h), satisfy equations (3.52c) with $\widehat{rhs}_\psi = \widehat{rhs}_\phi = 0$ and with the boundary conditions (3.53)-(3.54). The particular solutions (ϕ^p , ψ^p) satisfy (3.52c) but

with simplified boundary conditions (i.e all conditions that cannot be satisfied directly by the multi-step solver are replaced by homogeneous Dirichlet conditions). This can be written as:

$$\begin{aligned}\psi &= \psi^p + \psi^h = \psi^p + \sum \sigma_\psi^i \psi_i^t \\ \phi &= \phi^p + \phi^h = \phi^p + \sum \sigma_\phi^i \phi_i^t\end{aligned}$$

where $\{\psi_i^t\}$, $\{\phi_i^t\}$ – called the test functions – build the unknown homogeneous solutions. The influence matrix defines a linear system whose solution is $\{\sigma_\psi^i\}$ and $\{\sigma_\phi^i\}$.

After this qualitative digression, we return now to our problem. The test functions needed to construct the influence matrix are the following:

$$\begin{aligned}\{\hat{\phi}_k^t; k = 1, \dots, K\} &: \begin{cases} \hat{\sigma}_{f_\phi}|_{r=1}(z) = \delta(z - z_k) \\ \hat{\sigma}_{f_\phi}|_{z=\pm\frac{h}{2}}(r) = 0 \\ \hat{\sigma}_\phi|_{r=1}(z) = 0 \end{cases} \\ \{\hat{\phi}_n^t; n = 1, \dots, 2N^m\} &: \begin{cases} \hat{\sigma}_{f_\phi}|_{r=1}(z) = 0 \\ \hat{\sigma}_{f_\phi}|_{z=\pm\frac{h}{2}}(r) = \delta(r - r_n) \quad ; \quad z = \begin{cases} \frac{h}{2} & \text{if } n \leq N^m \\ -\frac{h}{2} & \text{if } N^m < n \leq 2N^m \end{cases} \\ \hat{\sigma}_\phi|_{r=1}(z) = 0 \end{cases} \quad (5.140) \\ \{\hat{\phi}_{k'}^t; k' = 1, \dots, K\} &: \begin{cases} \hat{\sigma}_{f_\phi}|_{r=1}(z) = 0 \\ \hat{\sigma}_{f_\phi}|_{z=\pm\frac{h}{2}}(r) = 0 \\ \hat{\sigma}_\phi|_{r=1}(z) = \delta(z - z_{k'}) \end{cases}\end{aligned}$$

where K denotes the axial resolution and $N^m \equiv N - \lfloor M/2 \rfloor$ is the number of radial polynomials associated with the m 'th Fourier mode. For non-axisymmetric modes we have additionally:

$$\{\hat{\psi}_k^t; k = 1, \dots, K\} : \begin{cases} \hat{\sigma}_{f_\psi}|_{r=1}(z) = \delta(z - z_k) \\ \hat{\sigma}_{f_\psi}|_{z=\pm\frac{h}{2}}(r) = 0 \end{cases} \quad (5.141)$$

where the braces to the right of (5.140)-(5.141) indicates how equations (5.132)-(5.133) and (5.137)-(5.138) must be modified in order to define the test solution. The notation $\delta(r - r_n)$, $\delta(z - z_k)$ should be understood as defining solutions whose boundary values are non-zero only at a single point or, in spectral space, for single spectral coefficient.

The test functions $\hat{\phi}_l^Y$ for the external potential ϕ^{vac} are defined by (5.118):

$$\{\hat{\phi}_l^Y; l = 1, \dots, 2N^m + K\} \equiv \{\rho^{-(l+m)} c_{l+m,m} P_{l+m,m}(z/\rho); l = 1, \dots, 2N^m + K\} \quad (5.142)$$

To simplify the presentation, we will not separate even and odd terms in the influence matrix. In practical implementation this should be done for reasons of both accuracy and performance. This separation can be performed in the same way as for the hydrodynamic problem in section 5.4.2.

Influence matrix for axisymmetric mode ($m = 0$):

On a schematic view below we present the influence matrix and the corresponding right-hand-side vector built from the particular solution which is obtained from (5.133) by setting $\hat{\sigma}_{f_\phi} = \hat{\sigma}_\phi = 0$.

$$\begin{array}{l}
 \Delta \hat{\phi}|_{r=1} : \\
 (\Delta_h \hat{\phi} + \partial_z \hat{\phi}^{vac})|_{z=\pm \frac{h}{2}} : \\
 (\partial_z \hat{\phi} - \hat{\phi}^{vac})|_{r=1} : \\
 \partial_r (\partial_z \hat{\phi} - \hat{\phi}^{vac})|_{\partial} :
 \end{array}
 \begin{array}{c}
 \hat{\phi}_k^t \quad \hat{\phi}_n^t \quad \hat{\phi}_{k'}^t \quad \hat{\phi}_l^Y \\
 \downarrow \quad \downarrow \quad \downarrow \quad \downarrow \\
 \left[\begin{array}{c|c|c|c}
 \Delta & \partial_z^2 & \partial_z^2 & 0 \\
 \hline
 \Delta_h & 0 & 0 & \partial_z \\
 \hline
 \partial_z & \partial_z & \partial_z & -\mathbb{1} \\
 \hline
 \partial_{rz}^2 & \partial_{rz}^2 & \partial_{rz}^2 & -\partial_r
 \end{array} \right]
 \begin{array}{c}
 \hat{\sigma}_{f_\phi}^k \\
 \hat{\sigma}_{f_\phi}^n \\
 \hat{\sigma}_\phi^{k'} \\
 \hat{\phi}_l^{vac}
 \end{array}
 =
 \begin{array}{c|c}
 \left[\begin{array}{c}
 -\Delta \hat{\phi}^p \\
 -\Delta_h \hat{\phi}^p \\
 -\partial_z \hat{\phi}^p \\
 -\partial_{rz}^2 \hat{\phi}^p
 \end{array} \right]
 \begin{array}{l}
 K \\
 2N \\
 K \\
 2N + K
 \end{array}
 \end{array}
 \end{array}
 \quad (5.143)$$

The solution to this linear system is a vector of unknown coefficients/boundary values. Coefficients $\{\hat{\sigma}_{f_\phi}^k, \hat{\sigma}_{f_\phi}^n, \hat{\sigma}_\phi^{k'}\}$ determine the internal solution for the poloidal potential $\hat{\phi}$ while $\{\hat{\phi}_l^{vac}\}$ define the external solution $\hat{\phi}^{vac}$.

We precise that the elements of the influence matrix defining the linear system (5.143) are actually the boundary values of the test functions $\{\hat{\phi}_k^t, \hat{\phi}_n^t, \hat{\phi}_{k'}^t, \hat{\phi}_l^Y\}$ after applying to them the corresponding parts of the boundary operators. We have placed the operator symbols inside the influence matrix in (5.143) to indicate that the corresponding matrix block is obtained by applying that operator to the corresponding test function (indicated above the influence matrix). The operators written to the left of (5.143) indicate which of the boundary conditions stated in (5.123)-(5.124) is being imposed by the corresponding matrix row. Numbers $K, 2N$ indicate either the size of the corresponding boundary (rows) or the number of the test functions (columns).

Influence matrix for non-axisymmetric modes ($m \neq 0$):

For the non-axisymmetric modes the influence matrix system can be constructed as follows:

$$\begin{array}{l}
 \hat{\phi}_k^t \quad \hat{\phi}_n^t \quad \hat{\phi}_{k'}^t \quad \hat{\psi}_k^t \quad \hat{\phi}_l^Y \\
 \downarrow \quad \downarrow \quad \downarrow \quad \downarrow \quad \downarrow \\
 (\Delta_h \hat{\phi} + \partial_z \hat{\phi}^{vac})|_{z=\pm \frac{1}{2}} : \\
 \Delta \hat{\phi}|_{r=1} : \\
 \partial_r (\partial_z \hat{\phi} - \hat{\phi}^{vac})|_{r=1} : \\
 \mathcal{C}(\hat{\phi}, \hat{\psi})|_{r=1} : \\
 (\partial_z \hat{\phi} - \hat{\phi}^{vac})|_{\partial} :
 \end{array}
 \begin{array}{c}
 \left[\begin{array}{c|c|c|c|c}
 \Delta_h & 0 & 0 & 0 & \partial_z \\
 \hline
 \partial_z^2 & \Delta & \partial_z^2 & 0 & 0 \\
 \hline
 \partial_{rz}^2 & \partial_{rz}^2 & \partial_{rz}^2 & im & -\partial_r \\
 \hline
 \mathcal{C}_\phi^1 & \mathcal{C}_\phi^1 & \mathcal{C}_\phi^1 & \mathcal{C}_\psi^1 & 0 \\
 \hline
 \partial_z & \partial_z & \partial_z & 0 & -\mathbb{1}
 \end{array} \right]
 \begin{array}{c}
 \hat{\sigma}_{f_\phi}^n \\
 \hat{\sigma}_{f_\phi}^k \\
 \hat{\sigma}_\phi^k \\
 \hat{\sigma}_\psi^k \\
 \hat{\phi}_l^{vac}
 \end{array}
 =
 \begin{array}{c}
 \left[\begin{array}{c|c}
 -\Delta_h \hat{\phi}^p & 2N^m \\
 \hline
 -\Delta \hat{\phi}^p & K \\
 \hline
 -\partial_{rz}^2 \hat{\phi}^p & K \\
 \hline
 RHS_C & K \\
 \hline
 -\partial_z \hat{\phi}^p & 2N^m \\
 & +K
 \end{array} \right]
 \end{array}
 \end{array}
 \quad (5.144)$$

where $\mathcal{C} \equiv \mathcal{C}^1 - \mathcal{C}^0$ is a time-discretized form of the magnetic compatibility condition, with \mathcal{C}^1 and \mathcal{C}^0 defined as follows:

$$\begin{aligned}
 \mathcal{C}^1 \{ \hat{\phi}(t), \hat{\psi}(t) \} &= \mathcal{C}_\psi^1 \hat{\psi}(t) + \mathcal{C}_\phi^1 \hat{\phi}(t) \\
 \mathcal{C}_\psi^1 \hat{\psi}(t) &= \left(\mathbb{1} - \underbrace{\Delta t R m^{-1}}_\epsilon (\Delta - r^{-2}) \right) imr^{-1} \hat{\psi}(t) \\
 \mathcal{C}_\phi^1 \hat{\phi}(t) &= \left(\mathbb{1} - \underbrace{\Delta t R m^{-1}}_\epsilon (\Delta - r^{-2}) \right) \partial_{rz}^2 \hat{\phi}(t) + \epsilon \frac{2im}{r^3} \partial_z \hat{\phi}(t) \\
 \mathcal{C}^0 \{ \hat{\phi}(t), \hat{\psi}(t) \} &= imr^{-1} \hat{\psi}(t - \Delta t) + \partial_{rz}^2 \hat{\phi}(t - \Delta t)
 \end{aligned}
 \quad (5.145)$$

For solutions represented by the homogeneous and particular parts the discretized magnetic compatibility condition can be written as:

$$\mathcal{C} \{ \hat{\phi}, \hat{\psi} \} = \mathcal{C}^1 \{ \hat{\phi}^p, \hat{\psi}^p \} + \mathcal{C}^1 \{ \hat{\phi}^h, \hat{\psi}^h \} - \mathcal{C}^0 \{ \hat{\phi}, \hat{\psi} \} = 0$$

thus, the expression RHS_C present in (5.144) has the following form:

$$RHS_C \{ \hat{\phi}^p, \hat{\psi}^p, \hat{\phi}, \hat{\psi} \} \equiv -\mathcal{C}^1 \{ \hat{\phi}^p, \hat{\psi}^p \} + \mathcal{C}^0 \{ \hat{\phi}, \hat{\psi} \}$$

The time discretization scheme used for the magnetic compatibility condition must be the same as that used for integration of the induction equation. In (5.145) we used the first-order implicit Euler scheme. In addition to the particular and test solutions, the final solution from the preceding timestep is necessary to evaluate the magnetic compatibility condition.

Evaluation of $\hat{\psi}_l^Y$:

The test functions $\hat{\psi}_l^Y$ and their derivatives $\partial_r \hat{\psi}_l^Y$ and $\partial_z \hat{\psi}_l^Y$ can be evaluated using (5.118) and (5.122) at the collocation points of either Chebyshev or radial polynomials, depending on whether the values are to be evaluated at the lateral or horizontal boundary. These values must to be transformed into spectral space before entering them into the influence matrix.

One can notice that the form of the radial dependence of $\hat{\phi}_l^Y \sim \rho^{-(l+m)}$ is very ill-conditioned for larger values of l and m . The reason for using this form of test functions was to simplify the presentation of the method. A possible better-conditioned method would be to solve the external Laplace problem for the test functions numerically in spherical coordinates mapping the semi-infinite range of the spherical radius ρ to a finite interval and then using Chebyshev polynomials. We would continue to use spherical harmonics in the angular directions and δ -type Dirichlet boundary conditions.

5.6.5 Elimination of external solution

One can notice that the right-hand sides of the influence matrix systems (5.143)-(5.144) do not depend on the external potential in the vacuum. This means that the coefficients $\{\hat{\sigma}_{f_\phi}, \hat{\sigma}_\phi, \hat{\sigma}_{f_\psi}\}$ defining the internal solution can be found independently from $\{\hat{\phi}_l^{vac}\}$ defining the external potential. The Schur factorization can be performed on the influence matrix: we can write the influence matrix system in a block-matrix form

$$\left[\begin{array}{c|c} A & B \\ \hline C & D \end{array} \right] \begin{bmatrix} \sigma \\ \phi^{vac} \end{bmatrix} = \begin{bmatrix} \alpha \\ \beta \end{bmatrix} \quad (5.146)$$

where A, B, C, D correspond to the matrix blocks in (5.143)-(5.144) separated by the thick solid lines. From (5.146) we obtain

$$\begin{aligned} A\sigma + B\phi^{vac} &= \alpha \\ C\sigma + D\phi^{vac} &= \beta \end{aligned} \Rightarrow \begin{aligned} \phi^{vac} &= D^{-1}(\beta - C\sigma) \\ &\Downarrow \\ (A - BD^{-1}C)\sigma &= (\alpha - BD^{-1}\beta) \end{aligned}$$

Therefore, we can define the influence matrix system for the internal problem as:

$$\mathbf{I}^{int} \sigma = RHS^{int}$$

where

$$\mathbf{I}^{int} \equiv (A - BD^{-1}C) \quad RHS^{int} \equiv (\alpha - BD^{-1}\beta)$$

The influence matrix \mathbf{I}^{int} can be constructed once and for all in the preprocessing step. The right-hand-side vector RHS^{int} must be evaluated at each timestep. The inverse matrix D^{-1} as well as $(\mathbf{I}^{int})^{-1}$ must be evaluated after regularizing the entire influence matrix (5.143) or (5.144) by the method explained in section 5.4.3.

5.7 Concluding remarks

In this chapter we have presented the linear part of the spectral Navier-Stokes solver for incompressible flows in toroidal-poloidal formulation. The classic τ -method for satisfaction of boundary conditions for the Poisson problem has been formulated: first, for one-dimensional problems in either axial or radial directions and then, for a two-dimensional solver in (r, z) plane. On top of the Poisson solver we have built our *multi-step* spectral solver in the toroidal-poloidal variable formulation. The *influence matrix* method for satisfaction of the high differential order coupled boundary conditions has been explained in detail. The relation between the influence matrix method and the classic Green function method has been outlined.

We have addressed technical issues concerning the singular character of the influence matrix. We have proposed the singular value decomposition for elimination of the singular vectors/values from the influence matrix. The problem of inversion of a regularized, but very ill-conditioned influence matrix, was solved by performing an appropriate scaling.

The precision of the method has been checked against exact polynomial solutions and against the numerically obtained solutions of the Stokes problem. The solver has been proved to have the properties expected of a spectral-precision method.

A method for solving the induction equation for the magnetic field in the toroidal-poloidal formulation has been introduced. By using an analogous methodology to that presented for the hydrodynamic Navier-Stokes solver we succeeded in defining the problem for the magnetic potentials satisfying the continuity conditions between the internal and external magnetic fields. The method allows us to solve for the internal field without determining the external field. Practical implementation of this method is left for the future work.

Chapter 6

Stability/Validation

In the preceding chapter we presented the spectral solver for the Stokes/Navier-Stokes equations, focusing on the problem of satisfaction of the boundary conditions in potential formulation. In this chapter we complete the presentation of the entire algorithm by discussing in detail problems concerning evaluation of the nonlinear term of the Navier-Stokes equations. We also discuss arguments for the choice of the time integration scheme best suited for the problem in hand. We validate our Navier-Stokes solver on 2D and 3D test problems well documented in the literature. Finally we discuss the convergence and stability properties of the complete implementation of the Navier-Stokes solver.

6.1 Nonlinear term

In order to evaluate the nonlinear term (6.2) the point-by-point product of functions must be computed. The product of two functions in physical space correspond to their convolution in spectral space (which is the statement of the *convolution theorem*):

$$\widehat{fg} = \hat{f} * \hat{g} \equiv \int \hat{f}(k') \hat{g}(k - k') dk' \quad \leftrightarrow \quad \left[\widehat{fg} \right]_k = \sum_{i+j=k} \hat{f}_i \hat{g}_j \quad \begin{array}{l} i, j \in [0, N-1] \\ k \in [0, 2(N-1)] \end{array} \quad (6.1)$$

Convolution of two functions sampled at N collocation points has therefore complexity of $O(N^2)$ and can be further optimized by using the fast transform based on the FFT algorithm (see Orszag [66]). We use the *pseudo-spectral* approach, introduced by Orszag [67], which is an alternative to computing the convolution and consists of the following steps:

- transforming the spectral field into physical space,
- computing functions products at collocation points corresponding to the Gauss-type quadrature abscissas for the spectral expansion used for the spectral solver,
- transforming the computed products back to spectral space.

In terms of computational complexity, the *pseudo-spectral* approach is equivalent to computing the convolution since the transformation spectral \leftrightarrow physical can be optimized using the FFT algorithm.

In the potential problem stated in (3.49) and (3.52) the nonlinear terms $s_{\psi_u} \equiv \hat{\mathbf{e}}_z \cdot \nabla \times \mathbf{s}_u$, $s_{\phi_u} \equiv \hat{\mathbf{e}}_z \cdot \nabla \times \nabla \times \mathbf{s}_u$ and $s_{\phi_B} \equiv \hat{\mathbf{e}}_z \cdot \mathbf{s}_B$, $s_{\psi_B} \equiv \hat{\mathbf{e}}_z \cdot \nabla \times \mathbf{s}_B$ can be computed in the spectral space once \mathbf{s}_u and \mathbf{s}_B are evaluated. We recall the form of \mathbf{s}_u and \mathbf{s}_B given also in (3.49c) and (6.2):

$$\mathbf{s}_u \equiv (\mathbf{u} \cdot \nabla) \mathbf{u} - (\mathbf{B} \cdot \nabla) \mathbf{B} \quad (6.2a)$$

$$\mathbf{s}_B \equiv -\nabla \times (\mathbf{u} \times \mathbf{B}) \quad (6.2b)$$

Terms (6.2) involve evaluation of the following generic nonlinear terms:

$$(\mathbf{f} \cdot \nabla) \mathbf{f} \quad (6.3a)$$

$$\mathbf{f} \times \mathbf{g} \quad (6.3b)$$

Computing (6.3a) in cylindrical coordinates require transformation of 12 three-dimensional fields into physical space. After that step 3 more inverse transforms for the three components of the nonlinear term must be computed. The total cost is therefore 15 transforms of a three-dimensional fields. The second form (6.3b) requires a total of 9 transformations. For situations where the curl of the Navier-Stokes equations is taken, the curl of the nonlinear term (6.3a) can be written as

$$\begin{aligned} \nabla \times [(\mathbf{f} \cdot \nabla) \mathbf{f}] &\equiv \nabla \times \left[-\mathbf{f} \times (\nabla \times \mathbf{f}) + \frac{1}{2} \nabla (\mathbf{f} \cdot \mathbf{f}) \right] \\ &\Downarrow \\ \nabla \times [(\mathbf{f} \cdot \nabla) \mathbf{f}] &\equiv -\nabla \times [\mathbf{f} \times (\nabla \times \mathbf{f})] \end{aligned} \quad (6.4)$$

where the right-hand-side of (6.4) requires only 9 transformations instead of 15.

Since, in this chapter, we will consider evaluation of the nonlinear term in the hydrodynamic problem ($\mathbf{B} \equiv 0$) only, then we will restore the simplified notation from the preceding chapter:

$$\mathbf{s} \equiv \mathbf{s}_u, \quad \psi \equiv \psi_u, \quad \phi \equiv \phi_u, \quad s_\psi \equiv s_{\psi_u}, \quad s_\phi \equiv s_{\phi_u}$$

Using (6.4) we can write the nonlinear terms s_ψ, s_ϕ in the following form:

$$s_\psi \equiv \hat{\mathbf{e}}_z \cdot \nabla \times \mathbf{s} = -\hat{\mathbf{e}}_z \cdot \nabla \times (\mathbf{u} \times \boldsymbol{\omega}) \quad (6.5a)$$

$$s_\phi \equiv -\hat{\mathbf{e}}_z \cdot \nabla \times \nabla \times \mathbf{s} = \hat{\mathbf{e}}_z \cdot \nabla \times \nabla \times (\mathbf{u} \times \boldsymbol{\omega}) \quad (6.5b)$$

where $\boldsymbol{\omega} \equiv \nabla \times \mathbf{u}$ is the vorticity.

6.1.1 Evaluation of $-\mathbf{u} \times \boldsymbol{\omega}$

Since all differential operators acting in the radial direction have a recurrence implementation (see section 4.4.4) which preserves the parity between the operand and solution, thus the modified methodology for evaluating of the components of the velocity \mathbf{u} and vorticity $\boldsymbol{\omega}$ as well as

of the nonlinear term components must be defined. In the cylindrical coordinates the velocity and vorticity are defined using the toroidal and poloidal potentials as:

$$\mathbf{u} \equiv \left(\frac{1}{r} \partial_\theta \psi_u + \partial_{rz}^2 \phi_u \right) \hat{\mathbf{e}}_r + \left(\frac{1}{r} \partial_{\theta z}^2 \phi_u - \partial_r \psi_u \right) \hat{\mathbf{e}}_\theta + (\Delta_h \phi_u) \hat{\mathbf{e}}_z \quad (6.6)$$

$$\begin{aligned} \boldsymbol{\omega} &\equiv \left(\frac{1}{r} \partial_\theta u_z - \partial_z u_\theta \right) \hat{\mathbf{e}}_r + (\partial_z u_r - \partial_r u_z) \hat{\mathbf{e}}_\theta + \frac{1}{r} (\partial_r r u_\theta - \partial_\theta u_r) \hat{\mathbf{e}}_z = \\ &= \left(\partial_{rz}^2 \psi_u - \frac{1}{r} \partial_\theta \Delta \phi_u \right) \hat{\mathbf{e}}_r + \left(\frac{1}{r} \partial_{\theta z}^2 \psi_u - \partial_r \Delta \phi_u \right) \hat{\mathbf{e}}_\theta + \frac{1}{r} (-\Delta_h \psi_u) \hat{\mathbf{e}}_z \end{aligned} \quad (6.7)$$

These expressions must be transformed into a form which preserves the parity of radial polynomials and make use only of the following set of radial operators:

$$\left\{ r^2, \frac{1}{r^2}, r \partial_r, r^2 \Delta_h, \Delta_h \equiv \frac{1}{r^2} (r^2 \Delta_h) \right\} \quad (6.8)$$

This is possible when instead of transforming \mathbf{u} and $\boldsymbol{\omega}$ into physical space one transforms the modified fields:

$$\mathbf{u}^* \equiv r u_r \hat{\mathbf{e}}_r + r u_\theta \hat{\mathbf{e}}_\theta + u_z \hat{\mathbf{e}}_z = (\partial_\theta \psi_u + r \partial_{rz}^2 \phi_u) \hat{\mathbf{e}}_r + (\partial_{\theta z}^2 \phi_u - r \partial_r \psi_u) \hat{\mathbf{e}}_\theta + (\Delta_h \phi_u) \hat{\mathbf{e}}_z \quad (6.9a)$$

$$\boldsymbol{\omega}^* \equiv r \omega_r \hat{\mathbf{e}}_r + r \omega_\theta \hat{\mathbf{e}}_\theta + \omega_z \hat{\mathbf{e}}_z = (\partial_\theta u_z - \partial_z u_\theta^*) \hat{\mathbf{e}}_r + (\partial_z u_r^* - r \partial_r u_z) \hat{\mathbf{e}}_\theta + (-\Delta_h \psi_u) \hat{\mathbf{e}}_z \quad (6.9b)$$

where the $\hat{\mathbf{e}}_r$ and $\hat{\mathbf{e}}_\theta$ components of \mathbf{u} and $\boldsymbol{\omega}$ have been multiplied by r . Modified vector components $u_r^* \equiv r u_r$, $u_\theta^* \equiv r u_\theta$, $\omega_r^* \equiv r \omega_r$, $\omega_\theta^* \equiv r \omega_\theta$ have the same parity as the scalar functions ψ and ϕ and can therefore be treated using the same differential operators (6.8). The modified nonlinear term \mathbf{s}^* obtained from (6.9) has the following form:

$$\begin{aligned} \mathbf{s}^* &= r s_r \hat{\mathbf{e}}_r + r s_\theta \hat{\mathbf{e}}_\theta + s_z \hat{\mathbf{e}}_z = -\mathbf{u}^* \times \boldsymbol{\omega}^* = \\ &= -(u_\theta^* \omega_z - u_z \omega_\theta^*) \hat{\mathbf{e}}_r - (u_z \omega_r^* - u_r^* \omega_z) \hat{\mathbf{e}}_\theta - \frac{1}{r^2} (u_r^* \omega_\theta^* - u_\theta^* \omega_r^*) \hat{\mathbf{e}}_z \end{aligned}$$

and finally the nonlinear terms used in (3.49) can be written as

$$s_\psi \equiv \hat{\mathbf{e}}_z \cdot \nabla \times \mathbf{s} = \frac{1}{r^2} [r \partial_r s_\theta^* - \partial_\theta s_r^*] \quad (6.10a)$$

$$s_\phi \equiv -\hat{\mathbf{e}}_z \cdot \nabla \times \nabla \times \mathbf{s} = -\frac{1}{r^2} [\partial_z (r \partial_r s_r^* + \partial_\theta s_\theta^*) - r^2 \Delta_h s_z] \quad (6.10b)$$

6.1.2 Regularity of the nonlinear term

Our multi-step spectral solver **not only** requires the right-hand-side \mathbf{s} to be regular (i.e. to obey the rules of correct parity and polynomial order) but also it requires this for its curl and the double curl. This means that the nonlinear term \mathbf{s} , obtained using the pseudo-spectral method, must be **super-regular**. While using the appropriate transforms for converting the modified physical field \mathbf{s}^* into its spectral representation ensures the regularity of $\hat{\mathbf{s}}^*$ then this cannot

ensure the regularity of s_ψ and s_ϕ . Acting with r^{-2} operator in (6.10) requires the operand to be dividable by r^2 in order to avoid a singular behavior. Even stronger conditions must be satisfied if one want to match the regularity condition for all Fourier modes of the nonlinear terms s_ψ and s_ϕ , for which the radial polynomials must be at least of order $O(r^m)$. To summarize, the necessary condition for regularity of the nonlinear term's Fourier mode m is:

$$\frac{1}{r^2} [r\partial_r s_\theta^* - im s_r^*] = \sum_{n \geq 0} \eta_n r^{2n+m} \quad (6.11a)$$

$$-\frac{1}{r^2} [\partial_z (r\partial_r s_r^* + im s_\theta^*) - r^2 \Delta_h s_z] = \sum_{n \geq 0} \zeta_n r^{2n+m} \quad (6.11b)$$

where we have further simplified notation by using $s \equiv \hat{s}$. The Nonlinear term \mathbf{s} must obey the same regularity rules as the velocity \mathbf{u} :

$$s_r = \sum_{n \geq 0} a_n r^{2n+|m-1|} \quad (6.12a)$$

$$s_\theta = \sum_{n \geq 0} b_n r^{2n+|m-1|} \quad (6.12b)$$

$$s_z = \sum_{n \geq 0} c_n r^{2n+m} \quad (6.12c)$$

but these are not all the conditions that \mathbf{s} must satisfy. It can be easily verified that, by substituting an arbitrary \mathbf{s} of the form (6.12) into (6.11), the obtained expression does not correspond to the sums stated to the right of (6.11). The nonlinear term \mathbf{s} is, however, not arbitrary: if no error is introduced by evaluation of the nonlinear term then, under condition that \mathbf{u} and $\boldsymbol{\omega}$ used to compute \mathbf{s} were regular, the regularity conditions stated in (6.11) and (6.12) are satisfied. One can verify this by substituting a regular form of velocity \mathbf{u} (being defined in the same way as (6.12)) into construction sequence (6.9)-(6.10). While performing this substitution, the singular terms can appear but they are canceled by opposite-sign singularities coming from different terms. Therefore it seems necessary that all terms be computed accurately in order to ensure this cancellation and, by consequence, the regularity of the final solution.

Unfortunately in a numerical code one should not expect this condition to be met. Spectral representation of the vector components of the nonlinear term \mathbf{s}^* are affected by several types of error: *aliasing*, truncation and limited precision of forward and back transforms. If we perform a full *dealiasing* (padding with twice the number of coefficients instead of the commonly used $\frac{3}{2}$ -rule) and apply the differential operator on the extended vectors of $2N$ coefficients then this error can be limited only to the negligible error of spectral \rightarrow physical \rightarrow spectral transformations. This approach is very costly, taking into account that the evaluation of the nonlinear term has complexity at best $O(N^3 \log_2 N)$. Full dealiasing will multiply the time necessary for evaluating of the nonlinear term by a factor ≈ 4.5 .

Matsushima & Marcus [58] suggest that all terms that could potentially suffer, in the spectral space, from singular operations (like dividing by r) should be evaluated in physical space (at collocation points excluding the coordinate origin) and transformed back to the spectral space using the radial transform ensuring the correct polynomial order for a given Fourier mode. This approach, while straightforward to apply for the nonlinear term \mathbf{s} , cannot be used

directly for s_ψ and s_ϕ which involve curl and double curl of the nonlinear term. The definition (6.10) involves evaluation of several differential terms that must be evaluated in spectral space. Therefore one would have to divide by r separately for each of these terms so as to perform in spectral space only secure operations (without division by r):

$$\frac{1}{r}\partial_r r s_\theta \Leftrightarrow \frac{1}{r}\partial_r r^2 \frac{s_\theta}{r} = \overbrace{(2+r\partial_r)}^{\text{secure}} \underbrace{\frac{s_\theta}{r}}_{\text{not allowed}}$$

Unfortunately the nonlinear term's components s_r and s_θ cannot be divided by r in physical space and transformed back to the spectral space using the transformation for mode m . They are of order $O(r^{|m-1|})$ and after dividing by r the result would be of order $O(r^{|m-1|-1})$ which is incompatible with transformation defined for mode m requiring $O(r^{|m-1|})$. In particular for $m = 1$ such terms would diverge at $r = 0$. The terms of order $r^{|m-1|-1}$ are subtracted for $m > 0$ while evaluating expressions

$$s_\psi = \frac{1}{r}(\partial_r r s_\theta - im s_r) \quad (6.13a)$$

$$s_\phi = -\frac{1}{r}(\partial_r r s_r + im s_\theta) + \Delta_h s_z \quad (6.13b)$$

In order to be able to annihilate the singular terms already in physical space we will separate the operators present in expressions (6.13) into two parts: "secure", giving the regular solution of order $O(r^m)$ regardless of the accuracy of the operand and "delicate" combination, which depends on accuracy and which we will evaluate in physical space. As an example, we can take the operator $\frac{1}{r^2}(r\partial_r - m)$ which we qualify "secure" because unlike $\frac{1}{r}\partial_r$ it can be applied to terms of order $O(r^m)$ without generating terms in r^{m-2} :

$$\frac{1}{r^2}(r\partial_r - m)r^m = \frac{1}{r^2}(mr^m - mr^m) = 0$$

Similarly, for s_ψ we will write:

$$\begin{aligned} s_\psi &= \frac{1}{r}\partial_r r s_\theta - \frac{im}{r}s_r - \overbrace{\frac{m}{r}s_\theta + \frac{m}{r}s_\theta}^0 = \\ &= \underbrace{\frac{1}{r^2}(r\partial_r - m)}_{\text{secure}} s_\theta^* + \underbrace{\frac{m}{r^2}[s_\theta^* - i s_r^*]}_{\text{delicate}} \end{aligned} \quad (6.14)$$

and for s_ϕ :

$$s_\phi = -\partial_z \left(\underbrace{\frac{1}{r^2}(r\partial_r - m)}_{\text{secure}} s_\theta^* + \underbrace{\frac{m}{r^2}[s_r^* + i s_\theta^*]}_{\text{delicate}} \right) + \underbrace{\Delta_h}_{\text{secure}} s_z \quad (6.15)$$

The horizontal Laplace operator $\Delta_h \equiv \frac{1}{r}\partial_r r\partial_r - \frac{m^2}{r^2}$ has the same property of annihilating r^{m-2} terms. The "delicate" terms can be evaluated in the quasi-physical¹ space because no differential operators acting in the $\hat{\mathbf{e}}_r$ or $\hat{\mathbf{e}}_z$ direction are involved. This evaluation in the quasi-physical space does not suffer from the aliasing errors in the $\hat{\mathbf{e}}_r$ and $\hat{\mathbf{e}}_z$ directions and is secure for dividing by r . Thus the singular terms can be annihilated with better precision in the physical space and then the almost regular combination which we will denote s_u^- and s_u^+ can be transformed back into spectral space using radial transformation compatible with Fourier mode m .

$$\hat{s}^- = \frac{m}{r^2} [(s_u^*)_\theta - i(s_u^*)_r] \quad \hat{s}^+ = \frac{m}{r^2} [(s_u^*)_r + i(s_u^*)_\theta] \quad (6.16)$$

This final transformation $(s^-, s^+) \rightarrow (\hat{s}^-, \hat{s}^+)$ of the almost regular quantities s^- and s^+ ensures, to the machine precision, the regularity of \hat{s}^- and \hat{s}^+ .

Conclusions on evaluation of the nonlinear term

The presented approach guaranties stable evaluation of the potential nonlinear terms s_ψ and s_ϕ because aliasing and truncation errors can appear here only after annihilation of the singular terms. Errors due to the limited precision of a spectral \leftrightarrow physical transforms do not affect seriously evaluation of $\frac{1}{r^2}$ operator in (6.16). For the delicate terms, $\frac{1}{r^2}$ is applied in the physical space where this operation has no severe regularity constraints and after transforming back to the spectral space, regularity is recovered since the transformation for radial polynomials enforces the correct polynomial order for a given Fourier mode m . Operators like $\frac{1}{r^2}(r\partial_r - m)$ or $\Delta_h^m \equiv \frac{1}{r}\partial_r r\partial_r - \frac{m^2}{r^2}$ behave regularly because they do not decrease the polynomial order of the operand.

The expression for s_ψ and s_ϕ can be stated as:

$$s_\psi = \underbrace{\frac{1}{r^2}(r\partial_r - m)s_\theta^*}_{\text{spectral space}} + \underbrace{s^-}_{\text{physical space}}$$

$$s_\phi = \underbrace{\frac{1}{r^2} \left(-\partial_z[(r\partial_r - m)s_r^* + \underbrace{s^+}_{\text{physical space}}] + r^2 \Delta_h^m s_z \right)}_{\text{spectral space}}$$

The additional cost that must be paid for applying this methodology is to perform one additional transform for s^- ($s^+ = -is^-$). This changes the cost of evaluation of the nonlinear term measured in the number of spectral \leftrightarrow physical transformations from 9 to 10. This can be considered negligible.

¹By quasi-physical, we mean that the only transformation performed is in the $\hat{\mathbf{e}}_\theta$ direction where the differential operator $\partial_\theta \leftrightarrow im$ is diagonal and can be easily evaluated.

6.2 Time integration

As was already suggested we will use an implicit scheme for the linear diffusive terms while treating all other terms with an explicit method. For choosing a particular scheme at hand, one should take into account the properties of implicit schemes for a given order. We consider six unconditionally stable (A-stable²) methods: first-order backward Euler, Crank-Nicolson (trapezoidal), backward differentiation (retarded Euler), Adams type, Lees type and two-step trapezoidal. The corresponding time-step evolution operators differ in their capability of damping the high spatial frequencies in an evolving function.

This property is of particular interest to us since the von Kármán flow has boundary layers situated next to the rotating cylinder bases. For higher Reynolds numbers, this layer can be very thin which requires high-frequency modes to represent it spectrally. Additionally the singular character of the boundary conditions in the cylinder corners generates and requires high frequency modes³. Hopefully these effects are most pronounced in the proximity of the boundaries, where the axial Chebyshev and radial polynomial grid is finest. In situations with counter-rotating bases, a shear layer can also require high frequency modes in order to be well represented.

We mention these phenomena to attract the reader's attention to the fact that the von Kármán flow, because of its nature, generates small scales, i.e. high spatial frequencies, and a time-integration scheme should take this fact into account in order to ensure stability of the solver. A necessary condition for spectral methods to work is that the spectral coefficients representing the solution should decay with their index or frequency. The nonlinear term in the Navier-Stokes equation can be seen as a generator and amplifier of high frequencies while the viscous term damps these high frequencies. The intensity of this damping depends on the particular time integration scheme and on the way the Laplacian is evaluated. For systems naturally generating higher frequencies (e.g. von Kármán flow) the damping must be strong enough to oppose the effect of the nonlinear term.

We present a brief and simplified analysis of this property for a one-dimensional diffusion equation

$$\frac{\partial u}{\partial t} = \nu \Delta u$$

For reasons of simplicity we will represent u in the Fourier basis (*von Neumann stability analysis*) rather than in Chebyshev or radial polynomials bases. This analysis will therefore have only qualitative meaning since in this approach the effect of boundaries is neglected. This is, however, sufficient to identify general properties of the time discretization schemes discussed. We then have

$$u(x, t) = \sum_k \hat{u}(k, t) e^{ikx}$$

A general two-step time integration scheme can be written after Beam & Warming [5] as follows:

$$(1 + \zeta) \hat{u}^{n+1} - (1 + 2\zeta) \hat{u}^n + \zeta \hat{u}^{n-1} = \underbrace{\Delta t \nu}_{\epsilon} (-k^2) \left[\theta \hat{u}^{n+1} + (1 - \theta + \eta) \hat{u}^n - \eta \hat{u}^{n-1} \right] \quad (6.18)$$

²A-stable methods can be at most second-order accurate.

³While the regularization of the boundary condition establishes a maximal sufficient frequency, this can be much higher than the frequency necessary to represent the flow far from the boundaries.

where we have substituted the eigenvalues $\text{spec}(\Delta) = -k^2$ in place of the Laplace operator. For unconditional stability, ζ, θ, η must satisfy

$$\begin{aligned}\theta &\geq \eta + \frac{1}{2} \\ \zeta &\geq -\frac{1}{2} \\ \zeta &\leq \theta + \eta - \frac{1}{2}\end{aligned}$$

and if $\eta = \zeta - \theta + 1/2$ then the scheme is second-order accurate.

We wish to write a two-step iterative process (6.18) in a one-step form of type

$$G_1 \bar{u}^{n+1} = G_0 \bar{u}^n \quad \Rightarrow \quad \bar{u}^{n+1} = \underbrace{G_1^{-1} G_0}_G \bar{u}^n \quad (6.19)$$

where G is called the *amplification factor*. To do so we introduce an auxiliary variable \hat{z} so that (6.18) can be written in matrix notation (6.19) by defining

$$\begin{aligned}\bar{u}^n &= \begin{bmatrix} \hat{u}^n \\ \hat{z}^n \end{bmatrix} \\ \hat{z}^n &= \hat{u}^{n-1}\end{aligned}$$

This makes it possible to write (6.18) using only two time steps $n+1$ and n :

$$\begin{aligned}(1 + \zeta + k^2 \epsilon \theta) \hat{u}^{n+1} &= [1 + 2\zeta - k^2 \epsilon (1 - \theta + \eta)] \hat{u}^n - (\zeta + k^2 \epsilon \eta) \hat{z}^n \\ \hat{z}^{n+1} &= \hat{u}^n\end{aligned} \quad (6.20)$$

so that (6.19) corresponding to (6.20) can be written as:

$$\begin{aligned}\begin{bmatrix} 1 + \zeta + k^2 \epsilon \theta & 0 \\ 0 & 1 \end{bmatrix} \begin{bmatrix} \hat{u}^{n+1} \\ \hat{z}^{n+1} \end{bmatrix} &= \begin{bmatrix} 1 + 2\zeta - k^2 \epsilon (1 - \theta + \eta) & k^2 \epsilon \eta - \zeta \\ 1 & 0 \end{bmatrix} \begin{bmatrix} \hat{u}^n \\ \hat{z}^n \end{bmatrix} \\ G_1 \bar{u}^{n+1} &= G_0 \bar{u}^n\end{aligned}$$

The *amplification matrix* $G \equiv G_1^{-1} G_0$ is characterized by its eigenvalues μ_1, μ_2 which can be found from the characteristic polynomial $P(\mu)$ of G :

$$P(\mu) = (1 + \zeta + k^2 \epsilon \theta) \mu^2 - (1 + 2\zeta - k^2 \epsilon (1 - \theta + \eta)) \mu - k^2 \epsilon \eta + \zeta$$

The values of θ, ζ, η corresponding to the time integration schemes considered are presented in table 6.2.

Schemes that attenuate the high frequencies have to satisfy the criterion

$$\lim_{k \rightarrow \infty} \max\{|\mu_1(k)|, |\mu_2(k)|\} < 1 \quad (6.21)$$

Method	θ	ζ	η	Order	μ_1, μ_2	$\lim_{k \rightarrow \infty} \max\{\mu_1, \mu_2\} $
Backward Euler	1	0	0	1	$0, \frac{1}{1+k^2\epsilon}$	0
Crank-Nicolson	1/2	0	0	2	$0, \frac{2-k^2\epsilon}{2+k^2\epsilon}$	1
Backward differentiation	1	1/2	0	2	$\frac{2 \pm \sqrt{1-2k^2\epsilon}}{3+2k^2\epsilon}$	0
Adams type	3/4	0	-1/4	2	$\frac{2 \pm \sqrt{4-4k^2\epsilon-3k^4\epsilon^2}}{4+3k^2\epsilon}$	$\sqrt{3}/3$
Lees type	1/3	-1/2	-1/3	2	$-\frac{k^2\epsilon \pm \sqrt{-3k^4\epsilon^2+9}}{3+2k^2\epsilon}$	1
Two-step trapezoidal	1/2	-1/2	-1/2	2	$\pm \frac{\sqrt{1-k^4\epsilon^2}}{1+k^2\epsilon}$	1

Table 6.1: List of A-stable one- and two-step schemes (based on Beam & Warming [6])

Asymptotic values for all the schemes as well as an expression for μ_1, μ_2 are presented in table 6.2. Only three methods have the property (6.21): backward Euler, backward differentiation and Adams type. The behavior of μ_1, μ_2 as of the functions of k for fixed $\epsilon = 1$ is presented on figure 6.2 for all schemes considered. We decided to use the first order backward Euler scheme

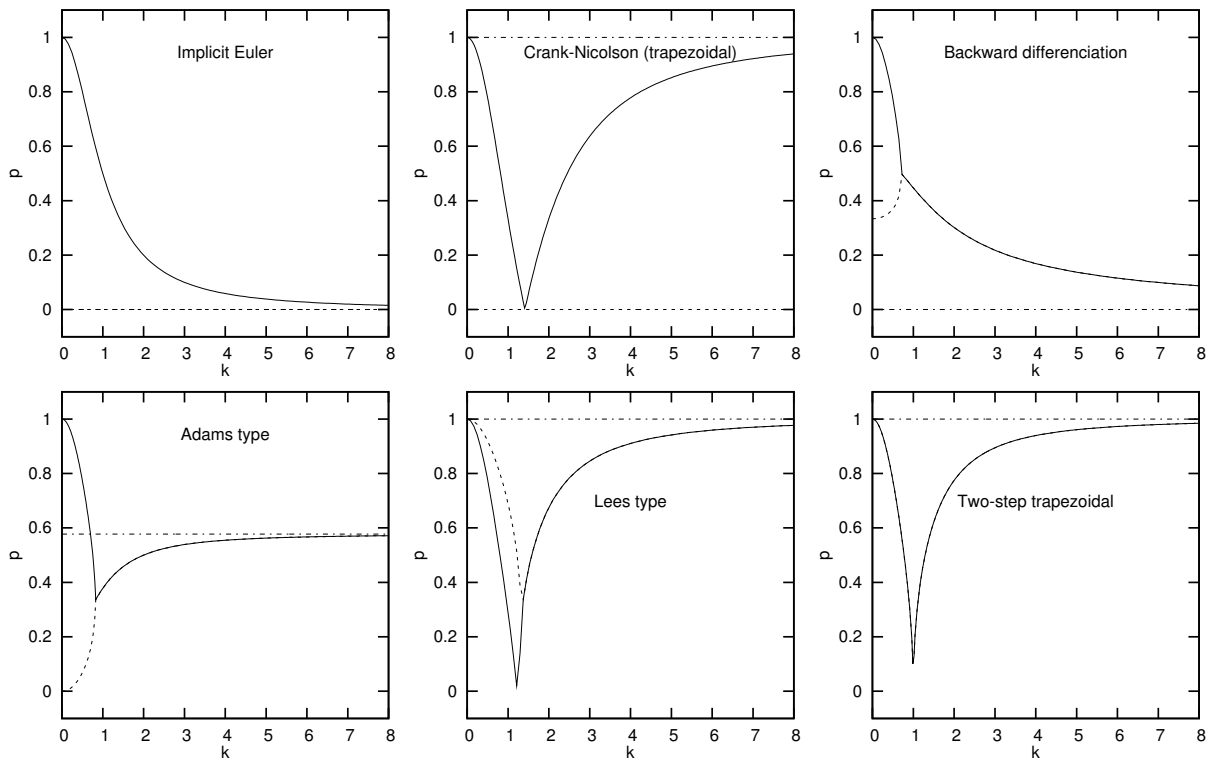


Figure 6.1: Plots of $p = \{ |\mu_1(k)| - \text{solid line}, |\mu_2(k)| - \text{dashed line}, \lim_{k \rightarrow \infty} \max\{|\mu_1(k)|, |\mu_2(k)|\} - \text{dot-dash line} \}$ for A-stable schemes.

for linear terms because it attenuates the high frequencies faster than all other methods. If second order accuracy is needed then the backward differentiation represent a natural choice

and the Adams-type scheme can possibly be considered for situations where weaker damping of high-frequency modes is sufficient. Tests performed with the Crank-Nicolson method confirmed that for this scheme, nonlinear simulation was unstable even for quite small Reynolds numbers $Re \approx 300$. This behavior was also observed for the von Kármán flow by Speetjens [81] and Lopez *et al.* [47] and also by Marcus [53] in the Taylor-Couette configuration. Choosing smaller values of the time-step helps very little in this situation since $\Delta t \sim k^{-2}$ for constant ϵ and the maximal time-step quickly becomes very small for higher spatial resolutions. The nonlinear term is treated by a second order explicit Adams-Bashforth scheme:

$$\mathbf{s}^{n+1} = \frac{1}{2} \left(3\mathbf{s}^n - \mathbf{s}^{n-1} \right)$$

so that the backward Euler/Adams-Bashforth time integration scheme for the Navier-Stokes equation can be written as

$$(\mathbb{1} - \epsilon\Delta)\mathbf{u}^{n+1} = \mathbf{u}^n + \frac{\Delta t}{2} \left(3\mathbf{s}^n - \mathbf{s}^{n-1} \right)$$

and the corresponding scheme for potentials $\hat{\psi}$ and $\hat{\phi}$ takes the following form:

$$(\mathbb{1} - \epsilon\Delta)\Delta_h\psi^{n+1} = \Delta_h\psi^n + \frac{\Delta t}{2} \left(3s_\psi^n - s_\psi^{n-1} \right)$$

$$(\mathbb{1} - \epsilon\Delta)\Delta\Delta_h\phi^{n+1} = \Delta\Delta_h\phi^n + \frac{\Delta t}{2} \left(3s_\phi^n - s_\phi^{n-1} \right)$$

The maximal time step Δt depends on the Reynolds number. Typically starting from state

Re	configuration	Δt	resolution ($M \times K \times N$)
< O(500)	2D	0.05 - 0.1	$1 \times 32 \times 16$
500 - 1000	2D	0.02 - 0.05	$1 \times 64 \times 32$
1000 - 3000	2D	0.01 - 0.02	$1 \times 96 \times 48$
3000 - 5000	2D	0.005 - 0.01	$1 \times 128 \times 64$
5000 - 10000	2D	0.001 - 0.0025	$1 \times 180 \times 90$
< O(500)	3D	0.04 - 0.1	$8 \times 64 \times 32$
500 - 1000	3D	0.01 - 0.04	$16 \times 80 \times 40$
1000 - 3000	3D	0.025 - 0.01	$32 \times 100 \times 60$
3000 - 5000	3D	0.001 - 0.0025	$(64-96) \times 128 \times 80$

Table 6.2: Typical values of time-step Δt and resolution for different configurations. Typical steepness of the regularization profile is $\delta \approx 0.01$

$\mathbf{u} = 0$ requires 4-10 smaller Δt compared to that which can be used for evolving a fully developed state at the same Reynolds number. This is because the state $\mathbf{u} = 0$ is incompatible with the boundary conditions. In first few iterations a boundary layer is created near the rotating cylinder lids. This also requires higher spatial resolution. This can be avoided by performing about 100 initial steps of the linear Stokes solver ($\hat{s} = 0$). In table 6.2 we present the values of Δt and spatial resolutions typically used for performing nonlinear simulations for different values

of Re . A comprehensive study of stability properties of different combinations of temporal and spatial discretization schemes is provided by Hirsch [36].

6.3 Tests

6.3.1 Axisymmetric rotor-stator configuration

The code was first tested on a well documented problems in the axisymmetric rotor-stator configuration for aspect ratio $h = 2$. The first test is the reproduction of the characteristic steady state for $Re \approx 1850$ where the flow exhibits two recirculation bubbles (one large and the other much smaller) situated approximately at $(r = 0, z = 1/2)$ and $(r = 0, z = 0)$. The contour plot

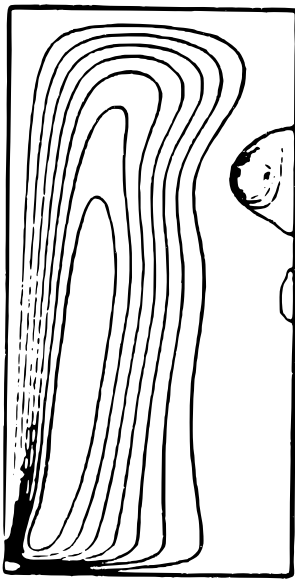


Figure 6.2: Contours of Stokes poloidal streamfunction η (from Daube [17]). $Re = 1850$, $h = 2$ (rotor-stator).

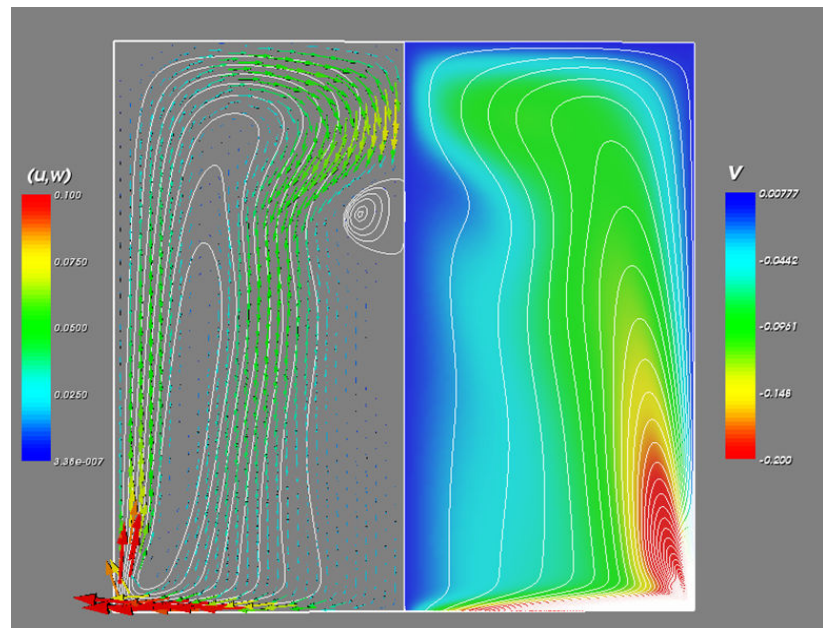


Figure 6.3: Rotor-stator configuration for $Re = 1850$ and the aspect ratio $h = 2$. Left half of the figure represents contours of the poloidal streamfunction η superposed with vector plot of poloidal velocity field $u_r \hat{e}_r + u_z \hat{e}_z$. The right half visualizes contours of toroidal streamfunction σ . The color map represents intensity of the toroidal flow u_θ .

of the Stokes streamfunctions defined as

$$\sigma(r, z) = -r \partial_r \psi_u^{m=0}(r, z) \quad \eta(r, z) = -r \partial_r \phi_u^{m=0}(r, z) \quad (6.23)$$

presented on figure 6.3 matches very well the one presented by Daube [17] (figure 6.2) and is similar to those of Lopez & Shen [48] but obtained for the aspect ratio $h = 2.5$. A quantitative matching between our results and the previous findings by Daube [17] and Lugt & Abboud [52] is established by comparing the profiles of axial velocity u_z on the cylinder's axis (see figure 6.5). This test shows an excellent agreement between our results obtained using poloidal-

toroidal formulation (fig 6.5b) and the *velocity-vorticity* code (fig. 6.5a).

It was observed experimentally by Escudier [24] and numerically by Daube & Sorensen [18], Lopez [46], Daube [17], Gelfgat *et al.* [29] and Speetjens [81] that this flow undergoes a Hopf bifurcation toward a flow oscillating with a frequency approximately 0.25 times the rotation frequency. This transition occurs at a Reynolds number near 2600. In this test we found the frequency $f = 0.0377$ which corresponds to the period $T = 26.55$. This result falls into the range of values previously found for this configuration (see table 6.3.1) and the remaining differences can be most probably attributed to the differences in the treatment of the boundary conditions (regularization). The simulation was performed at the time step $\Delta t = 0.01$ and high spatial resolution $K \times N = 140 \times 70$ in order to well represent the sharp regularization profile corresponding to $\delta = 0.06$ imposed on the lateral boundary $r = 1$ (see section 4.6.2) as proposed by Lopez & Shen [48] and also used by Speetjens [81]. The time evolution $u_\theta(r = 0.5, z = 0, t)$ was shown on figure 6.6. The normalized power spectrum of these oscillations is presented on figure 6.7.

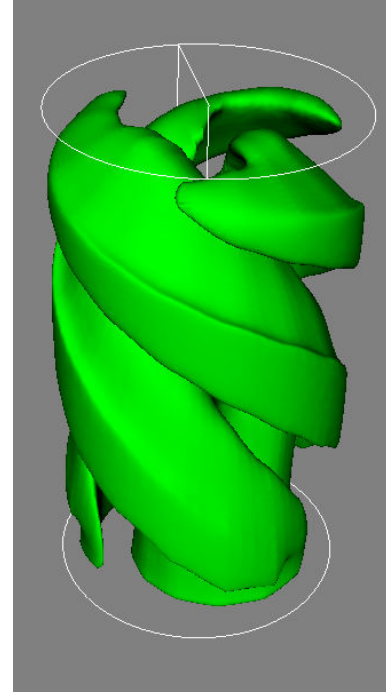


Figure 6.4: Configuration rotor-stator for $Re_c \approx 2150$ and the aspect ratio $h = 3.5$. The graph represents isosurface of axial velocity $u_z \approx 0$.

Method	Reference	T
$\mathbf{u} - \omega$	Daube [17]	25.52
$\eta - \omega$	Daube [17]	25.84
$\mathbf{u} - \omega$	Speetjens [81]	26.61
$\mathbf{u} - p$	Gelfgat <i>et al.</i> [29]	≈ 26.7
$\psi - \phi$	this work	26.55

Table 6.3: Oscillation period in rotor-stator configuration with $h = 2$ at $Re = 2800$.

6.3.2 First instability in 3D

To test the code's calculation of non-axisymmetric instabilities we have chosen a configuration with one rotating and one steady disk (rotor-stator). For the aspect ratio of $h = 3.5$ we found that the first bifurcating mode is $m = 3$ for Reynolds number $Re_c = 2116$. This result is in good agreement with preceding work of Gelfgat *et al.* [29] where the critical Reynolds number was estimated at $Re = 2131$. A characteristic spiral analogous to that visualized by Lopez *et al.* [47] for the same configuration is represented on figure 6.4.

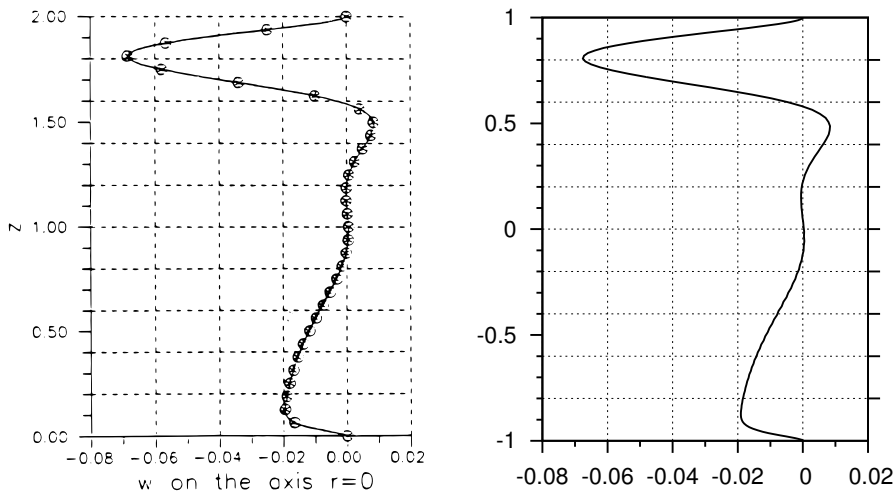


Figure 6.5: Profile of vertical velocity u_z at $r = 0$ for $Re = 1850, h = 2$ (rotor-stator). a) Profile from Daube [17]: results obtained using $\eta - \omega$ (*) and $\mathbf{u} - \omega$ (o) are superposed. b) Profile at $t = 3000$ obtained using poloidal-toroidal decomposition $\psi - \phi$.

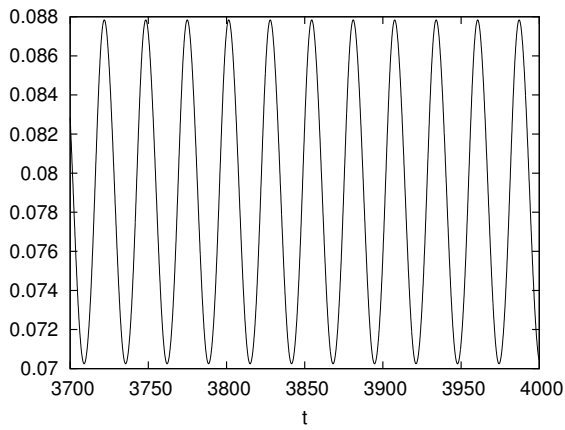


Figure 6.6: Saturated state of time evolution of $u_\theta(r = 0.5, z = 0)$ for the rotor-stator configuration at $Re = 2800, h = 2$.

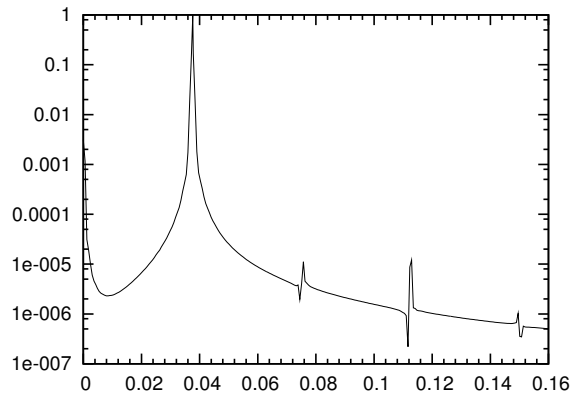


Figure 6.7: Density power spectrum of $u_\theta(r = 0.5, z = 0)$ from figure 6.6.

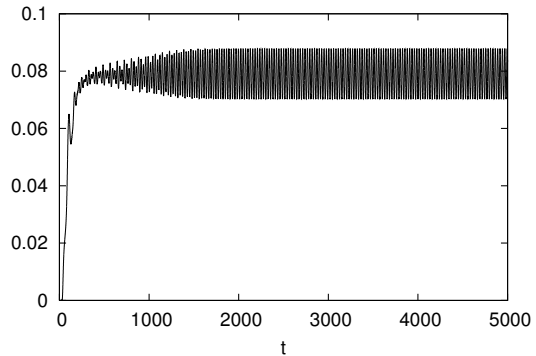
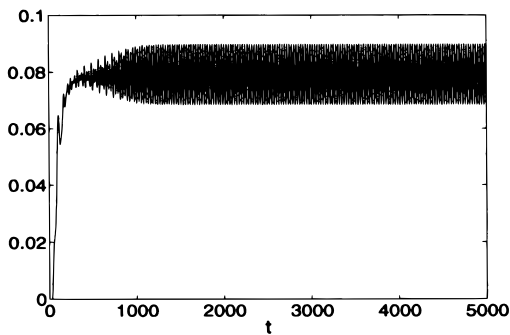


Figure 6.8: Time history of $u_\theta(r = 0.5, z = 0)$ for the rotor-stator configuration at $Re = 2800, h = 2$. Left: from Speetjens [81]. Right: current work.

6.4 Spectral convergence

The Navier-Stokes solver presents qualitatively the same convergence properties as the linear linear solver described in section 5.5. We present on figures (6.9)-(6.11) the decimal logarithm of absolute value of spectral coefficients for Fourier modes $m = 0, 1, 2$. The convergence of the nonlinear solution can be qualified as quasi-exponential, which is most probably due to the singular character of the solution to the Stokes equation near the cylinder corners.

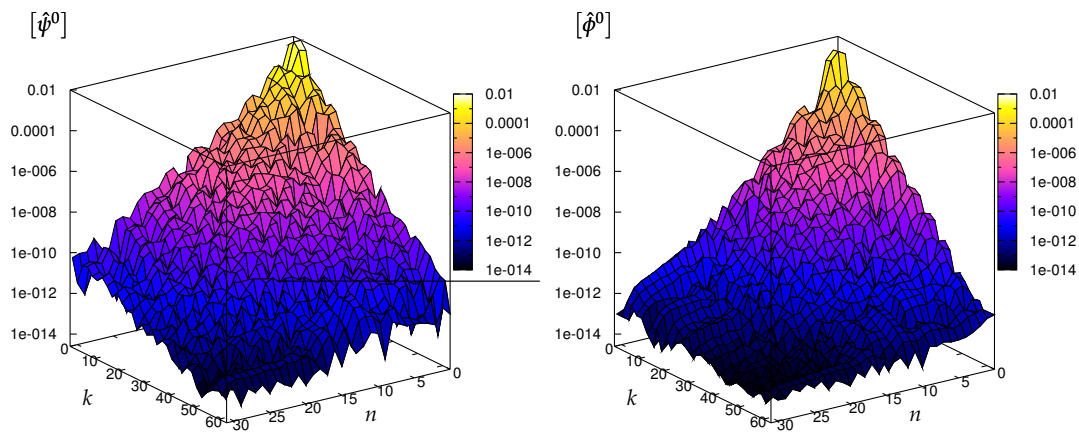


Figure 6.9: Spectral coefficients for $m = 0$, after 100 time-iterations of a nonlinear multi-step Navier-Stokes solver ($Re = 750$, $\Delta t = 0.01$). Resolution used: $K = 64$, $N = 32$. Left: $[\hat{\psi}^0]$; Right: $[\hat{\phi}^0]$.

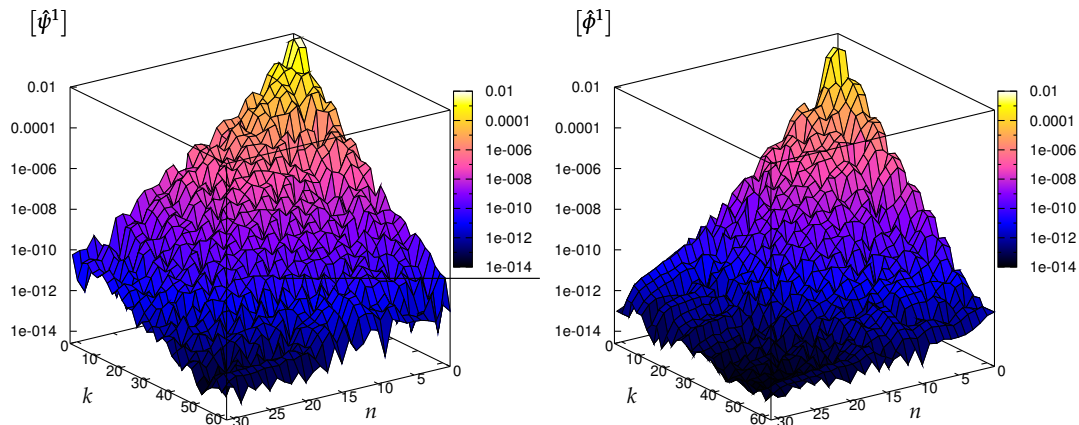


Figure 6.10: Spectral coefficients for $m = 1$, after 100 time-iterations of a nonlinear multi-step Navier-Stokes solver ($Re = 750$, $\Delta t = 0.01$). Resolution used: $K = 64$, $N = 32$. Left: $[\hat{\psi}^1]$; Right: $[\hat{\phi}^1]$.

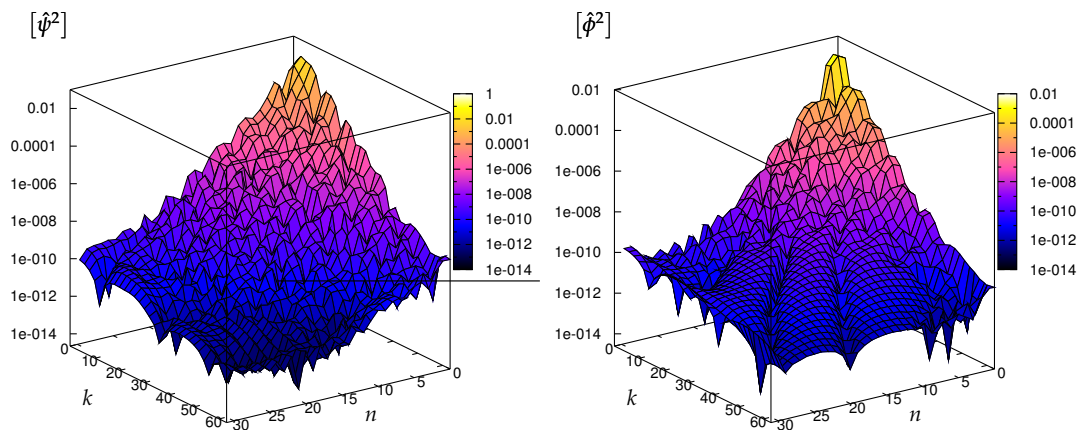


Figure 6.11: Spectral coefficients for $m = 2$, after 100 time-iterations of a nonlinear multi-step Navier-Stokes solver ($Re = 750$, $\Delta t = 0.01$). Resolution used: $K = 64$, $N = 32$. Left: $[\hat{\psi}^2]$; Right: $[\hat{\phi}^2]$.

6.5 Parallelization

As was already mentioned in the preceding chapters, the separability of almost the entire algorithm (except for the nonlinear term) between the Fourier modes make it possible to parallelize the code in a quite straightforward manner. Our code was parallelized using the MPI protocol which made it possible to run even a very time consuming three-dimensional simulations with resolutions like $128 \times 160 \times 90$.

Spectral methods are often considered to be poorly suited for parallelization as they require the exchange of all the data at each timestep of the simulation. In our code, all the necessary data exchange is done within two calls to the *MPI_Alltoall* MPI subroutine treating, in total, 10 three-dimensional fields at each time step. Even though this can seem a quite large operation, on the IBM Power4 architecture with 64 processors we found that the time overhead per timestep due to the data exchange is compensated by more optimal usage of the processor cache memory: each processor of the parallelized code treats smaller data portions which can more easily fit into processor's fast internal memory (cache). We observed that the CPU time consumed by the parallel code treating the same problem as the serial code is often smaller. We should however mention that the efficiency of the parallel code is conditioned by the speed and the latency of the inter-processor network: the IBM Power4 architecture, which we have tested, have particularly fast connection between the nodes which use the mixed model *fast network/shared memory* communication between processors. We can therefore conclude that for modern massively parallel computers parallelization of our pseudo-spectral code not only does not degrade its efficiency but can actually enhance it.

For additional technical information about the MPI parallelization of our code see appendix B.

6.6 Concluding remarks

In this chapter we considered the problem of regularity of the evaluation of the nonlinear term. We discuss the singularities due to truncation and finite precision errors typically committed during forward and backward transforms. We proposed a modified method for evaluating the nonlinear term⁴ in cylindrical geometry. This approach is not sensitive to the transformation nor to the aliasing errors since all potentially irregular operations are performed in physical and not spectral space.

The choice of the first-order *implicit Euler* time integration scheme for the Navier-Stokes solver was justified taking into account the frequency damping properties of several popular unconditionally stable algorithms. We found that the fast attenuation of the high frequencies naturally existing in the von Kármán flow is necessary for guaranteeing the stability of the solver. This is in agreement with observations of Marcus [53] concerning the Taylor-Couette flow as well as with experience of Lopez *et al.* [47] and Speetjens [81] for the von Kármán flow. The backward differentiation scheme used by Lopez *et al.* [47] is a possible candidate method which has the frequency-damping property and is second order accurate.

The Navier-Stokes solver was validated against well-documented test problems in axisymmetric and non-axisymmetric configurations. For all tests performed, we obtained a good agreement with previous results.

The code was parallelized using the MPI protocol which makes it possible to apply even to problems requiring high spatial resolutions.

⁴More exactly: axial component of the curl and double curl of the nonlinear term.

Chapter 7

Applications & perspectives

In this chapter we present the preliminary results of our ongoing projects concerning the turbulent bifurcation and axisymmetric turbulence. These findings can be considered as a presentation of the perspectives for future studies.

7.1 Turbulent bifurcation

The aim of this project is to investigate the bifurcation between two turbulent states in the von Kármán flow (Marié [54], Ravelet *et al.* [74]). This phenomenon was named by its discoverers *global bifurcation* but, since this term already has a well-defined and different meaning in dynamical systems theory, we shall use the term *turbulent bifurcation* instead. Experimentally, when one disk is rotated at high speed, the meridional flow is turbulent and consists of one large toroidal cell. When both disks counter-rotate at high speeds, either one or two toroidal cells may be obtained. Which of the two flows is realized depends on the path followed in increasing the disk rotation speeds. The control parameter for this bifurcation (which in the experiment is the torque difference) presents a strong hysteresis loop. Once the system inhibits the bifurcation from the symmetric two-cell configuration toward the one-cell flow it can only switch between the asymmetric one-cell flows, never reaching the symmetric state.

This bifurcation appears only when rotating disk is aided by curved blades (see fig. 7.2). These blades increase the poloidal flow, making the ratio of the toroidal to the poloidal flow close to 1. This can also be achieved using straight blades, but the turbulent bifurcation has never been observed in this configuration – transition from the two-cell to the one-cell flow is continuous if straight blades are used. The importance of the blade curvature is probably due to the fact that it modifies the intensity with which the disks eject the flow radially.

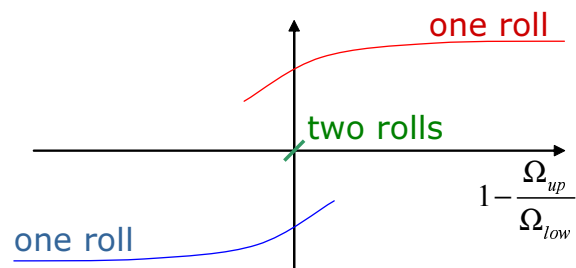


Figure 7.1: Hysteresis loop for bifurcation parameter – qualitative representation.

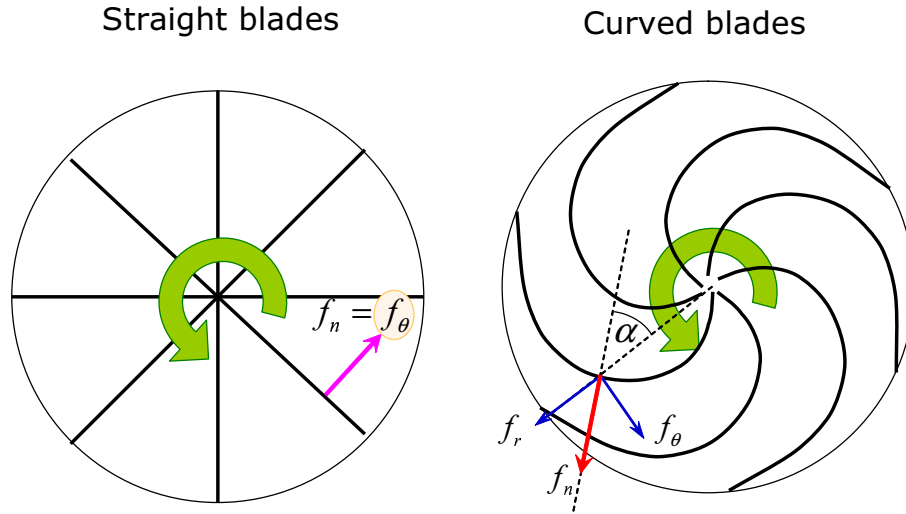


Figure 7.2: Schematic model of straight and curved blades. Vectors correspond to the forces which the blades exert on the flow. The angle α is defined as the line between a line joining a point on the blade's surface to the origin and the vector normal to the blade at this point.

This bifurcation, or coexistence, was discovered by Marié [54] at large Reynolds numbers – $Re \approx 10^6$ – a regime which cannot be attained by a realistic well-resolved numerical simulations on present-day computers. Ravelet *et al.* [74] recently discovered that this coexistence could also be observed at $Re \sim 5000$, which is accessible numerically. Modeling the blades in a numerical (especially spectral) code is not obvious and requires some approximations.

7.1.1 The effect of blades

Because we cannot implement the actual blades in our spectral code, we limit ourselves to modeling only their most important effect. We assume that these effects are: increasing the efficiency of the disks in forcing the flow and modulating the of radial injection rate of the flow near the rotating disks.

We model both effects by adding a bulk force which is axisymmetric and localized near the disks:

$$\mathbf{f}_\theta = f_n \sin(\alpha) \hat{\mathbf{e}}_\theta \quad (7.1a)$$

$$\mathbf{f}_r = f_n \cos(\alpha) \hat{\mathbf{e}}_r \quad (7.1b)$$

$$\mathbf{f}_n = f_n \hat{\mathbf{e}}_n = f_n \zeta(z) [(r\Omega(r) - u_\theta^{\text{axi}}) \sin(\alpha) - u_r^{\text{axi}} \cos(\alpha)]^3 \hat{\mathbf{e}}_n \quad (7.1c)$$

where forces $\mathbf{f}_r, \mathbf{f}_\theta, \mathbf{f}_n$ and angle α are represented on figure 7.2. Coefficient f_n corresponding to the intensity of forcing can be adjusted empirically. For a straight blade we have $\alpha = \frac{\pi}{2}$ and for curved blade $\alpha \equiv \alpha(r)$ is a parametric description of the blade's shape. For straight blades, the force is designed in such a way as to make the angular velocity closer to $\Omega(r)$ near the disks (this region is described by $\zeta(z)$); see figure 7.2-left. For curved blades, this force tends to anichlate the component of the relative (flow-blade) velocity which is normal to the blade

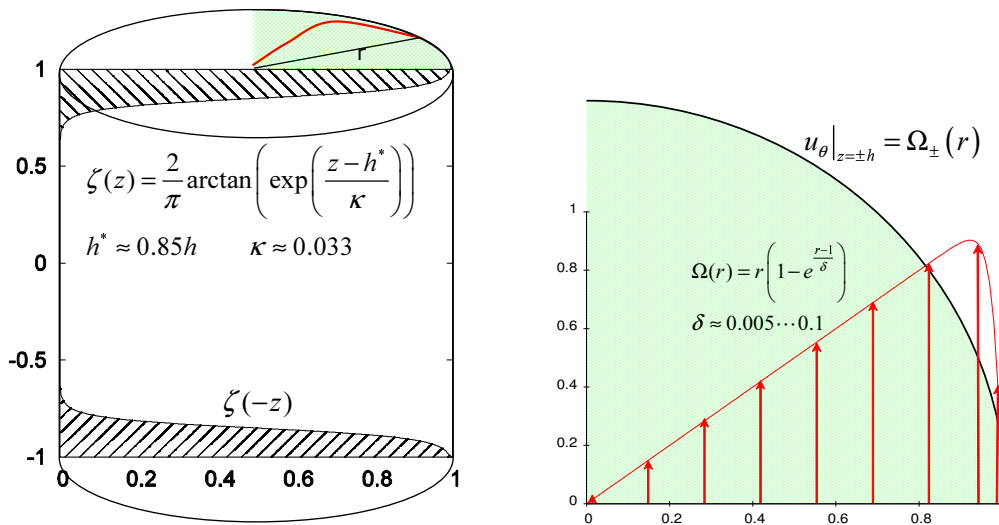


Figure 7.3: Left: Representation of limiting function $\zeta(z)$. Right: regularization profile $\Omega(r)$.

surface (see figure 7.2-right).

The envelope function $\zeta(z)$ is quite arbitrary and we have chosen the following shape (see figure 7.3-left)

$$\zeta(z) = \frac{2}{\pi} \arctan \left(\exp \left(\frac{|z| - h^*}{\kappa} \right) \right) \quad (7.2)$$

where h^* is the distance, from the cylinder mid-plane, at which the force starts to act on the flow. Parameter κ controls the steepness of the limiting function $\zeta(z)$.

The force defined in (7.1) is self-adapting to actual flow configuration. The nonlinearity $f_n \sim [\dots]^3$ of this force is designed to allow small deviations from the velocity that our forces tend to impose and, on the other hand, to act more strongly on larger deviations. These criteria are the result of empirical tests with differently behaving forces.

7.1.2 Preliminary results

At present we have tested our code only with the self-adapting force corresponding to straight blades ($\alpha = \pi/2$). According to observations of Ravelet *et al.* [74], we should not expect to reproduce the turbulent bifurcation in this configuration, but we can already check how well this force ensures the imposed velocity profile in the neighborhood of the rotating disks. At present we are interested in qualitative changes to the flow structure, especially the ratio of the poloidal to toroidal components of the velocity. All results presented in this subsection correspond to configurations with exactly counter-rotating disks ($s \equiv \frac{\Omega_+ = 1}{\Omega_-} = -1$).

Poloidal-to-toroidal ratio In the experimental setup, the role of blades is to make the intensities of the poloidal and toroidal flows comparable. The original, and main, motivation for this was to create a situation favorable for dynamo action in the VKS experiment. Experiments were performed in water to determine the optimal shape of the blades. It was found that the best forcing is obtained when the blades force the flow with their convex side. The turbulent bifurcation, in which we are interested, occurs, however, only when the blades force the fluid

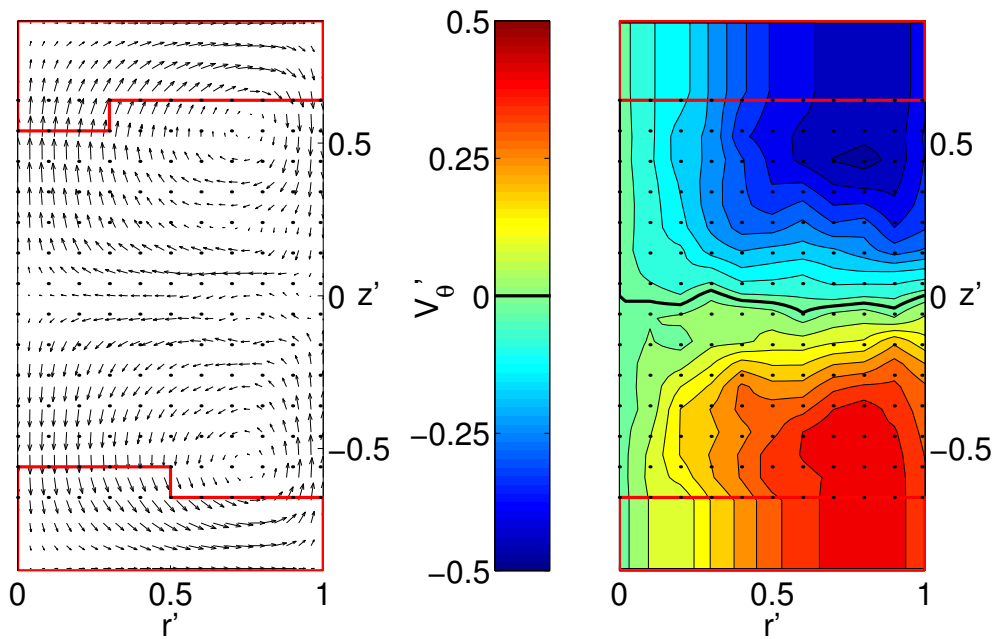


Figure 7.4: Configuration: Experimental data (laser Doppler velocimetry) for time-averaged flow for $Re = 1.25 \times 10^5$ (figure from Marié [54]). **Left:** poloidal velocity. **Right:** contour plot of angular velocity u_θ . Grid of black points correspond to locations at which the flow was probed. Red line separates the regions for which the data was obtained experimentally from those for which the data was obtained by extrapolation.

with their concave side.

Our aim is to obtain a flow whose qualitative topology is as close as possible to that observed experimentally. Figure 7.4 presents the time-averaged flow in the experimental configuration with straight blades [74]. The measurements have been obtained using laser Doppler velocimetry (LDV).

Axisymmetric flow at $Re = 500$ We have tested the effect of the forces modeling rotating blades on configurations with imposed axisymmetry ($Re = \{500, 1500\}$) and also on fully three-dimensional configurations ($Re = \{3000, 5000\}$). We have compared the simulation without internal bulk forces (*viscous forcing*) for several values of the Reynolds number, with simulations where the flow was additionally driven by the self-adapting force of different intensities (*inertial/bulk forcing*). In configurations with bulk forcing, the flow is strongly affected by the rotating disks only in a thin layer situated near the disks (fig. 7.5). For axisymmetric flow equation (6.6) shows that the poloidal potential ϕ generates the meridional velocity $u_r \hat{e}_r + u_z \hat{e}_z$ while the toroidal potential ψ generates the azimuthal velocity $u_\theta \hat{e}_\theta$. We will measure the intensity of these velocities by $\sup |u_r \hat{e}_r + u_z \hat{e}_z|$ and $\sup |u_\theta \hat{e}_\theta|$ ($\sup |u_\theta| = 1$ by our choice of nondimensionalization). The intensity of the poloidal flow is approximately 13% of that of the toroidal flow. The topology of this flow also matches the experimental observations concerning the flow forced using smooth disks. The situation remains qualitatively similar if one increases the Reynolds number. On figure 7.6 we present the flow structures for $Re = 1500$, a regime, in

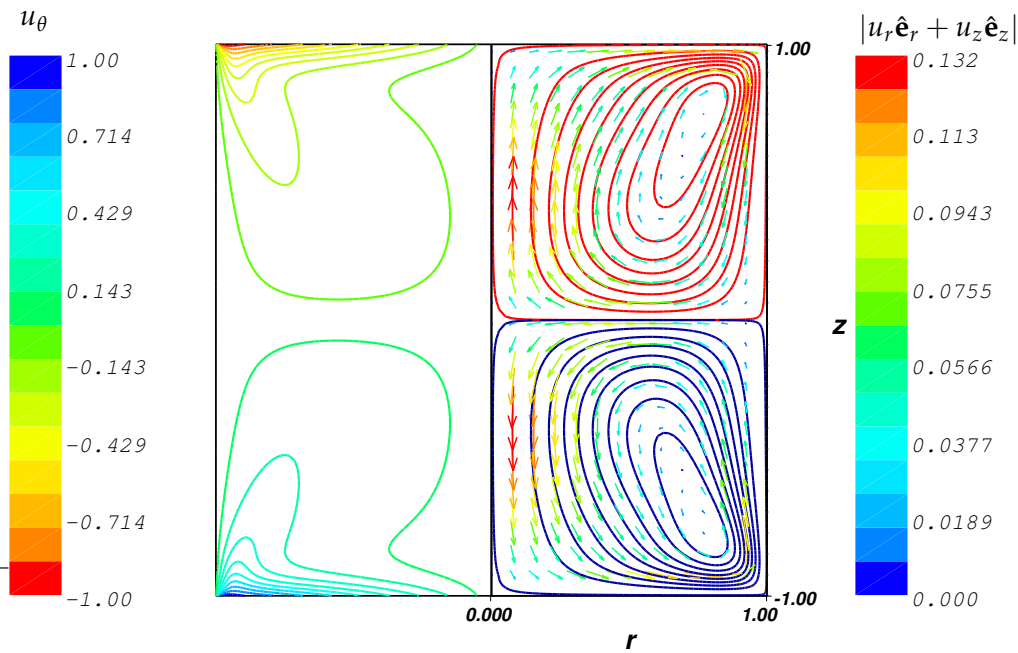


Figure 7.5: Configuration: imposed axisymmetry for $Re = 500$, $\delta = 0.006$, viscous forcing. **Left:** contours of u_θ . **Right:** contours of the poloidal stream function; clockwise (red/light) and counter-clockwise (blue/dark); arrows correspond to the poloidal velocity and they are colored according to their magnitude.

which the flow with imposed axisymmetry is steady. Even for Reynolds number $Re = 5000$, a regime in which the flow is three-dimensional and chaotic (figures 7.7, 7.14), the time-averaged flow (fig. 7.8), shows that the flow topology does not change significantly and the intensity of the poloidal flow still remains limited to only 13%.

The situation changes even if a weak bulk forcing is applied: the poloidal-to-toroidal ratio is increased up to 51% for the flow at $Re = 500$ (see fig. 7.9).

It is difficult to define a parameter corresponding to the actual intensity of forcing. The same coefficient f_n in (7.1) can correspond to strong forcing for low-Reynolds flows and to weak forcing for turbulent flows. We shall consider as weak the forcing which does not modify significantly the thickness of the boundary layer near the rotating disks. With viscous forcing the boundary layer is very thin (contours of u_θ are almost tangent to the cylinder bases). For extremely strong bulk forcing, velocity of the fluid selected by the function $\zeta(z)$ should be that of the corresponding rotating disks (contours of u_θ perpendicular to the cylinder bases).

The flow is strongest near the cylinder center, and results from a strong radial flow concentrated near the shear layer at $z = 0$. The toroidal flow is also much more equally distributed over the entire volume: the toroidal flow corresponding to 50% of the maximal flow speed reaches the area of the mid-plane shear layer. This new characteristic of the toroidal flow can also be seen on figure 7.4 corresponding to the experimental data.

One might expect that by further increasing the forcing intensity, this ratio might increase even further. This is, however, not the case, since the shear layer at the mid-plane of the cylinder is unstable with stronger forcing or for higher Reynolds numbers. As can be seen on figure 7.10,

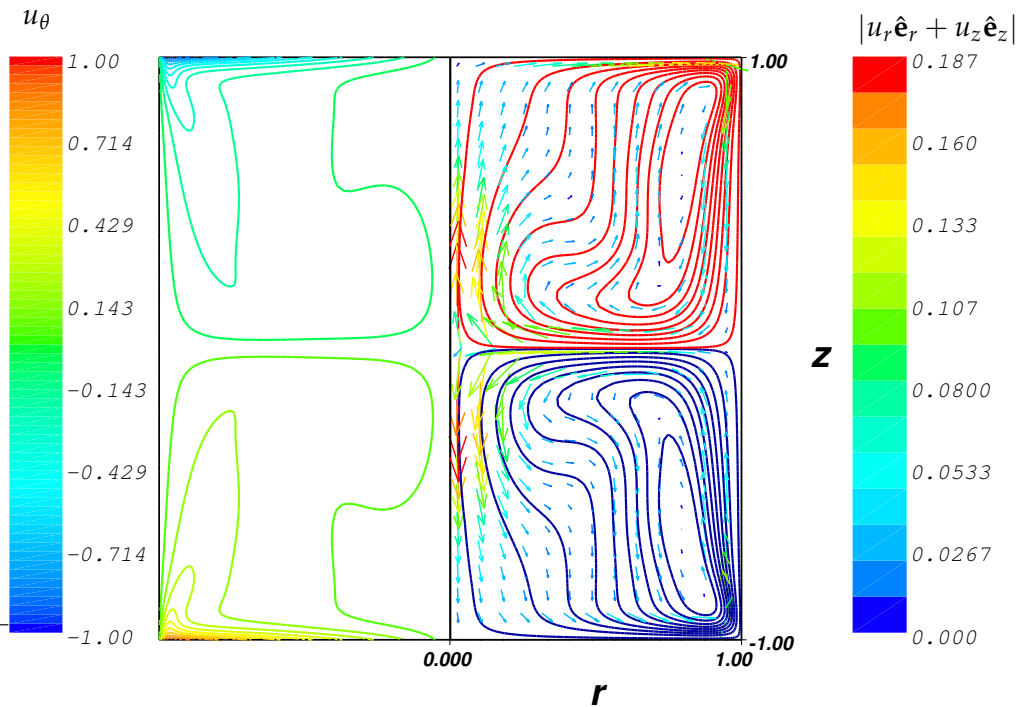


Figure 7.6: Configuration: imposed axisymmetry for $Re = 1500$, $\delta = 0.006$, viscous forcing. **Left:** contours of u_θ . **Right:** contours of the poloidal stream function; clockwise (red/light) and counter-clockwise (blue/dark); arrows correspond to the poloidal velocity and they are colored according to their magnitude.

for stronger forcing (still for $Re = 500$), the flow attains an oscillating (similarly to the flow at $Re = 5000$ without inertial forcing: see fig. 7.11) state for which the poloidal-to-toroidal ratio decreases to 45%.

The Reynolds number we use is based on the velocity of the boundary disks. A configuration with bulk forcing may be turbulent at the same Reynolds number for which a flow is laminar under viscous forcing. Since the self-adapting force changes in time and space during the simulation, it would be more intuitive to base the Reynolds number on, for example, the maximal velocity of the flow at some distance from the cylinder boundaries. This would give a better idea of how strong the forcing is or, by referring to the experiment, how efficient the blades are in forcing the fluid. Regardless of the Reynolds number, the flow with viscous forcing only can never have the same topology as the flow with inertial forcing.

In order to approach the turbulent regime of experimental configurations (for which $Re \approx 10^5$) we performed a simulation with weak inertial forcing for $Re = 3000$. The flow is not yet fully turbulent but is already very chaotic (see figures 7.15-left, 7.16 and the time series on figure 7.13). The flow structures, for time-averaged¹ state from which we extracted the axisymmetric mode, are represented on figure 7.12. Comparing to the time-averaged simulation performed

¹The flow was averaged over approximately 30 disk rotation periods.

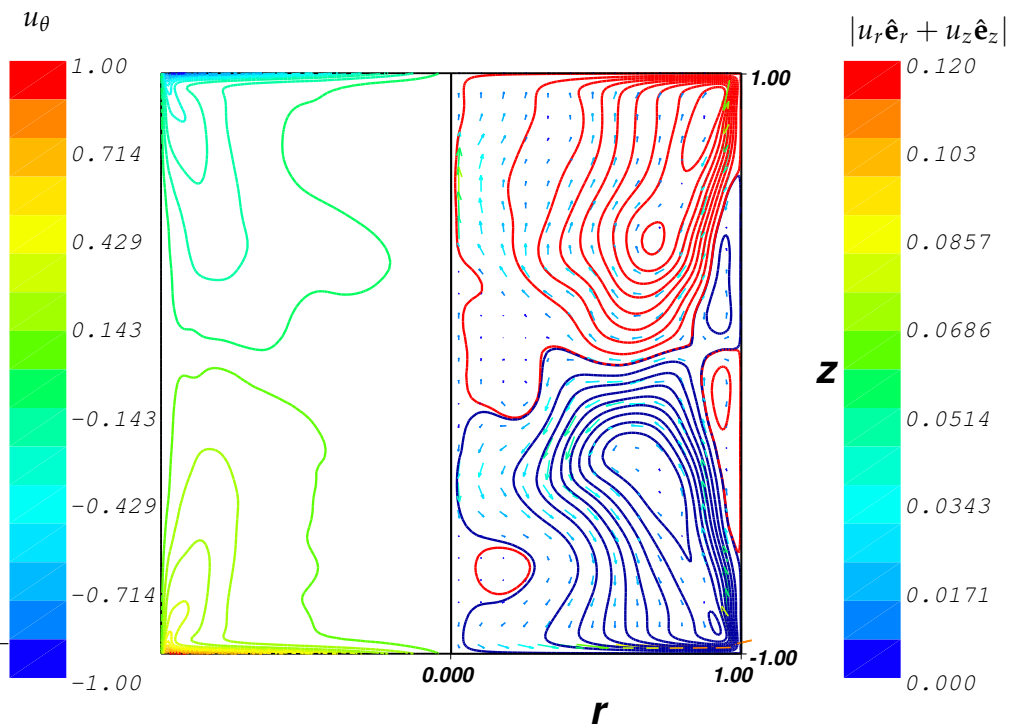


Figure 7.7: Configuration: three-dimensional simulation for $Re = 5000$, $\delta = 0.01$, viscous forcing. **Left:** contours of u_θ . **Right:** contours of the poloidal stream function; clockwise (red/light) and counter-clockwise (blue/dark); arrows correspond to the poloidal velocity and they are colored according to their magnitude.

at $Re = 5000$ with viscous forcing (fig. 7.8) the poloidal flow streamlines take on a more circular shape for bulk-forced flow at $Re = 3000$ (fig. 7.12). This also matches better the experimental measurements (fig. 7.4). The topology of the toroidal flow corresponds quite well to the experimental one. The flow undergoes strong angular rotation even near the shear layer (see fig. 7.15). This is very different from the situation with viscous forcing in which the strong toroidal flow remains limited to the neighborhood of the boundaries (fig. 7.14-right). We expect that with stronger forcing we should obtain a flow topology even more similar to the experimental one but, for numerical reasons, we could not check this yet.

We can conclude that the self-adapting force yields flow structures which are qualitatively similar to those observed in the experiment with disks reinforced by straight blades.

Turbulent bifurcation – perspectives At present, we have not reproduced the turbulent bifurcation observed by Marié [54] and Ravelet *et al.* [74]. As already mentioned, this bifurcation requires using curved blades. The self-adapting volume force corresponding to curved blades has not yet been tested. With straight blades, varying the rotation ratio of the disk from $s = -1$ to $s = -0.75$ displaces the shear layer toward the slower disk. The shear layer changes its position continuously with the rotation ratio s . This is in agreement with experimental observations made for straight blades (Marié [54]).

We plan to study the effect of self-adapting forces corresponding to curved blades and to

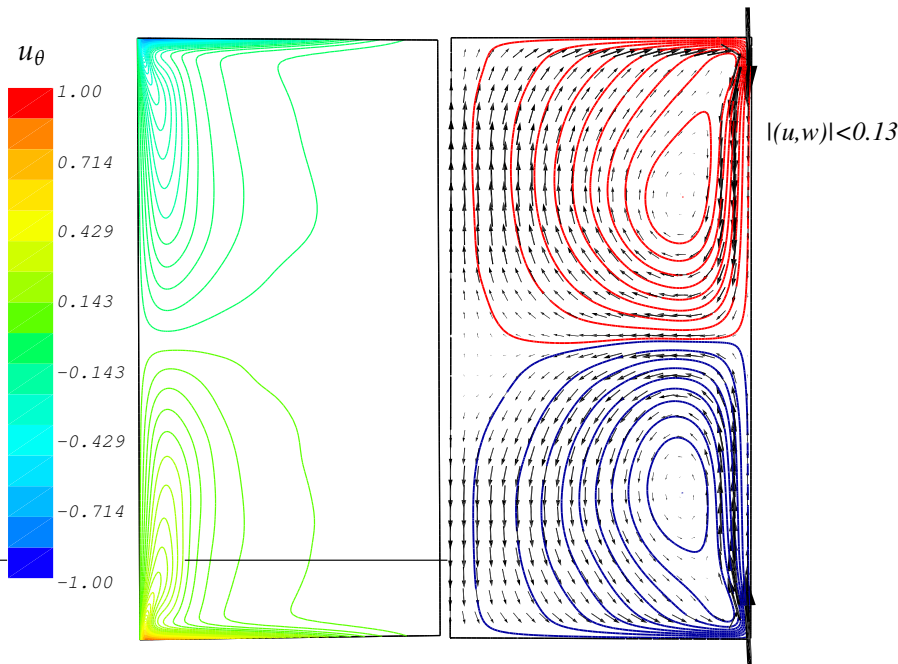


Figure 7.8: Configuration: three-dimensional, time-averaged flow for $Re = 5000$, $\delta = 0.01$, viscous forcing. **Left:** contours of u_θ . **Right:** contours of the poloidal stream function; clockwise (red/light) and counter-clockwise (blue/dark); arrows correspond to the poloidal velocity.

investigate other, possibly more stable, forms of volume forces. At present, the force adapts itself at each timestep without taking into account its form at the preceding time step. We will test different time integration schemes in order to select that which is the most effective and stable.

Stability/computational cost

Simulations without the self-adapting force were performed for $Re = 5000$ at resolution $(M = 128) \times (K = 120) \times (N = 90)$. Other parameters of this run were: $\delta = 0.01$, $\Delta t = 0.001$. Because only a few runs were executed, we are at present unsure whether the simulation could be performed with less resolution and/or a larger time step. For simulations without self-adapting forces, the timestep is conditioned by the stability of the nonlinear term of the Navier-Stokes equations.

When self-adapting forces are added, the stability of the time integration scheme is strongly affected. In order to run the simulation with a reasonable resolution and time-step, we had to run successive short-time simulations with forces whose intensity was progressively increased. The saturated state was simulated at $Re = 3000$, $\delta = 0.01$, $\Delta t = 0.001$.

In order to obtain time-averaged flows at least 100 rotations of cylinder disks were necessary. Each of the three-dimensional simulations ($Re = \{3000, 5000\}$) running on 64 IBM Power4 (1.3 GHz) processors took approximately 24 hours to complete 100 disk rotations. The code ran at approximately 2Gflops per single processor, i.e. 128 Gflops in total.

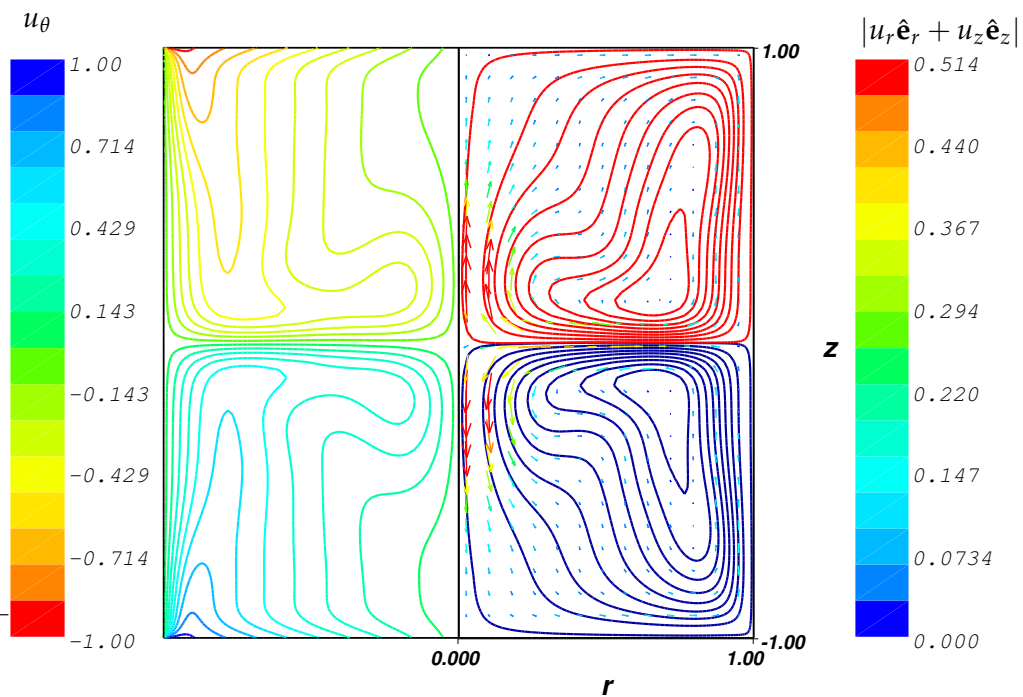


Figure 7.9: Configuration: imposed axisymmetry for $Re = 500$, $\delta = 0.006$, $\kappa = 0.033$, weak inertial forcing. **Left:** contours of u_θ . **Right:** contours of the poloidal stream function; clockwise (red/light) and counter-clockwise (blue/dark); arrows correspond to the poloidal velocity and they are colored according to their magnitude.

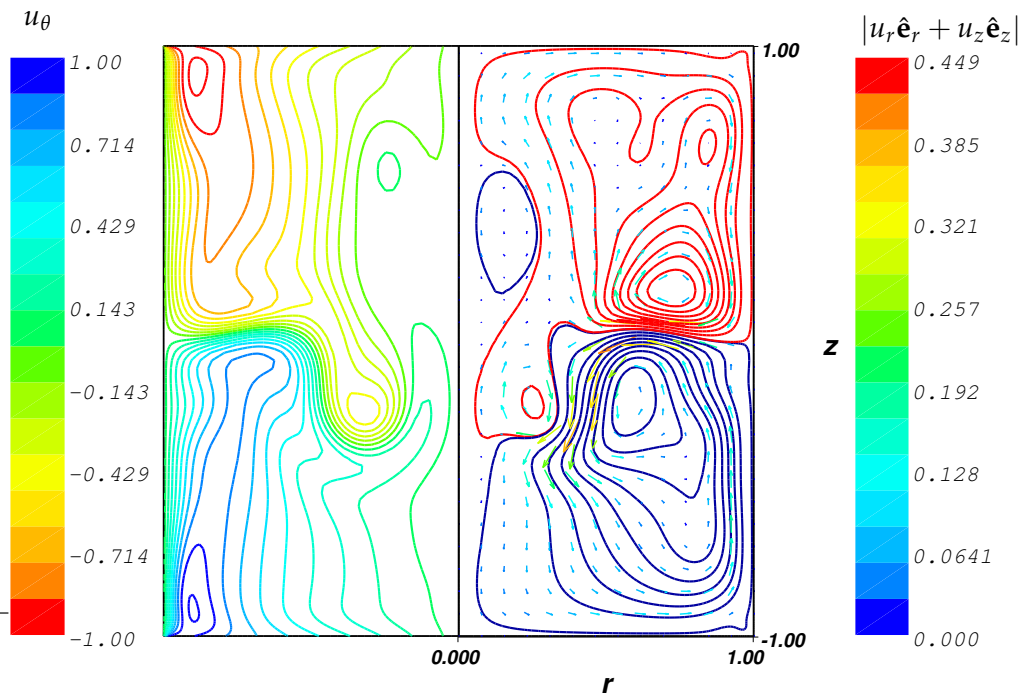


Figure 7.10: Configuration: imposed axisymmetry for $Re = 500$, $\delta = 0.006$, $\kappa = 0.033$, average inertial forcing. **Left:** contours of u_θ . **Right:** contours of the poloidal stream function; clockwise (red/light) and counter-clockwise (blue/dark); arrows correspond to the poloidal velocity and they are colored according to their magnitude.

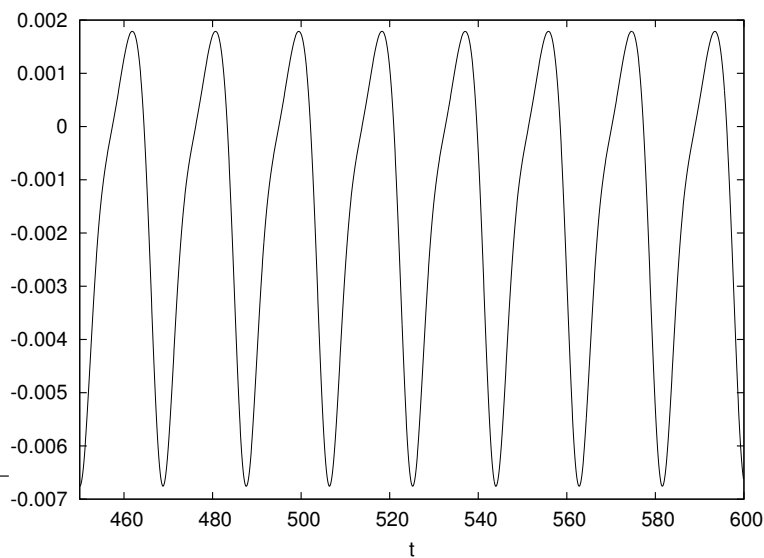


Figure 7.11: Time evolution of u_r at a particular flow location: imposed axisymmetry for $Re = 5000$, $\delta = 0.006$, viscous forcing.

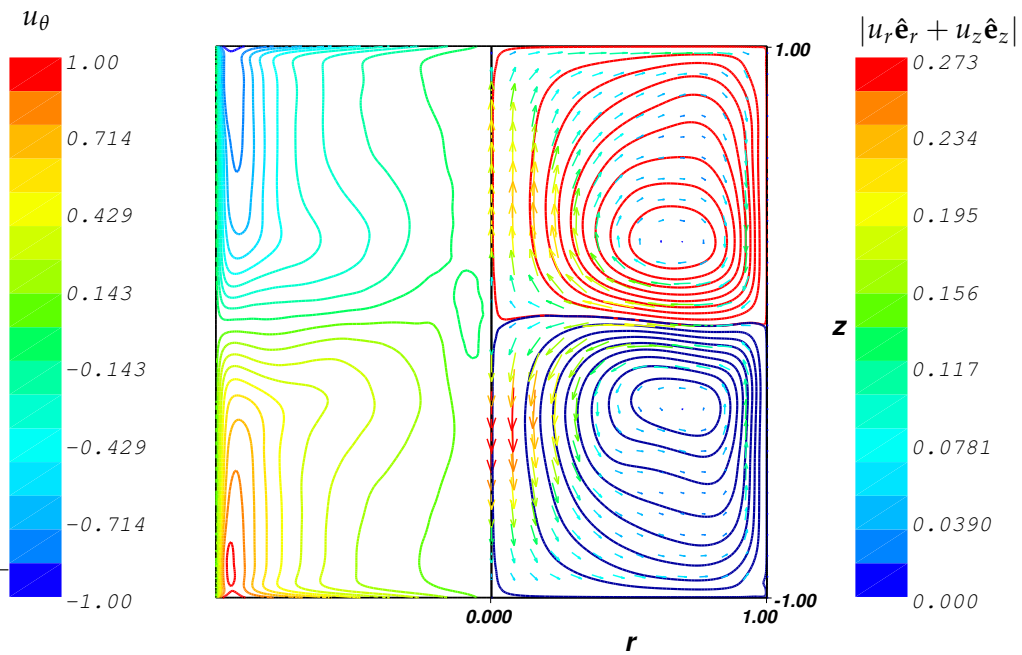


Figure 7.12: Configuration: three-dimensional, time-averaged flow for $Re = 3000$, $\delta = 0.01$, $\kappa = 0.033$, weak inertial forcing. **Left:** contours of u_θ . **Right:** contours of the poloidal stream function; clockwise (red/light) and counter-clockwise (blue/dark); arrows correspond to the poloidal velocity and they are colored according to their magnitude.

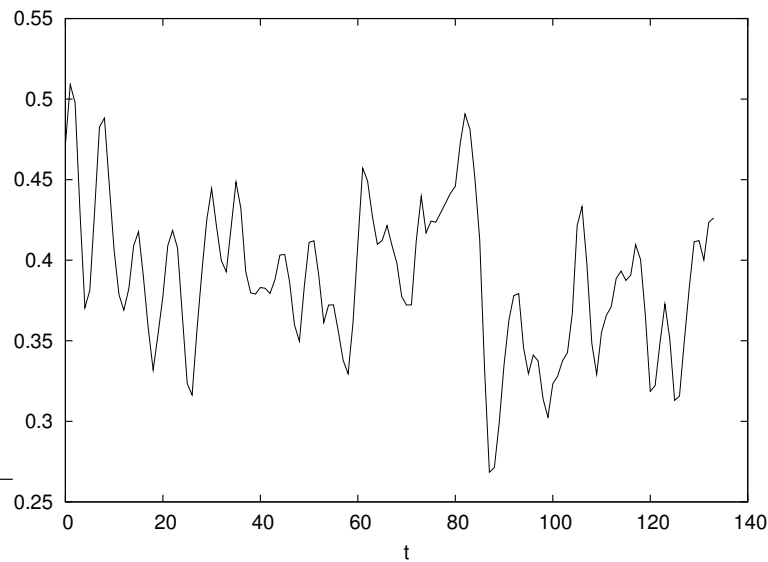


Figure 7.13: Time evolution of the maximal spectral coefficient of poloidal potential ϕ for Fourier mode $m = 0$: imposed axisymmetry for $Re = 3000$, $\delta = 0.01$, weak inertial forcing.

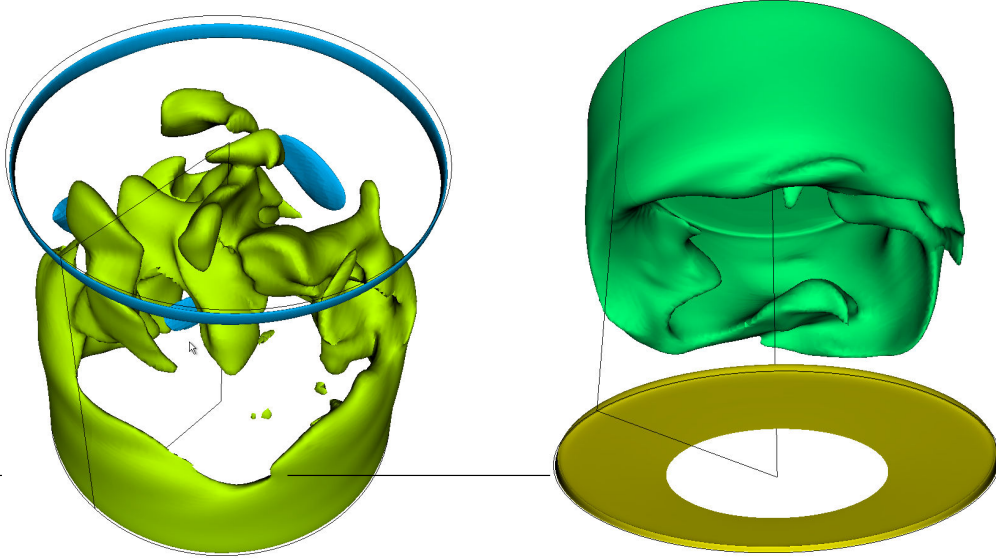


Figure 7.14: Configuration: instantaneous flow for $Re = 5000$, $\delta = 0.01$, viscous forcing. **Left:** isosurfaces of u_z ; 75% of min u_z (upper), 25% of max u_z (lower). **Right:** isosurfaces of u_θ ; 25% of max u_θ (upper), 75% of min u_θ (lower)

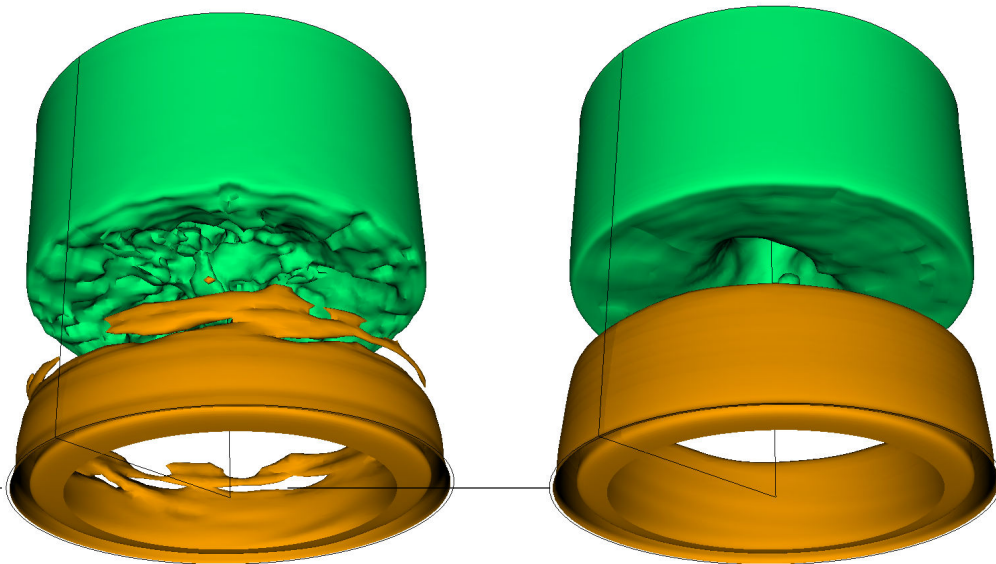


Figure 7.15: Configuration: $Re = 3000$, $\delta = 0.01$, weak inertial forcing. **Left:** isosurfaces of u_θ ; 75% of min u_θ (lower), 25% of max u_θ (upper). **Right:** isosurfaces of u_θ for time-averaged flow; 75% of min u_θ (lower), 25% of max u_θ (upper)

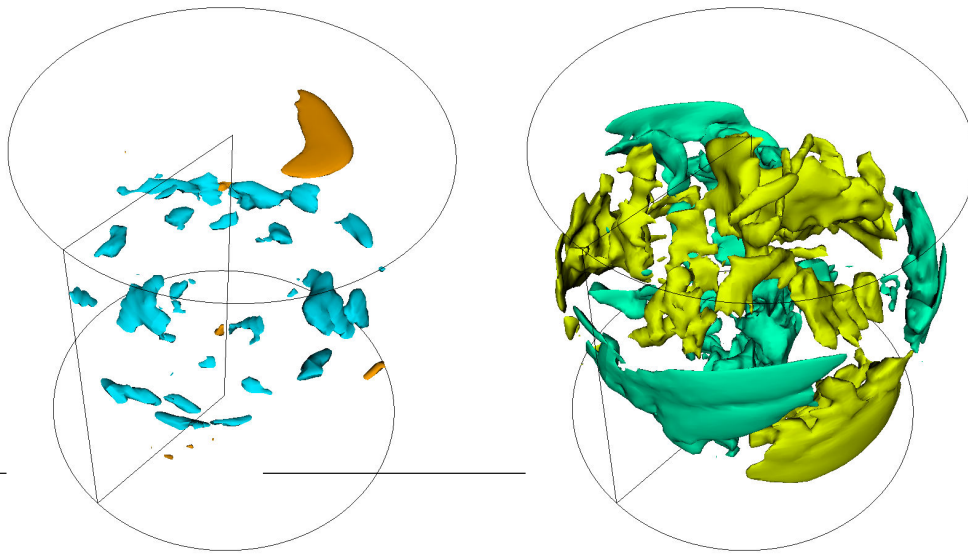


Figure 7.16: Configuration: $Re = 3000$, $\delta = 0.01$, weak inertial forcing. **Left:** isosurfaces of u_r ; 75% of min u_r (mid-plane), 75% of max u_r (near to the disks). **Right:** isosurfaces of u_z ; 75% of min u_z (green/dark), 75% of max u_z (yellow/light)

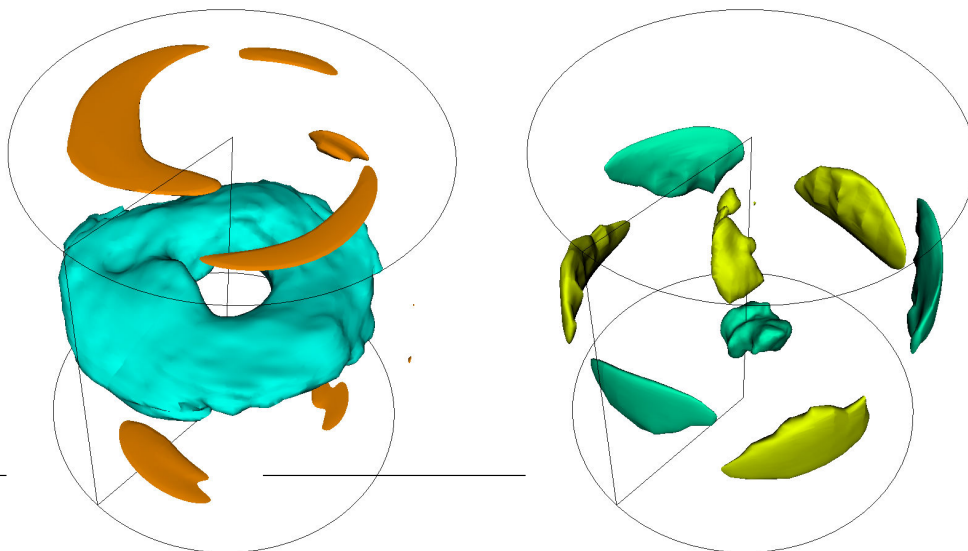


Figure 7.17: Configuration: time-averaged flow for $Re = 3000$, $\delta = 0.01$, weak inertial forcing. **Left:** isosurfaces of u_r ; 75% of min u_r (mid-plane), 75% of max u_r (near to the disks). **Right:** isosurfaces of u_z ; 75% of min u_z (green/dark), 75% of max u_z (yellow/light)

7.2 Axisymmetric turbulence

For two-dimensional turbulence in a Cartesian geometry, there exists a statistical description of the properties of these flows and of the conserved quantities. The goal of the project of N. Leprovost, B. Dubrulle, Chavanis and R. Monchaux ([45, 44, 60]) at CEA-Saclay is to establish equivalent relations for decaying axisymmetric turbulence.

7.2.1 Theoretical framework

The equations obeyed by the axisymmetric flow of an ideal fluid with cylindrical components (u_r, u_θ, u_z) are:

$$\partial_t u_r + u_r \partial_r u_r + u_z \partial_z u_r - \frac{u_\theta^2}{r} = -\frac{1}{\rho} \partial_r p, \quad (7.3a)$$

$$\partial_t u_\theta + u_r \partial_r u_\theta + u_z \partial_z u_\theta + \frac{u_\theta u_r}{r} = 0, \quad (7.3b)$$

$$\partial_t u_z + u_r \partial_r u_z + u_z \partial_z u_z = -\frac{1}{\rho} \partial_z p. \quad (7.3c)$$

where p is the pressure and ρ denotes the fluid density. To facilitate the comparison with the theory which uses specific notation, it is convenient to use the streamfunctions σ and η of the toroidal and poloidal components of the axisymmetric flow. We define:

$$\sigma = r u_\theta \quad (7.4a)$$

$$\xi = \frac{\omega}{r} \quad (7.4b)$$

$$y = \frac{r^2}{2} \quad (7.4c)$$

where $\omega = \boldsymbol{\omega} \cdot \hat{\mathbf{e}}_\theta$ is the vorticity and satisfies:

$$\omega = - \left[\frac{\partial_z^2}{r} + \partial_r \frac{\partial_r}{r} \right] \eta = - \left[\frac{1}{2y} \partial_z^2 + \partial_y^2 \right] \eta \Leftrightarrow \xi = -\Delta_* \eta \quad (7.5)$$

There exists a direct relation between the toroidal and poloidal potentials (ψ, ϕ)

$$\mathbf{u} = \nabla \times (\psi \hat{\mathbf{e}}_z) + \nabla \times \nabla \times (\phi \hat{\mathbf{e}}_z),$$

and the streamfunctions (σ, η) :

$$\sigma = -r \partial_r \psi \quad (7.6a)$$

$$\eta = -r \partial_r \phi \quad (7.6b)$$

We can rewrite (7.3) as:

$$\partial_t \sigma + \{\eta, \sigma\} = 0 \quad (7.7a)$$

$$\partial_t \xi + \{\eta, \xi\} = \partial_z \left(\frac{\sigma^2}{4y^2} \right) \quad (7.7b)$$

where $\{f, g\} \equiv \partial_y f \partial_z g - \partial_z f \partial_y g$ is the Poisson bracket.

For an ideal fluid undergoing no forcing, the following quantities are conserved over time:

- the energy:

$$\begin{aligned} E &= \frac{1}{2} \int u^2 d\mathbf{x} = \frac{1}{2} \int (u_r^2 + u_z^2) r dr dz + \frac{1}{2} \int u_\theta^2 r dr dz, \\ &= \frac{1}{2} \int \xi \eta dy dz + \frac{1}{4} \int \frac{\sigma^2}{y} dy dz \end{aligned} \quad (7.8)$$

- the Casimirs:

$$C = \int \mathcal{C}(\sigma) dy dz, \quad (7.9)$$

where \mathcal{C} is an arbitrary function (we will consider $\mathcal{C}(\sigma) \equiv C_n(\sigma) \equiv \sigma^n$).

- the helicity:

$$\begin{aligned} H &= \frac{1}{2\pi} \int \boldsymbol{\omega} \cdot \mathbf{u} r dr dz, \\ &= \int \xi \sigma dy dz. \end{aligned} \quad (7.10)$$

- the circulation:

$$\Gamma = \int \xi dy dz \quad (7.11)$$

Although when viscosity is included, these quantities are no longer conserved, it is interesting to investigate how they are dissipated. In addition it can be proved ([44], Monchaux *et al.* [60]) that the most probable flow for the steady solutions of (7.7) satisfy:

$$\sigma = F(\eta), \quad (7.12a)$$

$$-\Delta_* \eta = \xi = \frac{F(\eta)}{2y} F'(\eta) + g(\eta). \quad (7.12b)$$

where F and g are unknown functions. It remains to verify if, in the case of decaying turbulence, the relation (7.12a) is at least approximatively valid and if the hypothesis that $F(\eta) = \alpha\eta$ is a linear (or at least very simple) function is justified.

7.2.2 Experimental confirmations

The theory of two-dimensional turbulence in cylindrical geometry is formulated for an axisymmetric flow. It is not possible to impose axisymmetry of the turbulent flow in an experiment. It is, however, interesting to verify if the time-averaged three-dimensional turbulent flow obeys some of the predictions derived for the axisymmetric configuration. Its mean flow is axisymmetric so one can find corresponding poloidal and toroidal streamfunctions and verify whether there exists a correlation described by the function F present in (7.12a). The first experimental results, obtained using laser Doppler velocimetry in turbulent von Kármán flow² at $Re = O(10^5) - O(10^6)$, were recently obtained by Monchaux *et al.* [60] and show that there is a strong correlation between the streamfunctions σ and η of the time-averaged turbulent flow. The experimentally determined function F has been found to have the following form:

$$F(\eta) \approx a_1 \eta + a_3 \eta^3 \quad (7.13)$$

²Blades were placed on the rotating disks in order to ensure stronger forcing.

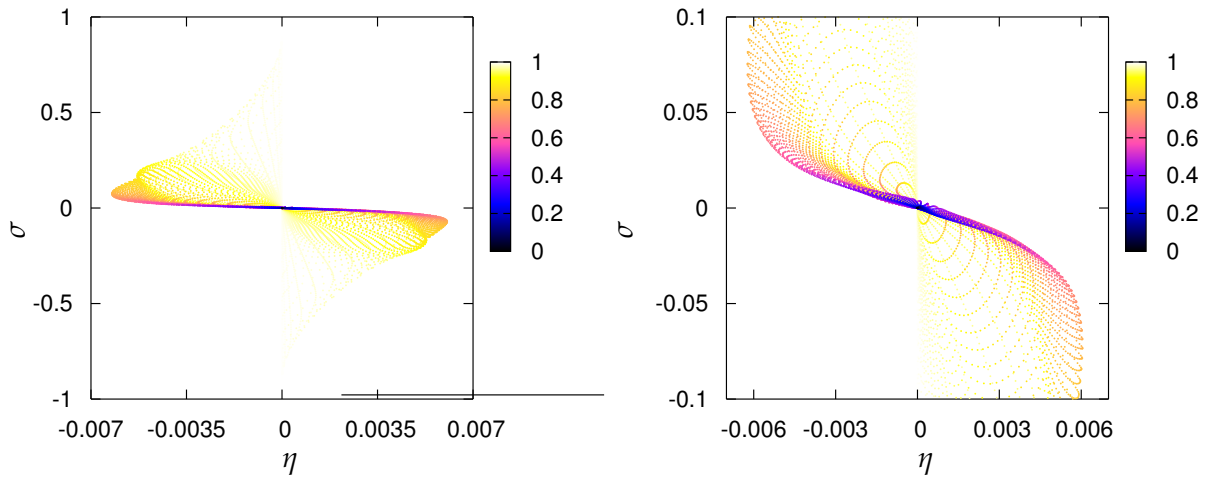


Figure 7.18: Scatterplot of $\sigma(\eta)$. Color denotes the distance from the cylinder center $d(r, z) = \max\{r, |z|\}$. Configuration: $Re = 5000$, time-averaged three-dimensional simulation (saturated chaotic state – see figs. 7.7 and 7.8), viscous forcing. **Left:** full domain; **Right:** enlargement of the locations distant from the cylinder boundaries ($d \ll 1$).

This relation seems to be valid only for the internal region of the container (i.e. sufficiently far from the boundaries). This is not surprising since the theory works for unforced fluid in the absence of boundaries. It should be noted that the form (7.13) represents only a general trend and the deviations from this formula increase when approaching the cylinder boundaries. It is not clear if the results obtained for the time-averaged flow can be considered relevant for a flow with imposed axisymmetry. The aim of our numerical study is to better understand the nature of the correlation (7.13) and to provide the results for configurations with imposed axisymmetry.

7.2.3 Numerical results

We have performed two kinds of analysis: for saturated and decaying turbulence at $Re = 5000$ with imposed axisymmetry, and for three-dimensional time-averaged flow at $Re = \{5000, 3000\}$. The flow at $Re = 3000$ was additionally forced by the self-adapting bulk force discussed in the preceding section (we will denote this configuration by $Re = 3000^*$). We will first present our observations concerning the three-dimensional time-averaged configurations since they correspond better to the experimental study of Monchaux *et al.* [60].

Time-averaged 3D

The flows that we have observed at $Re = 5000$ and $Re = 3000^*$ are not, strictly speaking, turbulent. They are rather chaotic. Up to this moment we have tested only fully developed chaotic states in three dimensions. We have not performed studies of decaying three-dimensional turbulence. It is impossible to obtain a reasonable time average of the decaying state at $Re = \{5000, 3000^*\}$. The flow becomes laminar in too quickly, which prevents us from computing a meaningful time average. This is also the reason for which the experimental measurements

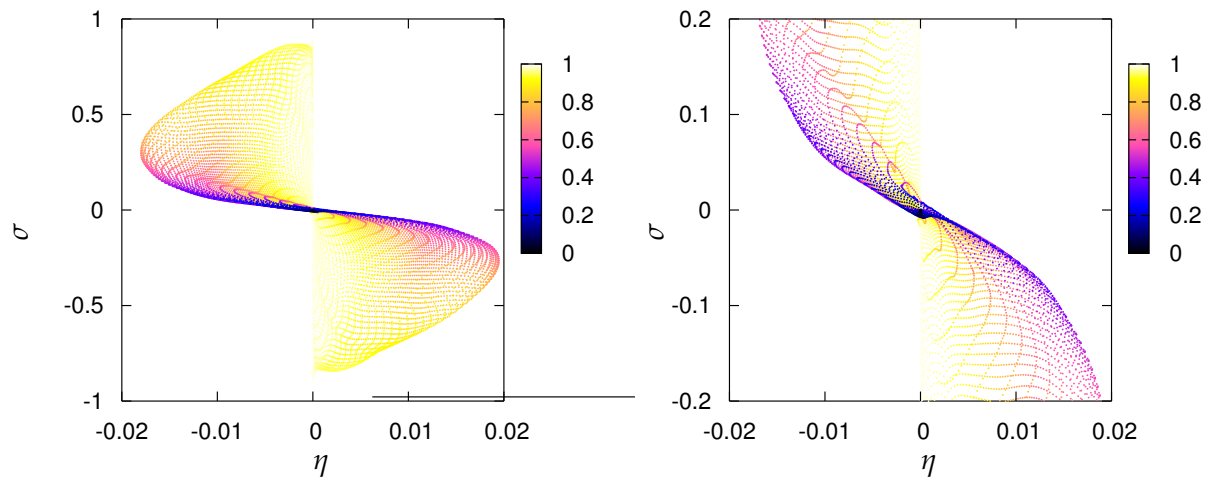


Figure 7.19: Scatterplot of $\sigma(\eta)$. Color denotes the distance from the cylinder center $d(r, z) = \max\{r, |z|\}$. Configuration: $Re = 3000^*$, time-averaged forced three-dimensional simulation (saturated chaotic state – see figs. 7.12), weak inertial forcing. **Left:** full domain; **Right:** enlargement of the locations distant from the cylinder boundaries ($d \ll 1$).

must be performed for very high Reynolds numbers.

The streamfunctions of the time-averaged flow corresponding to the fully developed state at $Re = 5000$ are represented on figure 7.8. The analogous structures are represented for $Re = 3000^*$ on figure 7.12. On figures 7.18 and 7.19 we show the scatter-plots of the toroidal streamfunction σ as a function of poloidal streamfunction η . The points are colored according to their distance d from the cylinder origin defined as:

$$d(r, z) = \max\{r, |z|\}$$

Violet (dark) points represent domain locations far from the boundaries ($d \ll 1$) and the yellow (light) points are situated near the boundaries $d \approx 1$. The figures 7.18 and 7.19 show that in the central region of the cylinder ($d \ll 1$) the streamfunctions obey approximately the relation:

$$\sigma \approx a_1\eta + a_3\eta^3 + \dots \quad (7.14)$$

This is especially true on 7.19-right which, for the reason explained in section 7.1, correspond better to the experimental configuration. These results agree with the experimental observations of Monchaux *et al.* [60]. The preliminary numerical study show, that even for forced flow the law $\sigma = F(\eta)$, predicted for unforced ideal fluid, seems to apply, at least approximatively, to the points distant from the boundaries. Our simulation of a forced three-dimensional flow corresponds well to the experimental configuration but is far from the mathematical model formulated for the two-dimensional flows. A study of a decaying turbulent (or nearly turbulent) flow in configuration with imposed axisymmetry should be, however, more relevant.

7.2.4 Imposed axisymmetry

We performed a simulation of decaying flow for $Re = 5000$ with imposed axisymmetry. The state was prepared by running a simulation without bulk forcing in an exactly counter-rotating configuration until we obtained saturated oscillating state (the axisymmetric flow at $Re = 5000$ is not yet chaotic). The disk rotation velocity was then set to zero. Figure 7.21 presents the flow at different times. The correlation between the toroidal and poloidal streamfunctions, far from the boundaries, is strongest on the middle figure ($t = 100$). This is probably because just after stopping the disks ($t = 10$) the flow still remembers the forced situation. On the other hand, in the later figure ($t = 200$) the flow near the cylinder origin almost disappears. The structures present near the boundaries are not directly correlated at any time.

The analysis performed using scatterplots (see 7.20) also confirms that the best correlation is obtained for time $t = 100$ when the structures far from the boundaries are still present and are not yet dominated by the vortices near the boundaries. The figure corresponding to $t = 200$ seems also to display the relation (7.14), but, enlargement shows that the correlation is already very perturbed near the cylinder origin. Figure 7.22 presents superposed poloidal (black contours) and toroidal (color) streamfunctions for times $t = \{10, 100, 200\}$. It is clear that the best correlation is realized for $t = 100$.

We expect that for more turbulent flows, several small-scale vortices should be produced by the flow and that their decay should be slower. The influence of boundaries on the decaying vortices should also decrease for higher Reynolds numbers. In the limit, in an ideal fluid the vortices should no longer feel the boundaries.

Our analysis, performed on an initially oscillating but not chaotic flow, qualitatively confirms that the unforced vortices, unperturbed by the boundaries, obey (but only approximately) the relation (7.14). In a viscous flow, in the presence of the boundaries, the conditions favorable for satisfaction of (7.14) can be realized only over a relatively short time.

We plan to extend our analysis of this problem by studying higher Reynolds numbers and also initial conditions for decaying flow prepared using bulk forcing simulating rotating blades. We hope that this will allow us to better understand the influence on (7.12a) of the forcing, the viscosity, and of the boundaries as well as to write more precisely the nature of this relation. We will also determine how quantities which are conserved in the ideal fluid are dissipated in the presence of viscosity. Finally, we will compare the time average of our 3D calculated fields with the experimental measurements of averaged velocities obtained by laser-Doppler velocimetry.

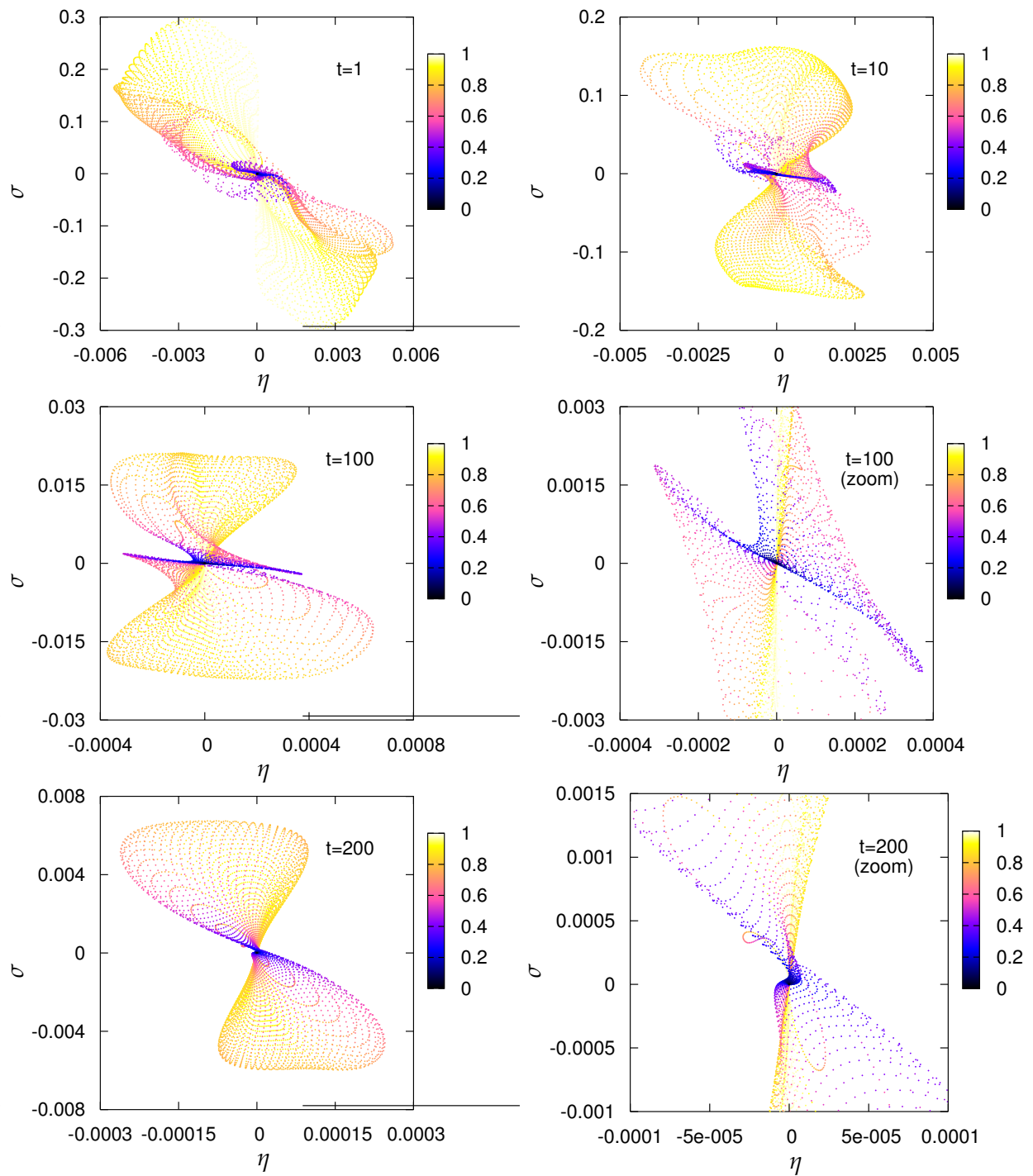


Figure 7.20: Scatterplot of $\sigma(\eta)$. Color denotes the distance from the cylinder center $d(r,z) = \max\{r, |z|\}$. Figures from top left to bottom right correspond to successive moments of decaying flow at $Re = 5000$ with viscous forcing and imposed axisymmetry (see also fig. 7.21).

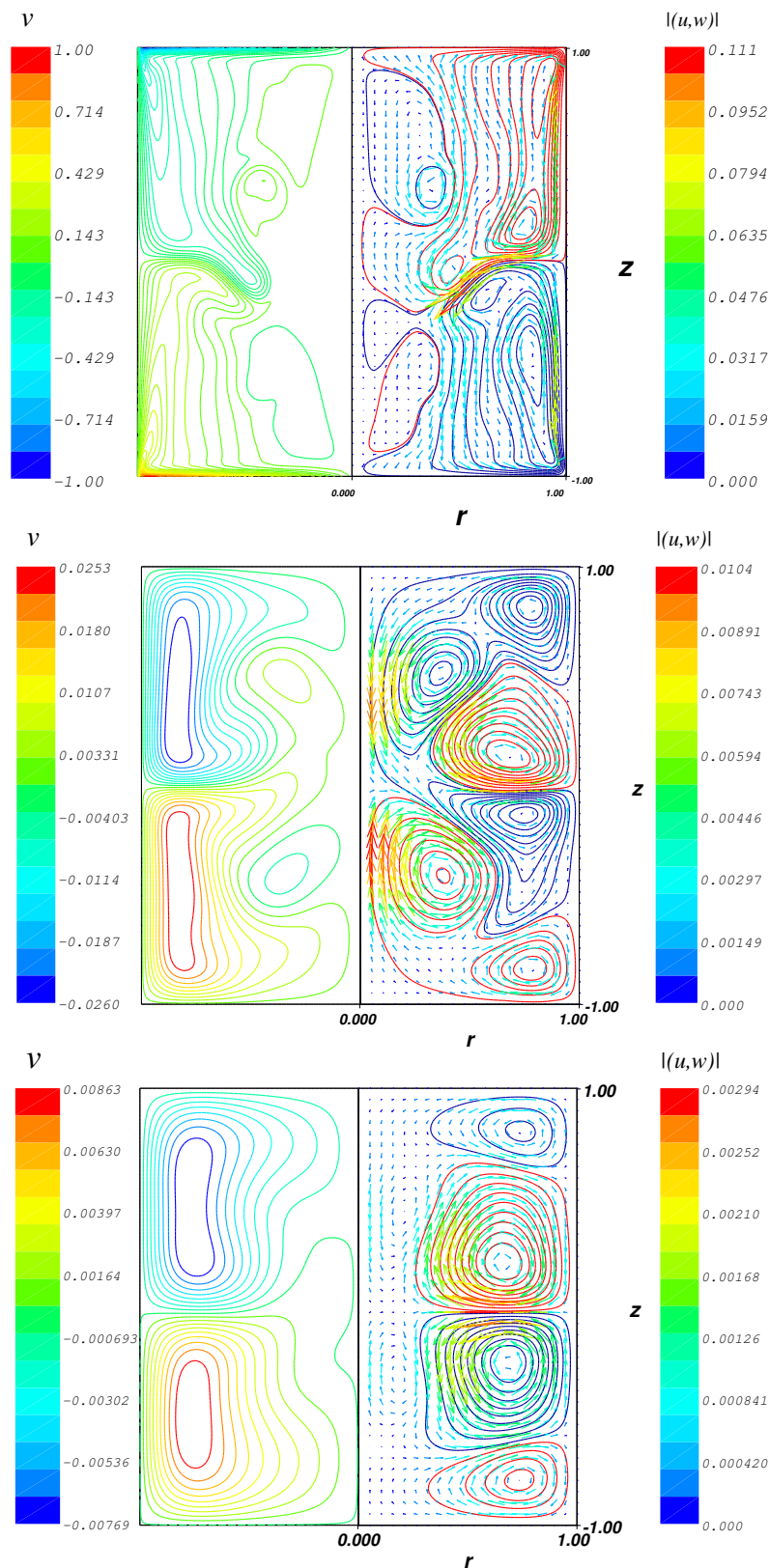


Figure 7.21: Successive states (from top to bottom) $t = \{1, 100, 200\}$ of decaying flow with viscous forcing and imposed axisymmetry for $Re = 5000$. Left: contours of toroidal streamfunction σ . Right: contours of poloidal streamfunction η .

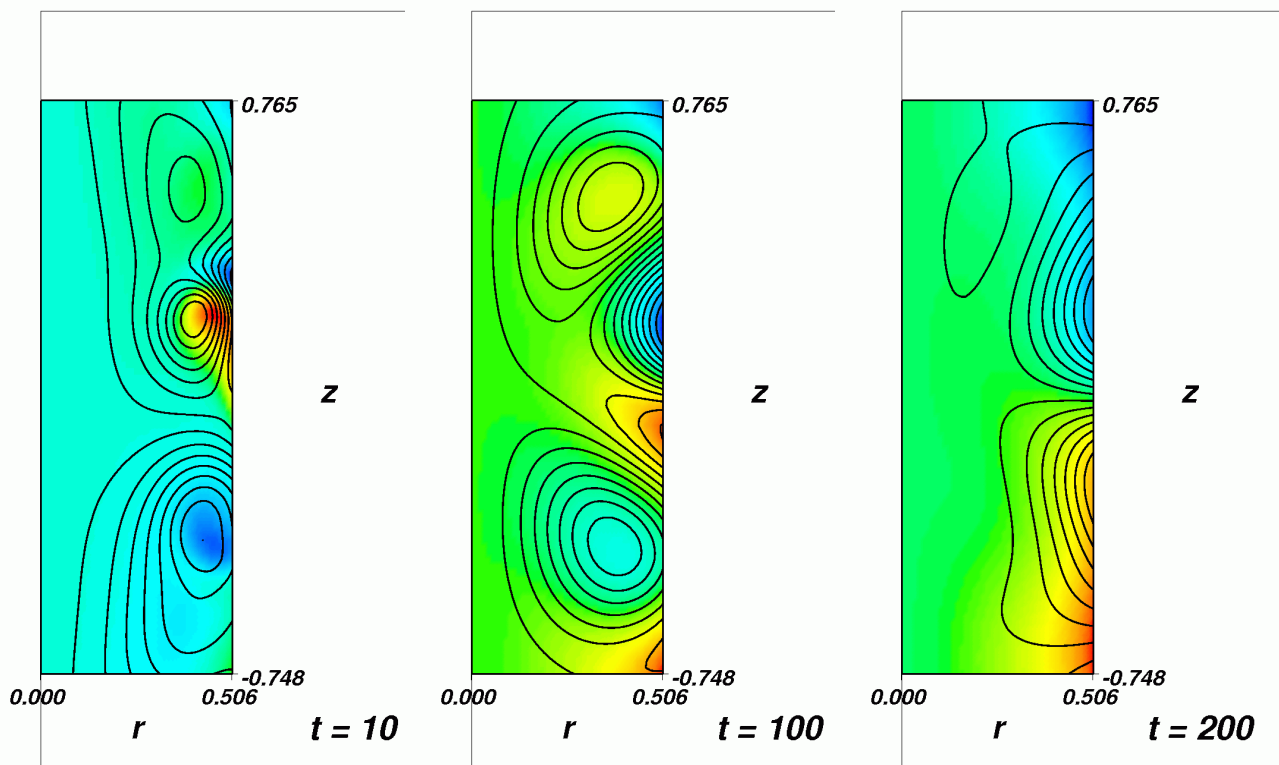


Figure 7.22: Successive states (from left to right) $t = \{10, 100, 200\}$ of decaying flow of imposed axisymmetry for $Re = 5000$ (viscous forcing). Contours of the poloidal streamfunction η are superposed with the toroidal streamfunction σ represented by the color map. The region of interest is $(r < 0.5, |z| < 0.75)$; the extent of the entire domain is $(r \leq 1, |z| \leq 1)$.

Chapter 8

Concluding remarks

Brief review

This work, motivated by a need for a numerical tool adequate for investigating the dynamo effect in cylindrical von Kármán flow, concentrate on developing of necessary numerical tools that could be applied to this phenomenon. The level of complexity of this problem required us to limit ourselves only to the most important and decisive aspects of the project undertaken. The most important element necessary to solve the equations of magnetohydrodynamics in the geometry of a finite cylinder is the developpment of a solver guaranteeing the solenoidal character of both velocity and magnetic fields. In three dimensions this is never a trivial task.

We presented throughout this dissertation a pseudo-spectral method for solving the three-dimensional incompressible Navier-Stokes equation in potential poloidal-toroidal formulation. We believe that this method can be further extended to the magnetic problem since the induction equation governing evolution of the magnetic field has a simpler structure than the Navier-Stokes equation and the method presented can be almost directly applied to this case. The main difficulty concerning inclusion of the magnetic field into the existing solver is satisfaction of the matching conditions between its internal (inside the cylinder) and external part (which extends to infinity). We developed at theoretical and algorithmic level a novel method for dealing with this problem and we demonstrated the idea of including it into the method presented for a purely hydrodynamical configuration.

The study, concerning solving the Navier-Stokes equations in the potential formulation can be considered as an independent and quite challenging problem. This kind of method, primarily introduced by Marques *et al.* [56] was already tested on a Raighlei-Benard convection problem. While preserving the original mathematical formulation proposed by Marques [55] we introduced a quite different methodology based on the *influence matrix* technique for dealing with the coupled boundary conditions emerging from the potential formulation. Such a method can be further extended to the magnetic problem.

Validation of the hydrodynamic code tested against well-documented problems in the literature proved that the poloidal-toroidal decomposition used in conjunction with the influence matrix approach can be successfully applied to impose the divergence-free character of time-dependent fields.

In view of future computationally expensive projects, the numerical code was parallelized

using the MPI protocol. This made it possible to simulate nearly turbulent flow for $Re = 5000$ with a spatial resolution of $128 \times 160 \times 90$.

Poloidal-toroidal decomposition

The potential formulation proposed by Marques in [55, 56] was further extended to the induction equation for the magnetic field. The boundary conditions ensuring correct matching between internal and external magnetic field were formulated. The evidence for the necessity of the *compatibility condition* was demonstrated for both the hydrodynamical and the magnetic problems written in poloidal-toroidal variables. This condition is a particular case of the condition derived by Marques [55] for general (and not only simply connected) domains.

The most important advantage of using the toroidal-poloidal decomposition is the exact (by construction) imposition of the divergence-free character of the velocity and magnetic fields. For the induction equation, the potential formulation make it possible to solve for the magnetic field without introducing an artificial (numeric) magnetic pressure which has no physical meaning. Additionally, using scalar functions instead of components of vector fields simplifies and homogenizes the usage of differential operators.

The most perturbing drawback of potential formulation are the high-order differential equations and coupled boundary conditions. This requires using complicated methods and makes the development and testing of tasks difficult to carry out.

Spectral solver

The spectral code described in this work solves the Navier-Stokes equation for an incompressible fluid in a finite cylinder geometry in the poloidal-toroidal formulation. The boundary conditions have been regularized to ensure a correct spatial convergence. The axis singularity inherent in the cylindrical coordinates is handled by using a regular basis of radial polynomials due to Matsushima & Marcus [58] having properties similar to those of the Legendre polynomials. This is, in our opinion, preferable to imposing regularity conditions on a general purpose spectral basis like Chebyshev polynomials up to some arbitrarily chosen polynomial order. Tests performed for analytical polynomial solutions to the single-step Stokes iteration with an adequate right-hand side showed that if the spectral solution is not truncated, then the solver reproduces analytical solutions with nearly machine precision. In a real situation when the solution is not a polynomial, the solver shows correct behavior manifested by an exponential convergence of spectral coefficients of the solution. The errors of satisfaction of the potential equations (corresponding to the curl and double curl of the Navier-Stokes equations) is very small $O(10^{-10})$ for the interior point. The less precise satisfaction of the equations at the boundary points is the consequence of singular character of solutions to the Stokes/Navier-Stokes problem in the cylinder corners. This singularity concerns, however, the double curl of the Navier-Stokes equations and not the equations themselves. The limit conditions are satisfied by our solver up to the machine precision.

This work proved that solving of high-order PDE with coupled boundary conditions is possible even if the mathematical description as well as the practical implementation are far from

simple. A method for preconditioning combined with the SVD decomposition of the *influence matrix* used for imposing some of the boundary conditions was proposed as a remedy for growth of the matrix condition number for higher spatial resolutions. It was reported by others (see Speetjens [81]) and also confirmed by ourselves that, without addressing this problem, the ill-conditioned influence matrix cannot be used for simulations requiring finer resolutions or smaller time steps.

Matching of the external magnetic field

We proposed a method for matching the internal and external magnetic fields for the magnetic problem in a spectral formulation. Similar method was already formulated for a spherical geometry by Dudley & James [22] and we generalized it to cylindrical geometry (and possibly others used for spectral methods). This method is based on decomposing the external solution in its natural basis of spherical harmonics for which boundary conditions can be defined separately for each basis function. We defined the problem of satisfaction of the continuity conditions at the cylinder's boundary by performing a change of coordinates from spherical to cylindrical. The resulting boundary conditions, which after this operation are no longer decoupled, can be solved by incorporating them into the influence matrix. The method also admits elimination of the external field from the solving protocol by performing a Schur decomposition of the influence matrix in the preprocessing step. Practical implementation of this method represents a near perspective and natural continuation for the work presented in this thesis.

Stability/Validation

The nonlinear term suffers from several types of errors which appear when one uses a pseudo-spectral evaluation of product of functions. These errors can seriously affect stability of the method in the case when a regular basis of polynomials is used in the radial direction. Such a regular basis is very sensitive to all operations, performed in spectral space, violating the regularity rules. We propose a remedy for this problem by using a modified methodology for pseudo-spectral evaluation of the nonlinear term. This method makes it possible to perform all potentially singular operations in the physical space where the singularity is not as severe as in the spectral space.

The nonlinear Navier-Stokes code has been tested on problems documented in the literature for which we obtained satisfactory results.

Applications & perspectives

The preliminary application of the code to the problems of decaying axisymmetric turbulence and to the *turbulent bifurcation* represent perspectives for future research.

In the context of axisymmetric decaying turbulence we discussed the validity of some theoretical predictions concerning correlation between two streamfunctions defined for an axisymmetric ideal fluid or decaying turbulence. The observed correlations seem, under several conditions, to confirm the theory. For a three-dimensional simulation followed by an analogous

study applied to the time-averaged flow we obtained results in qualitative agreement with experimental observations. The next step in advancing this work would be to determine how quantities like momentum, energy, helicity, which are conserved for a perfect fluid, are dissipated in the presence of viscosity.

In the context of the turbulent bifurcation the need for introducing internal boundaries in form of blades situated at the cylinder basis has been demonstrated by experiments. Curved blades are reported to be necessary to observe the turbulent bifurcation. Since inclusion of internal boundaries is not possible in a spectral code, we have introduced a mechanism which we believe to be capable of qualitatively reproducing the effect of blades used in the experimental setup. A self-adapting bulk forces has been incorporated into the explicit part of the time-integration scheme. The preliminary results obtained for a configuration modeling straight blades showed a big change in proportion between intensities of the poloidal and toroidal flows compared to the disk-driven flow. In experiment, the poloidal-to-toroidal ratio is approximately equal to 1. In our case, this ratio changed from ≈ 0.13 for disk-driven flow at $Re = 5000$, to ≈ 0.27 for the flow at $Re = 3000$ additionally driven by the bulk forces modeling blades. The topology of the time-averaged flow, simulated in this second configuration, also corresponds better to the topology of the experimental flow.

While we have not observed the turbulent bifurcation in few simulation performed up to now, the general changes observed in flow characteristics encourage us to continue this study. Investigating of a non-symmetric counter rotating configuration with volume forces modeling curved blades seems to be necessary in order to reproduce the experimental results.

Appendix A

Recursive formulas for radial polynomials

Recurrence formula for evaluating the radial polynomial $\mathcal{Q}_n^m(\alpha, \beta; r) \equiv \mathcal{Q}_n^m(r)$, corresponding to m^{th} Fourier mode, is given by:

$$\begin{aligned} & -(n - |m| + 2)(n + |m| + \beta + 1)(2n + \gamma - 3)\mathcal{Q}_{n+2}^m(r) \\ & + (2n + \gamma - 1) [(2n + \gamma - 3)(2n + \gamma + 1)r^2 - 2n(n + \gamma - 1) \\ & - 2|m|(|m| + \beta - 1) - (\gamma - 3)(\beta + 1)]\mathcal{Q}_n^m(r) \\ & - (n - |m| + \gamma - \beta - 2)(n + |m| + \gamma - 3)(2n + \gamma + 1)\mathcal{Q}_{n-2}^m = 0. \end{aligned} \quad (\text{A.1})$$

with starting values

$$\mathcal{Q}_m^m(r) = r^{|m|} \quad (\text{A.2a})$$

$$\mathcal{Q}_{m+2}^m(r) = \frac{2|m| + \gamma - 1}{2} \left(\frac{2|m| + \gamma + 1}{2|m| + \beta + 1} r^2 - 1 \right) r^{|m|}. \quad (\text{A.2b})$$

The recurrence relation for the normalizing coefficients I_n^m is:

$$I_n^m = \frac{(2n + \gamma - 5)(n - |m| + \gamma - \beta - 2)(n + |m| + \gamma - 3)}{(n - |m|)(n + |m| + \beta - 1)(2n + \gamma - 1)} I_{n-2}^m, \quad (\text{A.3})$$

where the starting values I_m^m are given by

$$I_m^m = \frac{\Gamma\left(|m| + \frac{\beta+1}{2}\right) \Gamma\left(\frac{\gamma-\beta}{2}\right)}{2\Gamma\left(|m| + \frac{\gamma+1}{2}\right)} \quad (\text{A.4})$$

and Γ is the gamma function: an extension of the factorial to complex and real number arguments.

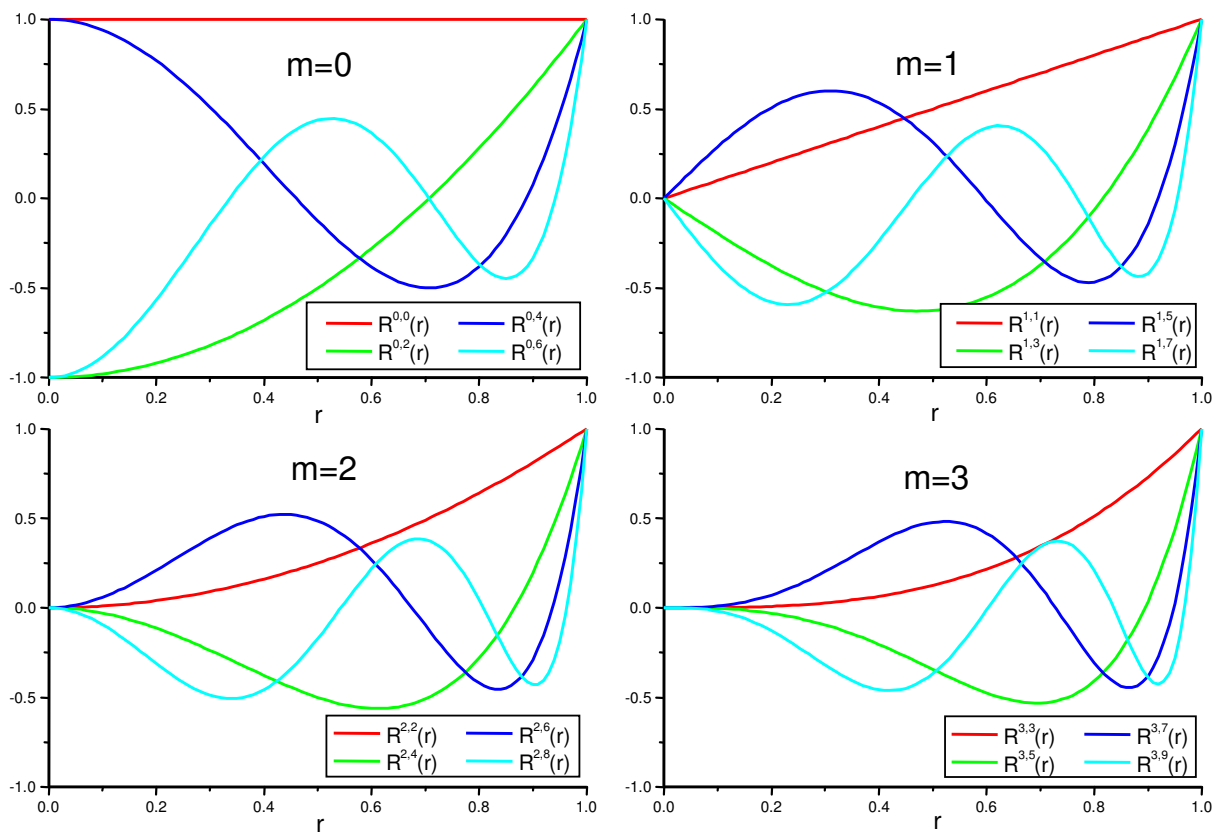


Figure A.1: Example of a few radial polynomials Q_n^m for Fourier modes $m = \{0,1,2,3\}$ (on figure: $R^{m,n}(r) \equiv Q_n^m(r)$).

Appendix B

Remarks concerning MPI parallelization

Most massively parallel machines use the distributed memory model i.e. each processor has its own amount of the accessible memory. This avoids some conflicts in accessing the particular memory location simultaneously by several processors. However, it requires data exchange to be realized over an inter-nodal network. The speed and the latency of that network is crucial for parallel applications requiring frequent exchange of large data.

The most computationally expensive part of a parallel pseudo-spectral code is evaluation of the nonlinear terms. The spectral→physical→spectral transformation must be performed at each timestep. This requires the entire data describing three-dimensional fields to be exchanged between processors at each timestep. In our case the total size of data is $9 \times M \times K \times N$, where M, K, N are the spatial resolutions in azimuthal, axial and radial directions, respectively. For higher resolution, this represents a very large data set.

In our pseudo-spectral code, parallelized according to the distributed memory model (here, the MPI protocol), each processor treats the data corresponding to a single (or a few) Fourier modes¹. More precisely, the processor treating the m^{th} Fourier mode uses the real parts of the poloidal potential $\hat{\phi}^m$ and the imaginary part of $\hat{\psi}^m$. Similarly, the processor treating the $-m^{\text{th}}$ Fourier mode uses real parts of the toroidal potential $\hat{\psi}^{-m}$ and the imaginary part of $\hat{\psi}^{-m}$. For azimuthal spatial resolution M , this makes it possible, to distribute the tasks between M processors.

The spectral↔physical transformations in the radial and axial directions can be performed independently by each processor. The FFT transform in the azimuthal direction requires, however, transposition of the entire data in order that each processor have access to all Fourier modes. There exist free parallel implementations of the FFT algorithm (like FFTW ver. <3.0) which performs this transposition, but we preferred to implement this operation ourselves and to apply after that step a serial FFT algorithm on each processor independently. This allowed us to reduce the number of data exchange operations to only **two** calls to the highly optimized MPI *collective communication* routines *MPI_Alltoall* per single simulation timestep.

On figure B.1 we present the schematic idea of distribution of the data between processors

¹Actually, since the real and imaginary parts of the Fourier modes of our spectral fields are decoupled, each processor can treat only half of the mode: either its real or imaginary part.

in spectral and physical space:

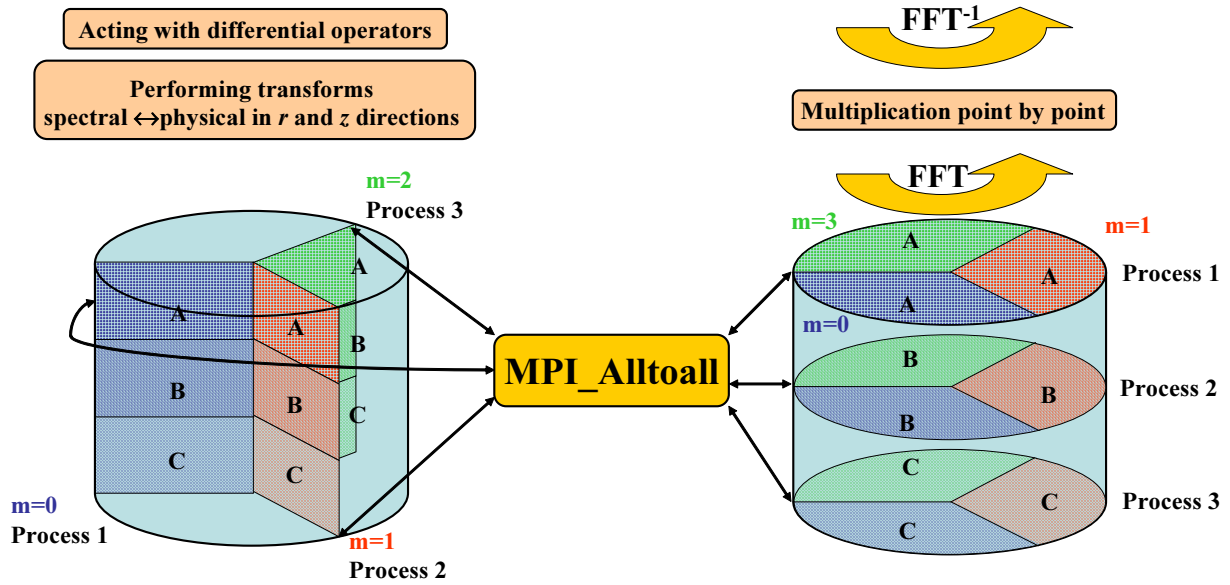


Figure B.1: Schematic model of distribution of the data between processors. Left: spectral space; Right: physical space.

Bibliography

- [1] BACKUS, G. 1958 A Class of Self-Sustaining Dissipative Spherical Dynamos. *Annals Phys.* **4**, 372–447.
- [2] BAROUD, C., PLAPP, B., SWINNEY, H. & SHE, Z. 2003 Scaling in three-dimensional and quasi-two-dimensional rotating turbulent flows. *Phys. Fluids* **15**, 2091.
- [3] BATCHELOR, G. K. 1951 Note on a class of solutions of the Navier-Stokes equations representing rotationally-symmetric flow. *Q. J. Mach. Appl. Maths.* **4**, 29.
- [4] BÖDEWADT, U. T. 1940 Die drehströmung über festem grunde. *Z. Angew. Math. Mech.* **20**, 241.
- [5] BEAM, R. M. & WARMING, R. F. 1980 Alternating direction implicit methods for parabolic equations with a mixed derivative. *SIAM J. of Sci. Stat. Comp.* **1**, 131–159.
- [6] BEAM, R. M. & WARMING, R. F. 1982 *Implicit numerical methods for the compressible Navier-Stokes and Euler equations*. von Kármán Institute Lecture Series 1982-04, rhode Saint Genese, Belgium.
- [7] BLACKBURN, H. M. & LOPEZ, J. M. 2000 Symmetry breaking of the flow in a cylinder driven by a rotating end wall **12**, 2698–2707.
- [8] BOTELLA, O. & PEYRET, R. 2001 Computing singular solution of the Navier-Stokes equation with the Chebyshev-collocation method. *Int. J. Num. Meth. Fluids* **36**, 125–163.
- [9] BOURGOIN, M., MARIÉ, L., PETRELIS, F., GASQUET, C., GUIGON, A., LUCIANI, J. B., MULIN, M., NAMER, F., BURGETE, J., CHIFFAUDEL, A., DAVIAUD, F., FAUVE, S., ODIER, P. & PINTON, J. F. 2002 Magnetohydrodynamics measurements in the von Kármán sodium experiment. *Phys. Fluids* **14**, 3046.
- [10] BRADY, J. F. & DURLOFSKY, L. 1987 On rotating disk flow. *J. Fluid Mech.* **175**, 363.
- [11] BULLARD, E. & GELLMAN, H. 1954 Homogeneous Dynamos and Terrestrial Magnetism. *Phil. Trans. Roy. Soc. London* **A247**, 213–278.
- [12] BUSSE, F. H. 1975 A Necessary Condition for the Geodynamo. *J. Geophys. Res.* **80**, 278–280.
- [13] CANUTO, C., HUSSAINI, M. Y., QUARTERONI, A. & ZANG, T. A. 1988 *Spectral Methods in Fluid Dynamics*. Springer-Verlag, New York.

- [14] COCHRAN, W. G. 1934 The flow due to a rotating disk. *Proc. Camb. Phil. Soc.* **30**, 365.
- [15] COLONIUS, T. 1997 Numerically nonreflecting boundary and interface conditions, for compressible flow and aeroacoustic computations. *AIAA J.* **35**, 1126.
- [16] COWLING, T. G. 1934 The magnetic field of sunspots. *Monthly Not. Roy. Astr. Soc.* **34**, 9–48.
- [17] DAUBE, O. 1992 Resolution of the 2D Navier-Stokes equations in velocity-vorticity form by means of an influence matrix technique. *J. Comput. Phys.* **103**, 402–414.
- [18] DAUBE, O. & SORENSEN, J. N. 1989 Simulation numérique de l'écoulement périodique axisymétrique dans une cavité cylindrique. *C. R. Acad. Sci. Paris* **308**, 463–469.
- [19] DEAN, W. & MONTAGNON, P. 1949 On the steady motion of viscous liquid in a corner. *Proc. Camb. Phil. Soc.* **45**, 389.
- [20] DIJKSTRA, D. & VAN HEJST, G. J. F. 1983 The flow between two finite rotating disks enclosed by a cylinder. *J. Fluid Mech.* **128**, 123.
- [21] DOBLER, W. & RÄDLER, K. H. 1998 An Integral Equation Approach to Kinematic Dynamo Models. *Geophys. Astrophys. Fluid Dyn.* **89**, 45–47.
- [22] DUDLEY, M. & JAMES, R. 1989 Time-dependent kinematic dynamos with stationary flows. *Proc. Roy. Soc. London A* **425**, 407–429.
- [23] ELSASSER, W. M. 1946 Induction effects in terrestrial magnetism. *Phys. Rev.* **69**, 106–116.
- [24] ESCUDIER, M. P. 1984 Observations of the flow produced in a cylindrical container by a rotating endwall. *Exp. Fluids* **2**, 189.
- [25] FOREST, C. B., BAYLISS, R. A., KENDRICK, R. D., NORNBURG, M. D., O'CONNELL, R. & SPENCE, E. J. 2002 Hydrodynamic and numerical modeling of a spherical homogeneous dynamo experiment. *Magnetohydrodynamics* **38**, 107.
- [26] GAILITIS, A., LIELAISIS, O., PLATACIS, E., DEMENTEV, S., CIFERSONS, A., GERBETH, G., GUNDRUM, T., STEFANI, F., CHRISTEN, M. & WILL, G. 2001 Magnetic field saturation in the Riga dynamo experiment. *Phys. Rev. Lett.* **86**, 3024.
- [27] GAUTHIER, G., GONDRET, P., MOISY, F. & RABAUD., M. 2002 Instabilities of the flow between co and counter-rotating disks. *J. Fluid Mech.* **473**, 1–21.
- [28] GAUTHIER, G., GONDRET, P. & RABAUD., M. 1999 Axisymmetric propagating vortices in the flow between a stationary and a rotating disk enclosed by a cylinder. *J. Fluid Mech.* **386**, 105–126.
- [29] GELFGAT, Y., BAR-YOSEPH, P. & SOLAN, A. 2001 Three-dimensional instability of axisymmetric flow in a rotating lid-cylinder enclosure. *J. Fluid Mech.* **438**, 363.
- [30] GEORGIU, G., OLSON, L. & SCHULTZ, W. 1973 The integrated singular basis function method for the stick-slip and the die-swell problems. *Int. J. Num. Meth. Fluids* **13**, 367–396.

- [31] GLATZMAIER, G. A. & ROBERTS, P. H. 1995 A three-dimensional self-consistent computer simulation of a geomagnetic field reversal. *Nature* **337**, 203.
- [32] GOLUB, G. H. & VAN LOAN, C. F. 1996 *Matrix Computations*. John Hopkins University Press, London.
- [33] GUEVREMONT, G., HABASHI, W. & HAFEZ, M. 1993 Finite element solution of the 3D compressible Navier-Stokes equations by velocity-vorticity method. *J. Comput. Phys.* **107**, 167–187.
- [34] HERZENBERG, A. 1958 Geomagnetic Dynamos. *Phil. Trans. Roy. Soc. London* **A250**, 543–585.
- [35] HILLS, C. & MOFFATT, H. 2000 Rotary honing : a variant of the Taylor paint-scraper problem. *J. Fluid Mech.* **418**, 119–135.
- [36] HIRSCH, C. 1982 *Numerical Computation of Internal and External Flows – Fundamentals of Numerical Discretization*, , vol. 1. John Wiley & Sons.
- [37] HORGAN, C. 1989 Decay estimates for the biharmonic equation with application to Saint-Venant principles in plane elasticity and Stokes flow. *Quart. Appl. Math.* **47**, 147–157.
- [38] ISKAKOV, A. B., DESCOMBES, S. & DORMY, E. 2004 An integro-differential formulation for magnetic induction in bounded domains: boundary element-finite volume method. *J. Comput. Phys.* **197**, 540–554.
- [39] JACKSON, J. D. 1999 *Classical Electrodynamics*, 3rd edn. John Wiley & Sons, Inc.
- [40] JUNG, S., STOREY, B., AUBERT, J. & SWINNEY, H. 2004 Nonextensive statistical mechanics for rotating quasi-two-dimensional turbulence. *Physica D* **193**, 252–264.
- [41] VON KÁRMÁN, T. 1921 Über laminare und turbulente Reibung. *Z. Angew. Math. Mech.* **1**, 233–252.
- [42] LARMOR, J. 1919 How could a rotating body such as the sun become a magnet? *Rep. Brit. Assoc. Adv. Sci.* **159**.
- [43] LEONARD, A. & WRAY, A. 1982 Ninth International Conference on Numerical Methods in Fluid Mechanics. Aachen.
- [44] LEPROVOST, N. 2004 Influence des petites échelles sur la dynamique à grande échelle en turbulence hydro et magnétohydrodynamique. PhD thesis.
- [45] LEPROVOST, N., DUBRULE, B. & CHAVANIS, P. H. 2005 Thermodynamics of MHD flows with axial symmetry. *Phys. Rev. E* **71**, 036311.
- [46] LOPEZ, J. 1990 Axisymmetric vortex breakdown: Part 1. Confined swirling flow. *J. Fluid Mech.* **221**, 533–552.
- [47] LOPEZ, J., MARQUES, F. & SHEN, J. 2002 An efficient spectral-projection method for the Navier-Stokes equations in cylindrical geometries - Three-dimensional cases. *J. Comput. Phys.* **176**, 384–401.

- [48] LOPEZ, J. & SHEN, J. 1998 An efficient spectral-projection method for the Navier-Stokes equations in cylindrical geometries - Axisymmetric cases. *J. Comput. Phys.* **139**, 308–326.
- [49] LOPEZ, J. M., HART, J. E., MARQUES, F., KITTELMAN, S. & SHEN, J. 2002 Instability and mode interactions in a differentially-driven rotating cylinder. *J. Fluid Mech.* **462**, 383–409.
- [50] LOPEZ, J. M., MARQUES, F. & SANCHEZ, J. 2001 Oscillatory modes in an enclosed swirling flow. *J. Fluid Mech.* **439**, 109–129.
- [51] LOWES, F. J. & WILKINSON, J. 1963 Geomagnetic Dynamo: A Laboratory Model. *Nature* **198**, 1158.
- [52] LUGT, H. J. & ABBOUD, M. 1987 Axisymmetric vortex breakdown with and without temperature effects in a container with a rotating lid. *J. Fluid Mech.* **179**, 179.
- [53] MARCUS, P. S. 1984 Simulation of Taylor-Couette flow. II. Numerical results for wavy-vortex flow with one travelling wave. *J. Fluid Mech.* **146**, 65–113.
- [54] MARIÉ, L. 2003 Transport de moment cinétique et de champ magnétique par un écoulement tourbillonnaire turbulent : influence de la rotation. PhD thesis, Université Paris 7.
- [55] MARQUES, F. 1990 On boundary conditions for velocity potentials in confined flows: Application to Couette flow. *Phys. Fluids A* **2**, 729.
- [56] MARQUES, F., NET, M., MASSAGUER, J. & MERCADER, I. 1993 Thermal convection in vertical cylinders. A method based on potentials. *Computer Methods in Applied Mechanics and Engineering* **110**, 157.
- [57] MARTIN-WITKOWSKI, L. & WALKER, J. S. 2002 Solutocapillary instabilities in liquid bridges. *Phys. Fluids* **14**, 2647–2656.
- [58] MATSUSHIMA, T. & MARCUS, P. 1995 A spectral method for polar coordinates. *J. Comput. Phys.* **120**, 365–374.
- [59] MOFFATT, H. 1964 Viscous and resistive eddies near a sharp corner. *J. Fluid Mech.* **18**, 1–18.
- [60] MONCHAUX, R., RAVELET, F., BORONSKI, P. & DUBRULLE, B. 2005 Characterisation of steady states of turbulent axisymmetric flows. In *accepted for congress: Fluctuations and Noise in Out of Equilibrium Systems*. Nice.
- [61] NAMIKAWA, T. & MATSUSHITA, S. 1970 Kinematic Dynamo Problem. *Geophys. J. Roy. Astr. Soc.* **19**, 319–415.
- [62] NGUYEN, S. 2005 Dynamique d'une interface en présence d'une singularité de contact solide/fluide. PhD thesis, Université Paris 11.
- [63] NORE, C., MOISY, F. & QUARTIER, L. 2005 Experimental observation of near-heteroclinic cycles in the von Kármán swirling flow. *submitted to Phys. Fluids* .
- [64] NORE, C., TARTAR, M., DAUBE, O. & TUCKERMAN, L. S. 2004 Survey of instability thresholds of flow between exactly counter-rotating disks. *J. Fluid Mech.* **511**, 45–65.

- [65] NORE, C., TUCKERMAN, L., DAUBE, O. & XIN, S. 2003 The 1:2 mode interaction in exactly counter-rotating von Kármán swirling flow. *J. Fluid Mech.* **477**, 51–88.
- [66] ORSZAG, S. A. 1970 Transform method for calculation of vector coupled sums: Application to the spectral form of the vorticity equation. *J. Atmosph. Sci.* **27**, 890–895.
- [67] ORSZAG, S. A. 1971 Numerical simulation of incompressible flows within simple boundaries: I. Galerkin (spectral) representations. *Stud. Appl. Math.* **50**, 293–327.
- [68] PARKER, E. N. 1955 Hydromagnetic dynamo models. *Astrophys. J.* **163**, 255–314.
- [69] PATERA, A. T. & ORSZAG, S. A. 1982 *Nonlinear problems: Present and Future*. A. R. Bishop, D. K. Campbell, B. Nicolaenko (North-Holland, Amsterdam).
- [70] PEARSON, C. E. 1965 Numerical solutions for the time-dependent viscous flow between two rotating coaxial disks. *J. Fluid Mech.* **21**, 623.
- [71] PONOMARENKO, Y. 1973 Theory of the hydromagnetic generator. *J. Appl. Mech. Tech. Phys* **14**, 775.
- [72] PRESS, W., TEUKOLSKY, S., VETTERLING, W. & FLANNERY, B. 1997 *Numerical recipes in C*. Cambridge Univ. Press.
- [73] PROCTOR, M. R. E. 1979 Necessary Conditions for the Magnetohydrodynamic Dynamo. *Geophys. Astrophys. Fluid Dyn.* **14**, 127–145.
- [74] RAVELET, F., MARIÉ, L., CHIFFAUDEL, A. & DAVIAUD, F. 2004 Multistability and memory effect in a highly turbulent flow: experimental evidence for a global bifurcation. *Phys. Rev. Lett.* **93**, 164501.
- [75] ROBERTS, P. 1967 *An Introduction to Magnetohydrodynamics*. Longmans Green, London.
- [76] DE SAINT VENANT, A. 1856 Mémoire sur la flexion de poutres. *J. de Mathématiques pures et appliquées* **1**, 83–96.
- [77] SCHULTZ, W., LEE, N.-Y. & BOYD, J. 1989 Chebyshev pseudospectral method for viscous flows with corner singularities. *J. Sci. Comput.* **4**, 1–24.
- [78] SHEN, W. & LOC, T. 1997 Numerical methods for unsteady 3D Navier-Stokes equations in velocity-vorticity form. *Computers & Fluids* **26**, 193–216.
- [79] SHEW, W. L., SISAN, D. R. & LATHROP, D. P. 2002 Mechanically forced and thermally driven flows in liquid sodium. *Magnetohydrodynamics* **38**, 121.
- [80] SOLOMON, L. 1968 *Principe de Saint-Venant*. Masson et Cie.
- [81] SPEETJENS, M. 2001 Three-dimensional Chaotic Advection in a Cylindrical Domain. PhD thesis, Eindhoven University of Technology.
- [82] STEGLITZ, R. & MÜLLER, U. 2001 Experimental demonstration of a homogenous two-scale dynamo. *Phys. Fluids* **13**, 561.

- [83] STEGLITZ, R. & MÜLLER, U. 2002 Experimental demonstration of a homogenous two-scale dynamo. *Magnetohydrodynamics* **38**, 27.
- [84] STEWARTSON, K. 1953 On the flow between two rotating coaxial discs. *Proc. Cambridge Phil. Soc.* **3**, 333–341.
- [85] TILGNER, A. 1997 A kinematic dynamo with a small scale velocity field. *Phys. Rev. A* **A 226**, 75–79.
- [86] TUCKERMAN, L. 1989 Divergence-free velocity fields in nonperiodic geometries. *J. Comput. Phys.* **80**, 403–441.
- [87] TUCKERMAN, L. 1989 Transformation of Matrices into Banded Form. *J. Comput. Phys.* **84**, 360–376.
- [88] VICHNEVETSKY, R. & BOWLE, J. 1982 *Fourier analysis of numerical approximations of Hyperbolic Equations*. SIAM, Stud. in Appl. Math., Philadelphia.
- [89] WILLIS, A. P. & BARENGHI, C. F. 2002 A Taylor-Couette Dynamo. *Astronomy & Astrophysics* **393**, 339–343.
- [90] YIN, Z. 2004 On final states of two-dimensional decaying turbulence. *Phys. Fluids* **16**, 4623–4634.
- [91] ZANDBERGEN, P. J. & DIJKSTRA, D. 1987 Von Kármán swirling flows. *Annu. Rev. Fluid Mech.* **19**, 465–491.